

**A resonant system  
for electromagnetic induction imaging  
of concealed conductive targets**

A thesis submitted to University College London  
for the degree of Doctor of Philosophy  
in the faculty of Mathematical and Physical Sciences

Roberta Guilizzoni



Department of Physics and Astronomy

March 2018

## Declaration

I, Roberta Guilizzoni, confirm that the work presented in this thesis is my own. Where information has been derived from other sources, I confirm that this has been indicated in the thesis.

Signed.....Roberta Guilizzoni

Date: 08/03/2018

"Enlightenment is when a wave realizes it is the ocean."

*Thich Nhat Hanh*

Ph.D. thesis

# **A resonant system for electromagnetic induction imaging of concealed conductive targets**

Roberta Guilizzoni

March 2018

First Supervisor: Prof. Ferruccio Renzoni

Second Supervisor: Dr. Stan Zochowski

## **Abstract**

The possibility of revealing the presence and identifying the nature of electrically conductive targets is of central interest in many fields, including security, medicine, industry, archaeology and geophysics. In many applications, these targets are electromagnetically shielded by other external materials and thus cannot be directly accessed and detected. Hence, material interrogation techniques are required that allow penetration through the shielding materials, in order for the targets to be identified.

Electromagnetic interrogation techniques represent a powerful solution to this challenge, as they enable penetration through conductive shields. Two resonant electromagnetic induction imaging (EII) methods, based on the use of LCR circuits, were developed in this research work. These proof-of-principle EII methods were based, respectively, on position-resolved-measurements of resonant frequency and Q-factor shifts, which occurred as a consequence of eddy current induction inside the conductive targets to be detected. The proposed techniques were applied to 2D imaging of conductive targets (having conductivities  $\sigma$  ranging from 0.54 to 59.77 MSm<sup>-1</sup>), both unshielded and shielded by an aluminium shield (1.5-mm-thick).

The experimental results achieved in the first part of this work highlighted a limitation in the LCR resonant circuits used for EII investigations, linked to the Q-factor low absolute

values (between 7 and 23). Therefore, investigations were conducted, leading to the implementation of an improved version of the EII system, based on active bandpass filters.

The sensitivity of the novel EII system was found to be larger by a factor of 3.5 compared to the previously used LCR-based system, when both systems were used for imaging copper. Additionally, the new system allowed achieving images with higher contrast.

The research work reported in this thesis led to establishing a proof-of-principle method for EII of conductive samples, also in the interesting scenario where the samples were shielded by conductive shields preventing them from being directly accessed.

## Acknowledgments

This research was funded by AWE and UCL Impact Studentship scheme. I would like to express my gratitude to my supervisor, Prof. Ferruccio Renzoni, who provided insight and expertise for this research. I am extremely grateful to Dr. Paul Bartlett for proofreading this thesis and providing helpful suggestions and contributions. Many thanks to Dr. Joseph Watson and Dr. Neil Gaspar (AWE) for taking part in discussions related to this research work. I would also like to thank my colleagues and friends Dr. Brendan Darrer and Dr. Luca Marmugi for their useful contributions and for sharing with me important moments of my PhD. I would like to thank also Dr. Stan Zochowski, Dr. Giorgio Savini, Cameron Deans, Soliman Edris, Derek Thomas, Jawad Rafid, Bernard Bristoll and Kelvin Vine, who all contributed to the progress of this research.

Last but not least, a huge 'GRAZIE' to my parents Dr. Marina Manca and Dr. Piero Guilizzoni, without whom the completion of this work most likely would not have been possible.

# Contents

<b>Abstract.....</b>	<b>4</b>
<b>Acknowledgements.....</b>	<b>6</b>
<b>Contents.....</b>	<b>7</b>
<b>List of Figures.....</b>	<b>10</b>
<b>List of Tables.....</b>	<b>24</b>
<b>List of Symbols.....</b>	<b>28</b>
<b>Nomenclature.....</b>	<b>29</b>
<b>1 Introduction.....</b>	<b>30</b>
<b>2 Theoretical principles.....</b>	<b>42</b>
2.1 Eddy current induction.....	42
2.2 Maxwell's equations and electromagnetic waves in conductors.....	49
2.3 2D imaging of shielded conductive samples.....	51
2.4 Eddy current detection in non-ferrous metals.....	53
<b>3 An LC resonant system for 2D imaging of conductive materials.....</b>	<b>58</b>
3.1 Description of the early stage experimental system.....	58
3.2 Resonant frequency changes due to eddy currents.....	62
3.3 Position-resolved measurements of the resonant frequency.....	65
3.4 Imaging copper, aluminium and steel samples.....	70
3.5 Towards optimisation of the imaging system .....	75
3.6 Comparison between Q-factor and resonant frequency measurements.....	79
3.7 Discussion and conclusions.....	83
<b>4 An automated Electromagnetic Induction interrogation system.....</b>	<b>84</b>
4.1 Description of the initial experimental apparatus.....	84
4.2 Experimental procedure for 2D imaging of metallic samples.....	86
4.3 Improvements to the initial LC system.....	89

4.4	<i>Description of the LabVIEW program.....</i>	<i>92</i>
<b>5</b>	<b><i>2D imaging of unshielded conductive samples.....</i></b>	<b><i>96</i></b>
5.1	<i>Study of the influence of lift-off on resonant frequency and Q-factor measurements.....</i>	<i>96</i>
5.1.1	<i>Description of the experimental procedure.....</i>	<i>97</i>
5.1.2	<i>Results and discussion.....</i>	<i>98</i>
5.2	<i>Imaging of high-conductivity samples made of copper and aluminium....</i>	<i>100</i>
5.2.1	<i>Description of the experimental procedure.....</i>	<i>100</i>
5.2.2	<i>Results and discussion.....</i>	<i>100</i>
5.3	<i>Material characterisation: comparison between resonant frequency and Q-factor techniques.....</i>	<i>103</i>
5.3.1	<i>Description of the experimental procedure.....</i>	<i>103</i>
5.3.2	<i>Results and discussion.....</i>	<i>106</i>
	5.3.2.1 <i>High-conductivity metals.....</i>	<i>109</i>
	5.3.2.2 <i>Low-conductivity metals.....</i>	<i>110</i>
5.4	<i>Edge estimation with resonant frequency and Q-factor techniques.....</i>	<i>118</i>
5.4.1	<i>Description of the experimental procedure.....</i>	<i>119</i>
5.4.2	<i>Results and discussion.....</i>	<i>121</i>
5.5	<i>LCR circuit optimisation.....</i>	<i>127</i>
5.5.1	<i>Description of the experimental procedure.....</i>	<i>128</i>
5.5.2	<i>Results and discussion.....</i>	<i>130</i>
5.6	<i>Resolution study.....</i>	<i>133</i>
5.6.1	<i>Description of the experimental procedure.....</i>	<i>134</i>
5.6.2	<i>Results and discussion.....</i>	<i>135</i>
<b>6</b>	<b><i>Penetrating power of the LCR system.....</i></b>	<b><i>138</i></b>
6.1	<i>Summary about 2D imaging of unshielded conductive targets.....</i>	<i>138</i>
6.2	<i>Investigations on 2D imaging of shielded conductive targets.....</i>	<i>144</i>

6.2.1	<i>Experimental method.....</i>	<i>146</i>
6.2.2	<i>Results and discussion.....</i>	<i>148</i>
6.2.3	<i>Mathematical model for the problem.....</i>	<i>156</i>
6.2.4	<i>Conclusions.....</i>	<i>161</i>
<b>7</b>	<b><i>An improved EII system based on active filters.....</i></b>	<b><i>162</i></b>
7.1	<i>Active bandpass filters.....</i>	<i>164</i>
7.2	<i>IGMF active filters.....</i>	<i>165</i>
7.3	<i>State-variable active filters.....</i>	<i>171</i>
7.4	<i>Modified state-variable filter with inductor for EII of conductive samples.....</i>	<i>180</i>
7.5	<i>Discussion.....</i>	<i>186</i>
7.6	<i>Measurements of Q-factor shifts to detect the presence of metals.....</i>	<i>187</i>
7.7	<i>Discussion.....</i>	<i>194</i>
7.8	<i>Initial investigations to determine the sources of spurious peaks.....</i>	<i>196</i>
7.9	<i>Towards the optimisation of a novel EII system for detection of conductive objects.....</i>	<i>200</i>
7.9.1	<i>Active-filter-based circuit connected to the impedance analyser.....</i>	<i>202</i>
7.9.2	<i>LCR system used in conjunction with the impedance analyser.....</i>	<i>203</i>
7.10	<i>Removal of spurious peaks and 2D imaging of conductive samples.....</i>	<i>205</i>
7.11	<i>Results and discussion.....</i>	<i>207</i>
<b>8</b>	<b><i>Conclusions.....</i></b>	<b><i>211</i></b>
<b>9</b>	<b><i>Future work.....</i></b>	<b><i>215</i></b>
<b>10</b>	<b><i>List of Author's Publications and Presentations.....</i></b>	<b><i>217</i></b>
<b>11</b>	<b><i>References.....</i></b>	<b><i>218</i></b>

## List of Figures

Fig. 2.1. Primary and secondary magnetic field generated by eddy currents induced inside an electrically conductive material [38].....44

Fig. 2.2. Left: Resonating system “in air”, i.e. with no metallic sample coupled to it. The system is a parallel LCR circuit with resistance  $R_0$ , capacitance  $C$  and inductance  $L_0$ . Right: Modified resonating system including a metallic sample in the shape of a disk, inductively coupled to it. The inductance and resistance of the modified system are labelled  $L_1$  and  $R_1$ , to distinguish them from the components of the resonating system with no metallic sample coupled to it (left).....46

Fig. 2.3. Qualitative behaviour of a resonating system in air (left) and with a conductive non-magnetic sample inductively coupled to it (right). The graphs show the two systems’ impedance, plotted against the frequency. They show the decrease in the Q-factor and increase in resonant frequency occurring due to the presence of the conductive sample.....48

Fig. 3.1. Left: Picture of the experimental system used at the initial stage of the project, to test whether the presence of a metallic sample could be detected by using a LCR-based system. The sample in this picture is a copper disk (6-cm-diameter, 2-mm-thickness), and the coil is a pancake coil (No. turns= $400 \pm 1$ , outer diameter  $43.0 \pm 0.5$  mm, inner diameter  $22.0 \pm 0.5$  mm, height  $20.0 \pm 0.5$  mm). Two Perspex layers were used as a non-magnetic structure to support the coil and maintain it in a fixed position w.r.t. the sample. The coil was part of a LCR circuit whose capacitance could be varied to make the system resonate at different values of resonant frequencies. This was achieved by selecting appropriate capacitance values from the “Jay-Jay instruments - Type no. VC5” capacitor bank (Educational Measurements Limited), shown in the picture on the right.....59

Fig. 3.2. Left: Front view of the Precision Impedance Analyzer 6500B (Wayne Kerr) used to measure the resonant frequency and Q-factor of the system, in air and in the presence of conductive samples. The display shows the resonance peak on a  $Z$  vs frequency plot. The instrument was connected to a parallel LC circuit, with electronic schematic shown on the right of the figure, which consisted in a coil (e.g. pancake coil with inductance  $L=970 \mu\text{H} \pm$

10%) and a capacitor selected from a capacitor bank (“Jay-Jay instruments - Type no. VC5” – Educational Measurements Limited).....60

Fig. 3.3. Experimental set-up. The impedance analyser acted as an AC current generator. A copper disk was used as a test sample and moved by means of a Perspex support. The instrument was connected to a pancake coil inside which eddy currents were induced. These currents altered the measured impedance. A capacitor bank was used in order to move the resonance peak to lower frequency values, to investigate the possibility of achieving eddy current penetration through materials shielding the sample.....60

Fig. 3.4. Representation of aluminium and copper disks used as test samples. The values of electrical conductivity ( $\sigma$ ) and magnetic susceptibility ( $\chi$ ) reported here were tabulated in [66]. Uncertainties in the disk diameters were equal to 0.5 mm.....61

Fig. 3.5. Images of all coils tested in this work, having characteristics as follows: (a) air-cored coil (No. turns= $100 \pm 1$ , inner diameter  $8.0 \pm 0.5$  mm, outer diameter  $9.0 \pm 0.5$  mm, height  $8.5 \pm 0.5$  mm); (b) ferrite cored coil (No. turns= $145 \pm 1$ ,  $\varnothing = 7.8 \pm 0.5$  mm, height= $9.5 \pm 0.5$ mm); (c) pancake coil (No. turns= $400 \pm 1$ , outer diameter  $43.0 \pm 0.5$  mm, inner diameter  $22.0 \pm 0.5$  mm, height  $20.0 \pm 0.5$  mm).....62

Fig. 3.6. Simplified sketch showing the experimental configuration in which a flat metallic sample was inductively coupled to an inductor (“ferrite-cored coil”) at a fixed value of lift-off, i.e. vertical distance between the sample and the ferrite-cored coil. The inductor shown here (made by “multicomp”, part no. MCSCH895-681 KU) was connected to a capacitor as shown in Figs. 3.2-3.3. This figure represents one of the two configurations used in the experiments, the second one being characterised by the LC system “in air”, i.e. with no metallic sample present.....62

Fig. 3.7. Resonant frequency (Hz) vs external capacitance ( $\mu\text{F}$ ) measured with 1) coil in air, 2) coil above 2-pence magnetic coin and 3) coil above 3-mm-thick steel sample. Frequency values were measured at fixed capacitance values, set up using a capacitor bank (“Jay-Jay instruments - Type no. VC5”), by means of the Impedance Analyzer 6500 B (Wayne Kerr). Quantities uncertainties were smaller than the dimensions of data points in this graph and are therefore not visible.....63

Fig. 3.8. Sketch representing the scanning area, made up of  $n \times n$  total positions, or nodes, at each of which the measurements were acquired, by using the impedance analyser. The coil, represented by the yellow circles, was maintained at a fixed position wr.t. the metallic sample (light blue), which was initially placed at starting position labelled “1”, and was then moved by hand to the right (position “2”) and so on, until the first row of the scan was completed. The sample was then moved to the next row of the scan below the first one, and then to third one etc., until  $n \times n$  measurements were acquired, corresponding to all the positions of the sample along the scanning area.....66

Fig. 3.9. Pancake coil (left) and ferrite-cored coil (right) used to image a copper disk (left) and an aluminium disk (right) with the aid of Perspex layers. Graph paper was used to keep track of the motion of the disk samples.....66

Fig. 3.10. Resonant frequency measured with a copper disk at different positions along the x axis (different colours in figure) and y axis (abscissa of the graph). The key reported on the right of the graph indicates the rows at which the measurements were taken by moving the disk along a  $4 \times 4 \text{ cm}^2$  area, as specified in the following. ‘Central row’ means that the disk was positioned on 16 equally-spaced-places along the horizontal line at the centre of the scanning area; ‘up’ and ‘down’ respectively refer to rows above and below the central row of the scan.....67

Fig. 3.11. Resonant frequency (kHz) measured with unshielded (square) and shielded (diamond) copper disk at different positions along the x axis of the scanning area.....67

Fig. 3.12. 2D Surface plot obtained with *Matlab* and representing a 6-cm-diameter copper disk, imaged by means of a resonant frequency scan. The shape of the disk seen from the above is clearly reproduced in the image, and the diameter in the figure, measured with a ruler, is in agreement with the actual diameter of the real sample.....68

Fig. 3.13. 2D surface plot of a 6-cm-diameter copper disk shielded with an aluminium foil, and imaged by means of a resonant frequency scan. The shape of the disk is clearly reproduced in the image and the diameter in the figure corresponds to the real one.....69

Fig. 3.14. Resonant frequency measured values (kHz) vs coil position along x axis (cm). The data sets obtained with aluminium (diamond), copper (square) and steel (triangle) were fitted with second order polynomials.....71

Fig. 3.15. 2D image of a 6-cm-diameter copper disk. The image was obtained by plotting the resonant frequency values (kHz) against coil positions along x and y axis (cm) and interpolating the values with a piecewise cubic fit within *Matlab*.....73

Fig. 3.16. 2D image of a 6-cm-diameter aluminium disk. Resonant frequency values (kHz) were plotted against coil positions along x and y axis (cm).....73

Fig. 3.17. 2D image of a 1x1 cm<sup>2</sup>, 3-mm-thick specimen of mild steel. Resonant frequency values (kHz) were plotted against coil positions along x and y axis (cm).....74

Fig. 3.18. Resonant frequency (kHz) vs number of points acquired during each scan, obtained with the LC system in air.....75

Fig. 3.19. Resonance frequency measured with a copper disk (6-cm-diameter, 2-mm-thickness) at different positions along the y axis (values are included in the key of the graph, and different colours represent profiles obtained with the same y value) and x axis (abscissa of the graph).....76

Fig. 3.20. Plot of impedance ( $\Omega$ ) vs frequency (Hz) showing resonant frequency and Q factor  $Q=\omega_0/\Delta\omega$  obtained for a 6-cm-diameter, 2-mm-thick aluminium sample (a) and a 6-cm-diameter, 2-mm-thick copper sample (b).....80

Fig. 3.21. Change in Q-factor and resonant frequency between copper and aluminium, calculated using Eq. 3.7, with different capacitance values. Measurements were performed using a ferrite-cored coil (Fig. 3.5b). The different axes scales used here for  $\Delta f$  and  $\Delta Q$  should be noted.....81

Fig. 3.22. Image reproducing a 6-cm-diameter copper disk obtained by measuring the Q-factor. The ferrite-cored coil (Fig. 3.5b) was used to perform the scan in this experiment.....82

Fig. 3.23. Image reproducing a 6-cm-diameter aluminium disk obtained by measuring the Q-factor. The ferrite cored coil (Fig. 3.5b) was used to perform the scan in this experiment.....82

Fig. 4.1. Electronic schematic of the initial EII system, which consisted in a parallel LC circuit made up of a ferrite-cored coil (No. turns= $145 \pm 1$ ,  $\varnothing=7.8 \pm 0.5$  mm, height= $9.5 \pm 0.5$ mm, inductance= $680 \pm 10\%$   $\mu$ H), and a capacitor selected from the capacitor bank.....84

Fig. 4.2. Sketch showing the front view of the wooden structure containing the experimental system. This included a ferrite-cored coil, being part of a LC system (with schematic as in Fig. 4.1), a xy stepper motor and a sample made of metal, which was moved along the x and y direction during a scan. A non-magnetic support was used to adjust the lift-off of the sample w.r.t. the coil.....85

Fig. 4.3. Picture of the XY stage used to position the metallic samples used in this work onto different positions along the scanning area.....85

Fig. 4.4. Picture showing the wooden structure containing the experimental setup. This was based on the xy stage with which the metallic sample was moved, the coil (not visible here, as it is fixed to the wooden upper layer) and the computer used for data acquisition and analysis.....86

Fig. 4.5. Electronic schematic of the resonant electromagnetic induction system used in this study. The system capacitance can be adjusted (selecting the desired value from the capacitor bank), thus enabling penetration through a metallic shield covering the metallic target, and therefore facilitating the target identification. The resistor value in most experiments was equal to  $R = 1 \text{ k}\Omega \pm 1\%$ , and the inductor used was a ferrite-cored coil (7.8 mm x 9.5 mm,  $L= 680 \mu\text{H} \pm 10\%$  at 1 kHz).....91

Fig. 4.6. Sketch of the experimental apparatus, made up of a ferrite-cored coil connected to a capacitor and a resistor, as in Fig. 4.6. A xy stage was used to move a metallic sample (such as the disk made of Cu shown in red), thus allowing to perform a scan for imaging purposes. The apparatus was enclosed in a non-magnetic structure (made of wood), in order for the experiment to be electromagnetically isolated.....91

Fig. 4.7. Picture showing the experimental apparatus, including the two decade boxes allowing selection of resistance and capacitance (bottom right).....91

Fig. 4.8. Picture showing the impedance analyser during a Z vs frequency sweep (in the background) and the two decade boxes used for resistance and capacitance selection, connected to the coil mentioned above, which is not shown in this picture.....92

Fig. 5.1. Normalised Q-factor (diamond) and resonant frequency (square), plotted against lift-off (cm), to study the influence of lift-off on the measured quantities. Data was acquired using a 25x25x1 mm<sup>3</sup> aluminium sample.....98

Fig. 5.2. 2-cm-diameter, 2-mm-thick aluminium disk imaged via position-resolved measurements of the resonant frequency (top) and of the Q-factor (bottom). The resonant frequency and Q-factor values- measured at the centre of the object and normalised to the value in air- were equal to  $f_r=1.01\pm0.03$  and  $Q=0.93\pm0.04$ .....101

Fig. 5.3. Image of a 25x25x1 mm<sup>3</sup> copper sample obtained via position-resolved measurements of the resonant frequency (top) and the Q-factor (bottom). The normalised resonant frequency and Q-factor at the centre of the sample were equal to  $f_r=1.01\pm0.03$  and  $Q=0.94\pm0.04$ .....102

Fig. 5.4. Change in Q-factor and resonant frequency plotted against conductivity for each of the 14 metals listed in Tab. 5.1 [66]. The physical quantities were measured at  $C = 1 \mu\text{F}$ . The two data points that are detached from the main trends of  $\Delta Q$  and  $\Delta f$  (labelled “Fe”) correspond to measurements acquired with iron (99.5% purity).....106

Fig. 5.5. Change in resonant frequency plotted against conductivity of each of the 14 metals listed in Tab. 5.1 [66]. The physical quantities were measured at  $C=1 \mu\text{F}$  (diamond data set) and  $C=0.5 \mu\text{F}$  (square data set). Dots that are detached from the main trends (producing  $\Delta f$  equal to -0.25 % and -0.3 %) correspond to measurements taken with iron (99.5% purity).....108

Fig. 5.6. Images of a 25x25x1 mm<sup>3</sup> manganese sample obtained via position-resolved measurements of the resonant frequency, for a capacitance  $C=1 \mu\text{F}$ .....111

Fig. 5.7. Images of a 25x25x1 mm<sup>3</sup> bismuth sample obtained via position-resolved measurements of the resonant frequency, for a capacitance C=1 μF. Values on the z axis are resonant frequency measured in presence of the sample, normalised w.r.t. values in air.....111

Fig. 5.8. Images of a 25x25x1 mm<sup>3</sup> manganese sample obtained via position-resolved measurements of the Q-factor, for a capacitance C=1 μF. Values on the z axis are resonant frequency measured in presence of the sample, normalised w.r.t. values in air. The shape of the sample resembles the shape of the actual sample in this case.....112

Fig. 5.9. Images of 25x25x1 mm<sup>3</sup> manganese (top) and bismuth (bottom) samples obtained via position-resolved measurements of the Q-factor, for a capacitance C=1 μF. The shape of the sample resembles the shape of the actual sample in this case, unlike what appeared in Fig. 5.6.....112

Fig. 5.10. Image of a 25x25x1 mm<sup>3</sup> manganese sample obtained via position-resolved measurements of the resonant frequency, for a capacitance C=0.5 μF. The imaged sample is now visible due to the increase of resonant frequency produced by selection of a lower capacitance value than the previously used value of C=1 μF.....114

Fig. 5.11. Image of a 25x25x1 mm<sup>3</sup> bismuth sample obtained via position-resolved measurements of the resonant frequency, for a capacitance C=0.5 μF. The imaged sample is now visible due to the increase of resonant frequency produced by selection of a lower capacitance value than the previously used value of C=1 μF.....114

Fig. 5.12. Normalised Q-factor plotted against metal's conductivity [66], at lift-off=1 cm and lift-off=0. The minima values of the two curves differ of a factor 1.7.....116

Fig. 5.13. Canny edge detection algorithm applied to grey scale image of aluminium metallic sample (25x25x1 mm<sup>3</sup>), obtained with resonant frequency imaging technique, for a capacitance C=1 μF. Values on the z axis refer to resonant frequency measured in the presence of the sample, normalised w.r.t. air.....121

Fig. 5.14. Canny edge detection algorithm applied to grey scale image of aluminium metallic sample (25x25x1 mm<sup>3</sup>), obtained with Q-factor imaging technique, for a capacitance C=1 μF.

Values on the z axis refer to Q-factor measured in the presence of the sample, normalised w.r.t. air.....122

Fig. 5.15. Ratio between Canny-detected edge and ‘actual’ edge of each sample of conductivity  $\sigma$  (Tab. 4.1), plotted against  $\sigma$ . Edge values were estimated from the images obtained with a capacitance  $C=0.5 \mu\text{F}$ . The diamond-shaped data set includes values obtained using the resonant frequency imaging technique, whereas the squared-shaped data set represent values obtained using the Q-factor imaging technique.....123

Fig. 5.16. Estimated diameter vs measured diameter of 1.5, 1.7, 2 and 3 cm diameter copper disks. The two dots corresponding to  $x=3$  cm refer to copper samples of thicknesses equal to 2 mm (higher y-axis-value) and 0.7 mm (lower y-axis-value). The trends obtained with the Q-factor technique (diamond) and the trend obtained with the resonant frequency technique (square) are both linear.....124

Fig. 5.17. Estimated diameter vs measured diameter of 1.5, 1.7, 2 and 3 cm diameter aluminium disks. The trends obtained with the Q-factor technique (diamond) and the resonant frequency technique (square) are both linear.....124

Fig. 5.18. Diameter of copper disks calculated by means of relations derived from the linear fits shown in Fig. 5.15, plotted against the diameter estimated by using the Canny edge detection algorithm. Note that the x-axis-values of these graphs are the y-axis-values in Figs. 5.16-5.17.....125

Fig. 5.19. Diameter of aluminium disks calculated by means of relations derived from the linear fits shown in Fig. 5.15, plotted against the diameter estimated by using the Canny edge detection algorithm. Note that the x-axis-values of these graphs are the y-axis-values in Figs. 5.16-5.17.....126

Fig. 5.20. Relative change of resonant frequency (Eq. 5.1), produced by a  $25 \times 25 \times 1 \text{ mm}^3$  Al sample for the 8 LCR circuits listed in Tab. 5.3, having values of Q-factor ranging from 7.6 to 22.3.....130

Fig. 5.21. Relative change of Q-factor (absolute value of  $\Delta Q$  in Eq. 5.2), produced by a 25x25x1 mm<sup>3</sup> Al sample for the 8 LCR circuits listed in Tab. 5.3, having values of Q-factor going from 7.6 to 22.3.....131

Fig. 5.22. Estimated diameter (obtained by applying the Canny edge detection algorithm) plotted against measured diameter of actual samples, obtained for a set of aluminium disks of different diameter (from 1.5 cm to 7.6 cm).....135

Fig. 5.23. Ratio between measured and estimated diameter (measured for the actual samples and estimated using the Canny edge detection algorithm, respectively) plotted against measured diameter of aluminium disks.....136

Fig. 6.1. Left: sketch representing the LCR parallel circuit used to image a conductive sample (labelled “target”) having rectangular cross section and volume equal to 25x25x1 mm<sup>3</sup>. The x axis is included to show the distance between the coil and the target (lift-off). Right: Sketch representing the lift-off used in the configuration shown on the left of the figure. The ferrite-cored coil (made by “multicomp”, part no. MCSCH895-681 KU) is part of the LCR circuit shown on the left side of the figure (the labels “metallic sample” and “target” both refer to the sample object).....139

Fig. 6.2. Image of a copper sample (25x25x1 mm<sup>3</sup>) obtained by means of position-resolved-measurements of the Q-factor. The system’s capacitance was set to the value  $C=11 \mu F$ ; the corresponding skin depth in copper was equal to  $\delta=2.6$  mm. The data points in Figs. 6.2-6.7 represent the positions along the scanning area where the measurements were taken.....140

Fig. 6.3. Image of a copper sample (25x25x1 mm<sup>3</sup>) obtained by means of position-resolved-measurements of the resonant frequency. The system’s capacitance was set to the value  $C=11 \mu F$ ; the corresponding skin depth in copper was equal to  $\delta=2.6$  mm.....140

Fig. 6.4. Image of a manganese sample (25x25x1 mm<sup>3</sup>), obtained by means of position-resolved-measurements of the Q-factor, with the system’s capacitance set to the following value:  $C_1=0.5 \mu F$ ; the corresponding skin depth was equal to  $\delta_1=12.7$  mm.....141

Fig. 6.5. Image of a manganese sample (25x25x1 mm<sup>3</sup>), obtained by means of position-resolved-measurements of the resonant frequency, with the system's capacitance set to the following value:  $C_1=0.5 \mu\text{F}$ ; the corresponding skin depth was equal to  $\delta_1=12.7 \text{ mm}$ .....141

Fig. 6.6. Image of a manganese sample (25x25x1 mm<sup>3</sup>), obtained by means of position-resolved-measurements of the Q-factor, with the system's capacitance set to the following value:  $C_2=11 \mu\text{F}$ ; the corresponding skin depth was equal to  $\delta_2=27.7 \text{ mm}$ .....142

Fig. 6.7. Images of a manganese sample (25x25x1 mm<sup>3</sup>), obtained by means of position-resolved-measurements of the resonant frequency, with the system's capacitance set to the following value:  $C_2=11 \mu\text{F}$ ; the corresponding skin depth was equal to  $\delta_2=27.7 \text{ mm}$ .....142

Fig. 6.8. Sketch representing the LCR parallel circuit used to image a conductive target, with rectangular cross section (25x25x1 mm<sup>3</sup>), hidden behind a conductive shield in the shape of a 110.0x80.0x1.5 mm<sup>3</sup> piece of Al. The x axis is included to show that the concept of lift-off changed from the scenario represented in Fig. 6.1, due to the presence of the Al shield.....145

Fig. 6.9. Sketch representing the scanning area ("n x n" total positions, or nodes), where the coil (yellow circle) is maintained at a fixed position, and the metallic sample (light blue) is moved onto different positions, starting from "1", going to "2", tracing a horizontal path forming the first row of the scan, and then proceeding onto the next rows below.....147

Fig. 6.10. Image of a copper target (25x25x1 mm<sup>3</sup>) obtained by means of position-resolved-measurements of the Q-factor, at the following value of skin depth:  $\delta_1=0.4 \text{ mm}$ . During these measurements, the target was shielded by a 1.5-mm-thick aluminium sheet.....149

Fig. 6.11. Image of a copper target (25x25x1 mm<sup>3</sup>) obtained by means of position-resolved-measurements of the Q-factor, at the following value of skin depth:  $\delta_2=0.6 \text{ mm}$ . During these measurements, the target was shielded by a 1.5-mm-thick aluminium sheet.....149

Fig. 6.12. Image of a copper target (25x25x1 mm<sup>3</sup>) obtained by means of position-resolved-measurements of the Q-factor, at the following value of skin depth:  $\delta_3= 1.8$  mm. During these measurements, the target was shielded by a 1.5-mm-thick aluminium sheet.....150

Fig. 6.13. Image of a copper target (25x25x1 mm<sup>3</sup>) obtained by means of position-resolved-measurements of the Q-factor, at the following value of skin depth:  $\delta_4= 2.9$  mm. During these measurements, the target was shielded by a 1.5-mm-thick aluminium sheet.....150

Fig. 6.14. Image of a copper target (25x25x1 mm<sup>3</sup>) obtained by means of position-resolved-measurements of the resonant-frequency, at the following value of skin depth:  $\delta_1=0.4$  mm. During these measurements, the target was shielded by a 1.5-mm-thick aluminium sheet.....151

Fig. 6.15. Image of a copper target (25x25x1 mm<sup>3</sup>) obtained by means of position-resolved-measurements of the resonant-frequency, at the following value of skin depth:  $\delta_2=0.6$  mm. During these measurements, the target was shielded by a 1.5-mm-thick aluminium sheet.....152

Fig. 6.16. Image of a copper target (25x25x1 mm<sup>3</sup>) obtained by means of position-resolved-measurements of the resonant-frequency, at the following value of skin depth:  $\delta_3= 1.8$  mm. During these measurements, the target was shielded by a 1.5-mm-thick aluminium sheet.....153

Fig. 6.17. Image of a copper target (25x25x1 mm<sup>3</sup>) obtained by means of position-resolved-measurements of the resonant-frequency, at the following value of skin depth:  $\delta_4= 2.9$  mm. During these measurements, the target was shielded by a 1.5-mm-thick aluminium sheet.....153

Fig. 6.18. Image reproducing a manganese target (25x25x1 mm<sup>3</sup>), shielded by a 1.5-mm-thick aluminium sheet, obtained by means of position-resolved-measurements of the Q-factor, with a skin depth through aluminium equal to 3.3 mm.....154

Fig. 6.19. Image reproducing a manganese target (25x25x1 mm<sup>3</sup>), shielded by a 1.5-mm-thick aluminium sheet, obtained by means of position-resolved-measurements of the resonant-frequency, with a skin depth through aluminium equal to 3.3 mm.....155

Fig. 6.20. Plot equivalent to the one shown in Fig. 5.23, obtained for aluminium disks of different diameter, shielded by a 1.5-mm-thick aluminium shield. Estimated diameter stands for the diameter derived by applying a Canny edge detection algorithm to the images of the disks; measured diameter indicates the actual sample diameter.....156

Fig. 7.1. Circuit schematic of a RC highpass filter.....165

Fig. 7.2. Circuit schematic of a RC low-pass filter.....165

Fig. 7.3. Schematic of IGMF circuit (in a 2-pole lowpass configuration) used to investigate the possibility of using this configuration to build a new version of the EII system used in this research. This sketch was created with LTSpiceXVII.....166

Fig. 7.4. Sketch of the pinouts constituting the op-amp OP27GPZ [77].....166

Fig. 7.5. Experimental set-up assembly. The IGMF filter (Fig. 7.3) is contained inside the black box at the centre of the picture. The signal generator Hameg Instruments 25 MHz HMF 2525 is shown on the left. The oscilloscope ISO-TECH IDS-6052-U is shown on the right side.....168

Fig. 7.6. Curve obtained by measuring the IGMF active filter gain and plotting it against the frequency of the signal generator.....169

Fig. 7.7. Schematic of the 2-pole filter “state-variable filter” built for this investigation [76].....169

Fig. 7.8. Resonance curve of the filter shown in Fig. 7.7, obtained with a resistor value  $R_F=1\text{ M}\Omega$ , corresponding to the last position on the rotary switch (Tab. 7.4).....176

Fig. 7.9. Picture of the experimental setup, including the active filter, the Network Analyser E5061B (Keysight) and the power supply “elc” ALF 1502D.....179

Fig. 7.10. Resonance curve obtained from data acquired using the Network Analyser, when the circuit’s resistance  $R_F$  was equal to 23.6 k $\Omega$ .....179

Fig. 7.11. Resonance curve obtained from data acquired using the Network Analyser, when the circuit's resistance  $R_F$  was equal to 19.9 kHz.....180

Fig. 7.12. Resonance curve obtained from data acquired using the Network Analyser, when the circuit's resistance  $R_F$  was equal to 16.1 kHz.....180

Fig. 7.13. Electronic schematic produced with LTSpiceXVII, representing the electronic circuit on which the improved version of the EII system, object of this work, was based.....182

Fig. 7.14. Screenshot from the Network Analyser, obtained after inducing a stimulus (start frequency 10 kHz – stop frequency 30 kHz) in the circuit, having set the circuit's resistance to  $R_F = 6.8 \text{ K}\Omega$ .....183

Fig. 7.15. Simulation (from LTSpiceXVII) of the electronic circuit's response, when its components had values as in Fig. 7.13, and its resistance  $R_F$  was equal to  $R_F = 6.8 \text{ K}\Omega$ .....183

Fig. 7.16. Screenshot from the Network Analyser, obtained after inducing a stimulus (start frequency 10 kHz – stop frequency 30 kHz) in the circuit, having set the circuit's resistance to  $R_F = 8.2 \text{ K}\Omega$ .....184

Fig. 7.17. Simulation (from LTSpiceXVII) of the electronic circuit's response, when its components had values as in Fig. 7.13, and its resistance  $R_F$  was equal to  $R_F = 8.2 \text{ K}\Omega$ .....184

Fig. 7.18. Screenshot from the Network Analyser, obtained after inducing a stimulus (start frequency 10 kHz – stop frequency 30 kHz) in the circuit, having set the circuit's resistance to  $R_F = 9.9 \text{ K}\Omega$ .....185

Fig. 7.19. Simulation (from LTSpiceXVII) of the electronic circuit's response, when its components had values as in Fig. 7.13, and its resistance  $R_F$  was equal to  $R_F = 9.9 \text{ K}\Omega$ .....185

Fig. 7.20. Picture of the coil used in this study ( $L=79.4\pm 10\% \mu\text{H}$ , height  $1.8\pm 0.1 \text{ cm}$ , inner diameter  $2.0\pm 0.1 \text{ cm}$ , outer diameter  $2.3\pm 0.1 \text{ cm}$ ). The coil was connected to the other circuits' components as in Fig. 7.13.....186

Fig. 7.21. Resonance curve obtained with the Network Analyser when the coil of the EII system was in air, i.e., no metallic sample was present.....189

Fig. 7.22. Resonance curve obtained with the Network Analyser, when the coil part of the EII system with schematic as in Fig. 7.13 was in contact with the Al disk sample.....189

Fig. 7.23. Comparison between the average Q measured with the Network Analyser, when the system was resonating at 23.6 kHz and it was coupled to the following materials: material “1”: air, material “2”: Cu, material “3”: Mn, material “4”: Fe. Error bars were added, by calculating the standard deviation of the measured quantities.....192

Fig. 7.24. Comparison between the average Q measured with the Network Analyser, when the system was resonating at 19.5 kHz and it was coupled to the following materials: material “1”: air, material “2”: Cu, material “3”: Mn, material “4”: Fe. Error bars were added, by calculating the standard deviation of the measured quantities.....193

Fig. 7.25. Comparison between the average Q measured with the Network Analyser, when the system was resonating at 16.2 kHz and it was coupled to the following materials: material “1”: air, material “2”: Cu, material “3”: Mn, material “4”: Fe. Error bars were added, by calculating the standard deviation of the measured quantities.....193

Fig. 7.26. Plot of  $\Delta Q = Q(\text{air}) - Q(\text{metal})$  vs resonant frequency values  $f_{ri}$  (as in Tab. 7.12), obtained from results of 20 consecutive Q-factor shift measurements (Tab. 7.12), compared to the shifts measured with the “old” LCR-based system, in the following scenarios: system in air and coupled to copper (blue, diamond data-set); system in air and couple to manganese (red, square data-set); system in air and coupled to iron (green, triangle data-set).....194

Fig. 7.27. Image representing a 3-cm-diameter Cu disk, obtained with the EII active filter-based system developed in this study.....209

Fig. 7.28. Image representing a 3-cm-diameter Cu disk, shielded with a 1 mm-thick Al shield. The image was obtained with the EII active filter-based system developed in this study, resonating at a frequency  $f_r = 23.6$  kHz.....210

## List of Tables

Tab. 3.1. Maximum, minimum and average value of $\Delta f\%$ at growing values of the y coordinate, from -3.5 to +3.5 cm. The samples used were 6-cm-diameter, 2-mm-thick copper and aluminium disks. The interesting column is the third one, which shows that the average $\Delta f\%$ is lower than 0.3% at all positions along the y axis. This value was smaller than 0.5%, which was the standard deviation obtained from 10 consecutive measurements of the resonant frequency, meaning that the resonant frequency variation is not significant to discriminate between a copper and an aluminium sample.....	77
Tab. 5.1. List of conductivity values of 14 metallic samples (25x25x1mm <sup>3</sup> ) used in the “Material characterisation” study [66]. The metals are numbered in the third column, based on the order in which they appear on the x axis of the graph in Fig. 5.4, from the right side (higher $\sigma$ ) to the left side (lower $\sigma$ ).....	104
Tab. 5.2. List of copper and aluminium disks of different diameters and thicknesses included in the investigation aimed at imaging high-conductivity samples.....	119
Tab. 5.3. Values of resistance (second column) and capacitance (third column) that were chosen to build eight different LCR circuits (labelled with numbers I-VIII reported in the first column of this table).....	129
Tab. 5.4. Diameter values (cm) of the eight different Al disks which were used for the resolution study aiming at identifying the minimum-diameter-disk that could be imaged.....	134
Tab. 6.1. Capacitance values (C), resonant frequency values ( $f_r$ )- measured at the centre of the shielded copper target- and corresponding skin depths in aluminium and copper, for each of the images shown in Figs. 6.10-6.17 (see next section).....	148
Tab. 7.1. Values of resonant frequency at which the electronic system was made to resonate (first column), and corresponding values of skin depth (second column), obtained by using Eqs. 2.13-2.16, and assuming that the EII system’s operational frequency was equal to the active filter’s resonant frequency $f_r$ (first column).....	172

Tab. 7.2. Values of components used to build the circuit represented in Fig. 7.6, measured with Keysight U1731C handheld LCR meter. Tolerance ranges for resistance and capacitance values were equal to 1%.....173

Tab. 7.3. Column 1: positions on rotary switch, numbered 1 to 7; column 2: ‘theoretical’ values of resistors  $R_F$ , each corresponding to a position on the rotary switch; column 3: theoretical values of  $f_r$  (predicted by using Eq. 7.13); column 4: values of  $f_r$  expressed in kHz.....174

Tab. 7.4. Expected values of resonant frequency  $f_r$ , derived by inserting the measured values for  $R_F$  into Eq. 7.13. Resistance values were measured with a tolerance range of 1%.....174

Tab. 7.5. Expected and measured values of resonant frequency, plus ratio between them.....176

Tab. 7.6. Expected and measured values of G and Q, plus ratio between each pair of them.....177

Tab. 7.7. Measured values of the circuit’s components. Their tolerance value was equal to 1%.....178

Tab. 7.8. Measured values of resistors making up the rotary switch; corresponding resonant frequency values that were expected; corresponding skin depth in Al at those frequencies. Resistor tolerance was equal to 1%.....178

Tab. 7.9. First column: resonant frequency of the three state variable filters that were built; second column: Q-factor, measured with the Network Analyser as average values of 10 consecutive measurements; third column: uncertainties of Q, as standard deviation; fourth column: measured values of maximum gain (average of 10 consecutive measurements); fifth column: standard deviation of gain.....181

Tab. 7.10. Values of Q measured with Network Analyser when the EII system was in air, when an Al sample was placed under the coil, for both the air-cored and the ferrite-cored coil. The percentage difference between the Q factors in air and Al was calculated (last column).....188

Tab. 7.11. Comparison between the Q-factor values obtained when the new EII system with air-cored coil and ferrite-cored coil was in air (second column) and when a Cu sample was introduced (third column). These Q-factor differences (DeltaQ) were compared to the ones obtained with the previously used LCR-based system (“Old system”, described in Chapter 5).....191

Tab. 7.12. Values of average and standard deviation of DeltaQ (first column), at the following resonant frequency values:  $f_{r1}=24$  kHz (second column),  $f_{r2}=20$  kHz (third column) and  $f_{r3}=16$  kHz (fourth column). DeltaQ/Q(air) are ratios of DeltaQ divided by the Q-factor values measured in air.....192

Tab. 7.13. Results of the study of the influence of the automatic averaging of the NA. In the table, “meas” stands for “measurements”; av(Q) stands for average of Q, calculated by taking 30 and 100 consecutive measurements without using the NA averaging function (3<sup>rd</sup> and 4<sup>th</sup> rows of the first column) and performed using the NA averaging function of the same number of measurements (third column); corresponding standard deviation values are reported in the second and fourth columns ( $\sigma Q$ ).....197

Tab. 7.14. Results showing the influence of the power supply being left on, or switched on and off in between consecutive measurements.....198

Tab. 7.15. Results of 10 consecutive measurements of Q-factor, resonant frequency, inductance, capacitance and resistance, measured when the active filter-based system was in air and when a piece of Cu was placed under the coil.....202

Tab. 7.16. Results of 10 consecutive measurements of Q-factor, inductance, capacitance and resistance, measured when the LCR system was in air and when a piece of Cu was placed under the coil.....203

Tab. 7.17. Q-factor average values in air and with Cu (2<sup>nd</sup> and 4<sup>th</sup> columns), differences between these two values, DeltaQ=Q(air)-Q(metal) (6<sup>th</sup> column), standard deviations (3<sup>rd</sup>, 5<sup>th</sup> and 7<sup>th</sup> columns); measurements were obtained with the IA=impedance analyser (first two rows) and the NA (last three rows).....204

Tab. 7.18. Average values of Q-factor Q and inductance L obtained after the Matlab fitting routine was run to the modified curve of S21 vs frequency obtained with the NA, after applying the peak removal algorithm. Uncertainties were calculated as standard deviation of the measurements and relative variations between values obtained in air and after a Cu sample was coupled to the system were calculated using Eqs. 7.21-7.22 (4<sup>th</sup> and 6<sup>th</sup> columns). These results were obtained when the resonant frequency of the active-filter-based system was set to the value  $f_r = 23.6$  kHz.....207

## List of Symbols

$B$  — Magnetic flux density (T or  $\text{Wb}\cdot\text{m}^{-2}$ )

$E$  — Electric field ( $\text{V}\cdot\text{m}^{-1}$ )

$H$  — Magnetic field strength ( $\text{A}\cdot\text{m}^{-1}$ )

$M$  — Magnetization ( $\text{A}\cdot\text{m}^{-1}$ )

$J$  — Current density ( $\text{A}\cdot\text{m}^{-2}$ )

$V$  — Electric potential / Voltage (V) / Potential difference (p.d.) in volts (V)

$\phi_{B,S}$  — Magnetic flux through closed surface area  $S$  (Wb)

$\delta$  — Skin depth (mm)

$\epsilon$  — Electrical permittivity ( $\text{F}\cdot\text{m}^{-1}$ )

$\mu$  — Magnetic permeability ( $\text{H}\cdot\text{m}^{-1}$ )

$\chi_v$  — Volumetric magnetic susceptibility (dimensionless)

$\sigma$  — Electrical conductivity ( $\text{S}\cdot\text{m}^{-1}$ )

$\omega$  — Angular frequency (rad/s)

## **Nomenclature**

MIT — Magnetic Induction Tomography

EII — Electromagnetic Induction Imaging

ECT — Electrical Capacitance Tomography

EIT — Electrical Impedance Tomography

ERT — Electrical resistance tomography

NDE — Non-Destructive Evaluation

OAM — Optical Atomic Magnetometer

e.m.f – Electromotive Force

p.d. – Potential Difference

# 1 Introduction

Electromagnetic induction imaging (EII) [1]–[23] has wide application in diverse fields such as medicine [1]–[11], industry [12]–[21], archaeology [22] and geophysics [23]. For instance, it has been largely exploited in Non-Destructive Evaluation (NDE) for crack detection during industrial inspections and characterisation of the materials' level of corrosion [14]–[16]. Electromagnetic induction imaging presents some advantages in comparison to other existing imaging techniques, being non-invasive and contactless. Furthermore, it is sensitive to all the electromagnetic properties of materials: conductivity, permittivity and permeability. Its working principle is based on the induction of eddy currents in a conductive sample placed in the alternating (AC) magnetic field generated by a coil. Eddy current induction [24]–[25] leads to a change in the magnetic field detected by an array of sensor coils, which can be exploited to produce conductivity maps of the sample under investigation [3] [11]. In particular, the presence of the sample inside the magnetic field generated by the coil (*primary field*) is the cause of eddy currents being induced in the sample itself. A secondary magnetic field is generated by the eddy currents (Biot-Savart's law), which opposes the primary one, due to Lenz's law [26]. The total field is therefore different from the primary field, and induces an e.m.f. across a sensor coil that can be measured and provide information about the sample which caused the eddy current induction process to take place (Faraday's law) [26].

One of the application fields of electromagnetic imaging techniques is medicine. In particular, these imaging techniques can be used to determine the human-body composition, due to their ability to differentiate between fat and fat-free tissues, as well as outline the internal and external geometry of simple conductive objects. These techniques have the advantage of being suitable for *in vivo* images of the body while being non-invasive [1].

*In vivo* body imaging techniques include x-ray based computed tomography (CT)[27]–[28], magnetic resonance imaging (MRI) and electrical impedance tomography (EIT)[29]–[30]. Other tomographic techniques, used between the 1980s and the beginning of the 1990s, are electrical capacitance tomography (ECT)[31]–[33] and electrical resistance tomography (ERT) [34]–[35]. These techniques were later replaced by electromagnetic induction imaging, which some authors also called both magnetic induction tomography (MIT)[3], and electromagnetic

inductance tomography (EMT)[2]. First publications about MIT systems appeared in the second half of the 1990s [2]-[4]. The common factor to all of these electromagnetic techniques is that they became attractive, from the 1980s, for a number of reasons. Among these are their potentially high imaging-speeds and low cost, as well as their non-invasive and non-hazardous nature [2].

Electrical impedance tomography (EIT) works by applying small alternating electric currents by means of electrodes that are attached to the surface of a human subject. Measurements of the electric potentials, on an array of electrodes attached around the body [9], provide a data-set from which conductivity or permittivity distributions can be inferred via 'inverse problem' methods [19] [36].

Electrical resistance tomography (ERT) is a geophysical technique that measures the electrical resistivity and images sub-surface structures. This is done by means of measurements either at the surface or by electrodes suspended in boreholes. Image reconstruction processes are used to produce conductivity or resistivity maps of sub-surface layers. ERT is applied to both geophysical prospecting and imaging of the interior of process vessels and pipelines [35].

Electrical capacitance tomography (ECT) exploits capacitive measurements taken on the outside of an object to calculate the spatial distribution of dielectric permittivity inside the object. This calculation is normally achieved by solving an inverse problem. The idea of an inverse problem is that a set of observations are used to calculate the properties that caused these observations. In MIT, the conductivity spatial-distribution is calculated from a set of p.d. measurements taken with coils arranged around a sample. This is accomplished by firstly modelling the forward problem, which consists of inferring the results from the cause, by applying Maxwell's equations. Once this is done, the solution to the forward problem is inverted to provide solution to the inverse problem. The way in which this is achieved includes an iterative process where an initial guess for the conductivity of the sample is determined [19] [36].

In ECT, electrodes that are sufficiently physically large to detect significant changes (i.e., measurable with small relative uncertainties) of capacitance are used. ECT has applications in the oil industry, where it employs image analysis to distinguish between oil and gas, and between oil and water mixtures. Despite its lower resolution, compared to other

electrical imaging techniques, it provides estimations of oil/water/gas mixtures that are sufficiently accurate for industrial investigations involving initial geophysical surveys. The poor resolution of ECT is compensated by the speed of this real time-imaging technique, which can reach values of 10 ms per image [6] [31] [32].

MIT allows the obtaining of permeability and conductivity distributions from inductance measurements. It provides some advantages when compared to EIT, ERT and ECT, being contactless. It has another advantage which makes it suitable for imaging of poorly conducting tissues: its working principle relies upon the application of a magnetic field to cause eddy current induction to take place inside the sample; such a magnetic field is not shielded by human body tissues such as bone [4]. Furthermore, in principle, it is sensitive to all the electromagnetic properties of materials: conductivity, permittivity and permeability [5].

The electromagnetic system described by Al-Zeibak and Saunders [1] is made up of a *drive coil*, i.e., a coil inducing the *primary* magnetic field (elsewhere named 'excitation coil' [4]), placed in the vicinity of the body and inducing a high frequency electromagnetic field, and a *pickup coil* (also named 'sensing' or 'sensor' coil [3] [4]), coaxial to the drive coil. The magnetic field detected by the pickup coil is modified by the presence of a body tissue, to an extent dependent on its electrical and magnetic properties.

Another MIT system based on an excitation coil and a sensing coil was developed by Griffiths [4]. The system was capable of imaging saline solutions of conductivities ranging from 0.001 to 6 Sm<sup>-1</sup>. The operating frequency was equal to 10 MHz and allowed improvement on previously developed MIT systems which were not capable of imaging biological tissues, due to their lower operating frequencies (2 and 5.5 MHz) [3].

Progress in the development of biomedical MIT systems has been made in the past few years. In particular, Zolgharni was able to detect cerebral haemorrhage by using a method based on a hemispherical coil array [9].

Medicine is only one of the fields of application of tomography techniques. Application of MIT in industry, such as metal processing and mining, is well attested in literature, for separation and mineral processing, crack and fault detection, characterisation of the level of corrosion of industrial materials, inspection of equipment, and monitor of processes in vessels

and pipelines (e.g., detection of the extent of solidification of molten metal flowing in a pipeline) [11] [14] [15].

Other two documented applications of electromagnetic imaging are:

- 1) archaeology for imaging submerged remains [17];
- 2) environmental monitoring for tracking the migration of pollutants underground [18].

Electromagnetic induction systems have similar characteristics to eddy current detection systems and MIT is closely related to Non-Destructive Evaluation (NDE). The latter is widely employed in technological inspections, such as thickness measurements, coating and surface treatment, residual stress assessment, materials' quality control and inspection, crack detection and the characterisation of aluminium foam structures [37]-[42].

In typical MIT and eddy current detection systems, sensing coils measure the magnetic field values in presence of the object that is to be imaged. This is completed for a number of projections, which are taken in sequence. The measured signals are processed by means of a computer, by using inverse problem techniques, and image reconstruction algorithms are operated, the result of which is an image of the object [2] [36].

The procedure of image reconstruction algorithms is complicated and time-consuming, because of the computational load on computers. For this reason, our research group developed a new EII technique which does not require image reconstruction algorithms and has proven suitable for 2D imaging of conductive targets. The system developed for this purpose differs from classical MIT systems because it does not involve the measurement of the difference between the primary and secondary magnetic fields produced when a conductive sample is introduced into the system. A second aspect that is worth mentioning is that our research group has introduced a novel field of application for electromagnetic induction systems: National Security. The main goal of the PhD project has been developing a technique which enables imaging and characterisation of potentially hazardous materials, such as explosives, by distinguishing between a piece of ordinary copper and another 'suspicious' material. To a larger extent, the goal of this work has been to develop a technique that could be useful for combating illicit trafficking in nuclear and radioactive materials.

Penetrating imaging, i.e. imaging of targets hidden behind a shielding material, is essential in the field of security. A detection system enabling electromagnetic imaging through metallic enclosures for national security purposes has been developed by Darrer *et al.* [43]-[46]. Penetrating imaging is also a fundamental requirement in biomedicine, where diagnosis maps of the organs of interest cannot be produced without penetrating through the layers of biological tissues surrounding them. In this context, an MIT-based optical method based on the use of optical atomic magnetometers (OAM) for diagnostic mapping of the heart's conductivity has been recently proposed by Marmugi *et al.* [47] [48] and Deans *et al.* [49]. This research work has been based on a different method and has some advantages with respect to OAM-based research. For instance, it involves the use of less expensive technology and the implementation of the measurement method is simple and highly practical.

In the past few years, research work on EII systems has been directed towards the development of high-sensitivity detection and imaging methods for industrial applications. Among the different realizations, Q-detection sensors have been used for condition monitoring of steel reinforcing bars embedded in concrete [50] to provide information about the health of its structure. Q-detection sensors, incorporating digital signal processing, have been exploited since the introduction of metal detectors. These sensors' working principle is based on the increase of the impedance of a coil, which occurs whenever a conductive object is inductively coupled to it. This increase is due to eddy current production inside the sample, occurring as a consequence of Faraday's law of induction (refer to Section 2.1). The Q-factor of a coil, within a tuned system, drops when high-conductivity targets of low permeability are exposed to the changing magnetic field generated by the coil. However, purely permeable targets cause an increase of Q-factor [50].

Q-detection sensors are part of a wider family of inductive sensors. High-sensitivity detection methods based on the use of inductive sensors are object of intense research. For instance, these sensors have been recently used for detection of metallic wear debris aimed at condition monitoring of rotating and reciprocating machinery [51]. A high-sensitivity method based on an inductance-capacitance resonance system was developed to this purpose by Du *et al.* [51]. The authors exploited the amplified impedance change at resonance, due to the presence of wear debris particles, to detect metallic specimens ranging from 32 to 172  $\mu\text{m}$  [51].

The use of resonating LCR circuits was the initial inspiration for this research work. It is documented in some bibliographic sources which were published in the past few years [50]-[53]. One of them is about the use of RLC resonators as biodegradable sensors for *in vivo* operations and wireless implant applications [52]. Bartlett *et al.* proposed a method based on a series LCR electrical circuit which was tuned to resonate at a particular frequency to achieve maximum power transfer [53]. The circuit was based on a dental-scaler drive coil, with various magnetostrictive materials acting as the core, connected in series to a capacitor bank. The authors showed that the impedance of the system could be significantly reduced by introducing a capacitor to create a resonant LCR electrical circuit at the required excitation frequency, i.e., the frequency of the drive signal. The proposed capacitance compensation method was able to reduce the losses associated with a resonant magnetostrictive dental-scaler transducer, thus allowing it to resonate with lower input power requirements [53].

In Chapters 3-6 of this thesis, the progress made with an EII measurement system initially designed and tested as a prototype, and later improved, is documented [54]-[56]. Such system was initially based on a resonant LC circuit and was then turned into a parallel LCR circuit, made up of a cylindrical ferrite-cored coil (with diameter  $D=7.80\pm 0.03$  mm, height  $H=9.50\pm 0.03$  mm, and inductance  $L=680\pm 10\%$   $\mu\text{H}$  at 1 kHz), connected to a capacitor bank (capacitance ranging from 100 pF to  $1\ \mu\text{F} \pm 1\%$ , with sensitivity of 0.1 nF) [54]. An AC current was applied to the coil, thus generating an AC primary magnetic field. The working principle of the system was based on eddy current induction inside a metallic sample, occurring when this was introduced into the AC magnetic field generated by the coil (due to Lenz's law). As a consequence of eddy current induction, the primary field was modified, according to Biot-Savart's law. The key point explaining the working principle of the LCR system developed in this work is that the inductance of the circuit was also modified, due to the presence of the sample, to an extent that depended on the sample's electrical conductivity and magnetic permeability. Such modification is known to increase when the detection system is operated at its resonant frequency [51]. The main assumption based on which the technique here illustrated was developed is that position-resolved measurements of either the inductance change or resonant frequency change could be exploited for identifying the presence of conductive objects and imaging them [54]. The initial hypothesis on which this technique has been developed is that, provided that the measurement system was sensitive enough to

detect changes in the measured quantity (resonant frequency), the system should allow to distinguish the object to be imaged from the background (i.e., free space/air). This was possible due to the inductive coupling established between the coil and the object, causing a change in the system's resonant frequency to take place.

Producing a 2D image representing conductive objects was the initial challenge of this research project. Looking further into the working principles of the system, a hypothesis was made based on which measurements of the resonant frequency changes could lead to accomplish materials' characterisation, i.e., distinguishing between objects having different values of electrical conductivity and magnetic permeability. This was shown to be possible by utilising a suitable system operated at resonance [54]. The impedance change occurring in such system, due to the presence of conductive samples (both of non-magnetic and ferromagnetic nature), changed the resonant frequency and Q-factor of the system, since these quantities were both dependent on the system's inductance, which was changed due to the presence of conductive samples that were introduced into the system. The importance of this result is that developing resonant systems such as the one described here may open a route to conductive materials' imaging and characterisation. Specifically, the detection of sample objects that produced a visible change in the measured quantities was found not only to allow distinguishing between different shapes and geometries, but also to provide information about the electrical conductivity and magnetic permeability of such objects.

The goals of this research project could be envisaged by developing a robust technique that allowed being in control of the circuit's components, in particular its capacitance and resistance, since assigning certain values to these parameters could enable the adjustment of the measured quantities (resonant frequency and Q-factor), such that changes in these quantities could be maximised and exploited for improving the imaging system's sensitivity.

As mentioned earlier, the initial experimental system developed in this context was based on a single coil connected to a capacitor bank, allowing selection of values of capacitance within the range 100 pF to 1  $\mu$ F. More details about this experimental setup will be given in Chapter 3. The circuit's components were chosen as to produce a visible resonance peak that could be detected with the instrument used to perform the measurements (impedance analyser, as indicated in Chapter 3). The change in the resonant frequency produced by conductive materials introduced into the LC system was measured and exploited

to image them. Limitations were found, due to these changes being smaller than needed to distinguish between materials having similar values of conductivity. The system was therefore modified, by using a parallel LCR circuit comprising the same ferrite-cored coil previously used, plus a variable resistor and capacitor [56]. The possibility of varying the system's resistance and capacitance implied that the system's resonant frequency and Q-factor could be adjusted accordingly (see Section 2.1). This could enable penetration through conductive shields to image hidden targets (see Section 2.3), thus enabling more sensitive detection, leading to improvements to the imaging and detection performance of the system. The EII technique based on the use of the developed LCR system is illustrated in Section 4.2. Experimental results reported in Chapters 5-6 prove that the proposed EII technique enabled both imaging and material characterisation (related to distinguishing between different materials) [54]. An essential feature of the EII method here developed is that the choice of using a system with an adjustable resonant frequency made it possible to select resonances that allowed magnetic-field penetration through conductive screens [55]. Chapter 6 elaborates on this central topic by addressing the problem of how to image and detect conductive samples with the LCR system, even when these were shielded behind a conductive material that was placed in between the coil and the sample of interest.

Detecting objects that are concealed behind metallic screens is a central problem in many fields. These include security, where the threat represented by illicit trafficking of materials, and in particular special nuclear materials (SNM), requires reliable techniques to be developed for hazard prevention [44]. In many scenarios, and typically in the case of maritime cargos, a hidden target is shielded by some other metallic material, often of unknown nature, and therefore cannot be directly identified. In principle, the possibility of identifying conductive hidden targets can be achieved by using an electromagnetic-based system operating at a frequency that causes the penetration depth (skin depth) to be at least equal to the thickness of the conductive material shielding these targets. Generally, standard electromagnetic imaging systems do not allow imaging through conductive barriers, due to limitations in the system's resonant-field penetration depth; their inherent resonant frequency is typically too high and the subsequent skin depth smaller than the thickness of the barrier [57]. Techniques are thus required that allow penetration through materials, in order for the hidden target to be detected [58] [59]. A novel approach was undertaken by our research group, which was based on a resonant electromagnetic induction interrogation

technique. This technique was used to carry out investigations on the possibility of imaging concealed metals shielded by conductive materials [55]-[56]. The theoretical principles lying behind this part of the research work are reported in Section 2.3 and experimental results obtained with the proposed interrogation technique are reported in Chapter 6.

The ultimate objective of the investigations carried out in this work was to satisfy the requirement for an EII system to be sensitive enough to allow characterisation of metallic materials having similar values of electrical conductivity, as well as to enable the identification of hidden materials. Chapter 7 describes a different, improved version of the EII system introduced in the previous chapters. This system was based on an active bandpass filter to which a coil was added, to allow eddy current induction and detection of the system's Q-factor changes, occurring when a conductive sample was introduced. The sharpened resonance peak of such system, compared with the previously used passive one, should allow more sensitive measurements to be performed. This is because larger Q-factor absolute values would imply larger Q-factor changes, thus allowing resonant peaks, produced by two conductive objects having similar values of electrical conductivities, to be resolved. The proposed method would also make identification of low-conductivity materials possible, due to the larger sensitivity of a higher-Q system, for detection of shifts in resonant frequency.

The main goals of the preliminary experiments described in Chapter 3 were: 1) to understand whether it could be possible or not to succeed at imaging metallic objects by using resonant frequency measurements, and 2) to develop a proof-of-principle method for 2D imaging of these objects. For these purposes, the following initial objectives were set up:

- To investigate changes in the resonant frequency when metals of different nature were placed under the inductor and w.r.t. when no object was used (coil "in air").
- To develop a proof-of-principle method to image a 6-cm-diameter copper disk (high-conductivity and simple geometry). This represented the first attempt to image an object by using the resonant frequency technique which is detailed in Chapter 3. Secondly, the developed proof-of-principle method was tested to achieve imaging of the same disk, after having placed an aluminium foil in contact with it, for shielding purposes.

- To image various metals by means of resonant frequency measurements, and verify whether the different magnetic properties of such metals were reflected by the different images which were obtained with the developed method.
- To perform measurements at different values of lift-off, to identify the impact of these variations on the resulting images, to improve them qualitatively and investigate whether it could be possible to distinguish between different samples by looking at their images (Section 5.1).
- To verify whether a method based on Q-factor position-resolved measurements rather than resonant frequency measurements would be able to distinguish between materials having different values of electrical conductivity. Part of this optimisation process included amendments that were made to the experimental system, as detailed Section 3.6.
- To develop a proof-of-principle method for 2D imaging of conductive metallic samples having simple geometries (e.g., disks or samples of rectangular cross section) based on measurements of the shifts of the system's resonant frequency and Q-factor.
- To apply the LCR-based system developed and tested for imaging of 'unshielded' metallic materials to accomplish imaging of 'shielded materials', i.e. conductive objects hidden behind a conductive screen, used to prevent recognition of the object.
- To improve the prototype EII system described in Chapter 3, based on the initial results that were obtained with a limited number of conductive samples (Chapter 4). Particularly, to change the measurement method by switching to an automated measurement system.
- To establish a new experimental method to successfully produce 2D images of 14 metallic objects, both magnetic and non-magnetic, with few different planar geometries, and values of conductivity ranging from  $0.54 \times 10^6$  to  $59.77 \times 10^6$  S/m.
- To conduct a quantitative analysis of the images by using a Canny-edge detection algorithm that enabled the contour of the imaged samples to be determined, with the goal of assessing the 'faithfulness' of the images produced by adopting the developed EII method.
- To optimise the values of components that were used to build the LCR-based system with a capacitor bank, used to adjust its resonant frequency to achieve penetration

through shielding materials. This was done to identify the best choice of resistance and capacitance, for achieving the highest Q-factor shift that could be obtained, when a conductive sample was placed in the vicinity of the coil.

- To improve the work done so far by increasing the low Q-factor absolute values that could prevent resolving resonance features and distinguishing between materials having different electromagnetic properties, thus representing a constraint for imaging of shielded metals. This issue was addressed in the second part of this work, which aimed at the implementation of a novel version of the EII system, which was based on an active bandpass filter, allowing high Q-factor values to be achieved.

The EII method here proposed was demonstrated to be suitable for non-invasive and contactless measurements, capable of revealing the presence of conductive materials, both when these were introduced into the system in air ('unshielded configuration') and when they were hidden by conductive shields ('shielded configuration').

This research work paves the path for more advanced research investigations, aimed at material characterisation for security applications.

A few final remarks about this research project should be given to highlight its novelty and relevance with respect to the scenario of security investigations. The originality of this work is linked to the experimental system being substantially different from conventional MIT systems. As mentioned earlier, such system is based on the use of a single coil, both inducing eddy currents in a sample and detecting changes in the system's resonance characteristics. An automated XY stage is employed, thus eliminating the need for an array of coils. The technique based on the use of a XY stage allows positioning the sample to be imaged at equally spaced places ('nodes') on a square scanning area (Chapter 4). The developed imaging method provides spatially distributed measurements of the system's changes due to the presence of the sample [54]. The acquisition of position-resolved-measurements at each of the nodes of the scanning area represents an efficient, low cost and low-computational-load alternative to the use of image reconstruction algorithms, as the reciprocal position between the coil and the sample is known *a priori*. Furthermore, the method here proposed is characterised by easy implementation, which makes it suitable for practical use.

Overall, the most important advantages of the EII system developed in this work are related to its being a low cost, simple technology, making no use of the conceptually and technically challenging inverse problem techniques adopted in traditional MIT systems.

## 2 Theoretical principles

### 2.1 Eddy current induction

In the early stages of this study, a basic EII system was designed and constructed. The system was tested for imaging of electrically conductive metallic samples, in both ‘unshielded’ and ‘shielded’ configurations. The physical principles on which the experiment was founded are related to eddy current theory and LCR circuit theory and are discussed in the following paragraphs.

An alternating current (AC) flows inside a coil, thus producing an AC magnetic field, which is called the *primary* magnetic field. This effect is shown by Ampère’s circuital law [50]:

$$\oint B \cdot dl = \mu I \quad (2.1)$$

In Eq. 2.1,  $B$  is the magnetic flux density (T),  $I$  is the current,  $l$  is a closed path and  $\mu$  is the magnetic permeability of the medium, which is linked to the relative permeability,  $\mu_r$ , and the permeability of free space,  $\mu_0$ , by:  $\mu = \mu_r \mu_0$  (where  $\mu_0 = 4\pi \cdot 10^{-7} \text{ Hm}^{-1}$  and  $\mu \approx \mu_0$  for a non-magnetic conductive specimen).

The magnetic field is modified when the metallic sample is placed in the vicinity of the coil, according to Faraday’s law of induction [38]:

$$\varepsilon = - \frac{d\Phi_B}{dt} \quad (2.2)$$

Faraday’s law explains how a time-varying magnetic induction flux density induces currents in an electrical conductor. It states that an electromotive force  $\varepsilon$  (having the same dimensions as a potential difference, p.d.) is induced, which is proportional to the time rate of change of the magnetic flux  $\Phi_B$ . For a coil situated normally in a field of intensity  $B$ , the flux is given by  $\Phi_B = NAB$ , where  $N$  is the number of turns in the coil and  $A$  is the coil area. In Eq. 2.2,  $\frac{d\Phi_B}{dt}$  is the rate of change of magnetic flux ( $\text{Wb s}^{-1}$ ) [38].

The system is perturbed by adding a metallic sample. Specifically, the inductive part of the impedance of the system is modified, as a consequence of eddy-current induction

inside the sample. In particular, the resonant frequency of the system constituted by the coil in air is changed when the metallic sample is inserted into the circuit. The reason why this occurs can be explained as follows.

Let us consider a coil in which an alternating current is flowing. Let  $Z_0$  be the coil impedance. When the coil approaches an electrically conductive non-ferromagnetic material, the primary alternating magnetic field penetrates the material and generates eddy currents. The induced currents flowing within the test piece generate a secondary magnetic field that tends to oppose the primary field, as shown in Fig. 2.1. This opposing magnetic field coming from the conductive material modifies the primary magnetic field and contributes to creating a total field, which is the field detected by MIT systems. A variation in the reluctance is experienced, and losses arise due to eddy-current induction. In other words, the imaginary part of the modified coil impedance decreases when the eddy current intensity in the test piece increases [50]. This is accounted for by the impedance definition:

$$Z_0 = R_0 + jX_0 \quad (2.3)$$

This expression refers to the coil impedance in air, which is a complex quantity, whose real part ( $R_0$ ) is the coil's resistance in air and whose imaginary part ( $X_0$ ) is the coil's reactance in air [38].

In the system to which this work refers, the coil is part of an LCR circuit. Therefore, the inductive reactance of the coil in air is defined by Eq. 2.4 [60]:

$$X_0 = \omega L_0 - \frac{1}{\omega C} \quad (2.4)$$

In this equation,  $L_0$  is the coil's self-inductance and  $C$  is the circuit's capacitance.

Eddy currents also contribute to the increasing of the power dissipation of energy that is responsible for changing the real part of the coil impedance. Section 2.4 will describe a mathematical model that explains the effect of eddy currents on the coil impedance. Let  $Z_1$  be the circuit impedance when the conductive material is placed into the magnetic field generated by the coil. This quantity is given by:

$$Z_1 = R_1 + jX_1 \quad (2.5)$$

Here,  $R_1$  and  $X_1$  are the resistance and reactance of the circuit, changed from Eq. 2.4 due to the presence of the conductive material.

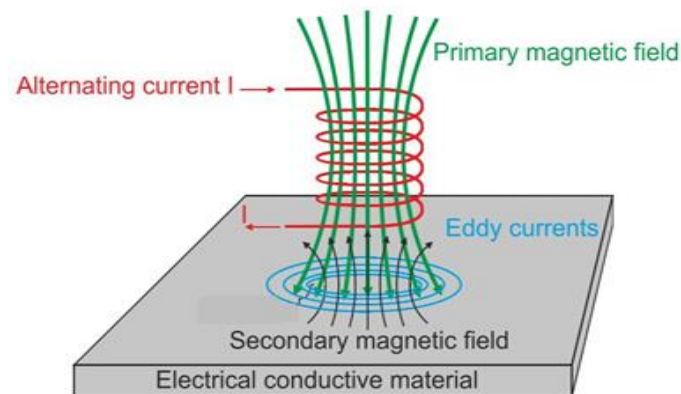


Fig. 2.1. Primary and secondary magnetic field generated by eddy currents induced inside an electrically conductive material [38].

In classical eddy current testing, measurement of the coil impedance variation from  $Z_0$  to  $Z_1$  can be obtained by either measuring the potential difference (p.d.) across a sensor coil, or the current signal detected with it [63]. The measured quantities can provide information about the nature of the material, because the eddy current amount depends on the electrical conductivity and magnetic permeability of the material in which they are induced [63].

In this work, a different approach was undertaken. A resonating LCR circuit was used in order to obtain the largest impedance change when a conductive target approached the system. The measured quantities were: 1) the system's resonant frequency and 2) the quality factor (Q-factor) of the resonance peak. This approach is supported by the considerations reported in the papers written by Gaydecki *et al.* and Du *et al.* [50]-[51]. The first paper describes the development of an inductive sensor based on a real-time digital processing system used for detection and imaging of steel reinforcing bars embedded in concrete and utilising the variation of the sensor's Q-factor due to the change of the real part of the impedance of the sensor coil [50]. Du *et al.* present a system based on an inductance-capacitance method for detection of small metallic wear debris particles and condition monitoring of rotating and reciprocating industrial machinery [51].

Let  $f_{r0}$  be the LCR circuit resonant frequency when the system is in air. This quantity is defined as [60]:

$$f_{r0} = \frac{1}{2\pi\sqrt{L_0C}}. \quad (2.6)$$

The system's resonant frequency is changed when a conductive material approaches it, as a consequence of the inductance change. In Eq. 2.6,  $L_0$  is the inductance of the system in air.

The quantity  $X_1$  in Eq. 2.5 is the reactance of the system to which the material is coupled, which includes the inductance of the system comprising the conductive material ( $L_1$  in Eq. 2.7). This can be seen by substituting the '0' subscripts in Eq. 2.4 with '1' subscripts, to account for the 'new' system, modified from the original one due to the presence of the material. The 'new' resonant frequency of such system can be expressed by:

$$f_{r1} = \frac{1}{2\pi\sqrt{L_1C}}. \quad (2.7)$$

Whenever a non-ferromagnetic conductive material is inductively coupled to the system, the total detected field decreases, due to the secondary magnetic field generated from eddy currents. The amount of field reduction depends on the frequency of the applied field. This effect has an important consequence on the circuit: the system's inductive reactance decreases. Therefore, the inductance decreases too, due to the definition of inductive reactance ( $X_L = \omega L$ ) [38]. The resultant effect on the resonant frequency is an increase in this quantity:

$$f_{r1} > f_{r0}. \quad (2.8)$$

Schematics of the system in air and when a copper (Cu) disk sample is inductively coupled to it are shown in Fig. 2.2, where the resistance and inductance have different subscripts, to indicate their change occurring due to the presence of the Cu sample.

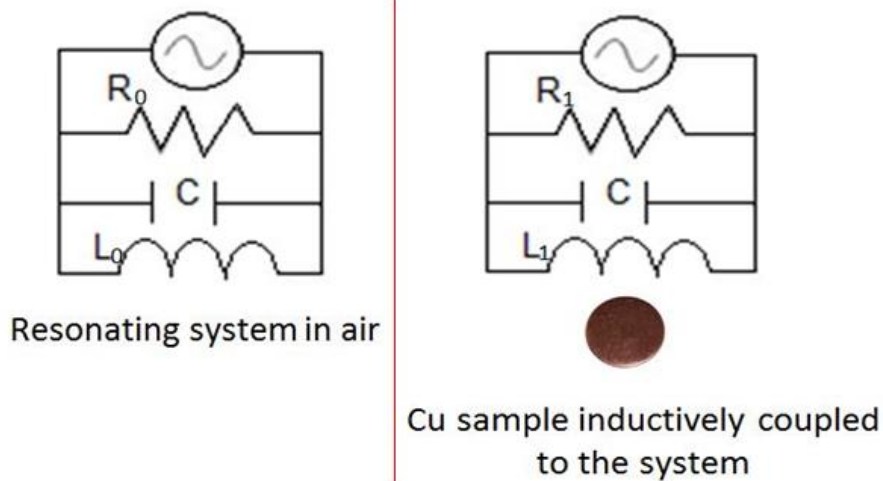


Fig. 2.2. Left: Resonating system “in air”, i.e. with no metallic sample coupled to it. The system is a parallel LCR circuit with resistance  $R_0$ , capacitance  $C$  and inductance  $L_0$ . Right: Modified resonating system including a metallic sample in the shape of a disk, inductively coupled to it. The inductance and resistance of the modified system are labelled  $L_1$  and  $R_1$ , to distinguish them from the components of the resonating system with no metallic sample coupled to it (left).

When the sample is ferromagnetic ( $\mu_r \gg 1$ ), the eddy current effect lowering the detected field is offset by the increase in the magnetic field due to magnetisation, as explained in the following. The amount of magnetisation occurring when an object of permeability  $\mu$  is placed into an applied magnetic field  $H$  can be expressed by the following equation [61]:

$$B = \mu H \quad (2.9)$$

In this formula,  $B$  is the magnetic flux density and  $H$  is the magnetic field strength [61]. The sample is magnetised and the B-field is increased proportionally to its permeability. The permeability  $\mu$  is a complicated function of the form  $\mu = \mu(T, f, p, MH, \text{etc.})$ , where  $T$  = temperature,  $f$  = frequency,  $p$  = pressure and  $MH$  corresponds to the AC magnetic history of the sample. The larger the material’s permeability is, the stronger the detected field becomes, because of the primary magnetic field being proportional to  $\mu$ . This effect is opposed to the one due to eddy current induction inside the sample.

The consequence of the enhancement in the magnetic field produced by a ferromagnetic material is an increase in the reactance of the system, due to the inductance being proportional to the B-field [61].

The inductive reactance of the system in air is defined as  $X_{L0} = \omega L_0$ , and the inductive reactance of the modified system including the ferromagnetic material of permeability  $\mu$  is defined as  $X_{L1} = \omega L_1$ . The two reactances are linked by the following relation:  $X_{L1} > X_{L0}$ . Due to the definitions of reactance, the inductance of the system increases when a ferromagnetic non-conductive material is exposed to the magnetic field generated by the coil. Mathematically:  $L_1 > L_0$ . As a result, the resonant frequency of the system decreases [38]:

$$f_{r1}^{ferromagnetic} < f_{r0} . \quad (2.10)$$

Resonant frequency measurements with the system in air and after introducing conductive samples (of both non-magnetic and ferromagnetic nature) constituted the first investigations of this research project.

The second quantity that was measured in the experiments is the quality factor of the circuit. A parallel LC circuit was initially built, whose inductance value was maintained fixed at  $680 \pm 10\% \mu\text{H}$  and whose capacitance was varied (see Chapter 3). A reminder about the physical meaning of the quality factor is summed up by the following relations [60]:

$$Q = 2\pi \frac{\text{energy stored}}{\text{energy dissipated per cycle}} = 2\pi f_r \frac{\text{energy stored}}{\text{power loss}} = \frac{\omega_0}{\Delta\omega} \quad (2.11)$$

In the last equation shown in 2.11,  $\omega_0$  is the angular frequency at resonance and  $\Delta\omega$  the frequency bandwidth of the resonator. According to the first two identities of Eq. 2.11, the quality factor (Q-factor) is the ratio of the energy stored in the oscillating resonator to the energy dissipated per cycle by damping processes.

For a parallel LCR circuit, Q is given by [57]:

$$Q = R \sqrt{\frac{C}{L}} \quad (2.12)$$

The presence of a conductive material in the magnetic field generated by a coil caused a quality factor shift which could be measured using an impedance analyser (see Chapter 3) that was sensitive enough (i.e., the shift was larger than the measurement uncertainty). Eq. 2.12 explains that the Q shift occurred as a consequence of the inductance change which was

experienced by the measurement system when a conductive material was put in the vicinity of the coil.

Let  $Q_0$  be the Q-factor of the system in air, and  $Q'$  be that of the system 'modified' by the presence of the conductive material. Due to the value of the inductance shifts occurring when materials of different nature are used, the Q-factor shift  $Q' - Q_0$  has negative value when a non-ferromagnetic conductive material is inductively coupled to the system, whereas it takes on positive values when a ferromagnetic material is present [50]. In the case of mainly conductive materials having low values of permeability, the new current flowing in the coil after eddy currents are induced leads (is in opposition to) the primary current and it is smaller than this original current, which means that the ohmic resistance of the coil increases [50]. The Q-factor of the coil drops, because it is proportional to the ratio of inductance and ohmic resistance, where the former decreases and the latter increases. This makes sense from a physical point of view because Q is the ratio between the input energy necessary to maintain oscillation and the energy lost (due to resistance) [50]. According to Eq. 2.12, in order for Q to drop the capacitance C of the system must decrease, by a greater amount than the amounts of decrease of L and increase of R. This is the case for a parallel LCR circuit like the one used in this experimental work.

The changes occurring to the resonance peaks, obtained when a resonating system is "in air" (no sample is present) and when a conductive, non-magnetic sample is placed in the vicinity of the coil, are represented qualitatively in Fig. 2.3.

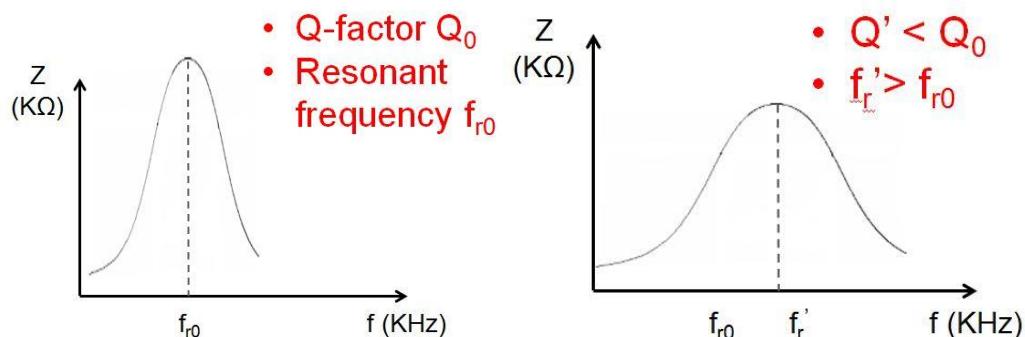


Fig. 2.3. Qualitative behaviour of a resonating system in air (left) and with a conductive non-magnetic sample inductively coupled to it (right). The graphs show the two systems' impedance, plotted against the frequency. They show the decrease in the Q-factor and increase in resonant frequency occurring due to the presence of the conductive sample [50].

## 2.2 Maxwell's equations and electromagnetic waves in conductors

The working principles of the EII system object of this work are based on the theory related to Electricity and Magnetism. This is governed by Maxwell's equations, which can be written in their generic, differential forms as follows [60]:

$$\nabla \times \mathbf{E} = -\mu \frac{\partial \mathbf{H}}{\partial t} \quad (2.13)$$

$$\nabla \times \mathbf{H} = \mathbf{J} + \varepsilon \frac{\partial \mathbf{E}}{\partial t} \quad (2.14)$$

$$\nabla \cdot \mathbf{E} = \frac{\rho}{\varepsilon} \quad (2.15)$$

$$\nabla \cdot \mathbf{H} = 0 \quad (2.16)$$

In Eqs. 2.13-2.16,  $\mathbf{E}$ ,  $\mathbf{J}$  and  $\mathbf{H}$  are vectors representing the electric field, the conduction current density and the magnetic field strength, measured in  $\text{Vm}^{-1}$ ,  $\text{Am}^{-2}$  and T, respectively. The quantities  $\mu$  and  $\varepsilon$  are, respectively, the magnetic permeability and permittivity of the medium (expressed in  $\text{NA}^{-2}$  and  $\text{Fm}^{-1}$ ), and  $\rho$  is the charge density ( $\text{Cm}^{-3}$ ).

Maxwell's equations can be used to derive the wave equation representing an electromagnetic (e.m.) wave travelling along the  $z$  direction, inside a conducting medium. The e.m. wave equation can be expressed as follows [64]:

$$\nabla^2 \mathbf{H} - \sigma \mu \frac{\partial \mathbf{H}}{\partial t} - \mu \varepsilon \frac{\partial^2 \mathbf{H}}{\partial t^2} = 0 \quad (2.17)$$

Eq. 2.17 assumes an e.m. wave characterised by a sinusoidal variation of its angular frequency  $\omega$ . In this case, the following relations stand for the first and second derivative of  $\mathbf{H}$  w.r.t. the variable  $z$  [64]:

$$\frac{\partial \mathbf{H}}{\partial z} = j\omega \mathbf{H} \quad (2.18)$$

$$\frac{\partial^2 \mathbf{H}}{\partial z^2} = -\omega^2 \mathbf{H} \quad (2.19)$$

If the e.m. wave travelling in the  $z$  direction is approaching the flat surface of a solid conductor, whose normal is in the  $z$  direction, then Eq. 2.17 can be written as follows [64]:

$$\frac{\partial^2 \mathbf{H}}{\partial z^2} - j\omega\sigma\mu\mathbf{H} + \omega^2\mu\varepsilon\mathbf{H} = 0 \quad (2.20)$$

The solution to the e.m. wave equation expressed by Eq. 2.20 can be proven to be given by [64]:

$$\mathbf{H} = \mathbf{y}H_0 \exp(j(\omega t - kz)), \quad (2.21)$$

which was obtained by considering that no variations occur in the x and y directions, and by making use of the identity:  $\nabla^2 \mathbf{H} = \frac{\partial^2 \mathbf{H}}{\partial z^2}$  [64].

In Eq. 2.21, the quantity  $k$  is called the wave number and is defined by the following relation:  $k^2 = \mu\varepsilon\omega^2 \left(1 - \frac{j\sigma}{\omega\varepsilon}\right)$ , where the complex quantity  $\frac{j\sigma}{\omega\varepsilon}$  is the ratio of the conduction current density  $\mathbf{J} = \sigma\mathbf{E}$  to the displacement current density  $\varepsilon \frac{\partial \mathbf{E}}{\partial t} = j\omega\mathbf{E}$  [64].

Let us now study the behaviour of the e.m. wave in two scenarios: 1) above the conducting medium; 2) within the conductor.

Above the conductor, the electrical conductivity  $\sigma$  equals zero. Hence, the equation for the wave number reduces to:  $k = \omega\sqrt{\mu\varepsilon}$  and  $k$  becomes a real quantity. This implies that the e.m. wave is not attenuated in the z direction [64].

Within the conductor, the quantity  $\frac{j\sigma}{\omega\varepsilon}$  is much larger than unity, therefore the displacement current can be neglected, and the electrical permittivity  $\varepsilon$  can be assumed to be zero. Mathematically, this leads to the following equation for the wave number  $k$ :

$$k = \sqrt{-j\omega\sigma\mu} = \sqrt{\frac{\omega\sigma\mu}{2}} (1 - j) \quad (2.22)$$

Substituting Eq. 2.22 into Eq. 2.20, the wave equation becomes [64]:

$$\frac{\partial^2 \mathbf{H}}{\partial z^2} = j\omega\sigma\mu\mathbf{H} \quad (2.23)$$

The solution to Eq. 2.23 can be found to be as follows:

$$\mathbf{H} = \mathbf{y}H_0 \exp\left(j\left(\omega t - \frac{z}{\delta}\right) - \frac{z}{\delta}\right) = \mathbf{y}H_0 \exp\left(-\frac{z}{\delta}\right) \cos\left(\omega t - \frac{z}{\delta}\right), \quad (2.24)$$

Eq. 2.24 describes an e.m. wave travelling through a material of conductivity  $\sigma$  and permeability  $\mu$  in the  $z$  direction. The magnitude of the wave is maximum at the conducting material's surface (where it is given by  $H_0$ ) and decreases exponentially with increasing distance  $z$  from the material's surface. The term  $-\frac{z}{\delta}$  inside the cosine in Eq. 2.24 represents the phase lag occurring between the surface wave and the wave at a depth  $z$  within the conductor [64].

In Eq. 2.24, the quantity  $\delta$  is called the standard penetration depth, or skin depth, of eddy currents, and is defined as:

$$\delta = \sqrt{\frac{2\rho}{\omega\mu}}, \quad (2.25)$$

where  $\rho$  is the resistivity of the conductor,  $\mu$  its magnetic permeability and  $\omega$  is the angular frequency of the e.m. wave [64].

The flow of current within the conductor can be calculated by using second Maxwell's equation (Eq. 2.14) and setting  $\epsilon = 0$ , which leads to the following expression, representing the current density circulating in a conductor:

$$\mathbf{J} = \nabla \times \mathbf{H} = -\mathbf{x} \frac{\partial H_y}{\partial z} = \mathbf{x} J_0 \exp\left(-\frac{z}{\delta}\right) \cos\left(\omega t - \frac{z}{\delta}\right), \quad (2.26)$$

In this equation,  $J_0 = (1 + j) \frac{1}{\delta} H_0$  is the current density at the conductor's surface.

Eq. 2.26 shows that the eddy current density within conductors is parallel to the magnetic field strength and obeys the same decaying relation with depth in the conductor [64].

### 2.3 2D imaging of shielded conductive samples

The first objective of this research work was to develop a method for identifying conductive samples of both non-magnetic and ferromagnetic nature, and image them. An EII system was developed for this purpose, as described in Chapters 3 and 4. The second objective of the investigations documented in this thesis was to test the ability of the developed EII system to penetrate through conductive barriers, and allow 2D imaging of

metallic objects concealed behind them. The theoretical principles behind this investigation are presented in the following paragraphs.

Eddy current flow is not uniformly distributed throughout the volume of a conductive sample. In particular, current flow is stronger at the surface of the sample, and it decreases exponentially with the distance from the surface. The skin depth,  $\delta$ , introduced in the previous section (Eq. 2.25), is defined as the depth within a conductor at which the eddy-current density decreases to a level equal to 37% of its surface value [64]. The skin depth can be expressed by Eq. 2.25, where  $\omega$  is the angular frequency at which the system is operated. The relation between the system's angular frequency and its frequency of operation, which in this particular experiment corresponds to the resonant frequency, is the following [34]:

$$\omega = 2\pi f_r \quad (2.27)$$

where  $f_r$  is the frequency at which the system is resonated [50]:

$$f_r = \frac{1}{2\pi\sqrt{LC}} \quad (2.28)$$

The skin depth will have to be sufficiently high in order for penetration through conductive barriers (shields) to occur. This statement raises an important requirement for the system: the latter should be operated at a suitable frequency, as shown by the definition of skin depth (Eq. 2.7) [49]. According to Eq. 2.16, penetrating through these shields can be achieved by decreasing the system's resonant frequency to an extent depending on the material's electromagnetic properties (identified by  $\sigma$  and  $\mu$ ). One way of decreasing  $f_r$  is to increase the capacitance, as is shown by the definition of resonant frequency expressed by Eq. 2.16.

The use of the electromagnetic induction interrogation technique here described, based on a resonant system where the inductor is the sensor, proved beneficial for attaining penetration through conductive shields. This is the case because coupling the inductor with a conductive object leads to changes in the resonant circuit's parameters, such as its resonant frequency or quality factor, which can be detected. The equation that governs the behaviour of the resonant system can be approximated by Eq. 2.16. In this equation,  $L$  and  $C$  are the inductance and capacitance of the system. The crucial point is that operating the system at its resonant frequency is known to enhance the sensitivity of detection [49]. In the present

work, the ability to adjust the system's resonant frequency has been exploited with the purpose of imaging through conductive shields.

The penetrating power of electromagnetic imaging through a shield of a given material is limited by the skin depth  $\delta$  [50] through which the oscillating magnetic field can penetrate through the material. In order to achieve a penetration through the shield, sufficient for the oscillating magnetic field to reach the target to be imaged, the value of the capacitance was chosen so that the skin depth was either larger or of the same order of magnitude of the thickness of the shield. Therefore, by selecting an appropriate value of capacitance, the system should allow penetration through a conductive target, even when this was hidden behind shielding conductive materials.

## 2.4 Eddy current detection in non-ferrous metals

The impedance of a coil having  $N$  turns, with axis perpendicular to a semi-infinite flat metal surface and operated at a frequency  $f = \omega/2\pi$ , is given by [65]:

$$Z_{coil} = \frac{i\omega\pi N^2 \bar{r}\mu}{(l_2-l_1)^2(r_2-r_1)^2} \int_0^\infty \frac{1}{\alpha_0^3 \alpha^3} J^2(r_1, r_2) \left\{ 2\alpha_0(l_2 - l_1) + 2e^{-\alpha_0(l_2-l_1)} - 2 + (e^{-2\alpha_0 l_2} + e^{-2\alpha_0 l_1} - 2e^{-\alpha_0(l_1+l_2)}) \frac{\alpha_0 - \beta_1}{\alpha_0 + \beta_1} \right\} d\alpha \quad (2.29)$$

Where:

$$\alpha_0 = [\alpha^2 - \bar{r}^2 \omega^2 \mu_0 \epsilon_0]^{1/2} \quad (2.30)$$

$$\bar{r} = \frac{r_1 + r_2}{2} \quad (2.31)$$

$$\beta_1 = [\alpha^2 - \bar{r}^2 \omega^2 \mu_0 \epsilon_0 + i\bar{r}^2 \omega \mu_1 \sigma_1]^{1/2} \quad (2.32)$$

$$J(r_1, r_2) = \alpha^2 \int_{r_1}^{r_2} r_0 J_1(\alpha r_0) dr_0 \quad (2.33)$$

Where

$\alpha$  = variable of the integration,

$\mu_0$  = permeability of free space,

$\epsilon_0$  = permittivity of free space,

$\mu_1$  = permeability of metal slab,

$\sigma_1$  = conductivity of metal slab, and

$J_1$  = Bessel function of the first kind.

The probe variables in Eqs. 2.29-2.33 and following equations of the next page are defined as follows:

$r_1$  = coil inner diameter,

$r_2$  = coil outer diameter,

$l_1$  = vertical distance from coil lower base to metal surface (lift-off distance),

$l_2$  = vertical distance from coil upper base to metal surface, and

$d_c = l_2 - l_1$  = coil longitudinal length (height).

For nonferrous metals,  $\mu_1$  may be considered equal to  $\mu_0$ . The approximation  $\alpha \approx \alpha_0$  will be applied in the following [65], assuming coil geometry characterised by radius  $r = 0.01$  m and frequency  $f = 100$  kHz.

The equation for the coil impedance (2.29) can be separated into parts that relate to the coil, the metal, and the coil to metal interaction. If all geometrical variables are constant as a specific coil is chosen, the equation can be separated into 5 parts that are functions related to the electromagnetic interaction. The 5 parts are as follows:

- 1) Coil property independent of the variable of integration:

$$A = \frac{\pi N^2 \bar{r} \mu}{(l_2 - l_1)^2 (r_2 - r_1)^2} \quad (2.34)$$

- 2) Coil property, a Bessel function and a function only of the variable of integration:

$$B(\alpha) = J^2(r_1, r_2) \quad (2.35)$$

3) Coil property, which is a function only of the variable of integration:

$$C(\alpha) = 2\alpha d_c + 2e^{-\alpha d_c} - 2 \quad (2.36)$$

4) Function of the coil-metal separation distance  $l_1$ :

$$D(\alpha, l_1) = e^{-2l_1}(e^{-\alpha d_c} - 1)^2 \quad (2.37)$$

5) Metal property, which is a function of conductivity and frequency:

$$R(\omega, \sigma, \alpha) + iI(\omega, \sigma, \alpha) = \frac{\alpha_0 - \beta_1}{\alpha_0 + \beta_1} \quad (2.38)$$

The original equation for the coil impedance can thus be rewritten as:

$$Z = i\omega A \int_0^\infty \frac{1}{\alpha^6} B(\alpha) C(\alpha) d\alpha + i\omega A \int_0^\infty \frac{1}{\alpha^6} B(\alpha) D(\alpha, l_1) (R + iI) d\alpha \quad (2.39)$$

All variables of Eq. 2.39 are now real. With other held constant, the impedance of the coil is a function of lift-off ( $l_1$ ), frequency ( $\omega$ ), and conductivity ( $\sigma$ ). Assuming that both lift-off and the product  $\omega\sigma$  are held constant, it can be proven that the inductance does not vary when two different frequencies are used to operate the coil and the latter is placed onto two different metals (with  $\sigma_1 \neq \sigma_2$ ) [65]. Under these assumptions, the inductance is given by:

$$L = A \int_0^\infty \frac{1}{\alpha^6} BC d\alpha + A \int_0^\infty \frac{1}{\alpha^6} BDR d\alpha \quad (2.40)$$

If the product  $\omega\sigma$  is constant, then the resistance of a coil operated at a frequency  $f_1 = \omega_1/2\pi$  and placed over a metal of conductivity  $\sigma_1$  is equal to:

$$R_1 = i^2 \omega_1 A \int_0^\infty \frac{1}{\alpha^6} BDI d\alpha \neq R_2 = i^2 \omega_2 A \int_0^\infty \frac{1}{\alpha^6} BDI d\alpha \quad (2.41)$$

Where  $R_2$  is the resistance of the coil when this is operated at a frequency  $f_2 = \omega_2/2\pi$  and it is placed over a metal of conductivity  $\sigma_2$ .

In Eq. 2.41, the integral remains constant but the effective coil resistance changes linearly with frequency.

In the experimental work that is detailed in this thesis, the quantities of interest are the resonant frequency and Q-factor expressed by equations 2.6, 2.7, 2.11 and 2.12. By

definition, these depend upon the coil inductance, as in Eq. 2.40. Specifically, the resonant frequency is given by:

$$f_r = \frac{1}{2\pi\sqrt{LC}} = \frac{1}{2\pi\sqrt{C} \sqrt{A \int_0^\infty \frac{1}{\alpha^6} BC d\alpha + A \int_0^\infty \frac{1}{\alpha^6} BDR d\alpha}} \quad (2.42)$$

The Q-factor for a generic LCR circuit with complex impedance  $Z_t = Z_r + iZ_i$  ( $Z_t$  is effectively  $Z$  in Eq. 2.39) is defined by the following equation [50]:

$$Q = \frac{\omega L}{Z_r} \quad (2.43)$$

Where  $Z_r$  is the real part of the impedance (as in Eq. 2.41),  $\omega$  is the operating frequency of the circuit and  $L$  the coil inductance. Using Eqs. 2.40 and 2.41, 2.42 can be rewritten as:

$$Q = - \frac{\int_0^\infty \frac{1}{\alpha^6} BC d\alpha + \int_0^\infty \frac{1}{\alpha^6} BDR d\alpha}{\int_0^\infty \frac{1}{\alpha^6} BDI d\alpha} \quad (2.44)$$

Functions  $R$  and  $I$  establish the  $Q$  dependence upon the conductivity of the material, function  $D$  links  $Q$  to the lift-off.

On the other hand, the resonant frequency depends on the same parameters (conductivity and lift-off), in a different way from the way in which  $Q$  is linked to those, through functions  $D$  and  $R$  contained in Eq. 2.40.

In cases where either the lift-off, the product  $\omega\sigma$  or both are non-constant, relations 2.40-2.44 cease to be valid and the resonant frequency and Q-factor depend on the lift-off and on the conductivity in a more complicated way. The former is dependent by definition on the inductance (Eq. 2.28), which is contained in the imaginary part of  $Z$ , as in Eq. 2.39. The latter depends on both the real and the imaginary part of  $Z = Z_t = Z_r + iZ_i$ . As underlined previously for the case in which  $\omega\sigma = \text{constant}$ , the lift-off dependence is given by function  $D$ , and the relation between the coil impedance and the conductivity of the sample is extant due to the functions  $R$  and  $I$  (Eqs 2.37-2.39).

What described in the previous paragraph shows that the dependency of the resonant frequency and the Q-factor on the lift-off and the conductivity of the sample is different. Therefore, the behaviour of these quantities can be understood only by treating them separately and analysing the limits of the function in Eq. 2.39 for low and high values of the

variables lift-off and conductivity, respectively. Chapter 5 contains experimental work aimed at deriving curves showing the lift-off dependence of measured resonant frequency and Q-factor, and later focuses on the behaviour of these measured quantities on the conductivity of the samples included in this experimental work.

### 3 An LC resonant system for 2D imaging of conductive materials

This chapter documents the early stages of the set-up of a 2D imaging system for the identification of conductive samples. Section 3.1 describes the initial LC resonant system and proof-of-principle method with which the initial measurements were carried out. The following sections are about a battery of experiments that were performed at the beginning of this PhD project. The strategy was identifying a proper method to achieve identification of conductive samples and 2D imaging by means of eddy current induction. Details about how each experiment was performed are given in the individual sections. Early results and discussion are reported in Sections 3.2-3.7.

#### 3.1 Description of the early stage experimental system

This section describes a prototype experimental system developed in the early stages of this research activity, which was based on a resonating system that included a metallic sample, an inductor ( $L=970 \mu\text{H} \pm 10\%$ ) and a capacitor bank, allowing selection of capacitance  $C$  values going from  $10^{-4}$  up to  $1.111 \mu\text{F}$ , with sensitivity equal to  $0.1 \text{ nF}$  (Fig. 3.1). The first inductor that was used for these experiments was a pancake coil (outer diameter  $43.0 \pm 0.5$  mm, inner diameter  $22.0 \pm 0.5$  mm, height  $20.0 \pm 0.5$  mm) (Fig. 3.1). The coil was placed in a lodge positioned on the upper layer of a Perspex support structure (non-magnetic). A second Perspex layer was used to position the sample (e.g., a 6-cm-diameter, 2-mm-thick copper disk) along a plane parallel to the disk's surface and perpendicular to the coil's axis (Fig. 3.1). This configuration allowed the sample to be 'seen' by the coil, and the two to be placed at a vertical distance from each other (lift-off) which was constant. The values assigned to the lift-off were varied throughout this work and are specified for each experiment described in the following. The inductor was connected in parallel to a capacitor bank, and the two together were connected to the Precision Impedance Analyzer 6500B (Wayne Kerr) (Figs. 3.2-3.3). The impedance analyser supplied the excitation signal, and the inductor initially established an AC magnetic field, which was then modified due to the presence of the conductive sample in

which the eddy currents were induced. The inductor was also used as a sensor, to detect changes linked to the presence of the sample. These changes were measured with the impedance analyser, which allowed performing frequency sweeps of various quantities, including the impedance and inductance of the system. The resonant frequency and Q-factor related to resonance could also be measured with the instrument.



Fig. 3.1. Left: Picture of the experimental system used at the initial stage of this research work, to test whether the presence of a metallic sample could be detected by using a LCR-based system. The sample in this picture is a copper disk (6-cm-diameter, 2-mm-thickness), and the coil is a pancake coil (No. turns= $400 \pm 1$ , outer diameter  $43.0 \pm 0.5$  mm, inner diameter  $22.0 \pm 0.5$  mm, height  $20.0 \pm 0.5$  mm). Two Perspex layers were used as a non-magnetic structure to support the coil and maintain it in a fixed position w.r.t. the sample. The coil was part of a LC circuit whose capacitance could be varied to make the system resonate at different values of resonant frequencies. This was achieved by selecting appropriate capacitance values from the “Jay-Jay instruments - Type no. VC5” capacitor bank (Educational Measurements Limited), shown in the picture on the right.

The prototype system described above was tested for 2D imaging of sample objects having different electrical conductivities, both ferromagnetic and non-magnetic, by means of resonant frequency measurements. These measurements were performed when the system was “in air” (no sample present) and when the samples were coupled to the LC system, thus modifying the system’s resonant frequency. The copper disk shown in Figs. 3.1 and 3.3 is one example among the samples used, which were characterised by different geometries and different electromagnetic properties. Two further examples of the samples are shown in Fig. 3.4, representing two aluminium disks of different values of diameter, both having 2-mm-thickness. The presence of the capacitor bank made it possible to tune the capacitance and investigate the effect of using different values of C to vary the resonance frequency of the system. This feature of the system was beneficial for investigating its capability to detect the presence of conductive materials shielded by conductive screens (Section 2.3). Moreover, the possibility of tuning C was advantageous for improving the system’s sensitivity of detection, which could allow the identification of poorly conductive materials (that produced eddy

currents of low magnitude), as well as enable distinguishing between different materials having similar values of conductivity, which therefore produced similar shifts in the system's resonant frequency.



Fig. 3.2. Left: Front view of the Precision Impedance Analyzer 6500B (Wayne Kerr) used to measure the resonant frequency and Q-factor of the system, in air and in the presence of conductive samples. The display shows the resonance peak on a Z vs frequency plot. The instrument was connected to a parallel LC circuit, with electronic schematic shown on the right of the figure, which consisted in a coil (e.g. pancake coil with inductance  $L=970 \mu\text{H} \pm 10\%$ ) and a capacitor selected from the capacitor bank.

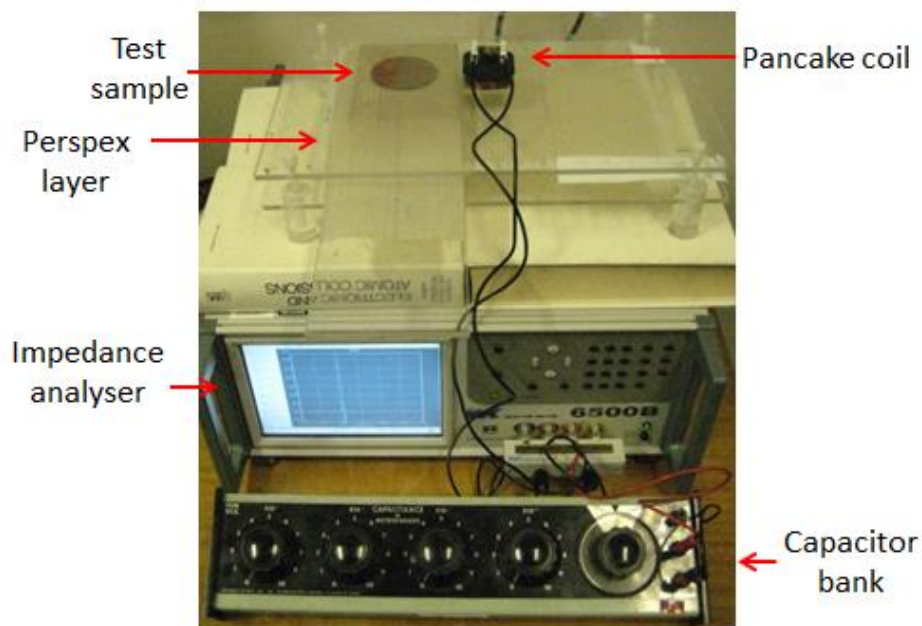


Fig. 3.3. Experimental set-up. The impedance analyser acted as an AC current generator. A copper disk was used as a test sample and moved by means of a Perspex support. The instrument was connected to a pancake coil inside which eddy currents were induced. These currents altered the measured impedance. A capacitor bank was used in order to move the resonance peak to lower frequency values, to investigate the possibility of achieving eddy current penetration through materials shielding the sample.

Initial investigations with the basic resonating system presented above (Figs. 3.2-3.3) included some test samples made of copper and aluminium disks ( $2.0 \pm 0.5$  mm thickness) of different diameters (Fig. 3.4). The behaviour of different types of coils (Fig. 3.5) coupled to the test samples specified above was investigated.

The main goals of the preliminary experiments described in the following sections were: 1) to understand whether it could be possible or not to succeed at imaging metallic objects by using resonant frequency measurements, and 2) to develop a proof-of-principle method for 2D imaging of these objects.

At the initial stage, the samples were placed under the coil constituting the LC system and the impedance analyser was used to measure the resonant frequency of the system, both in the presence of the metals and in their absence (“in air”), for comparison purposes. The hypothesis here was that the change in the system’s resonant frequency could be measured. A measurable change of resonant frequency was found when conductive samples of different nature and geometries were inductively coupled into the system (Section 3.2). This result set the basis for investigations around the possibility of producing 2D images revealing the presence and reproducing the shapes of the samples, by means of resonant frequency measurements, which were achieved by building a set-up consisting of a support based on two parallel Perspex layers, illustrated in Fig. 3.3. Q-factor measurements were performed after testing the method based on resonant frequency measurements, by adopting a similar method, as reported in Section 3.6.

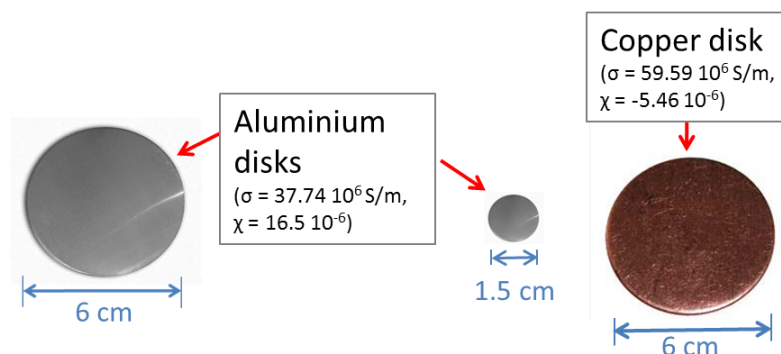


Fig. 3.4. Representation of aluminium and copper disks used as test samples. The values of electrical conductivity ( $\sigma$ ) and magnetic susceptibility ( $\chi$ ) reported here were tabulated in [66]. Uncertainties in the disk diameters were equal to 0.5 mm.

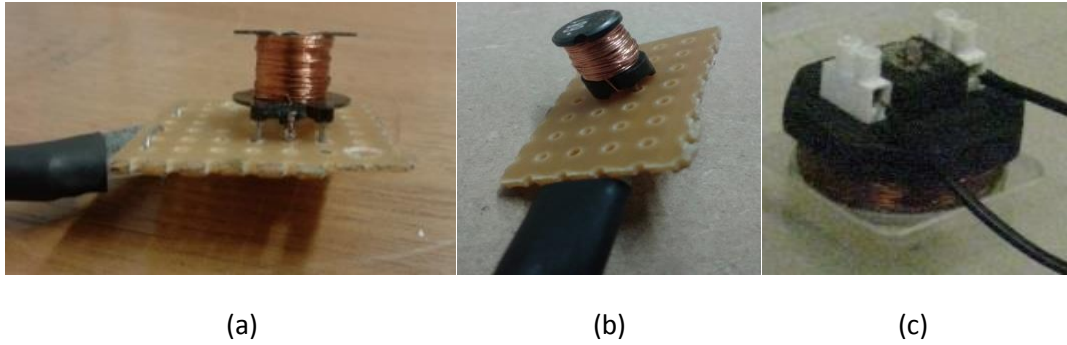


Fig. 3.5. Images of all coils tested in this work, having characteristics as follows: (a) air-cored coil (No. turns= $100 \pm 1$ , inner diameter  $8.0 \pm 0.5$  mm, outer diameter  $9.0 \pm 0.5$  mm, height  $8.5 \pm 0.5$  mm); (b) ferrite-cored coil (No. turns= $145 \pm 1$ ,  $\varnothing=7.8 \pm 0.5$  mm, height= $9.5 \pm 0.5$ mm); (c) pancake coil (No. turns= $400 \pm 1$ , outer diameter  $43.0 \pm 0.5$  mm, inner diameter  $22.0 \pm 0.5$  mm, height  $20.0 \pm 0.5$  mm).

### 3.2 Resonant frequency changes due to eddy currents

The primary purpose of the experiment reported in this section was to investigate changes in the resonant frequency when metals of different nature were placed under the inductor and w.r.t. when no object was used (coil “in air”) (Fig. 3.6).



Fig. 3.6. Simplified sketch showing the experimental configuration in which a flat metallic sample was inductively coupled to an inductor (“ferrite-cored coil”) at a fixed value of lift-off, i.e., vertical distance between the sample and the ferrite-cored coil. The inductor shown here (made by “multicomp”, part no. MCSCH895-681 KU) was connected to a capacitor as shown in Figs. 3.2-3.3. This figure represents one of the two configurations used in the experiments, the second one being characterised by the LC system “in air”, i.e., with no metallic sample present.

The method adopted in this experiment consisted in setting a series of capacitance values, using which the difference in resonant frequency values, measured in air and after adding different types of steel, was calculated. The resonant frequency values were measured

by means of the impedance analyser, after setting the external capacitor bank to a series of increasing values going from  $0.1 \mu\text{F}$  to  $1 \mu\text{F}$ , with steps of  $0.1 \mu\text{F}$ . Eqs. 2.6. and 2.7 showed the dependence of the resonant frequency on the capacitance in the two scenarios when the system was in air and after each metallic sample was introduced. Trends predicted by these equations were found after plotting measured values of resonant frequency against the selected values of capacitance. The plots shown in Fig. 3.7 were obtained by inductively coupling the following samples to the LC system:

- 2-pence ferromagnetic coin (copper-plated steel,  $25.0 \pm 0.5$  mm-diameter,  $1.0 \pm 0.5$  mm-thickness);
- $(40.0 \pm 0.5) \times (30.0 \pm 0.5) \times (3.0 \pm 0.5)$  mm<sup>3</sup> steel sample;
- $(40.0 \pm 0.5) \times (30.0 \pm 0.5) \times (1.0 \pm 0.5)$  mm<sup>3</sup> steel sample.

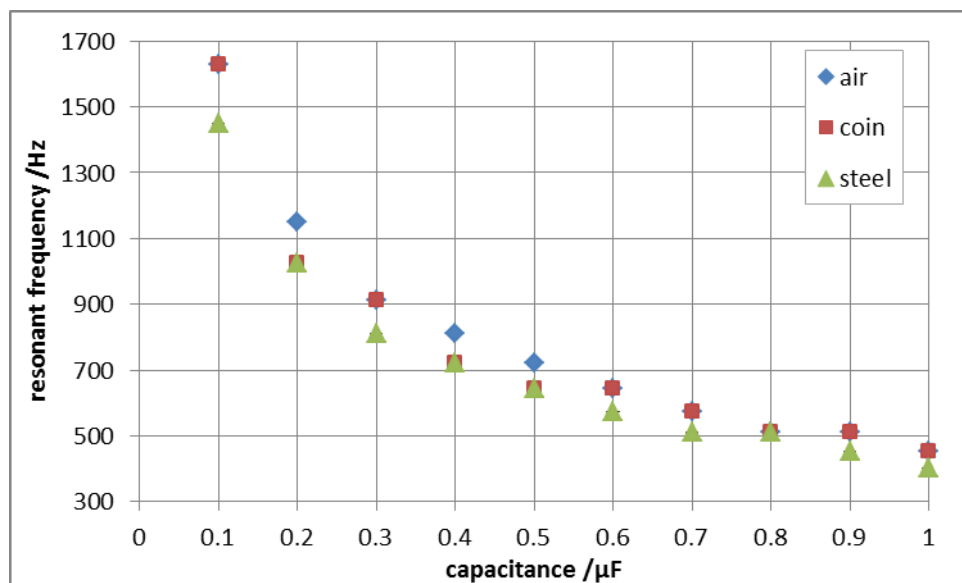


Fig. 3.7. Resonant frequency (Hz) vs external capacitance ( $\mu\text{F}$ ) measured with 1) coil in air, 2) coil above 2-pence magnetic coin and 3) coil above 3-mm-thick steel sample. Frequency values were measured at fixed capacitance values, set up using a capacitor bank (“Jay-Jay instruments - Type no. VC5”), by means of the impedance analyser. Quantities uncertainties were smaller than the dimensions of data points in this graph and are therefore not visible.

Since all the materials used in this experiment were ferromagnetic, the resulting resonant frequency values were lower than the corresponding ones obtained when the system was in air (Fig. 3.7). This behaviour was explained theoretically by Eqs. 2.6, 2.7 and

2.10 in Chapter 2, and is resembled by experimental observations. The trends shown in Fig. 3.7 indicated that the resonant frequency dependence on the capacitance expressed in Eq. 2.6 was valid in the range of capacitance used in this work, and thus justified the approach adopted in this work. Results similar to the ones shown in Fig. 3.7 were found by using non-magnetic samples, for which the resonant frequency was higher than the frequency measured in air. This confirmed the validity of the theoretical assumptions expressed in Eqs. 2.6-2.8. Quantitative information about the sample's magnetic properties was not available at this stage and this prevented further conclusions to be drawn with respect to the response of the system to samples having different characteristics of permeability. Section 5.7 is about investigations of this kind, conducted with the purpose of characterising materials, i.e., test samples having the same geometries and different electromagnetic properties. Iron with a known value of purity was chosen as a sample representative for the category of "ferromagnetic materials".

Values of resonant frequency obtained with the system in air, and after adding a coin, a 1-mm-thick steel sample and a 3-mm-thick steel sample were considered (Fig. 3.7). Changes between the resonant frequency of a coil in air and that of a coil above each of the three metals were calculated by using:

$$\Delta f (\%) = \frac{f(air) - f(sample)}{f(sample)} (\%) . \quad (3.1)$$

Percentage changes up to 12% were found (this value was attested to be significant after taking into account the measurement errors). This promising result was the input leading to carry out further investigations, which are detailed in the following sections.

### 3.3 Position-resolved measurements of the resonant frequency

The first objective of this experiment was to develop a proof-of-principle method to image a 6-cm-diameter copper disk. This represented the first attempt to image an object by using the resonant frequency technique which is detailed in the next paragraphs. Secondly, the developed proof-of-principle method was tested to achieve imaging of the same disk, after having placed an aluminium foil in contact with it, for shielding purposes. In such a way, two scenarios were studied, in which a visible object and a hidden one were to be identified. Measurements were performed by adopting the following procedure, which set the basis for the experimental method that was used in most of the investigations described in the next chapters (see Section 4.2).

- 1) Initially, a metallic sample was placed under the inductor, on the lower Perspex layer, while the coil was secured in a lodge extracted on the upper layer (Figs. 3.1a and 3.3). The coil was connected to the capacitor bank, in turn connected to the impedance analyser introduced in Section 3.1 (Fig. 3.2).
- 2) A scan of the sample to be imaged was achieved, as follows. The sample was moved by hand along a plane parallel to the plane defined by the lower base of the coil. The coil lift-off, measured with a ruler, was made equal to  $2 \pm 1$  mm. Such a large uncertainty was compensated for in the next phase of the experimental work, where an automated scanning system was set up and software was run to control the measurement acquisition (Chapter 4). The new experimental system allowed more accurate positioning of the sample and thus improved reliability of the results. Frequency sweeps were set with the impedance analyser, in order to identify the resonant frequency of the system at each position along the object plane, to produce a  $n \times n$  scanning area, as shown in Fig. 3.8. The scanning area was set to be larger than the area occupied by the samples to be imaged, to allow the samples' dimensions to fit the plot.
- 3) The frequency at which the LC circuit resonated was measured at each position of the sample along the x and y axis (Fig.3.8). The change in frequency occurred because of the different distances of the sample from the coil, at the various positions along the scanning area. The frequency, in turn, varied as a consequence of the change in the inductance of the system, as explained in Chapter 2.

- 4) 2D surface plots were generated with *Matlab* by means of interpolation with a piecewise cubic fit, by plotting position-resolved resonant frequency values (measured as detailed at point 3) against the x and y positions on the scanning area.

This measurement strategy provided a resonant frequency 2D scan and paved the way for the implementation of a novel imaging technique for metals identification. Pictures of two different coils used to test the proposed scanning method with copper and aluminium disks are shown in Fig. 3.9.

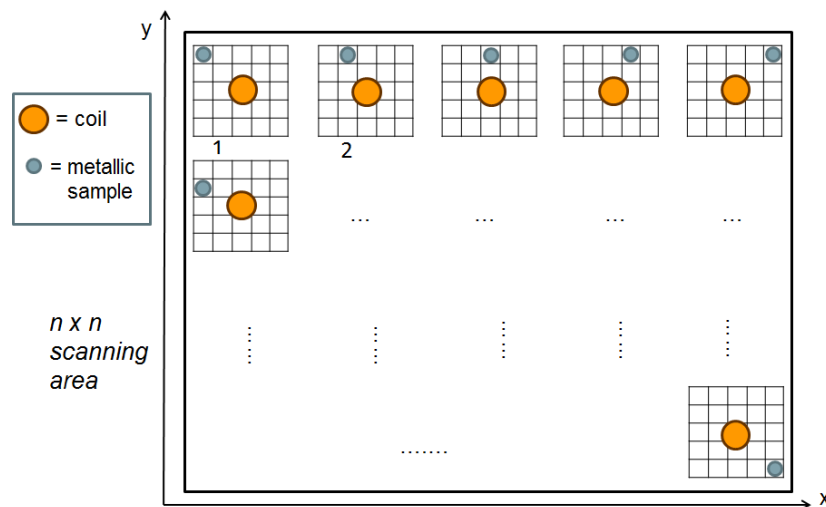


Fig. 3.8. Sketch representing the scanning area, made up of  $n \times n$  total positions, or nodes, at each of which the measurements were acquired, by using the impedance analyser. The coil, represented by the yellow circles, was maintained at a fixed position w.r.t. the metallic sample (light blue), which was initially placed at starting position labelled “1”, and was then moved by hand to the right (position “2”) and so on, until the first row of the scan was completed. The sample was then moved to the next row of the scan below the first one, and then to third one etc., until  $n \times n$  measurements were acquired, corresponding to all the positions of the sample along the scanning area.

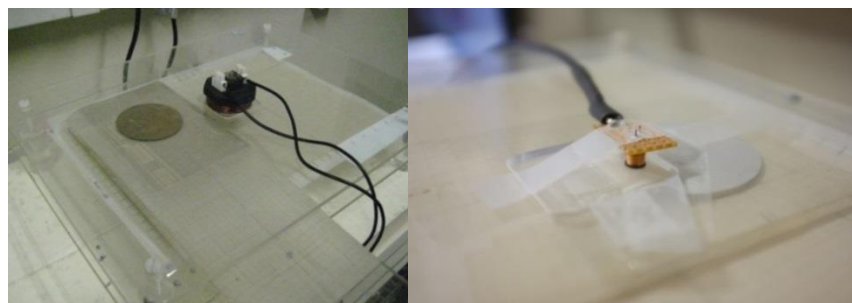


Fig. 3.9. Pancake coil (left) and ferrite-cored coil (right) used to image a copper disk (left) and an aluminium disk (right) with the aid of Perspex layers. Graph paper was used to keep track of the motion of the disk samples.

The experiments reported in this section involved the use of a 6-cm-diameter copper disk as a sample. Profiles obtained by moving the sample by hand along the y axis indicated in Fig. 3.8 are reported in Figs. 3.10 and 3.11. 2D surface plots generated with *Matlab* by plotting the resonant frequency against the xy positions are shown in Figs. 3.16 and 3.17. The data points shown in these figures and in similar ones reported in this thesis represent the positions where the measurements were taken.

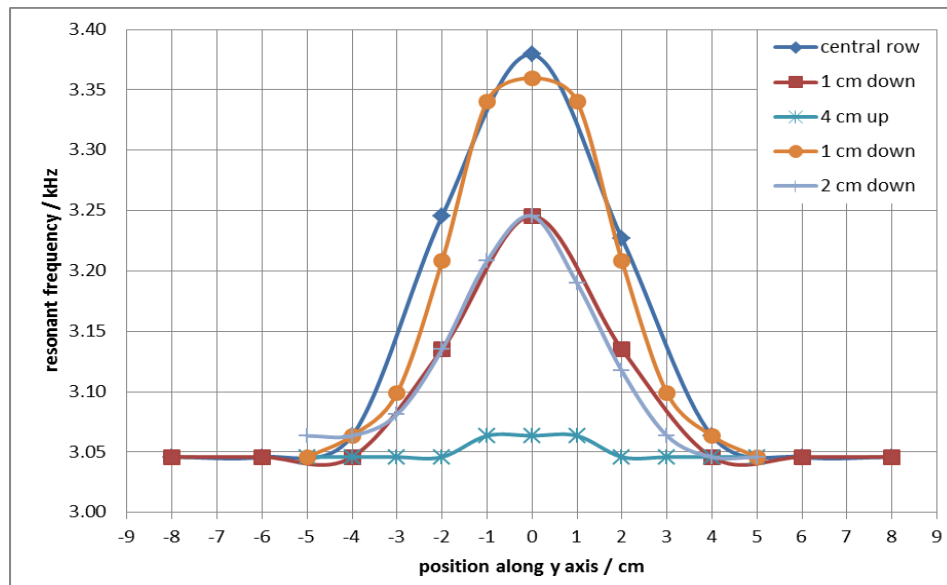


Fig. 3.10. Resonant frequency measured with a copper disk at different positions along the x axis (different colours in figure) and y axis (abscissa of the graph). The key reported on the right of the graph indicates the rows at which the measurements were taken by moving the disk along a  $4 \times 4 \text{ cm}^2$  area, as specified in the following. 'Central row' means that the disk was positioned on 16 equally-spaced-places along the horizontal line at the centre of the scanning area; 'up' and 'down' respectively refer to rows above and below the central row of the scan.

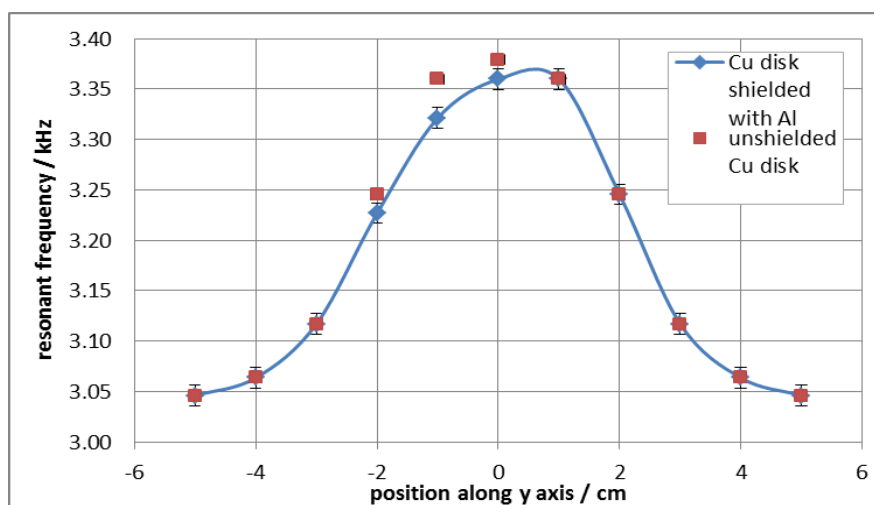


Fig. 3.11. Resonant frequency (kHz) measured with unshielded (square) and shielded (diamond) copper disk at different positions along the x axis of the scanning area.

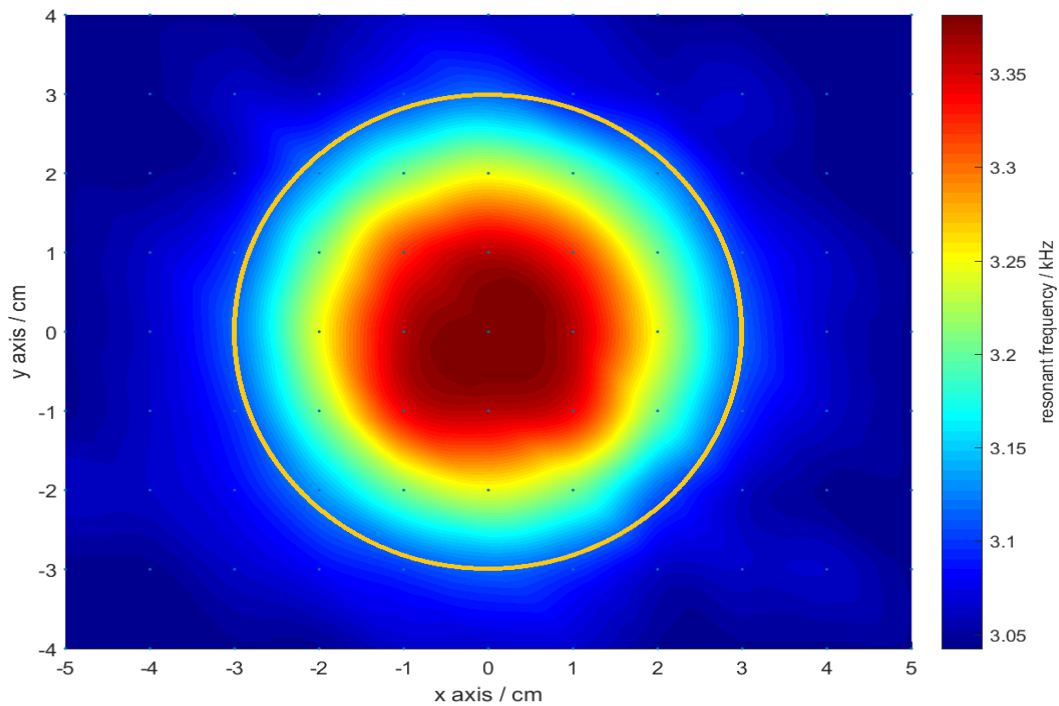


Fig. 3.12. 2D Surface plot obtained with *Matlab* and representing a 6-cm-diameter copper disk, imaged by means of a resonant frequency scan. The shape of the disk seen from the above is clearly reproduced in the image, and the diameter in the figure, measured with a ruler, is in agreement with the diameter of the actual sample. The data points in the plot represent the positions along the scanning area where the measurements were taken.

The developed method successfully imaged the disk by means of resonant frequency measurements, as shown by Figs. 3.10-3.14. Both curves reported in Figs. 3.10 and 3.11 revealed an asymmetry which was due to either the Perspex layer or the coil (or both) being tilted. This fault was intrinsic to the measurement method used in the early stage of this research, which was based on taking measurements by hand and therefore was not optimised. The importance of improving the system and measurement method led to modifying them, as described in the next chapter. The orientation of the sample object w.r.t. the coil plane was an essential parameter in these measurements, because resonant frequency values changed with the object-to-coil distance. Extra care needed to be paid when placing the object and the coil, in order to have their planes as parallel as possible. Otherwise, the curve of resonant frequency vs position coordinate would be asymmetric and, as a consequence, the resulting object image would be distorted.

The Al disk was then shielded by a piece of aluminium foil (thickness equal to  $0.016\pm 0.001$  mm) which was put in between the disk and the Perspex layer onto which the coil was placed. The image of the disk in the “shielded” configuration is reported in Fig. 3.15.

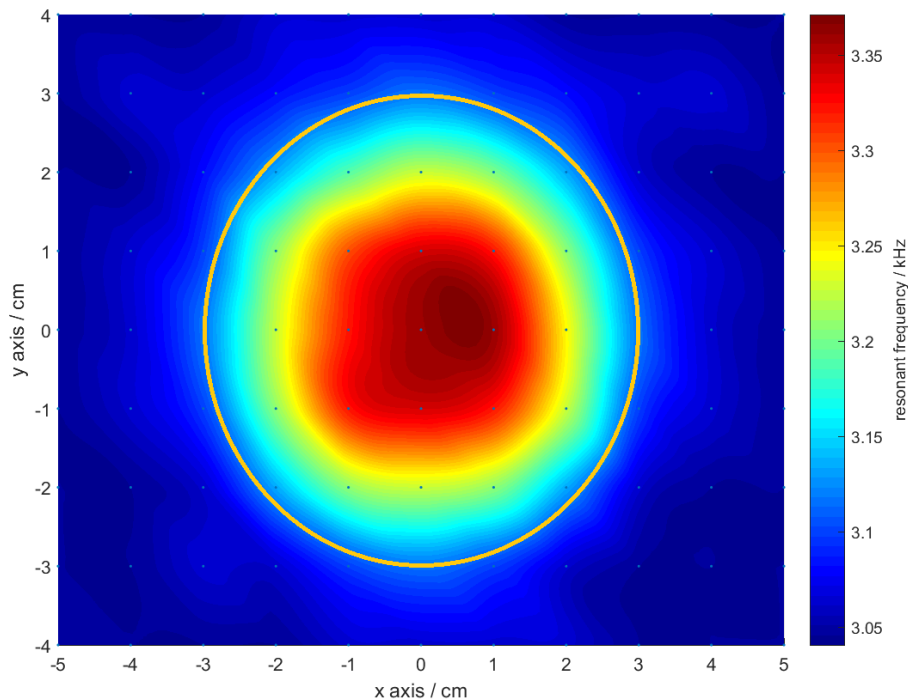


Fig. 3.13. 2D surface plot of a 6-cm-diameter copper disk shielded with an aluminium foil, and imaged by means of a resonant frequency scan. The shape of the disk is clearly reproduced in the image and the diameter in the figure corresponds to the one of the actual sample.

Images of copper disks unshielded and shielded with aluminium foil successfully revealed the presence of the metallic object, thus demonstrating the usefulness of the investigations being carried out (Figs. 3.12 and 3.13). This result showed that the proposed imaging technique was not only working with unshielded metallic samples, but also with samples hidden beneath a piece of aluminium foil shielding it.

The last part of this experiment was a test carried out to reinforce the choice made about using the value of capacitance  $C=0.03 \mu\text{F}$ . For this purpose, resonant frequency measurements obtained with a 6-cm-diameter, 2-mm-thick aluminium disk were measured with two different external capacitance values:  $C=0.03 \mu\text{F}$  and  $C=1.111 \mu\text{F}$ . Data corresponding to position  $y=0$  (i.e., the row of the scan passing through the centre of the disk,

as in Fig. 3.8) was taken into account. Differences (%) between values measured at subsequent positions along the horizontal x axis were calculated for data at  $C=0.03 \mu\text{F}$  and  $C=1.111 \mu\text{F}$ . Such differences were found to lie between -3% and 4% for data obtained at the lower capacitance value, whereas the frequency values were all equal, within the experimental uncertainty (between 0.04 and 0.06 for both  $f_r$  and Q), at  $1.111 \mu\text{F}$ . The latter value of capacitance would have prevented the system from working effectively to image conductive samples. This is because the change in resonant frequency due to the presence of these samples was not larger than the experimental uncertainty of resonant frequency measurements obtained in the absence of the samples. This conclusion justified the choice of a capacitance  $C=0.03 \mu\text{F}$ , which was made in the experiments described in this section.

### 3.4 Imaging copper, aluminium and steel samples

More objects, having different geometries and different values of electrical conductivity and magnetic susceptibility, were included in the research investigation about 2D imaging of conductive samples. In particular, specimens made of copper, aluminium and mild steel (i.e., general purpose steel commonly used for machining, suitable for lightly stressed components including gears and shafts, which is also called “low carbon steel”, due to carbon content from 0.04% to 0.30%, and also containing the following: silicon 0.40% max, manganese 0.70-0.90%, sulphur 0.040% max and phosphorous 0.040% max) were used. The aim of this experiment was to understand whether imaging by means of resonant frequency measurements was possible for various metals, and whether the different magnetic properties of such metals were reflected by the different images which were obtained with the developed method.

Aluminium and copper disks (6-cm-diameter, 2-mm-thickness) and a rectangular specimen made of mild steel (area  $4 \times 3 \text{ cm}^2$ , 1-mm-thickness) were imaged (Figs. 3.14-3.17). The graph reported in Fig. 3.14 shows profiles obtained by plotting the resonant frequency measured for the three metals vs the positions of the samples along the x axis (i.e., the horizontal axis passing across the centre of the scanning area, as shown in Fig. 3.8).

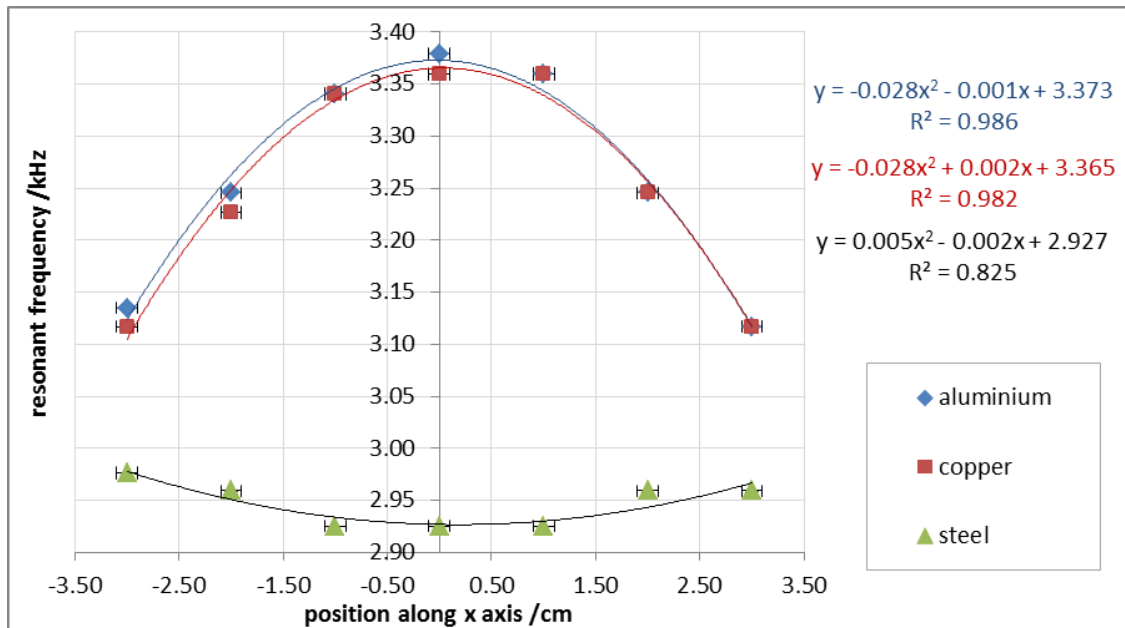


Fig. 3.14. Resonant frequency measured values (kHz) vs coil position along x axis (cm). The data sets obtained with aluminium (diamond), copper (square) and steel (triangle) were fitted with second order polynomials.

It is interesting to note that the curve obtained for steel was found to have different concavity than the two resulting from measurements performed by using aluminium and copper samples (Fig. 3.14). This was due to the different magnetic properties of these materials, which were respectively ferromagnetic and non-ferromagnetic. For non-magnetic copper and aluminium, the resonant frequency was maximum at the centre of the sample, i.e., when the inductor's centre and the disk's centre were aligned w.r.t. the plane of the scanning area. The positions of the sample at either side of this central position caused the sample to be 'seen' by the coil from angles different from the  $0^\circ$  angle corresponding to the central position. In other words, the distance between the centre of the sample and the coil centre became larger when the position along the x axis shown in Fig. 3.14 took on values larger than zero. Therefore, smaller changes in resonant frequency (w.r.t. the configuration of the system when it was "in air") occurred for increasing values on the x axis, corresponding to increasing distances between the coil and the sample.

The steel sample produced a trend showing a minimum resonant frequency corresponding to the position where the sample's centre was aligned with the coil's centre

(Fig. 3.14). The theoretical principles illustrated in Chapter 2 suggested that the resonant frequency values decreased when a sample made of ferromagnetic material was placed in the vicinity of the coil forming an LC system. This was the case for the data point corresponding to  $x=0$  in Fig. 3.14. The data points corresponding to symmetrical positions on both sides of the central one had increasing values of resonant frequency, getting closer to the one measured in the absence of the sample. These represented the sample occupying places along the  $x$  axis having increasing distances from the centre of the coil.

The asymmetry in the curves obtained for the three metals (Fig. 3.14) was due to the non-uniform lift-off, caused by the Perspex layer being tilted, which produced uneven inductive coupling between the coil and the metallic sample [24]. This was fixed as detailed in Chapter 4, as the weaknesses found in the experimental system and measurement method illustrated in this chapter gave the input for amending them and improving the experimental procedure. This included the use of a motorised stepper motor that prevented measurements from being taken by hand, and a structure made of wood to aid the experimental scans and produce uniform lift-off for the whole scanning area.

Representations of the copper and aluminium disks from the top (i.e., from the coil's view) are given in Figs. 3.15-3.16. Similarly, an image representing a  $10 \times 10 \times 3$  mm<sup>3</sup> mild steel specimen is shown in Fig. 3.17.

The two vertical yellow halos visible on the left and right sides of the disks represented in Figs. 3.15 and 3.16 were due to the Perspex layer being uneven and making the disk closer to the inductor. This was proved by the recurrence of these halos in both the images of copper and aluminium, suggesting that these were not a characteristic of one of the two conductive samples, but highlighted a "geometrical" systematic issue. The presence of five regions of different colours going from the external of the disk's area, towards its central core was linked to the scale used to create the plots. Differences can be noted between the two figures, in the contours of the ring-shaped regions and of the central zone, due to this imaging technique having been implemented by moving the object by hand.

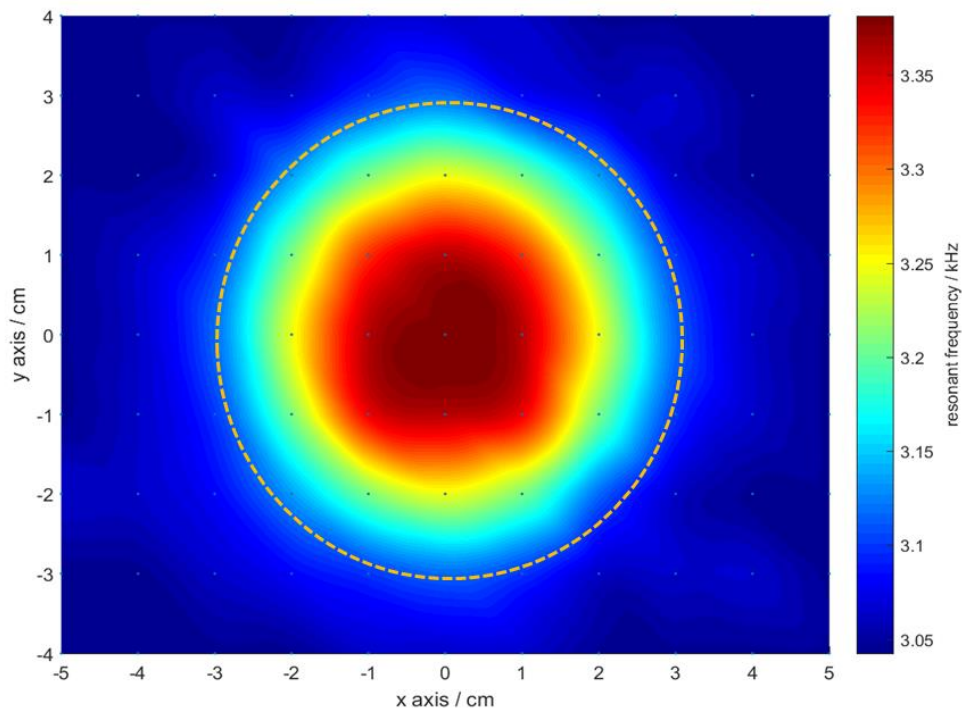


Fig. 3.15. 2D image of a 6-cm-diameter copper disk. The image was obtained by plotting the resonant frequency values (kHz) against coil positions along x and y axis (cm) and interpolating the values with a piecewise cubic fit within *Matlab*.

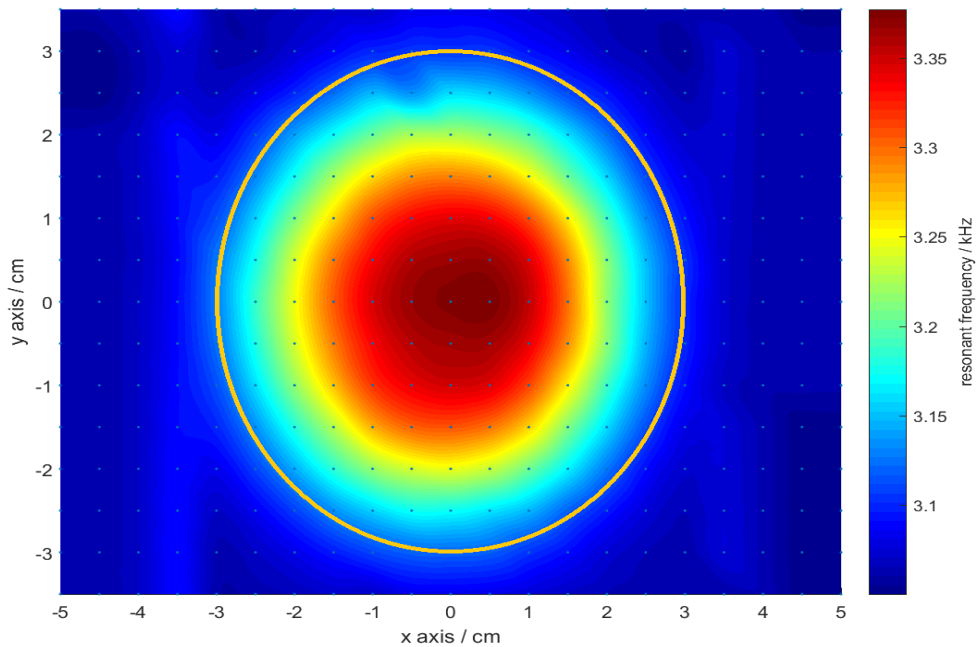


Fig. 3.16. 2D image of a 6-cm-diameter aluminium disk. Resonant frequency values (kHz) were plotted against coil positions along x and y axis (cm).

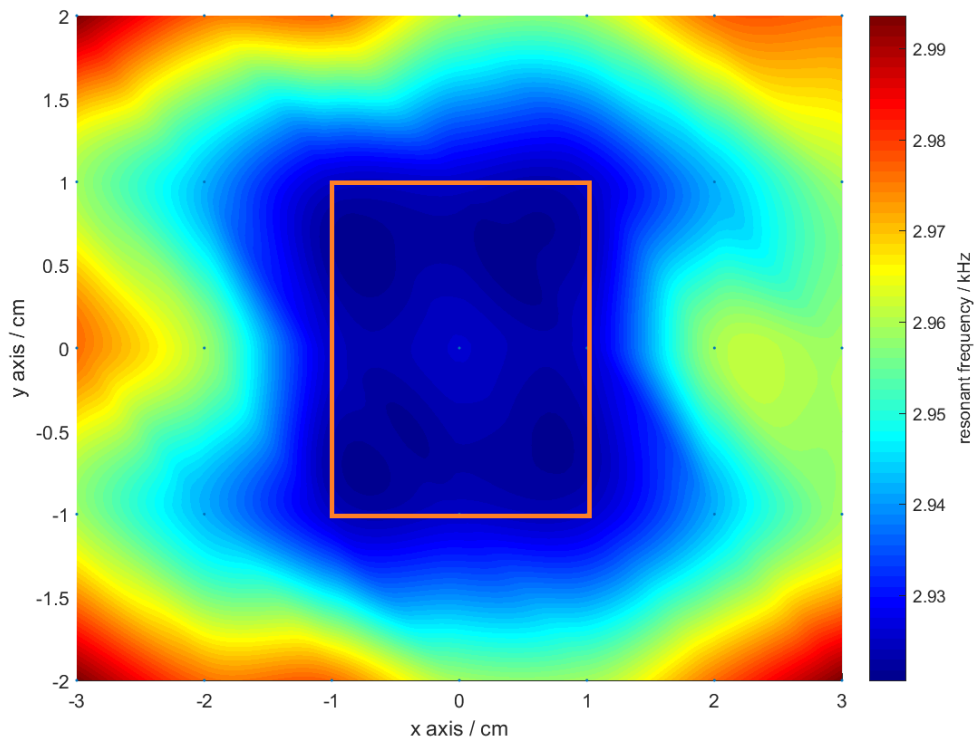


Fig. 3.17. 2D image of a 1x1 cm<sup>2</sup>, 3-mm-thick specimen of mild steel. Resonant frequency values (kHz) were plotted against coil positions along x and y axis (cm).

The results shown in Figs. 3.13-3.16 proved that the difference in the resonant frequency produced by the presence of highly conductive samples could lead to imaging them. The result obtained with the mild steel specimen stood out from the results achieved with non-ferromagnetic samples made of copper and aluminium (Fig. 3.17). The edges were less clearly defined in the former example, due to the ferromagnetic nature of the material, causing eddy currents to be less contained and more spread out (Fig. 3.17) [61].

At this stage, it was not possible to state the difference between the copper and the aluminium disks with this technique, as the two images representing the two samples were identical (and the same scale was used in Figs. 3.15 and 3.16). In the following work, focus was directed to identify the causes for this. In particular, the coil inductance, the lift-off and the measurement method were taken into consideration, in order to improve the robustness of the technique and, particularly, the system's resolution power. This was intended as the capability of the system to resolve two objects having different conductivity values, by measuring the resonant frequency at each position along a scanning area where the samples

were moved w.r.t. the coil. A more robust technique would allow different images to be produced by using different samples, with the same imaging technique. To improve the system and technique tested, different coils were considered, as the quantity of eddy currents was dependent on the coil's self-inductance, which in turns was dependent on the coil's geometrical and manufacturing characteristics. Measurements at different values of lift-off were also performed, to identify the impact of these variations on the resulting images, to improve them qualitatively and investigate whether it could be possible to distinguish between different samples by looking at their images (Section 5.1).

### 3.5 Towards optimisation of the imaging system

The impedance analyser used in this work can perform frequency sweeps of a circuit's impedance by using a certain number of data points to build a Z vs frequency plot [67]. This number can be set by the user. The higher the number, the slower the time required to complete the data acquisition during a frequency sweep and, due to the larger number of data points, the more precise the measurement acquisition process. Resonant frequency values were measured for the LC system in air, by setting the number of points of a frequency sweep to the following values: 50, 100, 200, 400, 800, 1200, 1600 (Fig. 3.18). This was done in order to identify the most precise measurement method.

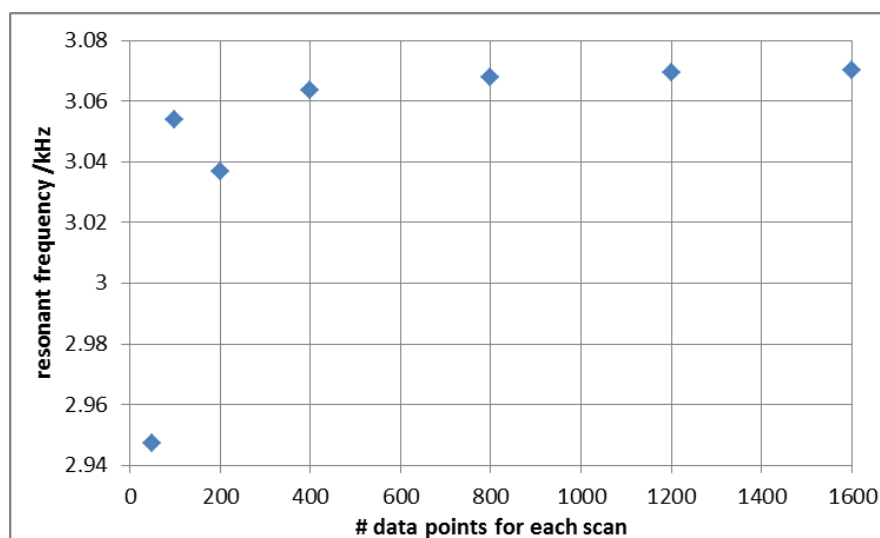


Fig. 3.18. Resonant frequency (kHz) vs number of points acquired during each scan, obtained with the LC system in air.

The graph reported in Fig. 3.18 showed that from # 400 points on, the change in the measured resonant frequency was negligible, as the values converged to the number 3.07 kHz. Therefore, choosing 400 or 1600 points introduced an error smaller than 0.1% (which is smaller than the experimental uncertainty, estimated to 0.5%) in the resonance frequency measurement (Fig. 3.18).

2D imaging of a 6-cm-diameter, 2-mm-thick copper disk was achieved by means of a 400-points scan. This number was the preferred point number, chosen as it would reduce scan time whilst not introducing an unacceptable uncertainty in the measurements. Profiles of the resonant frequency plotted against the position along the x axis of the scanning area (Fig. 3.8) were obtained using copper and are reported in Fig. 3.19.

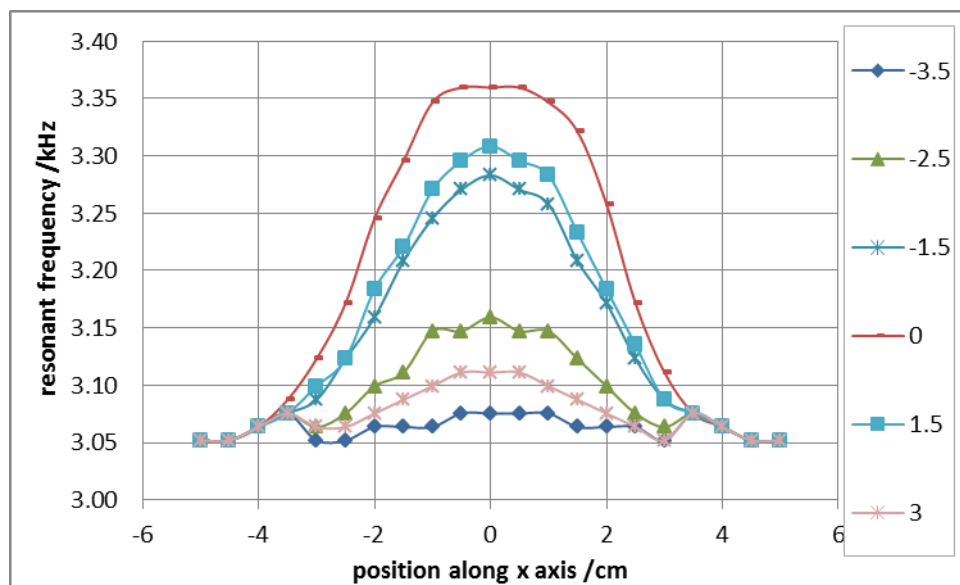


Fig. 3.19. Resonance frequency measured with a copper disk (6-cm-diameter, 2-mm-thickness) at different positions along the y axis (values are included in the key of the graph, and different colours represent profiles obtained with the same y value) and x axis (abscissa of the graph).

Resonant frequency values were measured with the impedance analyser and the change in resonant frequency between the two materials was calculated by using:

$$\Delta f (\%) = \frac{f(Al) - f(Cu)}{f(Cu)} (\%) \quad (3.2)$$

Maximum, minimum and average values of  $\Delta f\%$  at growing values of the y coordinate, from -3.5 to +3.5 cm, are listed in Tab. 3.1.

The difference in resonant frequency measured with copper and aluminium was found to be too low (i.e., smaller than the standard deviation of repeated measurements of the resonant frequency) to produce a visible change in the images of the two objects (Tab. 3.1). This prevented the two different materials to be identified and therefore constituted a limitation attributed to either the specific experimental system used or the measurement method adopted (or both). The presence of targets of unknown nature that may be hidden by protective shields raised the requirement for a system to be able to distinguish between metals having different electromagnetic properties. The issue highlighted by the experimental results described in this section will be addressed in the following chapters (particularly, Chapter 7).

Tab. 3.1. Maximum, minimum and average value of  $\Delta f\%$  at growing values of the y coordinate, from -3.5 to +3.5 cm. The samples used were 6-cm-diameter, 2-mm-thick copper and aluminium disks. The interesting column is the fourth one, which shows that the average  $\Delta f\%$  is lower than 0.3% at all positions along the y axis. This value was smaller than 0.5%, which was the standard deviation obtained from 10 consecutive measurements of the resonant frequency, meaning that the resonant frequency variation is not significant to discriminate between a copper and an aluminium sample.

<b>Y (cm)</b>	<b>Max <math>\Delta f\%</math></b>	<b>Min <math>\Delta f\%</math></b>	<b>Average <math>\Delta f\%</math></b>
-3.5	0.49	-0.44	0.16
-3	0.7	-0.02	0.26
-2.5	0.85	-0.12	0.23
-2	0.79	-0.25	0.27
-1.5	0.99	-0.37	0.30
-1	1.06	-0.44	0.28
-0.5	0.57	-0.63	0.09
0	0.49	-1.23	0.06
0.5	0.45	-0.94	-0.03
1	0.49	-0.5	-0.01
1.5	0.49	-0.93	-0.15
2	0.49	-0.92	-0.06
2.5	0.33	-0.76	0.03
3	0.29	-0.19	-0.02
3.5	0.49	-0.44	0.16

The attempt made to determine whether resolving the two materials was achievable directed the attention towards a different measurement method that could be successful at this. Gaydecki's paper [50] showed how Q-factor measurements may prove beneficial for the identification of materials when high sensitivity was required. Starting from this, further investigations were carried out and a more sensitive technique than the one involving resonant frequency measurements was developed, based on Q-factor measurements. The identification of the Q-factor as a candidate for measurements performed with the purpose of imaging and detecting unknown conductive materials was based on the following consideration. A resonating system may have larger absolute values of resonant frequency than Q-factor, but the aim of this research was to identify shielded conductive samples, as well as unshielded ones (used to demonstrate a proof-of-principle technique to start with). The requirement for the EII system to operate at sufficiently low frequencies to allow sufficiently large penetration depths to image the samples, meant that some values of resonant frequency were not ideal for this purpose. In particular, these values were larger than a few hundreds of kHz, when penetration through shields having thicknesses of the order of magnitude of a few mm was required. Simply looking at absolute values, for a given percentage difference  $\Delta f$  (Eq. 3.2) between resonant frequencies produced by two different conductive samples, the absolute difference  $\Delta f$  between the individual samples' frequencies ( $\Delta f = f_{sample1} - f_{sample2}$ ) is proportional to each of them ( $f_{sample1}$  and  $f_{sample2}$ ). The cut-off in the preferred resonant frequency values to achieve material penetration constituted a limitation towards obtaining large resonant frequency variations, as a consequence of a conductive sample being brought in the vicinity of the measurement system. For this reason, Q-factor measurements were likely to represent a better solution than resonant frequency measurements, which should prove suitable for EII of shielded targets, as well as unshielded ones.

### 3.6 Comparison between Q-factor and resonant frequency measurements

Further investigations about the development of an EII system for imaging of conductive samples were carried out, with the aim of verifying whether a method based on Q-factor position-resolved measurements rather than resonant frequency measurements would be able to distinguish between materials having different values of electrical conductivity. Part of this optimisation process included amendments that were made to the experimental system, as detailed in the following paragraphs.

Two changes were made in the choice of the coil, by substituting the pancake coil with an air-cored coil and eventually changing this for a ferrite-cored coil (see Section 3.1). The first substitution was applied for spatial resolution purposes, since reducing the size of the coil's diameter would imply improving the images' spatial resolution, thus allowing objects of smaller sizes to be imaged [40]. The following substitution was done because using a ferrite-cored coil would cause the magnetic field lines to be concentrated around the core, due to its high permeability, thus leading to a larger amount of eddy currents being induced inside the sample to be imaged. Another change was done with regards to the measurement method. The quality of the image (judged by considering defined contours and shapes, plus absence of halos and artefacts) and the possibility of visually distinguishing between metals having different values of electrical conductivity could be improved by adopting a measurement technique based on measuring some parameter whose change was larger than the one measured with the resonant frequency data. The Q-factor was chosen as a candidate for this purpose, since it was dependent on the coil inductance (Eq. 2.12), and therefore had to change as a direct consequence of the inductance change caused by the presence of a metallic object.

The same procedure described in Section 3.5 was repeated by measuring the Q-factor related to the resonance, instead of the frequency measured before. The Q-factor is visually represented in Fig. 3.20 that shows plots of impedance  $Z$  vs frequency, obtained using the impedance analyser and the LC system described in Section 3.1. The Q-factor could be determined from such plots by calculating the ratio between the resonant frequency

corresponding to the maximum  $Z$  and the frequency bandwidth ( $Q = \frac{\omega_0}{\Delta\omega}$ ). Section 2.1 contains the Physics principles on which the proposed method was based, and references of research involving Q-factor estimations for material identification purposes are Gaydecki *et al.* and Bartlett *et al.* [50][53].

The impedance analyser introduced in Section 3.5 was used to produce resonance curves in the presence of two samples, made of aluminium and copper (6-cm-diameter, 2-mm-thickness). Resonance curves similar to the ones reported in Fig. 3.20 were used to acquire measurements of the resonant frequency and the Q-factor in the experimental work reported in Chapters 3 to 6.

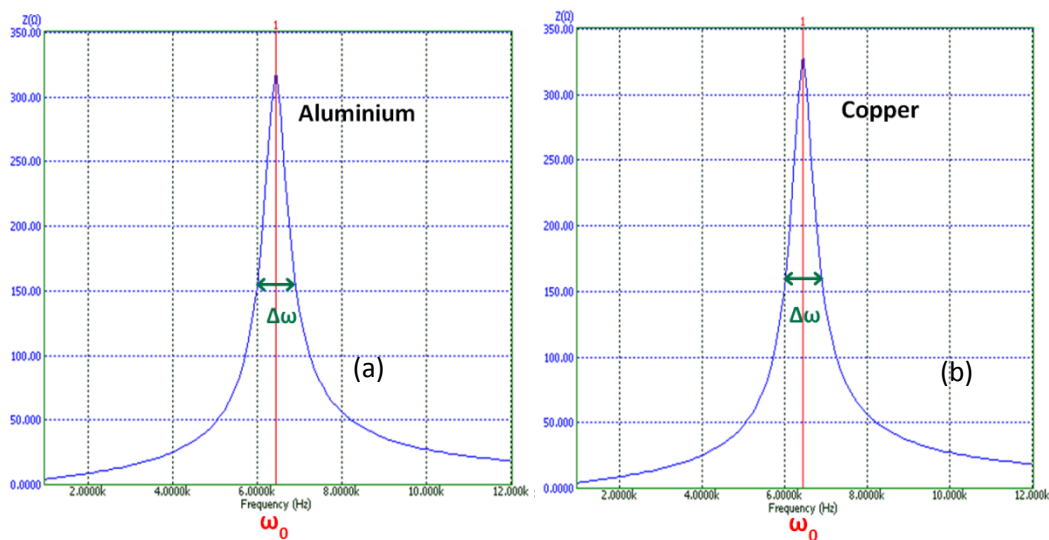


Fig. 3.20. Plot of impedance ( $\Omega$ ) vs frequency (Hz) showing resonant frequency and Q factor  $Q = \frac{\omega_0}{\Delta\omega}$  obtained for a 6-cm-diameter, 2-mm-thick aluminium sample (a) and a 6-cm-diameter, 2-mm-thick copper sample (b).

The change in the Q-factor values between copper and aluminium was compared to the change obtained with the resonant frequency measured in the same conditions. This was done by using Eq. 3.2 to compute the change in resonant frequency, and a similar equation, obtained by substituting  $f$  with  $Q$ , to derive the Q-factor change (Fig. 3.21). These changes were calculated after measuring resonant frequency and Q-factor, respectively, with the impedance analyser, by selecting increasing values of C from the LC system, from  $C=0.1 \mu\text{F}$  to  $C=1 \mu\text{F}$ , with steps equal to  $0.1 \mu\text{F}$ . The two different scales used for  $\Delta Q$  (diamond) and  $\Delta f$  (square) in the graphs should be noted. The change in Q was found to lie between 0.3% and

0.6% when measurements were acquired using an air-cored coil. Such range was between 2.4 and 3.6 % when the ferrite-cored coil was used (Fig. 3.21). The larger change obtained with the ferrite-cored coil was due to the larger amount of eddy currents resulting from the larger magnetic field concentration around the ferrite core. This justified the choice of using this coil. For comparison, changes of resonant frequency were found to be much smaller than changes of Q, and were lying between 0.1 and 0.3% for values measured with the ferrite-cored coil (Fig. 3.21).

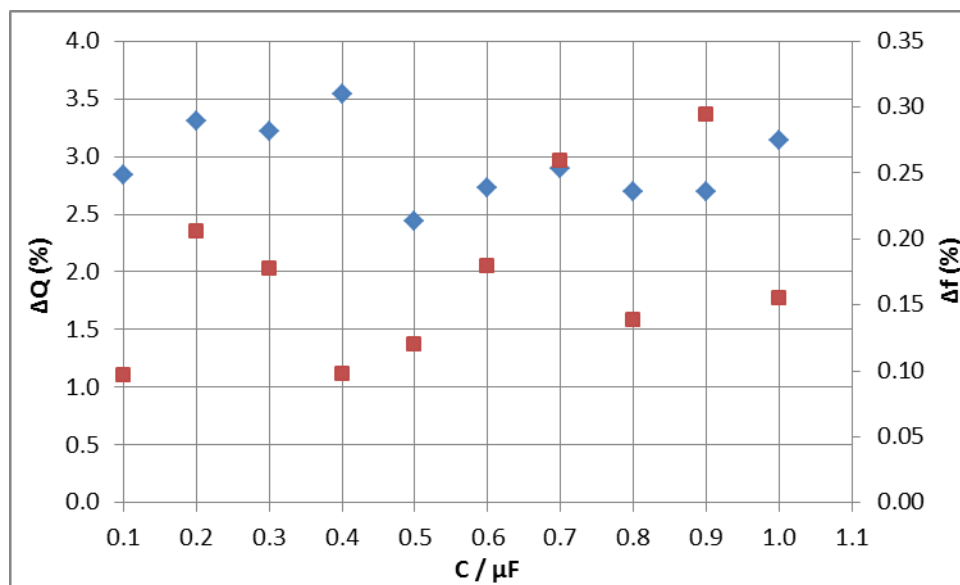


Fig. 3.21. Change in Q-factor (diamond) and resonant frequency (square) between copper and aluminium, calculated using Eq. 3.7, with different capacitance values. Measurements were performed using a ferrite-cored coil (Fig. 3.5b). The different axes scales used here for  $\Delta f$  and  $\Delta Q$  should be noted.

The larger change obtained with the Q-factor data underlined that measuring this parameter could improve quantitatively the results and improve the potential of the system to produce different images of metals having similar conductivity values.

Following the experimental observations, the use of the ferrite-cored coil in place of the previously used coils was established. Additionally, Q-factor measurements were investigated further, to test the feasibility of an imaging technique based on this parameter for 2D imaging of conductive samples.

2D surface plots were obtained by using 6-cm-diameter, 2-mm-thick copper and aluminium samples and the ferrite-cored coil, since this produced larger shifts in the measured quantities when the samples were introduced into the system (Figs. 3.22-3.23).

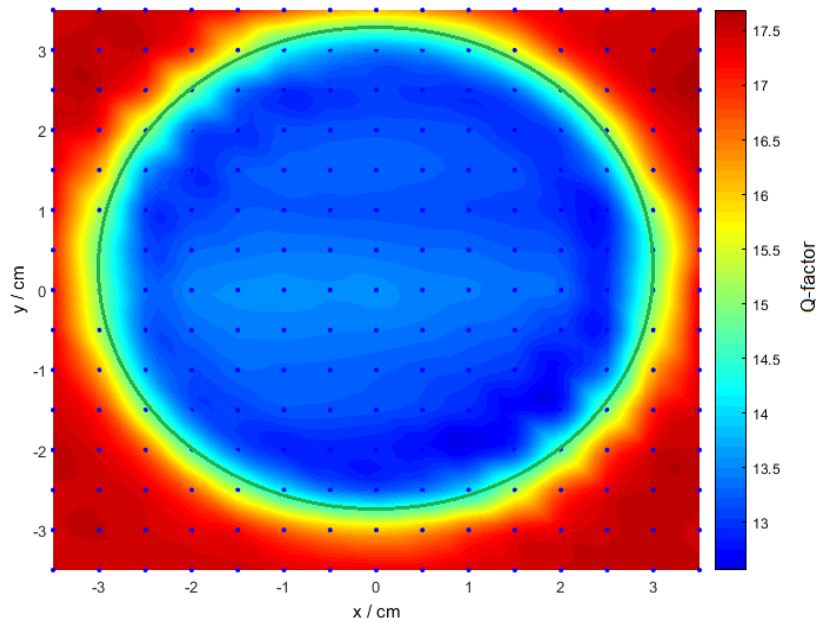


Fig. 3.22. Image reproducing a 6-cm-diameter copper disk obtained by measuring the Q-factor. The ferrite-cored coil (Fig. 3.5b) was used to perform the scan in this experiment.

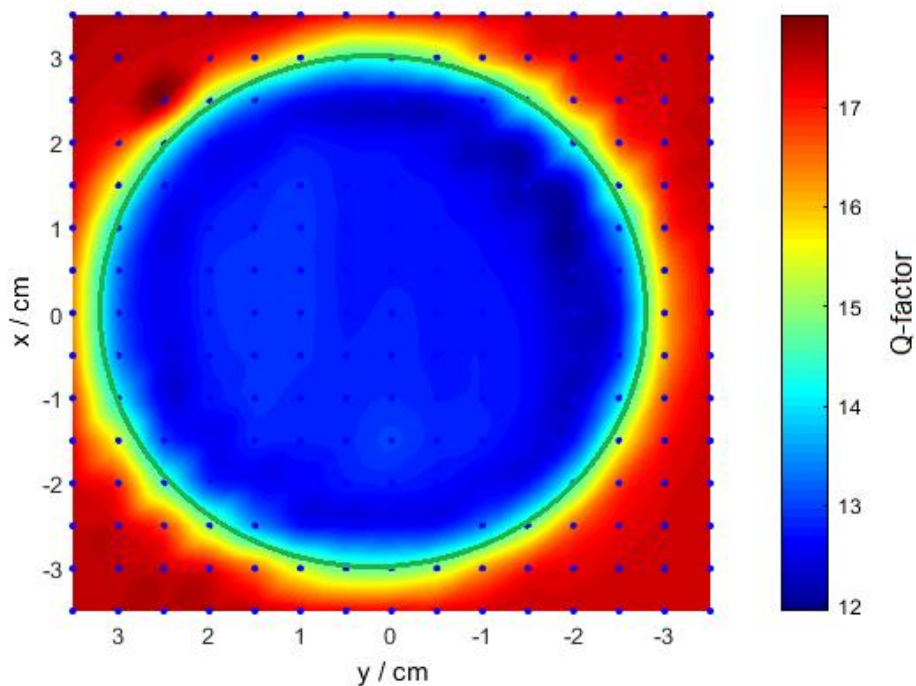


Fig. 3.23. Image reproducing a 6-cm-diameter aluminium disk obtained by measuring the Q-factor. The ferrite cored coil (Fig. 3.5b) was used to perform the scan in this experiment.

The shape of the disks was well reproduced in the images, which means that they appeared circular, as they were in reality when seen from the top. The technique based on measurements of the Q-factor produced an image of copper which looked different from the one obtained with the aluminium sample (Figs. 3.22-3.23). This result showed that such technique worked better than the resonant frequency technique, for distinguishing between different metallic samples, due to the larger Q-factor shifts obtained by switching from the configuration “in air” to the one with the sample inductively coupled to the coil. However, the variability in the values measured, showing up as different colours in the images reproducing the samples, could be reduced by using a more accurate method that would decrease the following sources of uncertainties: 1) measurements being done by hand; 2) uneven surface of the experimental set-up; 3) lack of an automated measurement acquisition process.

### 3.7 Discussion and conclusions

The results presented in this chapter made it possible to establish a proof-of-principle method for 2D imaging of conductive metallic samples having simple geometries (e.g., disks or samples of rectangular cross section). The experimental apparatus here introduced was a prototype EII system that was later improved (see Chapter 4), and the measurements during the scanning procedure were done by hand, highlighting the need for an automated system to allow higher precision in the positioning of the samples. This represented one of the solutions to the problems encountered with the prototype system, which are described in the first two sections of Chapter 4. Materials and methods will be presented in Chapter 4. In Chapter 5, focus will be given to experimental methods, results and discussion related to 2D imaging of unshielded conductive samples, whereas Chapter 6 will be about 2D imaging of shielded conductive samples. The final chapter involving the measurements (including experimental procedures, results and discussion) is Chapter 7, which is about a new EII imaging system, constituting an improved version of the one presented before.

## 4 An automated Electromagnetic Induction interrogation system

### 4.1 Description of the initial experimental apparatus

The experimental system on which this research work was based was similar to the one described in Chapter 3, with some amendments, as detailed in the following paragraphs.

The EII system was initially based on a cylindrical ferrite-cored coil (made by “multicomp”, part no. MCSCH895-681 KU), in which an AC primary magnetic field was induced. The coil was connected in parallel to a capacitor selected from a capacitor bank (Fig. 4.1). Together with the internal components’ internal resistance, this formed an LCR resonating system, which was modelled as a parallel LCR circuit in the following. Both the coil and capacitor bank were connected to the impedance analyser (Fig. 3.2). A metallic specimen was secured on a two-axis stepper motor system (XY stage) inserted into a wooden support structure having non-metallic fixtures (Figs. 4.2-4.4). The support structure was created in such a way as to allow positioning of the specimen at different lift-offs (i.e., vertical distances, measured along the sample’s axis, between the coil’s lower base and the sample).

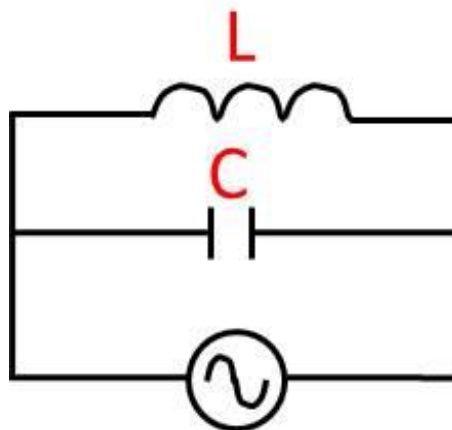


Fig. 4.1. Electronic schematic of the initial EII system, which consisted in a parallel LC circuit made up of a ferrite-cored coil (No. turns= $145 \pm 1$ ,  $\varnothing=7.8 \pm 0.5$  mm, height= $9.5 \pm 0.5$ mm, inductance= $680 \pm 10\%$   $\mu$ H), and a capacitor selected from the capacitor bank.

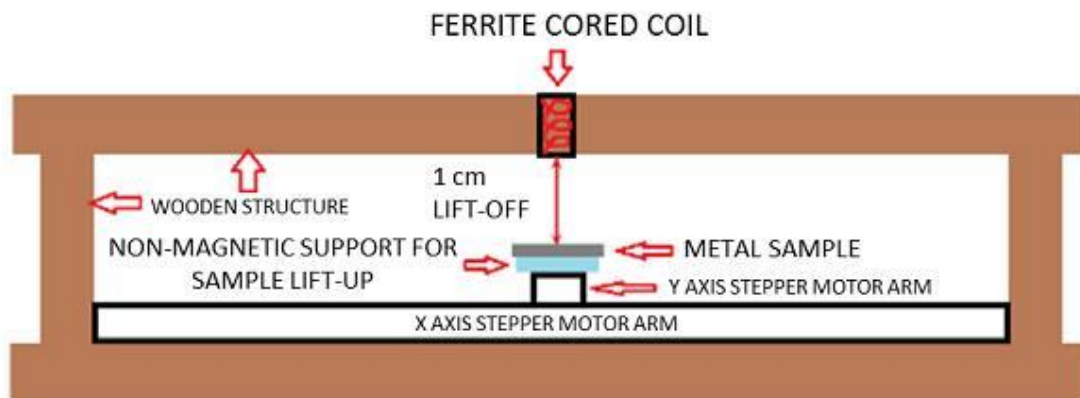


Fig. 4.2. Sketch showing the front view of the wooden structure containing the experimental system. This included a ferrite-cored coil, being part of a LC system (with schematic as in Fig. 4.1), a xy stepper motor and a sample made of metal, which was moved along the x and y direction during a scan. A non-magnetic support was used to adjust the lift-off of the sample w.r.t. the coil.

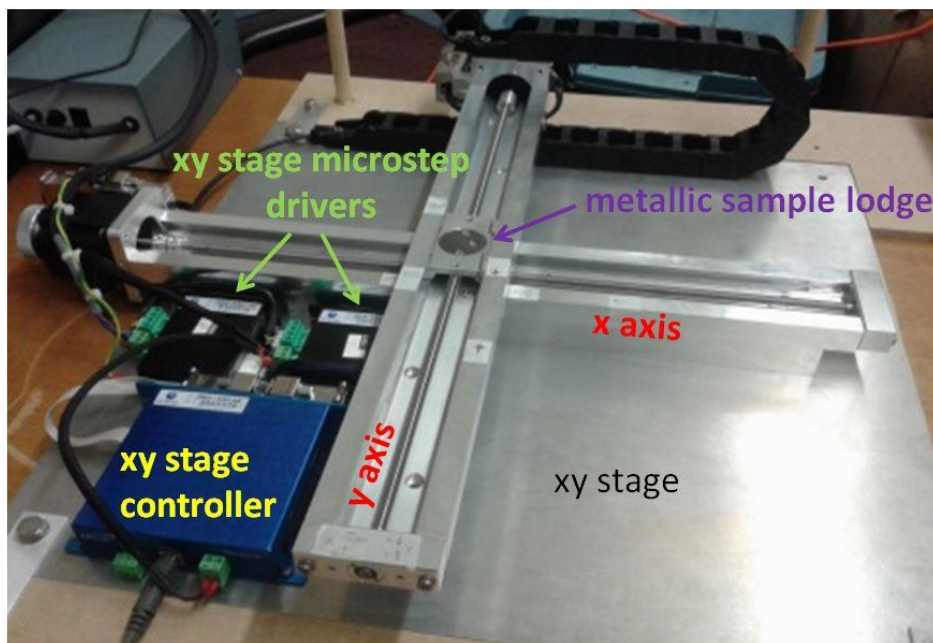


Fig. 4.3. Picture of the XY stage used to position the metallic samples used in this work onto different positions along the scanning area.

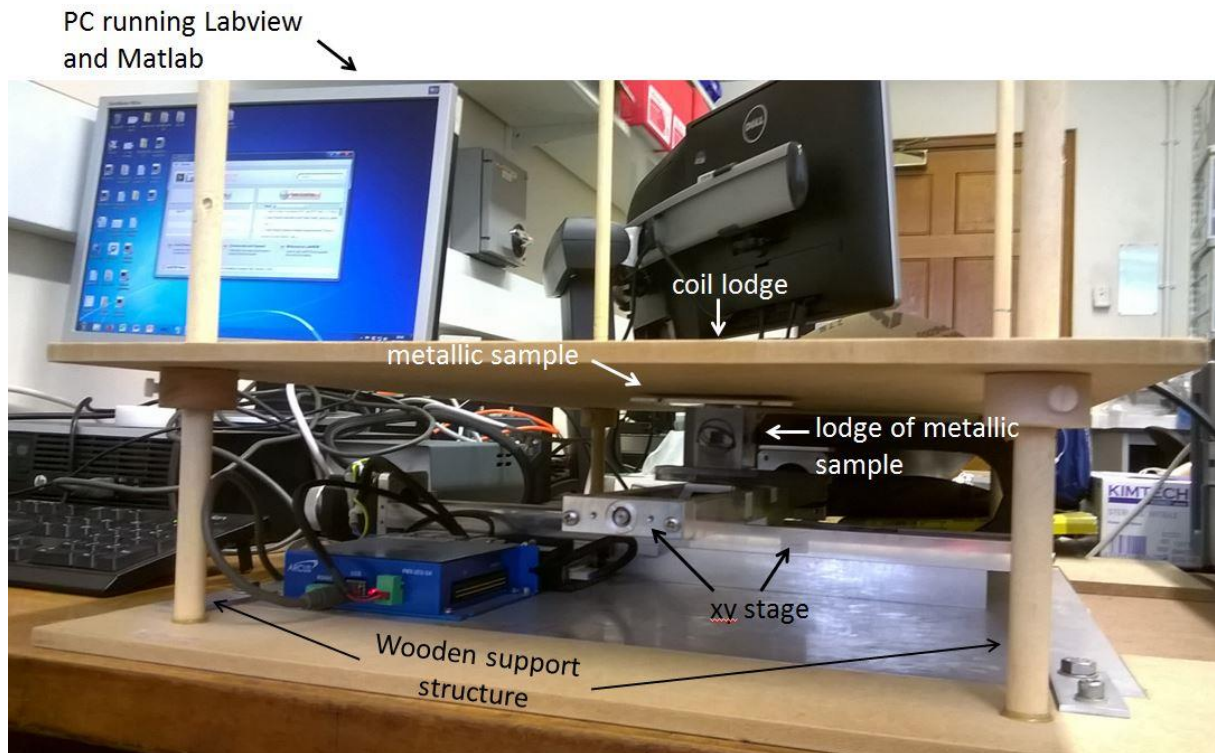


Fig. 4.4. Picture showing the wooden structure containing the experimental setup. This was based on the xy stage with which the metallic sample was moved, the coil (not visible here, as it is fixed to the wooden upper layer) and the computer used for data acquisition and analysis.

#### 4.2 Description of the procedure used for 2D imaging of metallic objects

A proof-of-principle method was developed to achieve 2D imaging of metallic objects by means of the resonating circuit described in Section 4.1. The process was similar to the scanning technique detailed in Section 3.5, with the difference that Q-factor measurements were performed, in addition to resonant frequency measurements. Since the experimental apparatus consisted of a different structure (made of wood instead of Perspex), and the scanning process and measurement acquisition was automated with the aid of a stepper motor and by means of LabVIEW, a complete description of the whole procedure is detailed in this section.

The method was based on position-resolved measurements of the resonant frequency and Q-factor shifts, occurring due to the presence of the metallic samples, w.r.t. the scenario in which no sample was present (“in air” or “background” measurements) (Figs. 2.2-2.3). A

procedure was developed that is based on scanning a given area by moving the conductive sample with the aid of an xy stage (Fig. 4.3), and plotting the measured values- obtained at each position along the scanning area vs the corresponding x and y coordinates. The scanning area was obtained by adopting the procedure described in Section 3.5. Resonant frequency and Q-factor measurements were performed by means of the impedance analyser introduced in Chapter 3 (Fig. 3.2). Ten independent values of each of these physical quantities were acquired for each of the nodes of the scanning grid represented in Fig. 3.8.

The experimental method utilised a computer automated system which linked, via Ethernet connections, a PC, the impedance analyser and a two-axis stepper motor system (Fig. 4.4). A LabVIEW *Virtual Instrument (VI)* was created to control the stepper motor movements as well as the data acquisition undertaken by the impedance analyser. A timed-sequence structure was created to perform the following operations:

- 1) move the metallic sample along the first row of the scanning area in 2.5-mm-steps;
- 2) stop the sample at each position and activate the impedance analyser;
- 3) perform a frequency sweep of the impedance amplitude in a frequency interval centred around the system's resonant frequency;
- 4) deactivate the impedance analyser and move the sample one step ahead;
- 5) repeat operations 1) to 4) for all rows of the scanning area.

The following mathematical operations were undertaken in order to determine the values of resonant frequency and Q-factor to be used to generate images. Impedance values ( $Z$ ) were plotted against the corresponding angular frequency values ( $\omega$ ) at each positional point along the scanning area. Measured  $Z$  vs  $\omega$  curves, showing the resonant peak at each position, were thus obtained for all positional data. Each of these curves was fitted by using the function for the impedance of a parallel LCR circuit (adapted from [57]):

$$Z(\omega) = \frac{1}{\sqrt{\left(\frac{1}{R}\right)^2 + \left(\frac{1}{\omega L} - \omega C\right)^2}} \quad (4.1)$$

In Eq. 4.1,  $R$ ,  $L$  and  $C$  are the fit parameters determined by the LabVIEW fitting routine.

The parameters obtained from the fit were used to calculate the Q-factor by means of Eq. 4.2 [56]:

$$Q = R \sqrt{\frac{C}{L}} \quad (4.2)$$

A value of Q-factor was, thus, obtained at each position of the specimen. In a similar way, resonant frequency values at each position of the specimen were determined by using Eq. 4.3 [56]:

$$f_r = \frac{1}{2\pi\sqrt{LC}}, \quad (4.3)$$

where  $L$  and  $C$  were derived from the fit of the  $Z$  vs  $\omega$  curve.

‘Background measurements’ of resonant frequency and Q-factor were first taken at each position of the scanned area with the coil in air (no sample present). These were acquired to verify that the “background” obtained in the absence of the sample was uniform. ‘Sample data’ was then taken after placing a metal object under the coil.

Normalised data was obtained by dividing sample data by the corresponding background data. This was achieved by means of a “for” loop implemented with LabVIEW. Such a normalisation procedure allowed to visualise the change between the quantities measured without the sample and the corresponding ones obtained after the sample was introduced into the system. 2D surface plots were generated by means of interpolation with a piecewise cubic fit, by plotting normalised data against the x and y coordinates of the imaged sample.

The described procedure was applied to two sets of data, based on resonant frequency data and Q-factor measurements, respectively. Two images were thus produced for each object. Experimental results obtained with the two techniques are reported and discussed in Sections 5.2.2, 5.3.2, 5.4.2.

### 4.3 Improvements to the initial LC system

The resonant system used for electromagnetic induction interrogation and described in the Sections 4.1 and 4.2 was improved, in order to achieve the following objectives;

- 1) accomplishing 2D imaging of metallic materials when these were not shielded;
- 2) being able to distinguish between materials of different electromagnetic nature, even when these had similar values of electrical conductivity;
- 3) exploring the possibility of imaging materials that were shielded, i.e., hidden behind some metallic material acting as a shield, for security purposes.

The experimental results obtained with the LC system based on a capacitor bank (introduced in Chapter 3) underlined that one of the limitations of the system was its sensitivity. This meant that the shift produced by a low-conductivity metal, as well as the difference of shifts caused by metals having similar values of electrical conductivity, could not be detected, as none of them was significant, compared to the measurement uncertainties. Specifically, the largest frequency difference between coil in air and coil over a 9-cm-diameter, 2-mm-thick copper disk - obtained with  $C=0.03\pm 1\% \mu\text{F}$  - was equal to  $\Delta f=0.29$  (Eq. 3.1). However, the measurement uncertainties were equal to 0.04 (4%) (Chapter 3). Therefore, the resonance method at that stage allowed distinguishing only between the system in air and the system with samples coupled to it, and between scenarios corresponding to two different samples made of magnetic and non-magnetic materials sequentially coupled to the system. Given the importance of varying the capacitance for the purpose of this research investigation (especially, penetration through conductive shields to image hidden objects), the previously used capacitor bank (Section 3.1) was substituted by a new one (Cosinus Messtechnik GmbH C1-250). This one allowed selection of capacitance over a broader range. Specifically, the minimum  $C$  was the same as before, equal to 0.1 nF, but the maximum  $C$  was 11.111  $\mu\text{F}$  vs 1.111  $\mu\text{F}$  of the previous capacitor bank. Being able to select larger values of capacitance w.r.t. the previous system was useful in order to carry out the investigations regarding the penetration behind metallic shields for object identification. The

larger the capacitance, the smaller the resonant frequency, and therefore the bigger the skin depth, as explained by Eq. 2.25.

Furthermore, the dependence of the measured parameters  $f_r$  and Q (i.e., resonant frequency and Q-factor) on the circuit's inductance and resistance, in addition to its capacitance, led to the need to carry out investigations based on the use of a resonant LCR system where the resistance values could be controlled, as well as the capacitance values. In the experimental work carried out prior to this (Chapter 3), the system was physically based on an inductor connected to a capacitor bank through cables. The components' parasitic capacitance (existing between the turns of the inductor, plus the smaller contribution originating in BNC cables), in addition to the resistance deriving from both the components and the cables used to connect them, contributed to forming an LCR system, with values of L, C and R represented by the circuit's effective inductance, capacitance and resistance. In this configuration, the values of resistance and capacitance were fixed and determined by the components' and cables' physical characteristics, thus resulting 'intrinsic' to the system used and not controllable externally.

The possibility to carry out experimental investigations based on the use of variable capacitor and resistor banks was explored. This guaranteed more freedom in selecting different values of C and R, and was done with the goal of determining the optimal conditions in which the system may be operated. Section 5.5 will detail the experimental investigations carried out with the purpose of testing the LCR system varying the C and R values. Previous sections of this chapter include results of electromagnetic induction investigations, performed by varying the capacitance of the circuit.

Two decade boxes (Cosinus Messtechnik GmbH RT1-1000, C1-250), allowing selection of different values of capacitance and resistance, were connected to the coil (Figs. 4.5-4.8). This allowed capacitance and resistance values to be selected in the following ranges: C between 100 pF and 11.111  $\mu$ F ( $\pm 1\%$ ; 100 pF steps); R between 1  $\Omega$  and 11.111 M $\Omega$  ( $\pm 1\%$ ; 1  $\Omega$  steps). These amendments resulted in a new experimental setup, representing an improvement from the one described in the previous section (Figs. 4.6-4.8).

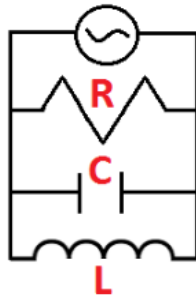


Fig. 4.5. Electronic schematic of the resonant electromagnetic induction system used in this study. The system capacitance can be adjusted (selecting the desired value from the capacitor bank), thus enabling penetration through a metallic shield covering the metallic target, and therefore facilitating the target identification. The resistor value in most experiments was equal to  $R = 1 \text{ K}\Omega \pm 1\%$ , and the inductor used was a ferrite-cored coil ( $7.8 \text{ mm} \times 9.5 \text{ mm}$ ,  $L = 680 \mu\text{H} \pm 10\%$  at  $1 \text{ kHz}$ ).

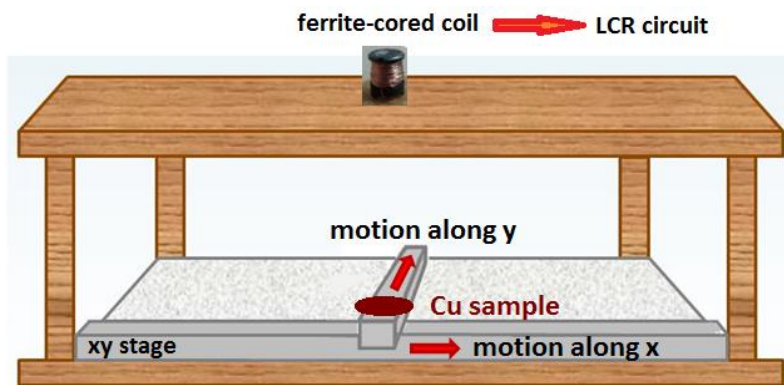


Fig. 4.6. Sketch of the experimental apparatus, made up of a ferrite-cored coil connected to a capacitor and a resistor, as in Fig. 4.6. A xy stage was used to move a metallic sample (such as the disk made of Cu shown in red), thus allowing to perform a scan for imaging purposes. The apparatus was enclosed in a non-magnetic structure (made of wood), in order for the experiment to be electromagnetically isolated.

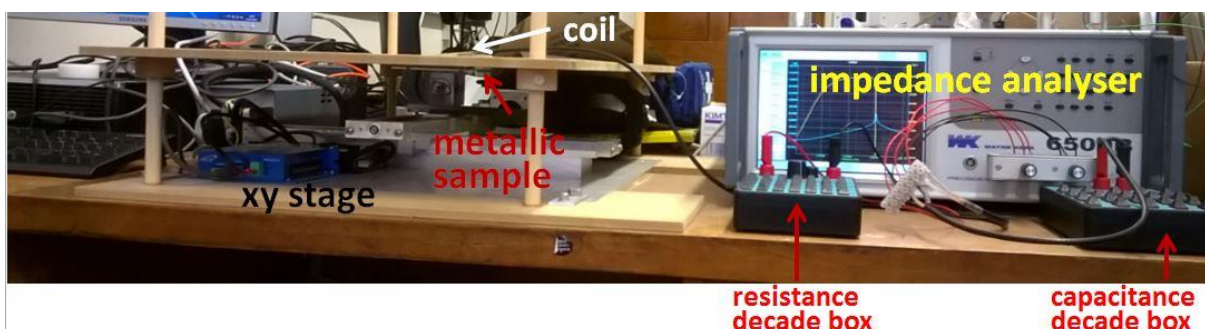


Fig. 4.7. Picture showing the experimental apparatus, including the two decade boxes allowing selection of resistance and capacitance (bottom right).

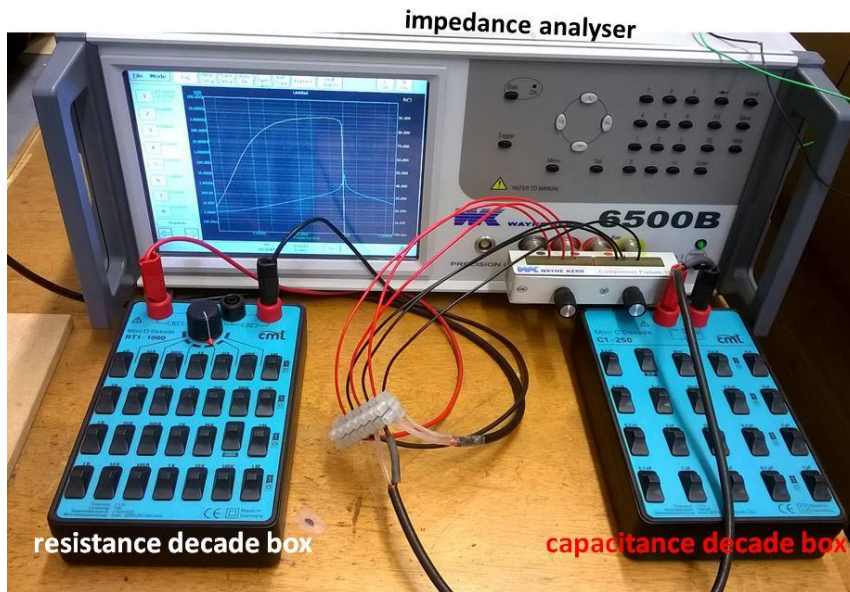


Fig. 4.8. Picture showing the impedance analyser during a  $Z$  vs frequency sweep (in the background) and the two decade boxes used for resistance and capacitance selection, connected to the coil mentioned above, which is not shown in this picture.

#### 4.4 Description of the LabVIEW program

The creation of electromagnetic images was automated by creating a LabVIEW program including a *Matlab* script, as will be detailed in this section.

LabVIEW (National Instruments, NI) was connected to the hardware described above to perform measurements. A LabVIEW VI was created for this purpose. The VI uses NI DAQ systems and instrument control to acquire measurements, including instrument configuration with NI MAX, instrument drivers and automation of the DAQ process. The final part of the LABVIEW VI embeds a *Matlab* program to process data and create an image out of interpolation, as will be detailed in the following.

NI Measurement & Automation Explorer (MAX) was set up to allow communication between the computer and the impedance analyser, as well as the XY stage. Physical connections were achieved by means of Ethernet and USB cables, respectively. The two connections were established by using NI-VISA (Virtual Instrument Software Architecture Application Programming Interface, API) as it uses the same communication method for

instruments connected using different interface types (GPIB, USB etc.), and allows the user to adopt the same (easy) language to perform various operations. The first step that was taken when writing LabVIEW code was the instrument configuration. A VISA Session was opened and a VISA Alias used as a nickname to the VISA Resource, with which the instrument was called throughout the application to perform DAQ operations. The VISA Session was closed at the end of the program and error handling performed for the VISA Session, as well as for all other parts of the VI, which helped debugging throughout the software development phase and VI testing.

The operations that needed to be performed by means of the impedance analyser involved measurement of the resonant frequency and Q-factor. Since the instrument drivers for these were unavailable, a considerable portion of the LabVIEW VI was written to accomplish this. The rationale behind this is explained in the following. The development of this part of the code required software development skills and was the most time consuming part of the programming phase involved in the PhD work described in this thesis.

A digital trigger was set up within LabVIEW, to control the moment at which the DAQ process started and was stopped by the user, from the LabVIEW VI Front Panel. The Trigger function configured a trigger to perform a specific action, with the Start trigger initiating it. Synchronisation was implemented in order to perform operations detailed in the previous section, which involved activating both the XY stage and the impedance analyser. Suitable waiting functions were implemented for this purpose. This included pausing the execution for the time required for the operations performed by the impedance analyser to be completed, as well as the time taken to move the XY stage to the next position along the scanning area.

Instrument drivers were used, when available, to select the impedance analyser measurement mode and control the frequency sweep settings, as well as the sampling rate and data logging and saving. The use of drivers allowed the VI to perform multiple instructions, as a sequence of events, as follows: 1) Initialize (establishing communication with the instrument); 2) Configure (configuring the instrument to perform specific operations); 3) Action/Status (commanding the instrument to carry out an action, or obtaining the current status of an instrument); 4) Data (e.g. reading data or transferring it to an array or matrix); 5) Utility (e.g. reset and self-test); 6) Close (last instrument driver to be called). The

downside to using instrument drivers in this work is that intervention was required in the case of one driver that contained a bug and therefore needed to be edited and tested. This was one of the drivers for the Network Analyser which will be introduced in Chapter 7. For instance, choice of resolution and range, selection of enable and disable auto range and use of a 'subVI' to read measurements were accomplished.

A structure made up of nested 'For Loops' was created and configured with a conditional terminal for the loop to stop when the entire scanning area had been completed. Similarly, 'for' loops were adopted for resonant frequency and Q-factor acquisitions in which the frequency sweep determined when the data acquisition had to stop, provided that the end frequency matched the value input by the user from the VI Front Panel. Wait functions were inserted into the loops because, without them, when a loop iteration is completed, the next iteration takes place immediately. Time to complete the tasks was needed because the whole execution relied on resonant frequency and Q-factor measurement, which required time to be completed, as well as motions of the XY stage, which needed to be accounted for too. Shift registers applied to predict the correct value at different loop iterations by storing data values from previous iterations of the 'for' loop. 'While' loops were also created to perform iterative operations until a certain condition was met. Tunnels were inserted into these loops to transfer data into and out of structures, and store them after the loop terminated. Error checking and error handling was implemented to stop the iteration of the loop in case an error occurred.

To acquire resonant frequency data from the impedance analyser, the phase of the complex impedance was measured within a frequency range selected from the Front Panel. A loop was used to iteratively acquire phase data for smaller frequency ranges centred around the resonant frequency, which was guessed each time the operation was repeated to improve accuracy. The frequency at which the phase was equal to zero was thus determined and logged as the resonant frequency for a certain position along the scanning area. Additionally, the impedance amplitude was recorded and plotted against the frequency for the initial frequency range centred around the resonant frequency, selected from the Front Panel. The measured data for the impedance amplitude was fitted using the analytical function (4.1) and

the plot of measured and theoretical data was plotted, together with the measurement error. The parameters R, L and C were then determined from the fit. These were used to calculate the Q-factor, as shown in Section 4.2.

The File I/O Palette for file operation functions was adopted to input variables in the form of 2D arrays into the *Matlab* script. Additionally, these arrays were written to .csv files which were named using string commands and saved in a defined location on the computer. Each of these 2D arrays contained data for resonant frequency and Q-factor as well as positional data calculated from the number of rows and columns in the scan, and the spacing between consecutive positions where data were acquired (all set from the VI Front Panel).

The second part of the LabVIEW routine executes a *Matlab* script, which calls the output 2D arrays. The resonant frequency data and the positional data arrays are concatenated. The concatenation is then repeated for Q-factor data and positional data. A single array containing three columns for (position x, position y, *measurement data*) is produced. The number of rows of the arrays depends on the number of positions of the scan, selected from the Front Panel, used to create a figure (samples of different dimensions required larger or smaller values of the scanning areas). Lastly, a 2D surface plot is generated by *Matlab* by interpolation of the measured data w.r.t. positions, by means of a piecewise cubic fit.

The next chapter reports experimental procedures and results and discussion, for a battery of experiments which were performed by using the experimental method described in this Chapter.

## 5 2D imaging of unshielded conductive samples

This chapter includes the experimental progress made by using the LCR circuit described in Chapter 4.3 and metallic samples having various values of conductivity, mostly non-magnetic, with the exception of iron (99.5% purity). The physical quantities of interest were the resonant frequency and Q-factor of the LCR system shown in Fig. 4.6, and specifically the change of these occurring after a conductive sample was placed in the vicinity of the coil, which was previously “in air” (Fig. 2.2). These quantities were measured by using the impedance analyser mentioned in Chapter 4, which was connected to the LCR circuit shown in Fig. 4.5. In some experiments, the metallic sample was placed in contact with the coil, such that the centre of the sample’s surface in contact with the coil’s lower base (Fig. 3.6) was in the same position as the centre of the coil’s lower base. In some other experiments, the coil and the sample were placed at a certain value of lift-off, which will be stated in the individual sections, and the measurement method adopted was the one explained in Section 4.2. Unless otherwise stated, the external capacitance and resistance of the LCR circuit were equal to the values:  $C=1 \mu\text{F} \pm 1\%$  and  $R=1 \text{ k}\Omega \pm 1\%$ .

### 5.1 Study of the influence of lift-off on resonant frequency and Q-factor measurements

The LCR-based experimental system presented at the end of Chapter 4 was initially tested to see whether it could detect the presence of metallic samples placed at different values of lift-off  $L$  (i.e., vertical distance between sample and coil), between  $L=0$  and  $L=(6.0 \pm 0.1)$  cm. The lift-off is an important parameter in NDE measurements, as it influences the inductive coupling between conductive samples and the coil of the LCR circuit [24].

Metallic samples were used having conductivity values ranging from lower conductivity of  $0.54 \text{ MSm}^{-1}$  (manganese, Mn) to higher conductivity of  $59.77 \text{ MSm}^{-1}$  (copper, Cu) [66]. The procedure described in the next section was undertaken with the purpose of producing 2D images for each of these conductive samples.

### 5.1.1 Description of the experimental procedure

A preliminary study was carried out in order to investigate the possibility of generating high-quality images of metallic samples by means of two contactless imaging techniques, based on resonant frequency and Q-factor measurements, respectively. The measured quantities obtained in the presence of each metallic sample were related to corresponding measurements with no sample present (“in air”). The hypothesis here was that identifying changes in the measured parameters (resonant frequency and Q-factor) could lead to image the sample (as documented in Chapter 3). “High-quality” is intended as the ability of the images to reproduce the shape and dimensions of the samples, with the colours corresponding to the sample ‘footprint’ being visibly different from the background, corresponding to peripheral sample’s positions along the scanning area, i.e., at larger distances between the sample’s upper surface and the coil’s lower base. The dependence of the image quality on the lift-off ( $L$ ) was studied by means of two experiments. The first experiment consisted in measuring the system’s resonant frequency and Q-factor when a square aluminium sample, having edges equal to  $(25 \pm 1)$  mm and thickness equal to  $(1.0 \pm 0.1)$  mm, was placed under a ferrite-cored coil. The following values of lift-off were chosen:  $L_1=(6.0 \pm 0.1)$  cm;  $L_2=(2.0 \pm 0.1)$  cm;  $L_3=(1.5 \pm 0.1)$  cm;  $L_4=(1.0 \pm 0.1)$  cm and  $L_5=0$ . Ten consecutive measurements of resonant frequency and Q-factor were acquired and the average (named  $f_r$  and Q from now on) and standard deviation ( $\sigma f_r$  and  $\sigma Q$ ) were calculated.

The second experiment applied the procedures described in Chapter 4 to the imaging process of the aluminium sample, at each lift-off value. The lift-off was measured from the coil’s lower base to the sample’s top surface (Fig. 3.6). The purpose of this part of the work aimed at qualitatively showing that the image quality was dependent on the choice of lift-off. This should be the case because the amount of eddy currents induced in a sample increases with the lift-off [24].

### 5.1.2 Results and discussion

The results of the study about the dependence of the measured quantities (resonant frequency and Q-factor) on the lift-off are reported in Fig. 5.1, where the values of resonant frequency and Q-factor, normalised to background values, are plotted against lift-offs.

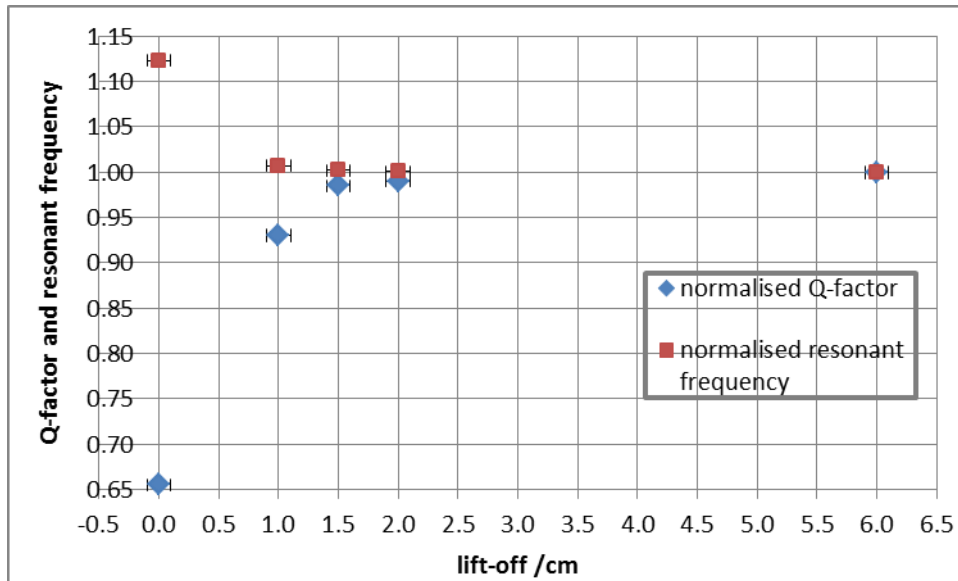


Fig. 5.1. Normalised Q-factor (diamond) and resonant frequency (square), plotted against lift-off (cm), to study the influence of lift-off on the measured quantities. Data was acquired using a 25x25x1 mm<sup>3</sup> aluminium sample.

The trend shown in Fig. 5.1 can be understood theoretically by utilising the mathematical model reported in Section 2.4. This includes a physical formulation showing the dependence of the coil impedance on the coil-to-sample lift-off, which must be treated as a variable in this specific case. The different trend of the resonant frequency and the Q-factor is due to their different dependence on the real and imaginary parts of the complex impedance. Specifically, in the model reported in Chapter 2, the resonant frequency of the system depends on the inductance of the coil, whereas the Q-factor depends on both the inductance and resistance, therefore the change in the coil complex impedance due to eddy current induction inside the metallic sample has different impacts on the quantities that are

measured in this work. In particular, these vary in a different way with the lift-off, as verified by the trend shown in Fig. 5.1.

The Q-factor curve had an increasing trend for lift-off values between 0 and 1.5; the Q-factor stopped changing with lift-off from the value  $L=2$  cm. On the other hand, the resonant frequency decreased with lift-off until  $L=1.5$  cm. From this value on, the resonant frequency change appeared to be zero. A comment about the values of lift-off chosen for this plot should be made. The “jump” between 0 and 1 on the x axis could not seem appropriate given the shape of the curves for both data sets, which have high gradient in this region. Nevertheless, it was established for practical reasons that values in between 0 and 1 cm should not be included, due to the larger uncertainty in positioning the sample at those distances from the coil. This was caused by the nature of the experimental setup and the measurement method, which was based on inserting the sample within the wooden structure enclosing the experimental system. In addition to the constraint in achieving this when using the laboratory experiment, the choice of lift-off values between 0 and 1 cm would not have made a meaningful difference when exporting this technique into an on-site system and conducting measurements in real-life applications. The images of the aluminium sample obtained for each value of lift-off showed good-quality reproduction of the sample’s shape and size at  $L < 6$  cm for both resonant frequency and Q-factor measurements. Examples of the images obtained after setting the lift-off to the value  $L=L_4=(1.0 \pm 0.1)$  cm are shown in the next section (Figs. 5.2 and 5.3). The reason why a decrease in sensitivity and resolution was observed at lift-offs higher than 1.5-2 cm was attributed to the magnetic field spreading out around the system sensitive area [37]. It was established that an optimal lift-off would be the result of a trade-off between reproduction of the shape and size of the imaged object and the need for a contactless imaging technique. The latter was beneficial as the possibility to detect objects and image them when the coil used in this work (acting as a probe in NDE systems) was not touching the sample was more interesting and useful than the opposite scenario, since accessing the sample is not always possible in real life applications. Based on this consideration, the lift-off chosen for the future experiments was  $L=L_4=(1.0 \pm 0.1)$  cm.

## 5.2 Imaging of high-conductivity samples made of copper and aluminium

### 5.2.1 Description of the experimental procedure

The imaging method described in Chapter 4 was initially tested with high-conductivity metallic samples. The goal of this experimental investigation was to verify the possibility of obtaining 2D images representing the samples, by adopting the proof-of-principle method based on position-resolved-measurements of the resonant frequency and Q-factor shifts, which was described in Chapter 4. Disk samples having diameter  $D=(2.00\pm 0.05)$  cm and thickness  $t = (2.0 \pm 0.5)$  mm (Tab. 5.2), made of copper and aluminium, were used for this purpose. An area  $A=4.25\times 4.25$  cm<sup>2</sup> was scanned by moving each sample along a plane parallel to the coil's lower base. The lift-off was equal to  $(1.0 \pm 0.1)$  cm, the resistance was set to  $R=1\pm 1\%$  K $\Omega$  and the capacitance  $C=(1.0000 \pm 0.0001)$   $\mu$ F. Ten consecutive measurements of resonant frequency and Q-factor were acquired and the average ( $f_r$  and Q) and standard deviation ( $\sigma f_r$  and  $\sigma Q$ ) values were calculated.

Copper and aluminium samples having dimensions  $25\times 25\times 1$  mm<sup>3</sup> (Tab. 5.1) were also imaged, in order to investigate the ability of the system to resolve shapes.

### 5.2.2 Results and discussion

Results of the imaging study about high-conductivity samples are reported in this section. Images of a 2-mm-thick, 2-cm-diameter aluminium disk were obtained via position-resolved measurements of the resonant frequency and of the Q-factor, respectively, and are reported in Fig. 5.2. The imaged samples were found to be distinguishable from the background image (Fig. 5.2). Qualitatively, both their shape and size compared very well with the actual ones. A quantitative analysis was carried out to support the qualitative observations, as reported in Section 5.4, with the purpose of comparing the dimensions of the samples reproduced in the images with the samples' actual dimensions. Similar results were obtained with a  $25\times 25\times 1$  mm<sup>3</sup> square copper sample after setting the capacitance to  $C=0.5\pm 1\%$   $\mu$ F (Fig. 5.3).

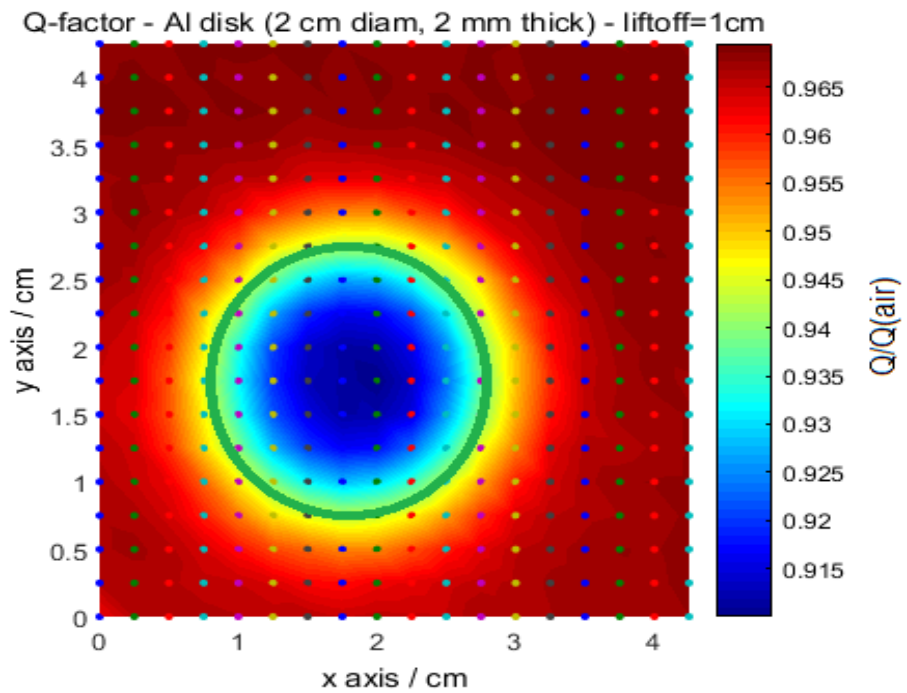
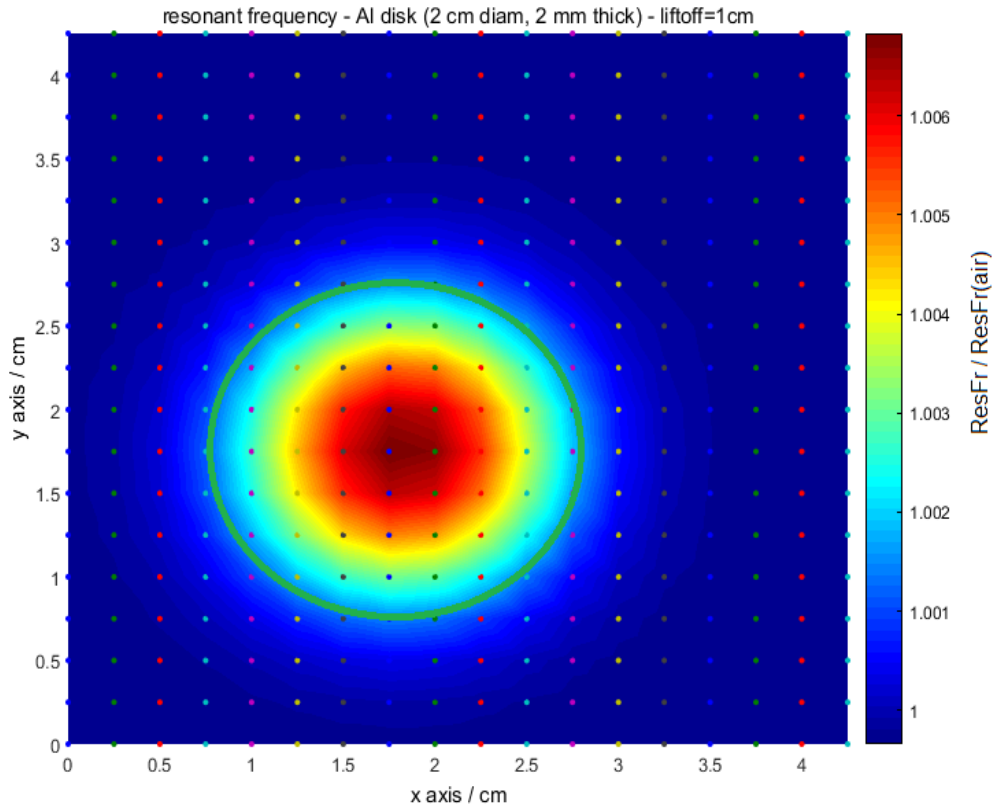


Fig. 5.2. 2-cm-diameter, 2-mm-thick aluminium disk imaged via position-resolved measurements of the resonant frequency (top) and of the Q-factor (bottom). The resonant frequency and Q-factor values- measured at the centre of the object and normalised to the value in air- were equal to  $f_r=1.01\pm 0.03$  and  $Q=0.93\pm 0.04$ .

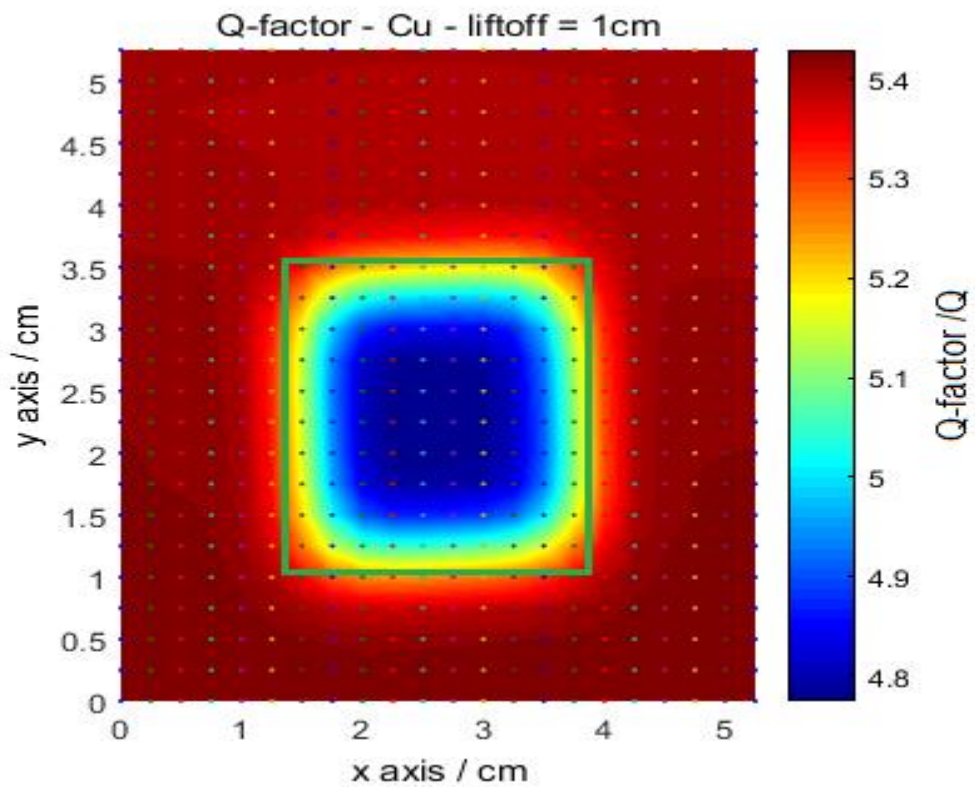
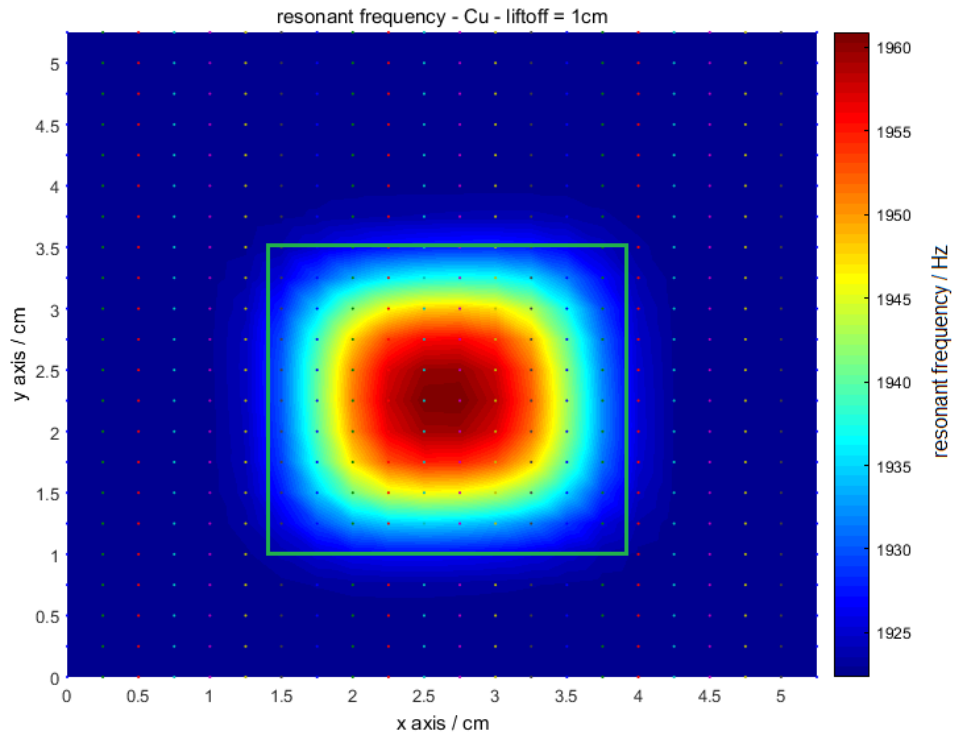


Fig. 5.3. Image of a 25x25x1 mm<sup>3</sup> copper sample obtained via position-resolved measurements of the resonant frequency (top) and the Q-factor (bottom). The normalised resonant frequency and Q-factor at the centre of the sample were equal to  $f_r=1.01\pm 0.03$  and  $Q=0.94\pm 0.04$ .

The normalised resonant frequency and Q-factor values measured at the centre of the object reported in Fig. 5.3 were found equal to  $f_r=1.01 \pm 0.02$  and  $Q=0.94 \pm 0.03$ , respectively. Images similar to the ones representing a copper sample were obtained with an aluminium sample having the same geometry as the copper one.

The results shown in Figs. 5.2-5.3 demonstrated the suitability of both resonant frequency and Q-factor methods for 2D imaging of high-conductivity samples of different shapes. At this stage, neither images of disks nor images of square samples were able to distinguish between the two metals. This was the case because the normalised resonant frequency and Q-factor at the centre of the aluminium sample were equal to the ones obtained for copper. This means that the different nature of the two samples could not be visually assessed by looking at the images reproducing them. More information of the images was obtained at a later stage by comparing the diameters/edges of the samples from the image to the ones of the actual samples, measured with a ruler. Section 5.4 details the experimental procedure used and includes results and discussion at the end.

Results reported in this section proved that the proof-of-principle methods based on position-resolved-measurements of the resonant frequency and Q-factor, respectively, made it possible to produce 2D images representing copper and aluminium samples having dimensions equal to  $25 \times 25 \times 1 \text{ mm}^3$ .

## 5.3 Material characterisation: comparison between resonant frequency and Q-factor techniques

### 5.3.1 Description of the experimental procedure

The results of the previous experiments highlighted the need for a new method enabling material characterisation. The eddy current amount depended on a number of factors, both geometrical (including lift-off and coil's geometry) and related to the sample's electromagnetic properties. Lower-conductivity samples were expected to produce a smaller change in the inductance of the measurement system, reflecting on smaller resonant

frequency and Q-factor changes, than the ones obtained with higher-conductivity samples [24]. Other metals, in addition to copper and aluminium, were thus included into the experimental work, in order to investigate whether the proposed proof-of-principle method (based on position-resolved measurements of the resonant frequency and Q-factor) could be extended to metals spanning a wide range of conductivities. A quantitative analysis was performed by measuring the resonant frequency and Q-factor changes occurring in the presence of 14 representative metallic samples, having values of conductivity ranging from  $0.54 \text{ MSm}^{-1}$  (Mn) to  $59.77 \text{ MSm}^{-1}$  (Cu), as reported in Tab. 5.1 [66].

Tab. 5.1. List of the  $25 \times 25 \times 1 \text{ mm}^3$  metallic samples imaged in this work. Their tabulated conductivity values [66] are reported in the second column. In the third column, the metals are ordered from the most conductive (Cu) to the least conductive one (Mn).

<b>Metal</b>	<b><math>\sigma</math> (<math>10^6 \text{ Sm}^{-1}</math>)</b>	<b>Number (x axis from right to left in Fig. 5.4)</b>
Copper (Cu)	59.77	1 (maximum conductivity $\sigma$ )
Gold (Au)	42.55	2
Aluminium (Al)	37.67	3
Zinc (Zn)	16.90	4
Iron (Fe)	10.30	5
Tin (Sn)	9.09	6
Niobium (Nb)	8.00	7
Tantalum (Ta)	8.03	8
Lead (Pb)	4.84	9
Vanadium (V)	4.03	10
Hafnium (Hf)	2.85	11
Titanium (Ti)	2.38	12
Bismuth (Bi)	0.94	13
Manganese (Mn)	0.54	14 (minimum conductivity $\sigma$ )

During the measurements, the samples were in contact with the ferrite-cored coil ( $L=680\pm 10\% \mu\text{H}$ ), which was part of the LCR circuit showed in Fig. 4.6. The resistance was equal to  $R=1 \text{ K}\Omega \pm 1\%$  and the capacitance was assigned the following values for comparison purposes:  $C=1 \mu\text{F}$  and  $C=0.5 \mu\text{F}$ . Ten consecutive measurements of resonant frequency and Q-factor were acquired and the average ( $f_r$  and  $Q$ ) and standard deviation ( $\sigma f_r$  and  $\sigma Q$ ) values were calculated.

The changes in resonant frequency and Q-factor values, due to the presence of a metallic object, were calculated by using the following equations:

$$\Delta f_r = \frac{f_r(\text{metal}) - f_r(\text{air})}{f_r(\text{air})} (\%) \quad (5.1)$$

$$\Delta Q = \frac{Q(\text{metal}) - Q(\text{air})}{Q(\text{air})} (\%) \quad (5.2)$$

In the equations above,  $f_r(\text{metal})$  and  $Q(\text{metal})$  represent the resonant frequency and Q-factor values measured when the metallic sample was placed under the coil (1 cm lift-off);  $f_r(\text{air})$  and  $Q(\text{air})$  refer to values measured in air, i.e., when no metallic sample was present in the vicinity of the coil.

The procedure was repeated with a value of lift-off  $L=0$  (i.e., sample in contact with the coil). The changes in Q-factor plotted against the samples' conductivity were compared for data obtained at  $L=(1.0\pm 0.1)$  cm and  $L=0$ . This experiment aimed at identifying a procedure which allowed to distinguish between different high-conductivity samples.

Both techniques based on resonant frequency and Q-factor measurements were adopted to see how changes produced by the presence of a sample at different values of lift-off varied. This aimed at establishing which technique was better at identifying conductive materials.

### 5.3.2 Results and discussion

This section reports on results of the study described in the previous section, in which materials of different conductivities were used and the resonant frequency and Q-factor values were measured in order to quantify the shift of these quantities from the case where the measurement system was in air (Fig. 2.2). Resulting changes of resonant frequency and Q-factor, estimated by using Eqs. 5.1 and 5.2, were plotted against the metal's conductivity values, taken from [66]. Results obtained after setting the capacitance to the value  $C=1\ \mu\text{F}$  are reported in Fig. 5.4. The capacitance value was later changed to  $C=0.5\ \mu\text{F}$  and the results were compared. These specific values were chosen because they produced the highest changes of  $f_r$  and Q, as detailed below. This implied that less distorted images of all metals could be obtained, in which the reproduction of the samples' shapes had higher quality.

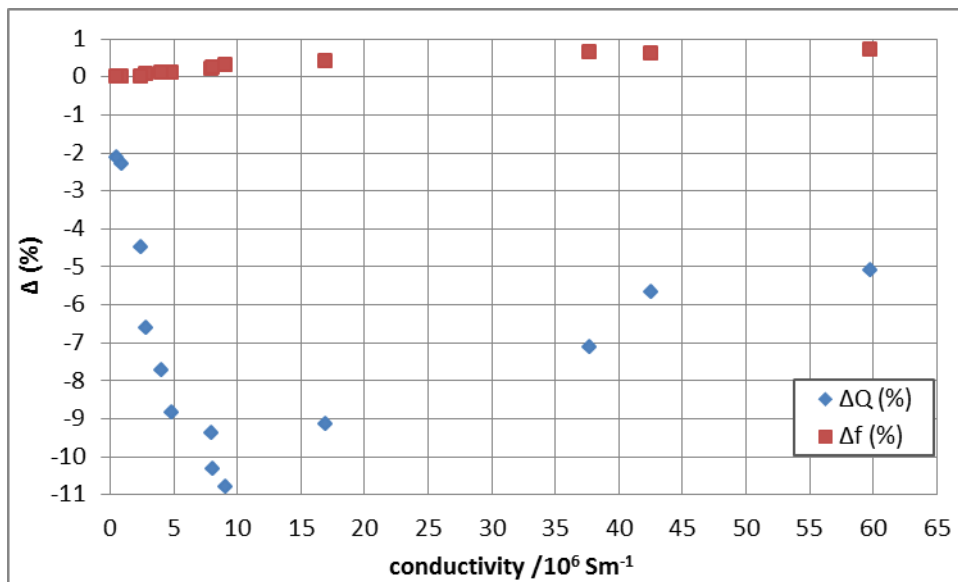


Fig. 5.4. Change in Q-factor and resonant frequency plotted against conductivity for each of the 14 metals listed in Tab. 5.1 [66]. The physical quantities were measured at  $C = 1\ \mu\text{F}$ . The two data points that are detached from the main trends of  $\Delta Q$  and  $\Delta f$  (labelled “Fe”) correspond to measurements acquired with iron (99.5% purity).

Fig. 5.4 showed that the Q-factor varied in a much wider interval than the resonant frequency:  $\Delta Q = [-11, -2]\%$ ,  $\Delta f = [-0.3, 0.7]\%$ . These values can be seen by looking at the two curves reported in Fig. 5.4, and represent the minimum and maximum Q-factor and resonant frequency change, respectively on the left and right side of the intervals defined by the

brackets. These intervals were found by considering changes of  $Q$  and  $f_r$  obtained for the 14 metals included in this study. Both the red and blue curves had a well-defined trend. This trend can be understood from a mathematical perspective by adopting the model illustrated in Section 2.4. The model introduces the analytical function for the coil impedance, when a flat metallic sample is placed at a constant lift-off from the coil. Assumptions about the geometry of the problem are made and the impedance is expressed as a mathematical function of the metal's properties and other variables (assuming non-ferrous metals). In particular, the impedance dependence on the conductivity is shown and this can be used by deriving the dependence of resonant frequency and Q-factor on  $\sigma$ . Derivation of the analytical function for the Q-factor, with respect to  $\sigma$  would show a minimum as can be seen in Fig. 5.4. This is not a straightforward calculation as it requires expressing the Q-factor with Bessel functions, in a way similar to the one in which impedance was derived by Dodd & Deeds in [65], utilising the Q-factor definition ( $Q = \frac{\omega L}{Z_r}$ , Eq. 2.43). In a similar fashion, the resonant frequency would need to be expressed as a function of the complex part of the coil impedance and its behaviour close at limits of low and high conductivity should be studied in an analytical way, in addition to the behaviour of its prime derivative with respect to  $\sigma$ .

The resonant frequency changes were found to increase with conductivity, by an amount lower than 0.8% over the whole conductivity range considered, as shown in Fig. 5.5. The Q-factor change, on the other hand, decreased for lower conductive metals, including tin, for which the absolute value of  $\Delta Q$  was maximum; after reaching the maximum,  $\Delta Q$  started to increase with conductivity, until the curve behaviour began to 'saturate', i.e., smaller change of  $\Delta Q$  occurred for high-conductivity metals from gold to copper, and such change was as low as 1.2% between aluminium and copper.

Plots similar to the ones shown in Fig. 5.4 were obtained by setting the capacitance to  $C=0.5 \mu\text{F}$ , showing that capacitance changes did not prevent the system from producing resonant frequency and Q-factor shifts that were linked to the conductivity of the material as in plots shown in Fig. 5.4. In this case, Q-factor and resonant frequency varied with conductivity within a range equal to  $\Delta Q=[-15, -3.8]\%$ ,  $\Delta f_r=[-0.25, 0.67]\%$ . The same notation used above was adopted here, with the brackets representing intervals of Q-factor and resonant frequency shifts, measured in the presence of the 14 samples listed in Tab. 5.1. The

values on the left of the brackets correspond to the lower values of  $\Delta Q$  and  $\Delta f_r$  within the given intervals, those on the right correspond to the higher values. Such values corresponded to tin in the case of  $\Delta Q$ , and to copper for  $\Delta f_r$ . The values reported on the right inside the brackets corresponded to the minimum absolute changes among the 14 samples. These values were found when manganese was used, with both measurements of  $\Delta Q$  and  $\Delta f_r$ . The other metals produced changes of resonant frequency and Q-factor which were inside the intervals defined by the brackets.

Comparison between the results obtained after setting the capacitance to the values  $C=1 \mu\text{F}$  and  $C=0.5 \mu\text{F}$  implied that the system's behaviour was similar, when the external capacitance value was changed, and generalised conclusions could thus be drawn. The data sets obtained by measuring the resonant frequency with  $C=0.5 \mu\text{F}$  and  $C=1 \mu\text{F}$  are shown in Fig. 5.5. The two trends are similar, showing an increase of  $\Delta f_r$  with  $\sigma$ .

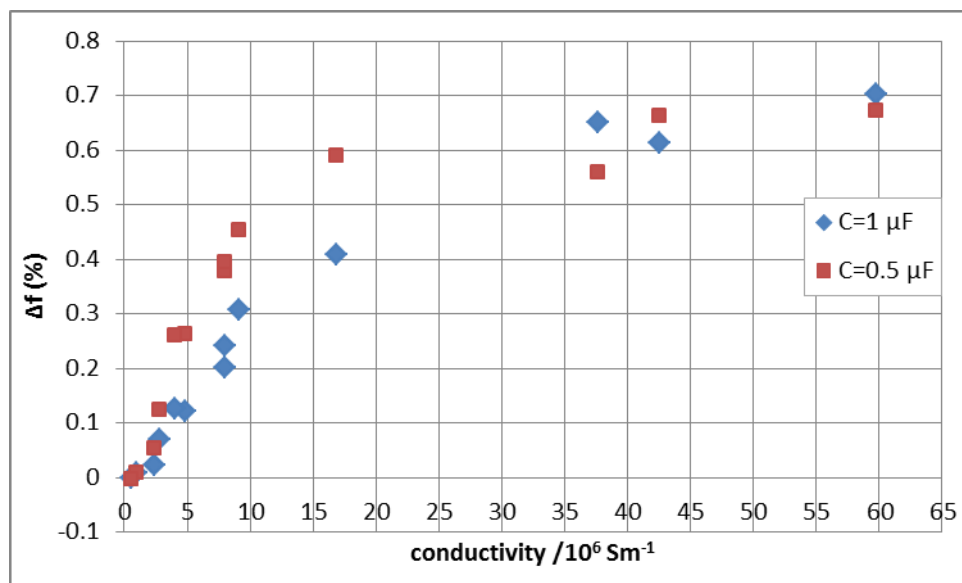


Fig. 5.5. Change in resonant frequency plotted against conductivity of each of the 14 metals listed in Tab. 5.1 [66]. The physical quantities were measured at  $C=1 \mu\text{F}$  (diamond data set) and  $C=0.5 \mu\text{F}$  (square data set). Dots that are detached from the main trends (producing  $\Delta f$  equal to  $-0.25\%$  and  $-0.3\%$ ) correspond to measurements taken with iron (99.5% purity).

Due to the behaviour of the  $\Delta Q$  data set, each value of Q-factor was not univocally related to a metal of certain conductivity (Figs. 5.4 and 5.5). Therefore, different metals could not be distinguished from each other by simply measuring the Q-factor. On the other hand, the resonant frequency trend (square data series) was represented by a monotonic function,

if the data point corresponding to iron is excluded (Fig. 5.5). This clearly showed the potential of this technique to achieve the goal of material characterisation. However, a higher change of resonant frequency than the one obtained was required, since the measured changes had the same order of magnitude as the experimental uncertainties ( $\sigma_{f_r}=0.02$ ).

The following sections report observations made about the system's behaviour in the regions corresponding to the limits of low and high conductivity ( $\sigma$ ).

### 5.3.2.1 High-conductivity metals

Fig. 5.4 showed that the Q-factor variation with  $\sigma$  was nearly null for values of conductivity corresponding to Cu and Al ( $\sigma=42.55 \times 10^6 \text{ Sm}^{-1}$  and  $\sigma=59.77 \times 10^6 \text{ Sm}^{-1}$ , respectively). This explained the difficulty of producing different images of copper and aluminium samples encountered earlier (Section 5.2). Another observation can be made about the reproduction of high-conductivity samples in the images. Figs. 5.2 and 5.3 represented images of copper and aluminium samples obtained with resonant frequency and Q-factor measurements. The *Matlab* images reported in these figures showed that the diameters of the imaged samples were in good agreement with the dimensions of the actual samples. A quantitative analysis was carried out to estimate the diameter of the imaged disks by adopting an edge-detection algorithm, as reported in Section 5.4.

### 5.3.2.2 Low-conductivity metals

The Q-factor change showed a large variation with conductivity for low-conductivity metals ( $\sigma$  ranging from 0.54 to  $4.03 \times 10^6 \text{ Sm}^{-1}$ ). On the other hand, samples with low-conductivity (particularly, bismuth and manganese) produced a negligible change of the resonant frequency of the circuit. This result was confirmed by images of manganese and bismuth shown in Figs. 5.6-5.7, in which the imaged samples could not be clearly distinguished from the background. Due to the small change of resonant frequency from the background value, it was not possible to visualise the manganese object, whereas the bismuth sample produced a visible 'signature', showing its presence, due to its larger conductivity. Although the change of resonant frequency from the background value for bismuth was bigger than the one obtained with lower-conductivity manganese, the object could not be clearly distinguished from the background. On the other hand, images of manganese and bismuth that were obtained via position-resolved-measurements of the Q-factor showed that the samples were very clearly distinguished from the background by means of the Q-factor technique (Figs. 5.8-5.9). This result is important because manganese has similar electromagnetic properties than uranium (they are both paramagnetic materials with similar values of magnetic susceptibility, equal to  $\chi(\text{Mn})=529 \times 10^{-6} \text{ cgs}$  and  $\chi(\text{U})=409 \times 10^{-6} \text{ cgs}$ , measured respectively at 293 and 298 K); therefore, being able to image it is relevant for the security applications on which this research is founded [66]. The findings resulting from these experimental observations led to establishing that the Q-factor measurement method was more successful than the resonant frequency method in order to achieve EII of poorly conductive samples.

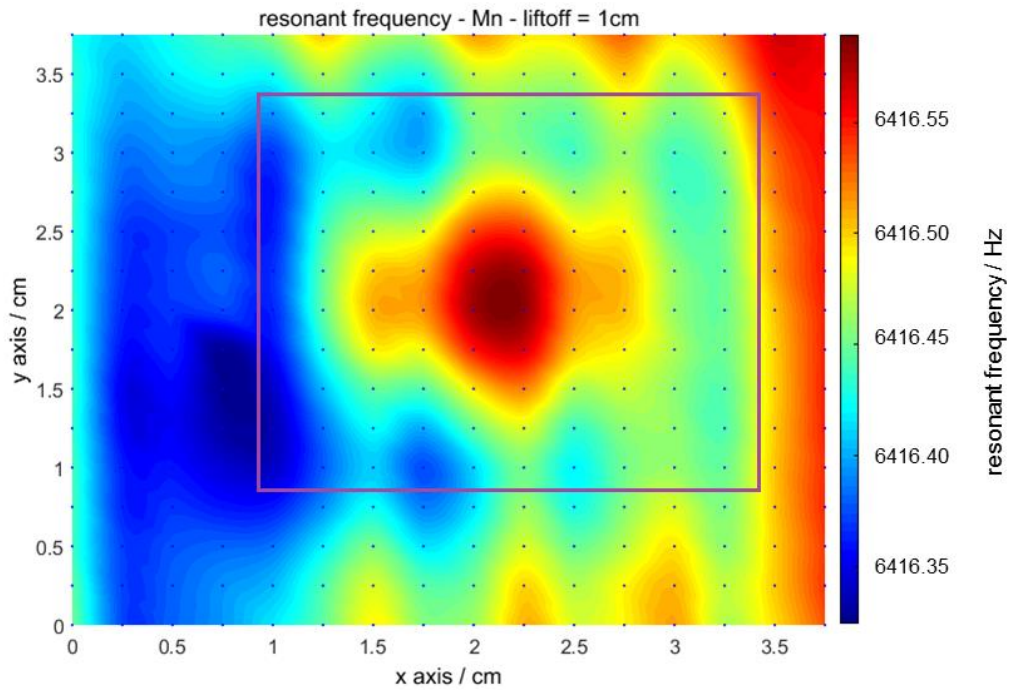


Fig. 5.6. Images of a 25x25x1 mm<sup>3</sup> manganese sample obtained via position-resolved measurements of the resonant frequency, for a capacitance C=1 μF.

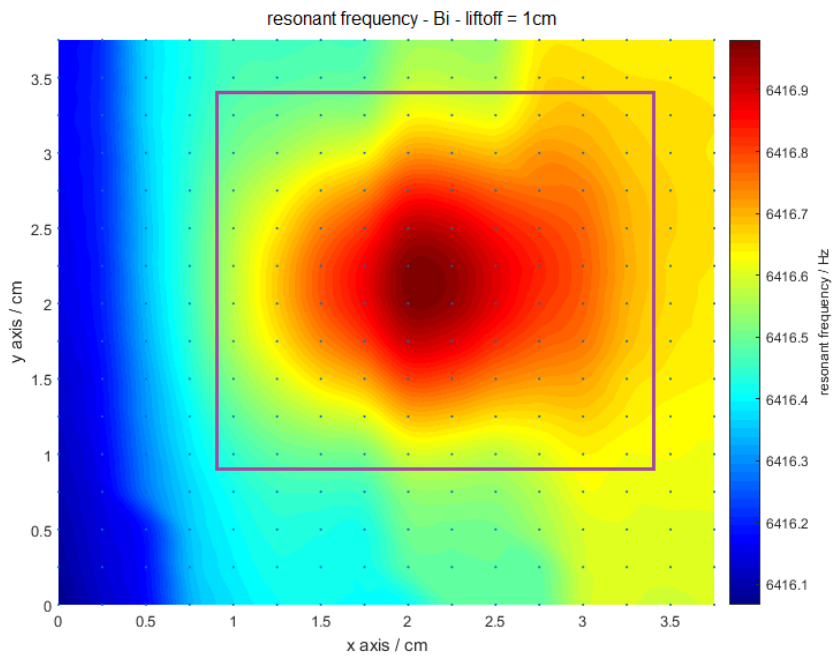


Fig. 5.7. Images of a 25x25x1 mm<sup>3</sup> bismuth sample obtained via position-resolved measurements of the resonant frequency, for a capacitance C=1 μF. Values on the z axis are resonant frequency measured in presence of the sample, normalised w.r.t. values in air.

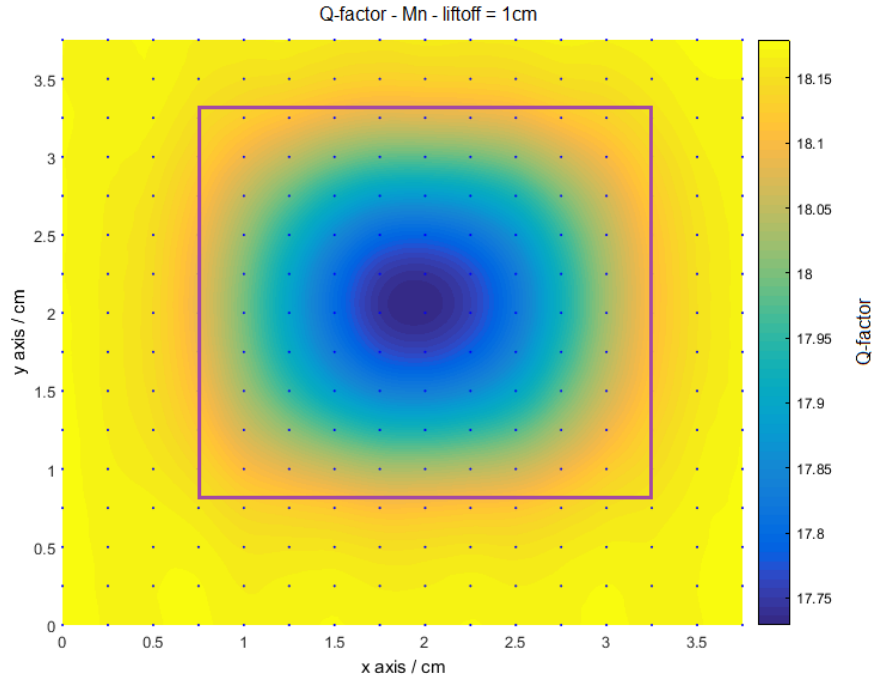


Fig. 5.8. Images of a 25x25x1 mm<sup>3</sup> manganese sample obtained via position-resolved measurements of the Q-factor, for a capacitance C=1 μF. Values on the z axis are resonant frequency measured in presence of the sample, normalised w.r.t. values in air. The shape of the sample resembles the shape of the actual sample in this case.

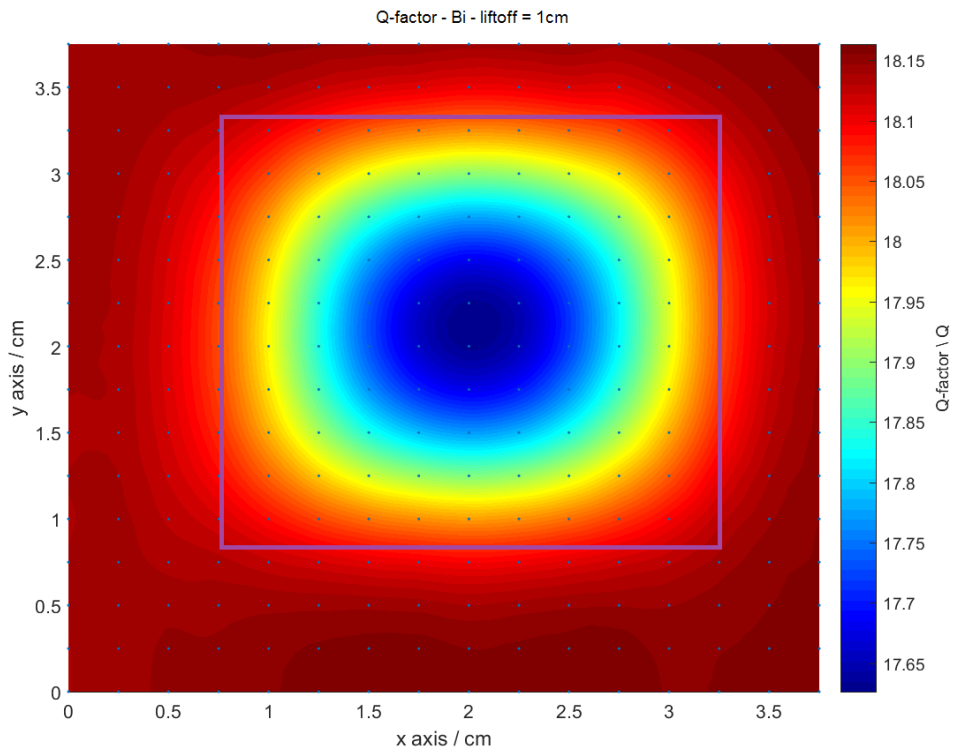


Fig. 5.9. Images of 25x25x1 mm<sup>3</sup> bismuth samples obtained via position-resolved measurements of the Q-factor, for a capacitance C=1 μF. The shape of the sample resembles the shape of the actual sample in this case, unlike what appeared in Fig. 5.6.

The results shown in Figs. 5.8-5.9 implied that the Q-factor imaging technique provided higher sensitivity than the resonant frequency imaging technique, as the Q-factor shifts produced by low-conductivity samples were larger than the resonant frequency shifts produced by the same samples, thus making it possible to distinguish the sample from the background in a Q-factor image. The Q-factor imaging technique allowed characterising materials having similar values of conductivity and allowed imaging over a broad range of conductivity. Consequently, experimental procedures illustrated in Chapter 7 were focused on Q-factor measurements. These could be more useful than resonant frequency measurements, especially for low-conductivity samples, as appeared by comparing Figs. 5.6 and 5.7 with Figs. 5.8 and 5.9.

The system's behaviour corresponding to the limits of low and high conductivity was investigated further.

Firstly, the capacitance value of the LCR system was reduced from  $C=1\ \mu\text{F}$  to  $C=0.5\ \mu\text{F}$ , in order to verify whether it could be possible to visualise low-conductivity samples by modifying the circuit's capacitance and, therefore, its resonant frequency. Secondly, an experiment was conducted to try to overcome the issue linked to Q-factor saturation (i.e., decrease of the  $\Delta Q$  change with  $\sigma$  observed at high values of  $\sigma$ ) at high conductivities.

With regards to the first experimental investigation, the following considerations are noted. The advantage of decreasing the system's capacitance was that the skin depth could then be increased, due to the skin depth's dependence on the frequency of the system, which in turn is dependent on the capacitance (Eqs. 2.13-2.16). Obtaining larger skin depth could thus be achieved by decreasing  $C$ , which could be useful for imaging hidden metals by penetrating through the conductive screens shielding them. This topic was covered in Section 2.2 and experimental investigations related to it are reported in Chapter 6. At this stage, the capacitance was reduced from  $C=1\ \mu\text{F}$  to  $C=0.5\ \mu\text{F}$ , and images of manganese and bismuth samples were obtained by means of resonant frequency measurements, after normalising the values w.r.t. air (Figs. 5.10 and 5.11).

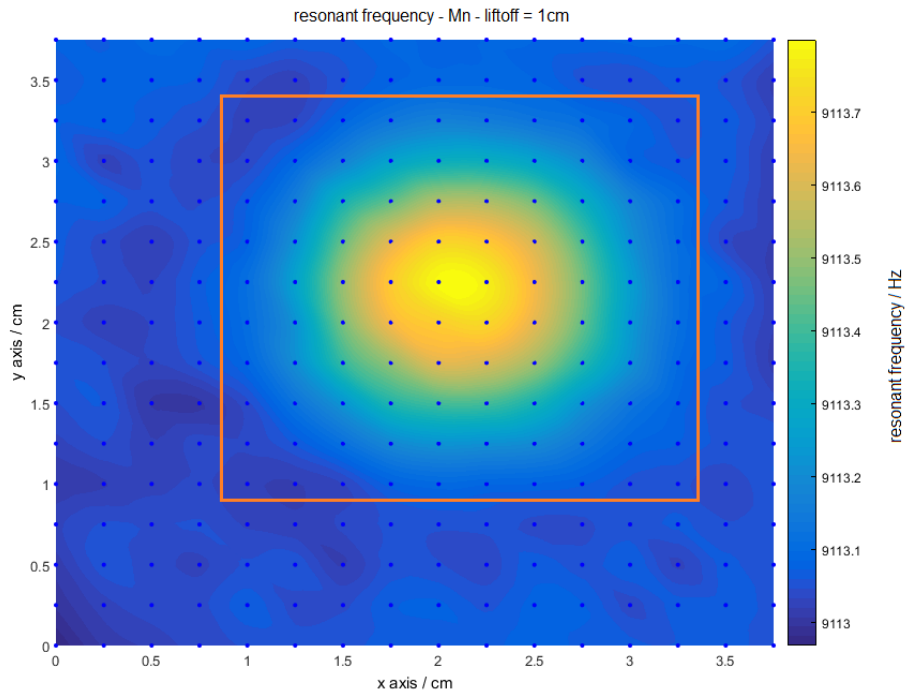


Fig. 5.10. Image of a 25x25x1 mm<sup>3</sup> manganese sample obtained via position-resolved measurements of the resonant frequency, for a capacitance  $C=0.5 \mu\text{F}$ . The imaged sample is now visible due to the increase of resonant frequency produced by selection of a lower capacitance value than the previously used value of  $C=1 \mu\text{F}$ .

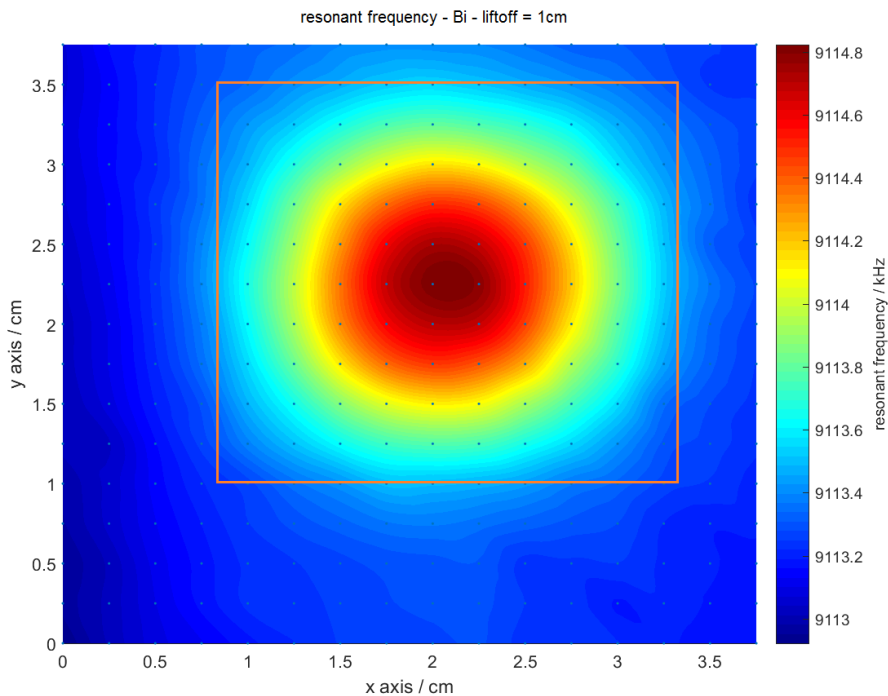


Fig. 5.11. Image of a 25x25x1 mm<sup>3</sup> bismuth sample obtained via position-resolved measurements of the resonant frequency, for a capacitance  $C=0.5 \mu\text{F}$ . The imaged sample is now visible due to the increase of resonant frequency produced by selection of a lower capacitance value than the previously used value of  $C=1 \mu\text{F}$ .

It was observed that, in the case of  $C=0.5 \mu\text{F}$ , the objects could be distinguished from the background, unlike what occurred at  $C=1 \mu\text{F}$  (Figs. 5.10 and 5.11). This was due to the increase of the resonant frequency occurring when the capacitance is decreased (Eq. 4.3). The absolute values obtained for  $f_r$  at  $C=0.5 \mu\text{F}$  were larger than the ones obtained with the same sample at  $C=1 \mu\text{F}$ . This was also the case for the scenario when no sample was present. This behaviour is reflected in a larger difference between  $f_{r0}$  measured with the system in air, and  $f_{r1}$  obtained when the conductive samples were inductively coupled to it, than the corresponding difference obtained at larger  $C$ . The images shown in Figs. 5.10 and 5.11 reproduced the shapes of both manganese and bismuth samples because in each of them the difference between the values of resonant frequency of the image background (corresponding to sample's positions located at the outer parts of the scanning area) differed from those corresponding to central positions of the scan, i.e., where the samples were moving closer to the coil until they were centrally aligned to it (the latter scenario corresponded to values at the centre of the disks in Figs. 5.10 and 5.11).

These results demonstrated that resonant frequency imaging of low-conductivity objects was possible by selecting an appropriate value of capacitance. However, this implied that the functionality of the resonant-frequency imaging method was restricted to only certain values of capacitance. On the other hand, the observed change of Q-factor at the two capacitance values used (larger, in both cases, than the measurement uncertainties by a factor greater than 4) made imaging of all conductivity samples possible, irrespective of the capacitance used, for the two values of  $C$  considered in these experiments ( $C=0.5 \mu\text{F}$  and  $C=1 \mu\text{F}$ ). A second weakness of the technique based on resonant frequency measurements was related to the shape reproduction of samples in the images. The shape of the  $25 \times 25 \times 1 \text{ mm}^3$  manganese and bismuth samples imaged in Figs. 5.10 and 5.11 was close to circular, although the actual samples were square. For comparison, the shapes reproduced in Figs. 5.8 and 5.9 with Q-factor measurements were closer to the shapes of the actual samples, although this imaging technique is not accurate enough to produce 90 degrees edges as the ones in a square should be. A representation of the samples' shapes closer to the real one was found with higher-conductivity copper sample, as shown in Fig. 5.3. Comparing this image with Fig. 5.2, obtained with aluminium, reveals that the ability to reproduce the shapes of the samples

is dependent on the sample's conductivity, for both the Q-factor and the resonant frequency imaging techniques.

To conclude this section about "Material characterisation", an experiment was conducted to try to overcome the issue linked to Q-factor saturation at high conductivities, i.e., the observed decrease of the  $\Delta Q$  change with  $\sigma$  observed at high values of  $\sigma$  (Fig. 5.4). As suggested by the trend of the diamond-shaped data set illustrated in Fig. 5.1, showing the variation with lift-off of the Q-factor (measured with a 25x25x1 mm<sup>3</sup> aluminium sample), the Q-factor change increased at values of lift-off lower than 1 cm. In order to extend this result to all the metals having different values of conductivity, the Q-factor change was measured for each sample at 1-cm-lift-off and 0-cm-lift-off (Fig. 5.12). This experiment compared a contactless method for imaging conductive samples, to an equivalent method where the procedure was the same except that a zero-lift-off was used, meaning that the coil and the sample were in proximity. This may not always be interesting from a practical point of view, but it quantifies the loss in the system's performance (in terms of Q-factor values normalised w.r.t. values in air) resulting from the transition between contact and contactless systems.

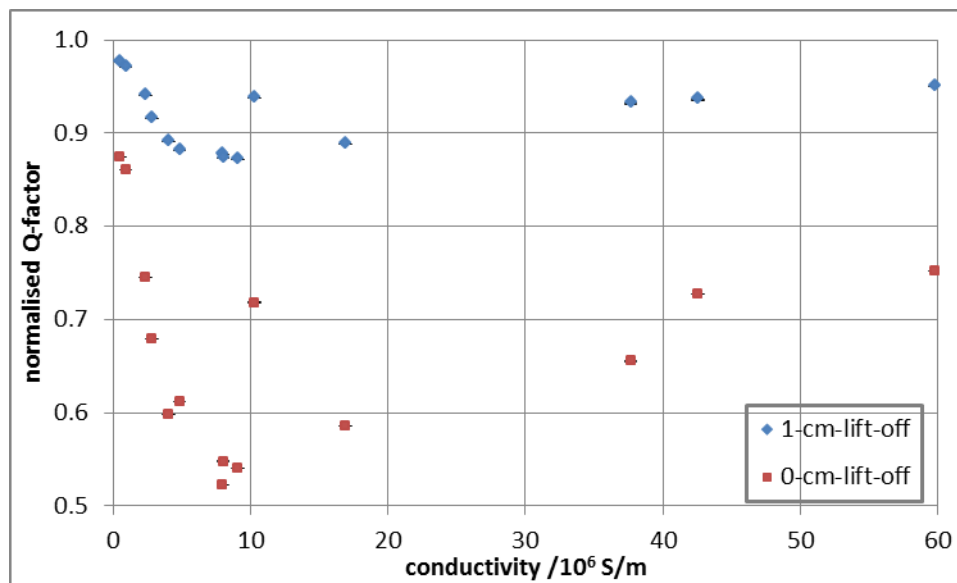


Fig. 5.12. Normalised Q-factor plotted against metal's conductivity [66], at lift-off=1 cm and lift-off=0. Error bars were estimated by propagating the measurement uncertainties, which were standard deviations of the Q-factor measurements. The minima values of the two curves differ of a factor 1.7.

Fig. 5.12 explained why it was not possible to distinguish between a copper and an aluminium sample by using the Q-factor technique at 1-cm-lift-off. These two metals

produced a Q-factor change of 1% in this case; such change doubled when the lift-off was lowered to zero. Changes between Q-factor values obtained for one metal and the ones having conductivities closer to the first metal were found to be larger when the measurements were taken “in contact” (at zero lift-off). The results obtained in this case differ from the measurements taken “in air” by 13% for low-conductivity metals and by 25% for high-conductivity metals (left and right hand sides of the square data set, respectively). The metal which produced the larger change in Q was tin, as found from earlier results, which led to a change of 48% from the configuration “in air”. For comparison, when a lift-off equal to 1 was used, changes of Q were found equal to 3% and 5% for manganese and copper, respectively, and to 13% for tin (diamond data set).

The requirement for an imaging system to allow distinguishing between conductive materials having similar values of electrical conductivities meant that it was important to quantify the difference between the Q-factor obtained with a metal, e.g. copper, and the corresponding value measured with the one closer to the first one in terms of electrical conductivity, e.g., aluminium. A difference larger than the measurement uncertainties would imply that the system was able to distinguish the two metals from each other with the Q-factor measurement technique. The change of Q between the two metals was calculated as:

$$\Delta Q = \frac{Q(Cu) - Q(Al)}{Q(Al)} (\%) \quad (5.3)$$

where  $Q(Cu)$  and  $Q(Al)$  were Q-factor values measured at the centre of the images representing the copper and aluminium samples, respectively. This experiment was done by acquiring ten measurements of Q for each position along a 16x16 scanning area, and calculating the average, standard deviation and maximum value. The resulting maximum average was taken as the one corresponding to the centre of the imaged sample.

The Q-factor change was found equal to  $\Delta Q = (1.93 \pm 0.06) \%$  when the lift-off was  $L = (1.0 \pm 0.1) \text{ cm}$  (diamond set, Fig. 5.12). In comparison, the change of resonant frequency, calculated in a similar fashion with the formula:

$$\Delta f = \frac{f(Cu) - f(Al)}{f(Al)} (\%) \quad (5.4)$$

was found equal to  $\Delta f = (0.38 \pm 0.04) \%$ .

The Q-factor change was found to be bigger than the corresponding resonant frequency change by a factor of 5, which allows drawing the conclusion about the better fit of the Q-factor techniques to imaging of high-conductivity samples and material characterisation aimed at distinguishing between two metals of different electrical nature.

Calculations of the Q-factor and resonance frequency changes were repeated for data obtained at a lift-off of  $L=0$  cm (square set, Fig. 5.12), by using Eqs. 5.3 and 5.4. The values for  $\Delta Q$  and  $\Delta f$  were found to be equal to  $\Delta Q = (14.82 \pm 0.07) \%$  and  $\Delta f = (0.40 \pm 0.05) \%$ .

It should be noted that the  $\Delta Q$  and  $\Delta f$  measurements gave information about the relative change, but what should be calculated to assess the capability of the system to distinguish between two metals is the absolute difference between the measured values obtained with one sample and the corresponding values obtained with the other sample.

These differences were found to be equal to the following:  $dQ(\text{lift-off} = 1) = 0.33$  and  $dQ'(\text{lift-off} = 0) = 1.76$ . These results established that samples made of copper and aluminium could be differentiated using the Q-factor imaging technique, when the metals were in contact with the coil ( $L=0$ ). This result is relevant, in relation to one of the goals of the entire research project, which is material characterisation. Indeed, being able to distinguish between samples having the same geometry and different values of conductivity is a key feature for imaging applied to both security inspection and medical diagnosis. Further work will be focused at increasing the differences  $dQ$  to be able to use a contactless Q-factor imaging technique to distinguish between two metals having different values of electrical conductivity, such as copper and aluminium. Chapter 7 will report on this.

#### 5.4 Edge estimation with resonant frequency and Q-factor techniques

Experimental results shown in Section 5.3 revealed that different conductivities have different weights on the shift of the measured quantities occurring due to the inductive coupling of samples to the LCR system. Specifically, changes of resonant frequency and Q-factor,  $\Delta f_r$  and  $\Delta Q$ , were found to vary with the conductivity of the samples (Figs. 5.4-5.5). This observation raised the interest in quantifying the impact on the imaging process that

inductive coupling of samples to the resonating system had, when samples having different conductivities were used. It was assumed that, due to the lower amount of eddy currents induced in poorly conductive samples, w.r.t. higher-conductivity ones, the images of low-conductivity samples were more blurred than images of higher-conductivity samples.

#### 5.4.1 Description of the experimental procedure

A study was conducted in order to detect the edge and diameter of the samples imaged in the previous experiments (Sections 5.2-5.3). This was accomplished by means of a Canny edge-detection algorithm [68]-[72] that enabled the edge of the images reproducing the samples (obtained as detailed in Sections 4.1-4.2) to be detected. A *Matlab* program was adopted to apply the detected edge to the images obtained by means of resonant frequency and Q-factor position-resolved measurements (reported in Sections 4.2, 5.2 and 5.3), representing both square samples (Tab. 5.1) and circular metallic samples (Tab. 5.2). The *Matlab* code was adapted to the measurement set-up, following the method developed by Brendan *et al.* [73]-[74].

Tab. 5.2. List of copper and aluminium disks of different diameters and thicknesses included in the investigation aimed at imaging high-conductivity samples.

<b>Metal</b>	<b>Diameter (mm, uncertainty <math>\pm 0.5</math>)</b>	<b>thickness (mm, uncertainty <math>\pm 0.5</math>)</b>
Copper	15.0	2.0
"	17.0	2.0
"	20.0	2.0
"	30.0	2.0
"	30.0	0.7
Aluminium	15.0	2.0
"	17.0	2.0
"	20.0	2.0
"	30.0	2.0

The method developed by Canny assumes that the image is made up of “step-edges” corrupted by white Gaussian noise [68]. The Canny edge-detector is given by a convolution filter that smooths the noise in the image and detects the edges. Such edge-detector meets the following three criteria [74]:

- 1) Detection. Detecting real edges is maximised, whereas detecting false edges is minimised. This translates in mathematical terms into maximisation of the signal-to-noise ratio (SNR).
- 2) Localisation. The distance between the detected edge and the real edge is minimised.
- 3) Number of responses. One real edge must not produce more than one detected edge.

A Gaussian function is used as a filter, since it is a close approximation to the optimised product between SNR and localisation [74].

Due to the Canny edge-detector being susceptible to noise present in the raw image data, this image is filtered or smoothed by convolution with a 2D circularly symmetric Gaussian, distributed as a “point-spread” function [74]. This prevents the raw image to be affected by noisy pixels and therefore these pixels cannot be mistaken for edges. The convolution manifests as a blurring of the raw image. The amount of filtering/smoothing is governed by the standard deviation of the Gaussian. Regions of the smoothed image with high first-derivatives are detected by a 2D first-derivative operator. Differentiation in two directions  $x$  and  $y$  enables to find the direction of the slope’s surface to determine the direction in which the edge is pointing [74]. The image representing the sample is turned into a greyscale image, as required by the Canny-edge detection method. The detected edge (coloured in yellow) is overlaid onto the grey scale image to trace the detected edge onto the imaged sample (Figs. 5.13-5.14), by means of a *Matlab* algorithm [74].

The Canny edge detection method was applied to the present work in order to quantify the suitability of the two techniques here proposed for imaging. Specifically, a new technique, including the Canny edge detection as an additional feature, was applied to the previously tested LCR-based system (Section 5.1), to assess its performance as imaging and dimensions’ identification capability. The results achieved by using the resonant frequency and Q-factor techniques, with the external capacitance set to the two values used in previous investigations ( $C=1\ \mu\text{F}$  and  $C=0.5\ \mu\text{F}$ ,  $\pm 1\%$ , as in Sections 5.1-5.3) were considered. The Canny-

edge quantitative analysis aimed at comparing the ability to resolve shapes of the resonant frequency imaging technique with the one of the Q-factor technique. Determination of the imaged samples' dimensions (edges or diameters) was undertaken to see which of the two techniques was closer to representing the samples as they were in reality.

#### 5.4.2 Results and discussion

This section contains the results obtained from the quantitative study that aimed at estimating the edge of the square imaged samples and the diameter of the imaged disks. Results of the study conducted with an aluminium sample by using the Canny-edge detection algorithm are shown in Figs. 5.13-5.14. The images are grey-scaled because grey-scale images were required for the Canny edge detector to be applied to them. The circular contour of the imaged samples is displayed in yellow. This contour has edges closer to 90 degrees square edges in the case of the image obtained with Q-factor position-resolved measurements (Fig. 5.14), than with resonant frequency measurements (Fig. 5.13).

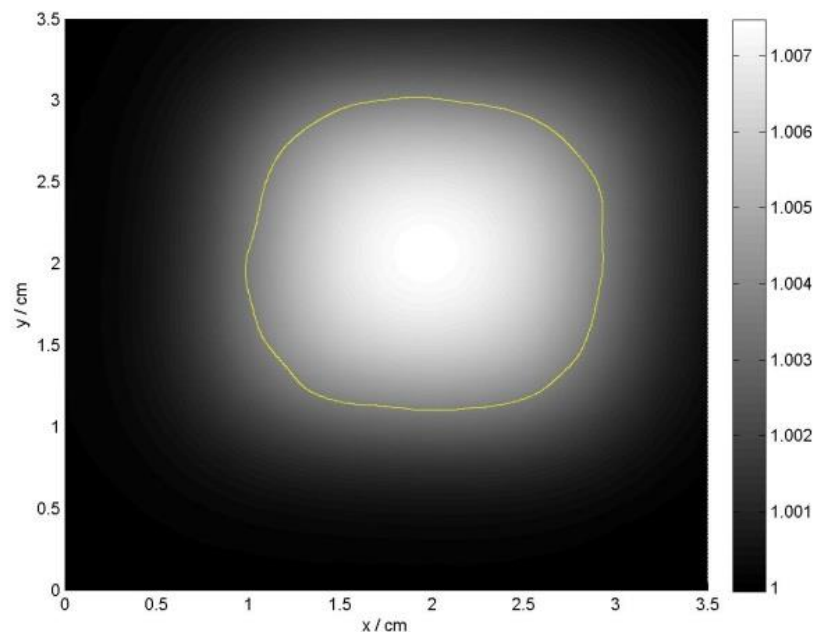


Fig. 5.13. Canny edge detection algorithm applied to the grey scale image of an aluminium square metallic sample ( $25 \times 25 \times 1 \text{ mm}^3$ ), obtained with resonant frequency imaging technique, for a capacitance  $C=1 \text{ }\mu\text{F}$ . Values on the z axis refer to resonant frequency measured in the presence of the sample, normalised w.r.t. air.

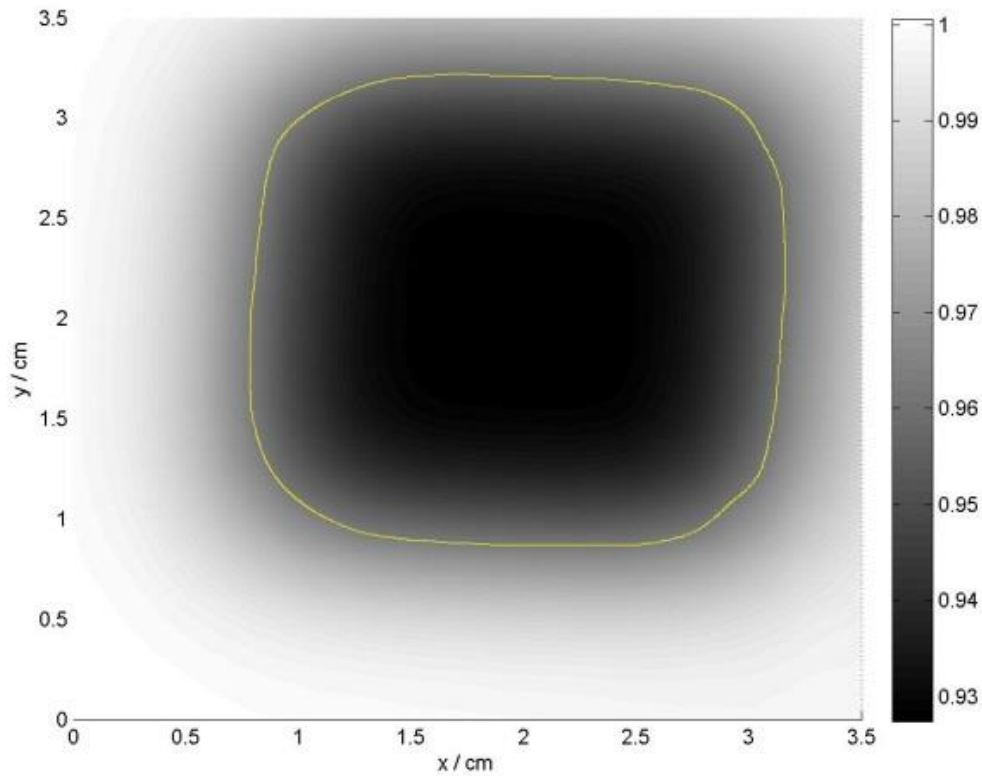


Fig. 5.14. Canny edge detection algorithm applied to grey scale image of aluminium metallic sample ( $25 \times 25 \times 1 \text{ mm}^3$ ), obtained with Q-factor imaging technique, for a capacitance  $C=1 \text{ }\mu\text{F}$ . Values on the z axis refer to Q-factor measured in the presence of the sample, normalised w.r.t. air.

Similar images were obtained with the other 13 square metallic samples used in the previous experiments (Tab. 4.1). Copper and aluminium disks were also included in this study (Tab. 5.2). Due to the limited number of different-diameter-disks available when this study was conducted, a similar study was repeated for a larger number of disks having different diameters and made of aluminium (Tab. 5.4). Experimental results obtained with them are shown in Section 5.6.2.

Results showed that the shape of the sample was best reproduced with the Q-factor technique (Fig. 5.14). This was confirmed by Fig. 5.15, in which the ratio between Canny-detected edge ( $L_{meas}$ ) and 'actual' one ( $L_{real}$ ) is plotted against the metal's conductivity. This figure shows that the edge estimation improves for metals with higher conductivities, where  $L_{meas}/L_{real}$  values of both data sets are closer to 1. This is due to the increase of inductance change with conductivity, causing the measured physical quantities to differ from the

background quantities by a greater amount. For this reason, the Q-factor technique provided a very good estimate of the edge of high-conductivity metals like copper, gold and aluminium ( $L_{meas}/L_{real} = 1$ ).

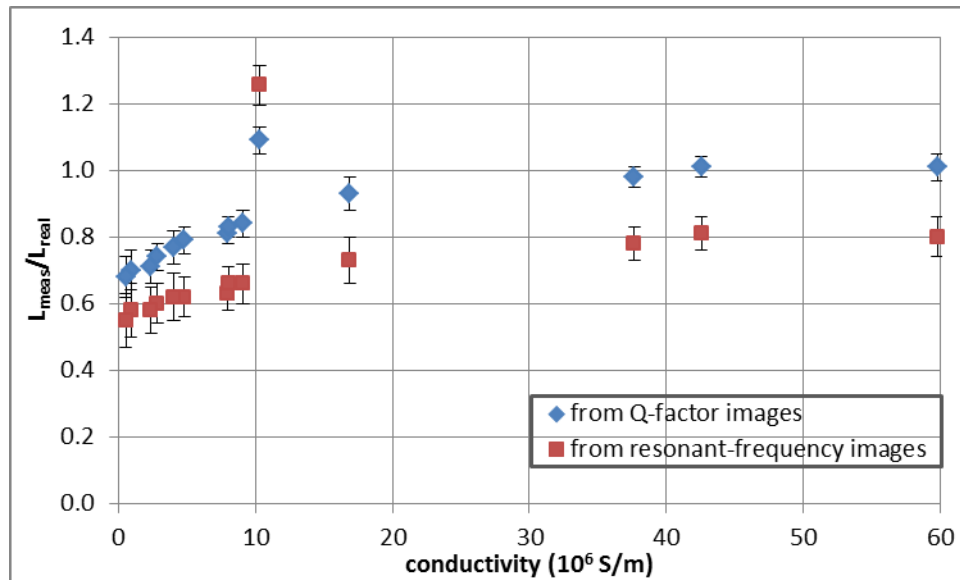


Fig. 5.15. Ratio between Canny-detected edge and ‘actual’ edge of each sample of conductivity  $\sigma$  (Tab. 4.1), plotted against  $\sigma$ . Edge values were estimated from the images obtained with a capacitance  $C=0.5 \mu\text{F}$ . The diamond-shaped data set includes values obtained using the Q-factor imaging technique, whereas the squared-shaped data set represent values obtained using the resonant frequency imaging technique.

The results obtained with copper and aluminium disks were used to produce plots of the diameter estimated by means of the Canny-edge detection technique, against the tabulated ‘actual’ diameter (Figs. 5.16-5.17).

The linear fits of Figs. 5.16-5.17 show that it is possible to determine the ‘actual’ diameter ( $D_t$ ) from the one estimated with the Canny-edge detection algorithm ( $D_e$ ). In particular, the following formulae can be used for copper and aluminium samples being imaged by means of the Q-factor technique:

$$D_t(Cu) = \frac{D_e(Cu)+0.09}{0.98} \quad (5.5)$$

$$D_t(Al) = \frac{D_e(Al)+0.21}{1.04} \quad (5.6)$$

Eqs. 5.5-5.6 were derived by writing the x variable (“measured diameter”) of linear fits of the diamond data sets reported in Figs. 5.16-5.17, in terms of the y variable (“estimated diameter”).

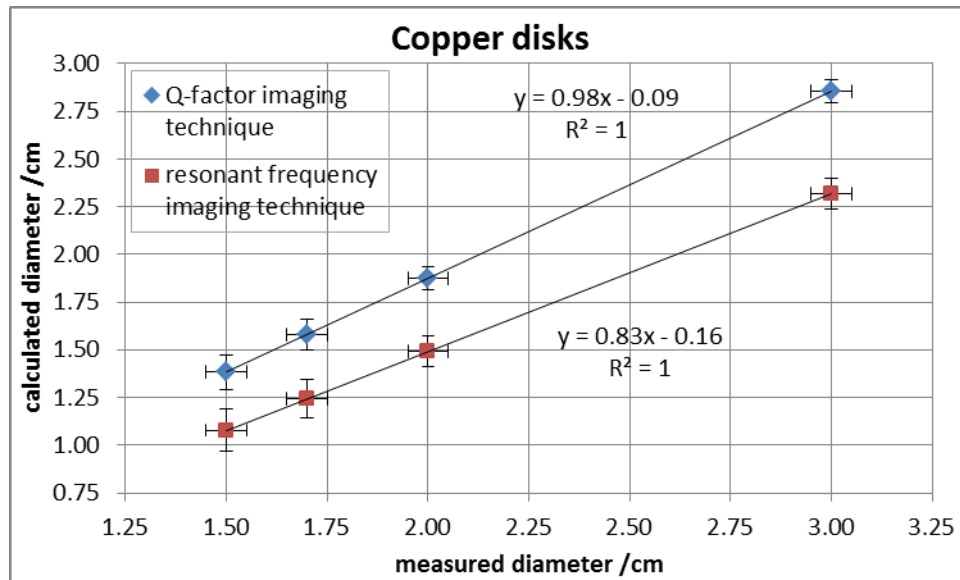


Fig. 5.16. Estimated diameter vs measured diameter of 1.5, 1.7, 2 and 3 cm diameter copper disks. The trends obtained with the Q-factor technique (diamond) and the trend obtained with the resonant frequency technique (square) are both linear.

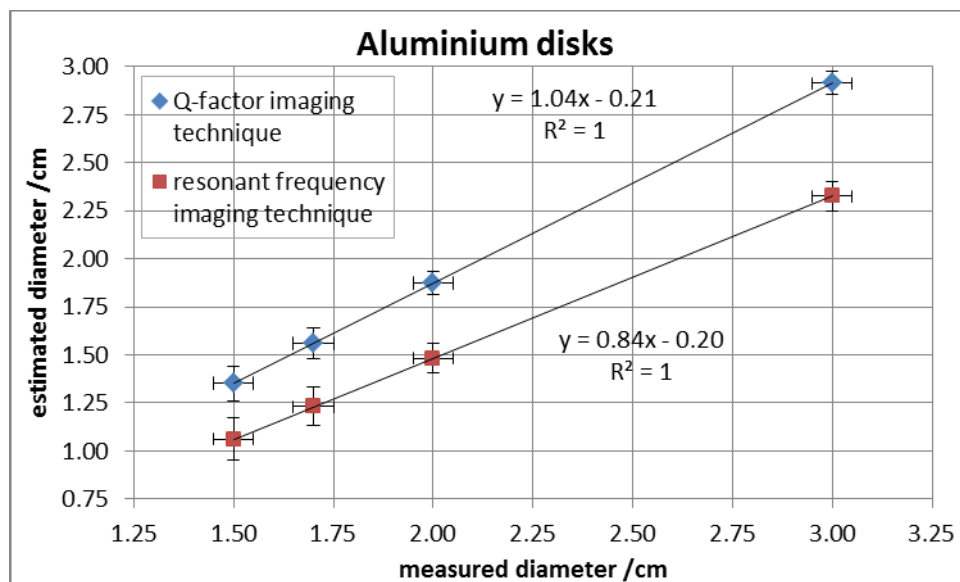


Fig. 5.17. Estimated diameter vs measured diameter of 1.5, 1.7, 2 and 3 cm diameter aluminium disks. The trends obtained with the Q-factor technique (diamond) and the resonant frequency technique (square) are both linear.

Equations similar to (5.5) and (5.6) were derived for copper and aluminium samples being imaged by means of the resonant-frequency technique, from linear-fit equations shown in Figs. 5.16-5.17:

$$D_t(Cu) = \frac{D_e(Cu)+0.16}{0.83} \quad (5.7)$$

$$D_t(Al) = \frac{D_e(Al)+0.20}{0.84} \quad (5.8)$$

Graphs similar to those shown in Figs. 5.16-5.17 were obtained with a capacitance  $C=0.5 \mu\text{F}$ . Therefore, also in this case the sample's diameter may be estimated by using Eqs. similar to 5.5-5.8 that could be derived from linear fits of data.

Figs. 5.18-5.19 contain plots of  $D_t$  ("calculated diameter") vs  $D_e$  ("Canny detected diameter"), obtained by using Eqs. 5.5-5.8.

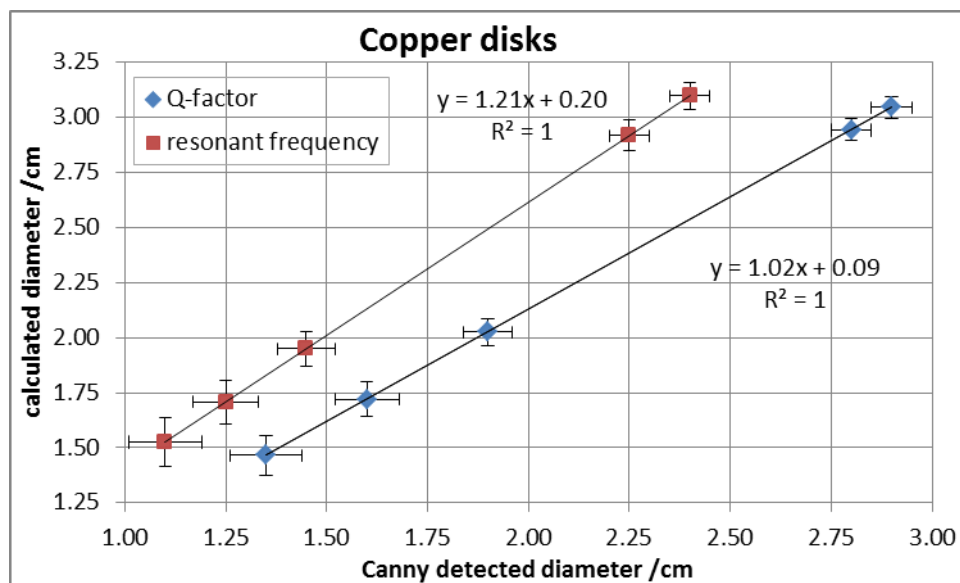


Fig. 5.18. Diameter of copper disks calculated by means of relations derived from the linear fits shown in Fig. 5.15, plotted against the diameter estimated by using the Canny edge detection algorithm. Note that the x-axis-values of these graphs are the y-axis-values in Figs. 5.16-5.17.

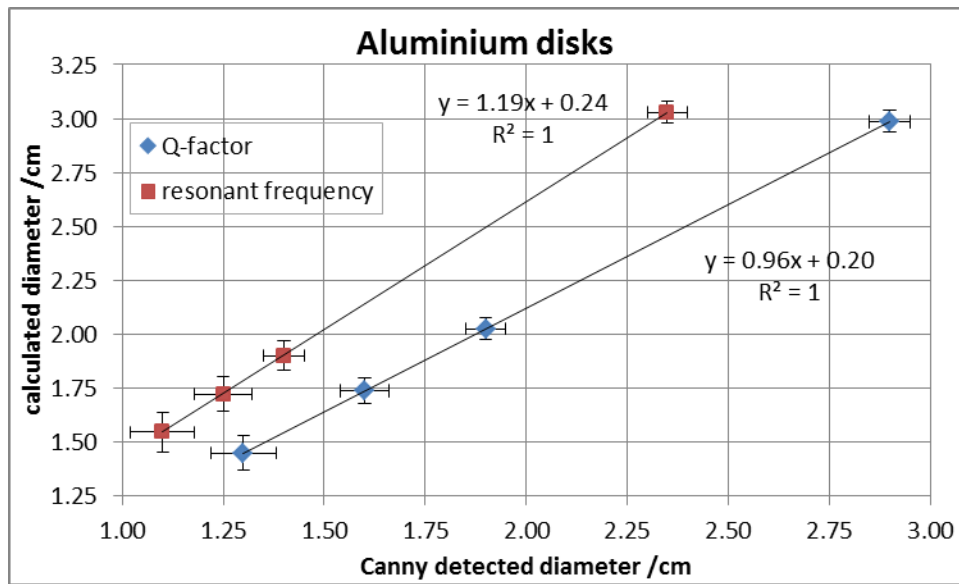


Fig. 5.19. Diameter of aluminium disks calculated by means of relations derived from the linear fits shown in Fig. 5.15, plotted against the diameter estimated by using the Canny edge detection algorithm. Note that the x-axis-values of these graphs are the y-axis-values in Figs. 5.16-5.17.

Results shown in Figs. 5.18-5.19 showed the goodness of fits obtained when the diameter of imaged disks was calculated by using Eqs. 5.5 and 5.6 (“calculated diameter” was named  $D_t$  in the equations) vs the diameter produced by applying the Canny edge detection algorithm (“Canny edge detected diameter”, named “ $D_e$ ” in the equations).

To summarise and conclude, the edge detection process was applied to the data acquired with both resonant-frequency and Q-factor imaging techniques, in order to evaluate and compare the whole system’s imaging capability. In particular, the capability of estimating the samples’ shape and size by using these two imaging techniques was assessed. The goal of this experiment was to determine the contours of the samples imaged as described in Sections 5.2-5.3. These “estimated” contours were related to the tabulated contours to the ‘actual’ samples.

Results demonstrated that formulae derived by using linear fits of data sets where the estimated Canny edge diameter was plotted vs the one of the actual sample, represented a valid tool for estimating the sample’s diameter by means of the Canny-edge detected diameter.

## 5.5 LCR circuit optimization

The imaging method, based on position-resolved measurements of the resonant frequency and the Q-factor and proposed in Sections 4.1-4.2, was proved to be suitable for imaging of samples having different values of conductivities. The next step of the process was optimising it. For this purpose, the EII system was firstly modified by adding variable resistor and capacitor decade boxes, as detailed in Section 4.3. This was done due to the dependence of the measured quantities, i.e., resonant frequency and Q-factor, from the circuit's components and the dependence of the skin depth on the circuit's capacitance (Eqs. 2.12, 2.13, 2.16). The purpose of this investigation was to increase the measurement sensitivity of the EII imaging system. In particular, the aim was to increase the Q-factor of the LCR circuit constituting the system, in order for it to acquire higher selectivity. As mentioned earlier, higher values of Q meant sharper resonance peaks and thus implied the possibility to differentiate between similar resonances. The dependence of Q on the circuit's inductance, resistance and capacitance (Eq. 2.12) led to assuming that higher Q-factor values could be obtained by changing two of these quantities (C and R), as will be detailed in the following paragraphs.

The purpose of this experiment was relevant for the research goal of distinguishing between materials of different nature that had similar values of conductivity and thus produced similar changes in the measured quantities ( $f_r$  and  $Q$ ). Increasing the system resonant frequency selectivity was also important to enable imaging of low-conductivity samples, in which small amounts of eddy currents were induced, thus producing small changes in the measured quantities with respect to the background values.

### 5.5.1 Description of the experimental procedure

An experiment was carried out with the purpose of varying the resistance and capacitance of the LCR circuit, in order to adjust the Q-factor and resonant frequency, according to Eqs. 4.2 and 4.3. The aim was to increase the Q-factor in order for the circuit to acquire higher selectivity, and make it possible to differentiate between similar values of resonant frequency. The question of why only the capacitance and resistance values were set as variables in this experiment might arise when one considers the dependence of the Q-factor on inductance as well as on capacitance and resistance. The reason for this decision was that the promising results obtained with the ferrite-cored coil (Sections 5.1-5.4) suggested that this inductor should be kept for the future measurements. Therefore, L was kept constant and the only quantities which were varied, in order to vary Q, were C and R.

The experiment was based on building eight parallel LCR circuits, like the one shown in Fig. 4.6, by selecting different combinations of resistance and capacitance, in order to vary the values of  $f_r$  and Q of the system, as predicted by Eqs. 4.2 and 4.3. The LCR circuits that were built are labelled with numbers I-VIII in column 1 of Tab. 5.3, and the corresponding combinations of resistors and capacitors are reported in columns 2 and 3 of the table. For each of them, measurements of resonant frequency and Q-factor were undertaken with a 25x25x1 mm<sup>3</sup> Al sample, which was placed under the ferrite-cored coil at a lift-off  $L=(1.0\pm0.1)$  cm.

Tab. 5.3. Values of resistance (second column) and capacitance (third column) that were chosen to build eight different LCR circuits (labelled with numbers I-VIII reported in the first column of this table).

LCR circuit number	Resistor value (uncertainties= ±1%)	C (μF, uncertainties= ±1%)	RC (s)
I	(3.000 ± 0.001) KΩ	2.0	0.006
II	(3.000 ± 0.001) KΩ	3.0	0.009
III	(3.000 ± 0.001) KΩ	5.0	0.015
IV	(1.000 ± 0.001) MΩ	2.0	2
V	(1.000 ± 0.001) MΩ	3.0	3
VI	(1.000 ± 0.001) MΩ	5.0	5
VII	(2.000 ± 0.001) MΩ	0.5	1
VIII	(4.000 ± 0.001) MΩ	1.0	4

Aluminium was chosen as it is a highly conductive material which produced optimal results when the procedure adopted before and shown in Sections 4.2 and 4.3 was used to image it. This experiment involved setting up an experimental EII system where each time the LCR circuit was one of the 8 LCR circuits with components values as reported in Tab. 5.3, wired as in Fig. 4.6. The choice for the specified value of lift-off was justified by it having produced a change in the resonant frequency and Q-factor that was higher than the one obtained with larger lift-off values (Section 5.1.2).

Eqs. 5.9 and 5.10 were used to calculate the resonant frequency and Q-factor change obtained with each of the LCR circuits listed in Tab. 5.3. In this way, the “optimal” circuit was found, as the one which caused the greatest change in the measured quantities to occur:

$$\Delta f_r = \frac{f(\text{sample}) - f(\text{background})}{f(\text{background})} (\%) \quad (5.9)$$

$$\Delta Q = \frac{Q(\text{sample}) - Q(\text{background})}{Q(\text{background})} (\%) . \quad (5.10)$$

In these equations,  $f(\text{background})$  and  $Q(\text{background})$  represent values measured for each LCR circuit when this was in air (i.e., in the absence of the sample), and  $f(\text{sample})$  and  $Q(\text{sample})$  resulted from measurements taken with the same circuit after placing a 25x25x1 mm<sup>3</sup> Al sample under the coil, at a lift-off  $L=(1.0\pm 0.1)$  cm.

## 5.5.2 Results and discussion

This investigation aimed at finding the optimal LCR circuit, defined as the circuit which caused the greatest change in the measured quantities  $\Delta f_r$  and  $\Delta Q$ , occurring when a  $25 \times 25 \times 1 \text{ mm}^3$  aluminium sample was inductively coupled to the system.

Results of the LCR circuit optimisation study are summarised here. Figs. 5.20-5.21 show the relative change in resonant frequency and Q-factor obtained by means of Eqs. 5.9 and 5.10, plotted against the measured Q-factor of each of the 8 LCR circuits listed in Tab. 5.3.

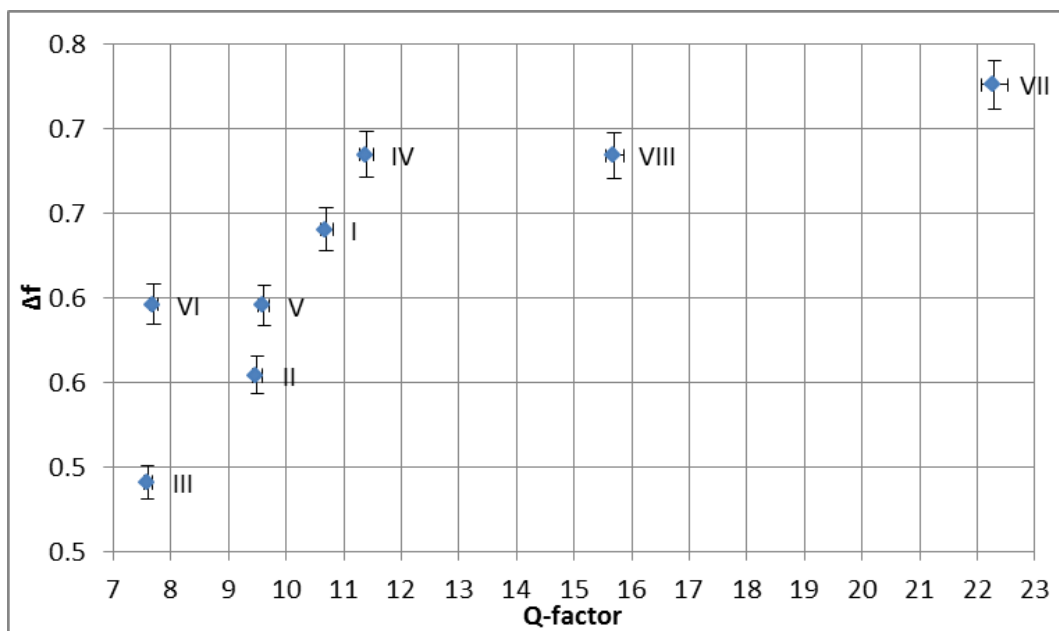


Fig. 5.20. Relative change of resonant frequency (Eq. 5.1), produced by a  $25 \times 25 \times 1 \text{ mm}^3$  Al sample for the 8 LCR circuits listed in Tab. 5.3, having values of Q-factor ranging from 7.6 to 22.3.

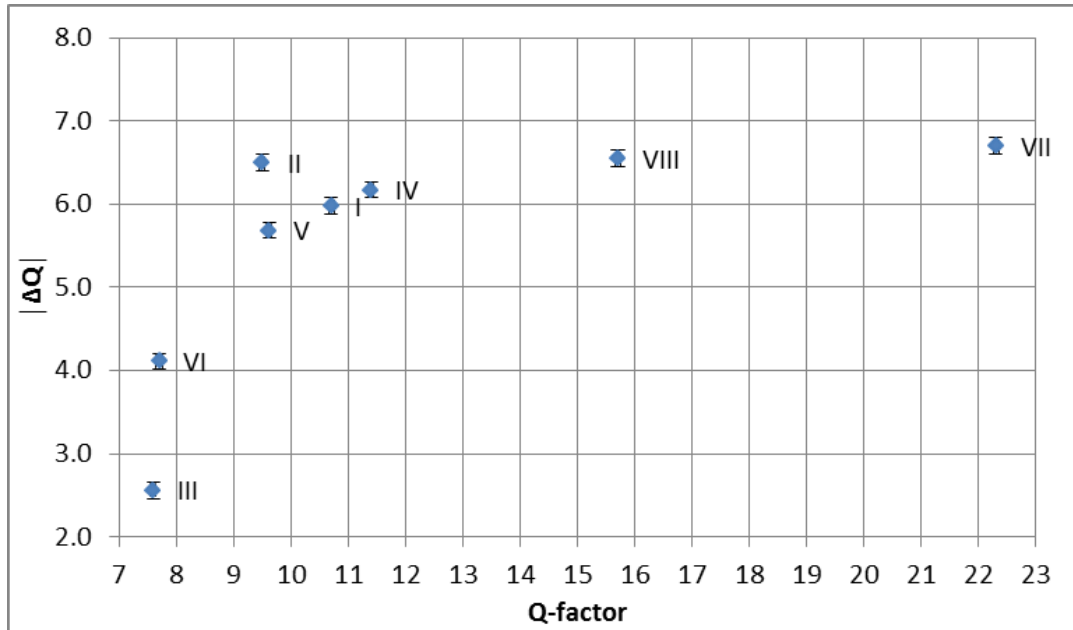


Fig. 5.21. Relative change of Q-factor (absolute value of  $\Delta Q$  in Eq. 5.2), produced by a 25x25x1 mm<sup>3</sup> Al sample for the 8 LCR circuits listed in Tab. 5.3, which had values of Q-factor ranging between 7.6 and 22.3.

Figs. 5.20 and 5.21 show that both the change in resonant frequency and the change in Q-factor increased with the Q-factor of the circuit. Choice of an appropriate combination of L, C and R, as detailed in rows of Tab. 5.3 corresponding to circuits “IV, VII, VIII” (R=1 M $\Omega$ , 2 M $\Omega$ , 4 M $\Omega$ ), provided a maximum change in the measured quantities, which was nearly equal to 6.7% for the Q-factor and was about 0.73% for the resonant frequency. This consideration justified the study which was undertaken, proving that there was a dependence of the changes in the measured quantities on the Q-factor of the system.

Results shown in Fig. 5.20 highlighted that values of  $C > 2 \mu\text{F}$  led to smaller changes of resonant frequency, and the optimal situation occurred when  $C=0.5 \mu\text{F}$  (circuit “VII”), although measurement uncertainties made the values of  $C=2 \mu\text{F}$  equivalent to  $C=0.5 \mu\text{F}$  (circuits “IV, VIII”), as the three data points found on the right of the graph (higher values of Q on the axis) did not differ significantly from each other, considering their error bars. This result was in agreement with the results shown in Sections 5.1-5.3, where C was assigned values lower than 2  $\mu\text{F}$ , i.e.,  $C=0.5 \mu\text{F}$  and  $C=1 \mu\text{F}$ . Findings shown in Figs. 5.20 and 5.21 demonstrated that results reported in previous sections were obtained in the optimal range of Q-factor, as given by the values on the x axis of Figs. 5.20-5.21. Modifying the resistance

values, as was done for the circuits on the left hand side of the graph of Fig. 5.20 (labelled “III, VI, II, V, I” and having Q-factor values  $Q < 11$ ), was not effective in improving the resonant frequency change, which was smaller than the one obtained for circuits “IV, VII, VIII”, in which the larger R values (1 M $\Omega$ , 2 M $\Omega$ , 4 M $\Omega$ ) made Q larger too (Q is proportional to R, as shown by Eq. 4.2). Trends shown in both Figs. 5.20 and 5.21 revealed an increase in the change of the resonant frequency and Q-factor with the circuit’s Q-factor, with a decreased rate of change with increasing Q.

An interesting observation could be made by looking at Fig. 5.21: the Q-factor change became small for Q-factor circuits having values of  $Q > 16$  (the curve’s gradient approached zero). This behaviour was less pronounced when resonant frequency change was taken into account (Fig. 5.20). The Q-factor trend could be a useful tool for the imaging experiments carried out in this research work, because it meant that increasing Q up to values higher than 16 was not necessary to accomplish a larger change in the measured quantities, i.e., resonant frequency and Q-factor.

The explanation for these findings is backed up by the following theoretical considerations about LCR circuits’ behaviour.

Firstly, the circuit impedance  $R'$  ( $R' \neq R$ ), given by Eq. (5.11) (derived by taking the modulus of the impedance expression as in Eq. 4.1), decreases when the capacitance C is increased:

$$R' = \frac{R}{1 - jR\left(\frac{1}{X_C} + \frac{1}{X_L}\right)} = \frac{R}{1 + jR\left(\omega C - \frac{1}{\omega L}\right)} \quad (5.11)$$

Secondly, the way in which Q increases with C is given by  $Q \sim \sqrt{C}$  (Eq. 4.2). On the other hand, the dependence of Q on  $R'$  is given by  $Q \sim R'$  (Eq. 4.2, where R is substituted by  $R'$ , since it is the impedance, and not just the resistance, which needs to be taken into account). As the change of Q per unit change of  $R'$  is larger than the change of Q per unit change of C ( $Q \sim R'$  vs  $Q \sim \sqrt{C}$ ), the net effect is an increase of Q with  $R'$ . Moreover, when C is increased, the resulting decrease of  $R'$  (Eq. 5.11) leads to the decrease of Q.

The considerations above mean that the only solution to the initial goal of increasing the selectivity of the EII system by increasing its Q-factor, had to be a trade-off between increasing Q and increasing C, to achieve both higher selectivity for the system and capability

to penetrate through shielding materials. The latter objective led to the requirement for a higher C when increasing the skin depth was necessary, which was the case when imaging of shielded conductive samples was required. Optimising the Q-factor change by making it as large as possible to allow low-conductivity samples to be imaged and samples of different conductivity values to be distinguished was a goal already mentioned in Section 5.3.

According to the aim of optimising the Q-factor change on the one hand, and the experimental results shown in Fig. 5.21 on the other hand, the following conclusion can be drawn: increasing Q to a value larger than 16 was not necessary, and satisfactory change in the measured quantity could be obtained for  $9.5 < Q < 16$ , as can be seen by looking at the graph in Fig. 5.21. Due to this conclusion, values of R equal to 1, 2 and 4 M $\Omega$  and values of C between 0.5 and 2  $\mu$ F were established to be optimal choices of components for creating LCR parallel circuits suitable to accomplish EII of conductive samples.

## 5.6 Resolution study

A resolution study was undertaken by imaging 8 Al disks (2-mm-thickness) having values of diameter listed in Tab. 5.4. The procedure described in Chapter 4 was used and the LCR circuit assigned the following values:  $L=680\pm 10\% \mu$ H,  $R=1\pm 1\% \text{ M}\Omega$ ,  $C=1 \mu$ F. The aim of this experiment was to determine the system resolution for imaging of aluminium disks, defined as the minimum-diameter disk which gave a Canny edge detected diameter distinguishable from the nearest diameter disk of the same type.

### 5.6.1 Description of the experimental procedure

2D images were produced for the samples listed in Tab. 5.4 and their diameter were estimated by using the Canny edge detection method detailed in Section 5.4.

Tab. 5.4. Diameter values (cm) of the eight different Al disks which were used for the resolution study aiming at identifying the minimum-diameter-disk that could be imaged.

<b>Disk number</b>	<b>Disk diameter (mm, uncertainty <math>\pm 0.5</math>)</b>
1	15.0
2	17.0
3	20.0
4	30.0
5	40.0
6	50.0
7	60.0
8	76.0

Position-resolved measurements of both the resonant frequency and the Q-factor were performed to create the images. Canny edge detected diameters obtained for both series of images were compared with diameters of the actual sample, to establish the limits for imaging in terms of the EII system's resolution. Aluminium was chosen as it is a highly conductive sample which produced optimal results when the Canny edge detection algorithm was used to find the image contours and establish the dimensions of the samples (Section 5.4).

### 5.6.2 Results and discussion

Values of the “estimated diameter”, obtained by applying the Canny edge detection method to the images obtained by means of position-resolved measurements of resonant frequency and the Q-factor, were plotted against the “measured diameter” of actual samples. The trend was found to be linear, as found in previous data (Section 5.4), and showed very good agreement between values estimated with the Canny-edge detection technique and values measured with a ruler ( $R^2$  nearly equal to 1, in Fig. 5.22). This confirmed the conclusions of the study reported in Section 5.4 and reinforced them, thanks to the higher number of data.

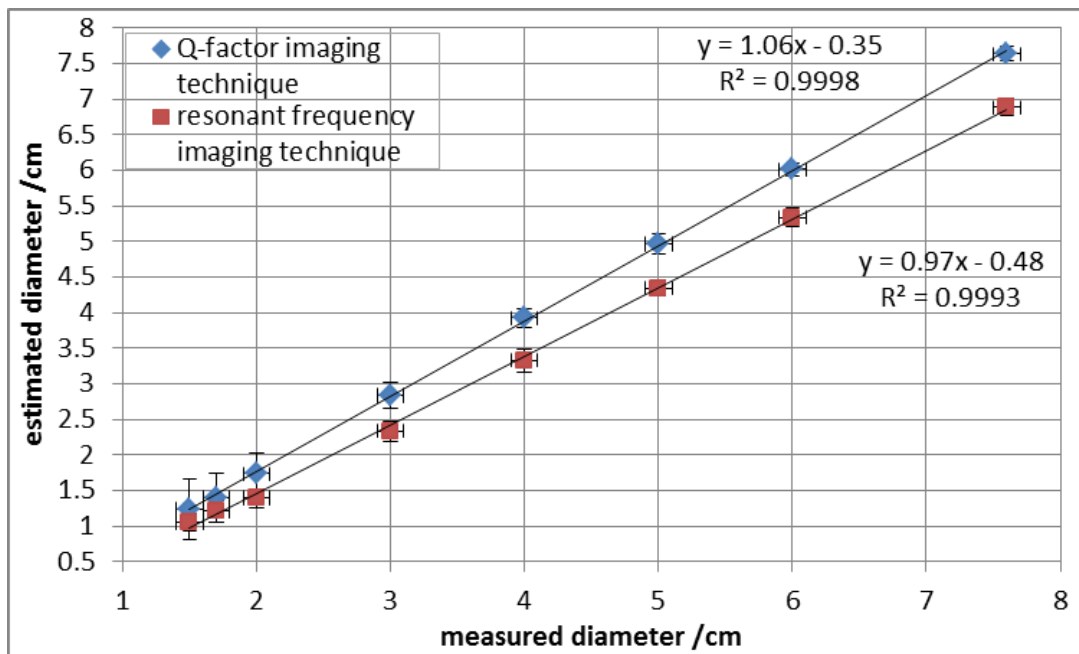


Fig. 5.22. Estimated diameter (obtained by applying the Canny edge detection algorithm) plotted against measured diameter of actual samples, obtained for a set of aluminium disks of different diameter (from 1.5 cm to 7.6 cm).

The ratio  $r$  between “measured” and “estimated” diameter was also plotted against the measured diameter in Fig. 5.23. The trend showed that the Q-factor imaging technique allowed an accurate estimate of the sample dimensions (ratio  $r \approx 1$ ) for disks having diameter  $d > 4$  cm. Diameters of disks within this range were underestimated when the resonant-frequency imaging technique was used (ratio  $r$  between 1.2 and 1.1).

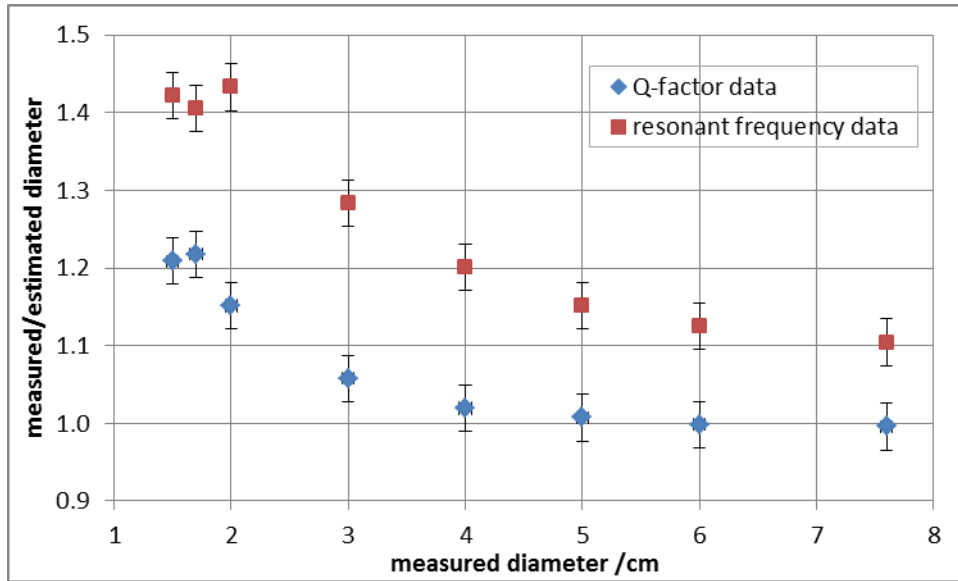


Fig. 5.23. Ratio between measured and estimated diameter (measured for the actual samples and estimated using the Canny edge detection algorithm, respectively) plotted against measured diameter of aluminium disks.

Moreover, uncertainties of the estimated diameter (calculated by means of standard deviation of Canny-edge-detected values, as explained in Section 5.4) were found to be decreasing with increasing diameters for Q-factor data, for disks having diameters  $d < 4$  cm (st. dev.  $\sim 0.1-0.4$ ), whereas uncertainties in resonant-frequency data were steady at all diameter values (st. dev.  $\sim 0.1$ ) (see error bars in plots of Fig. 5.22). This highlighted a larger spread of Q-factor measurement values with respect to the one obtained with resonant-frequency measurement values, for disks having smaller diameters.

Results of the resolution study clearly showed that the resolution of the system was lower than 1.5 cm (Fig. 5.22). Further work will be needed in order to assign a value to such resolution limit. A hypothesis was made about this limit, which would be equal to the coil diameter, also according to results reported in [74]. This is because the sample edges produce discontinuities in the electromagnetic field induced inside and around the sample, which behave in a similar way w.r.t. eddy current propagation, to cracks present in samples that are detected with eddy current testing techniques. Probes used for this purpose are generally designed such that their sensitive area has dimensions comparable to the dimensions of the cracks, which is required to identify and detect cracks, in a similar way to what has been done

in this work, where identifying edges allowed imaging samples by means of the discontinuity between regions within the metal bulk and surrounding regions acting as a dielectric (air) [24].

Results reported in this section validated the reliability of the imaging system for unscreened conductive target objects.

## 6 Penetrating power of the LCR system

This chapter focuses on experimental investigations aimed at testing whether the LCR-based EII system and method proposed in Sections 4.2-4.3 could be used to image conductive targets hidden behind a conductive shield. Theoretical considerations about the way in which such system could be successful for this purpose were given in Section 2.2. To summarize them, the external capacitance of the LCR circuit could be adjusted such that the eddy currents were allowed to penetrate through the conductive screen and reach the target to be imaged.

The chapter is divided into two parts. Section 6.1 reports on experimental method and relevant results about 2D imaging of unshielded conductive targets, and acts as a bridge between Chapters 5 and 6. Section 6.2 includes description, results and discussion of experimental investigations involving 2D imaging of shielded conductive targets.

### 6.1 Summary about 2D imaging of unshielded conductive targets

The imaging capabilities of the EII system based on a parallel LCR circuit (Section 4.3) were first investigated for unshielded samples, i.e. without any conductive material in the shape of a sheet covering it. A simplified sketch of the experimental configuration used for this purpose was shown in Fig. 3.6 and a representation including the LCR system is reported in Fig. 6.1 below. Chapter 5 described several experimental investigations carried out with unshielded samples and included results and discussion. This section is a summary of the work done and includes some observations that will be used to highlight differences between the behaviour of the same LCR-based EII system, when this was used to image unshielded metals, compared to when a conductive shield, covering the conductive target, was introduced into the system (see Section 6.2).

The magnetic coupling of a conductive target object with the inductor, which was part of the LCR circuit, led to a change of the circuit characteristics (L and R), and in particular of the system's resonant frequency and Q-factor (Section 2.1). These were the physical

properties being monitored during the experiments. Sections 5.2-5.3 demonstrated that an image representing the target could be generated by performing position-resolved-measurements of the resonant frequency and the Q-factor, obtained by displacing the object with respect to the inductor, by using a computer-controlled XY stage. For each position, the system resonant frequency and the Q-factor were measured with the Precision Impedance Analyzer 6500B (Wayne Kerr) (Section 4.2). The description of the experimental apparatus was detailed in Section 4.3.

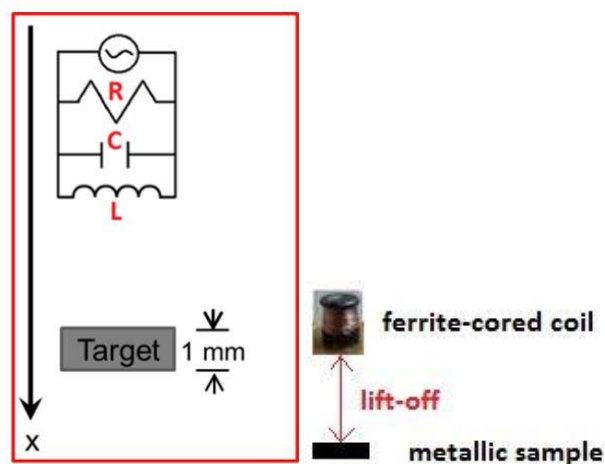


Fig. 6.1. Left: sketch representing the LCR parallel circuit used to image a conductive sample (labelled “target”) having rectangular cross section and volume equal to  $25 \times 25 \times 1 \text{ mm}^3$ . The x axis is included to show the distance between the coil and the target (lift-off). Right: Sketch representing the lift-off used in the configuration shown on the left of the figure. The ferrite-cored coil (made by “multicomp”, part no. MCSCH895-681 KU) is part of the LCR circuit shown on the left side of the figure (the labels “metallic sample” and “target” both refer to the sample object).

Typical results of resonant frequency and Q-factor position-resolved-measurements, in the form of 2D plots, are shown in Figs. 6.2-6.3 for a conductive, non-magnetic sample of large conductivity (copper,  $\sigma=59.77 \text{ MSm}^{-1}$  [66]), and in Figs. 6.4-6.7 for a low-conductivity sample, made of manganese ( $\sigma=0.54 \text{ MSm}^{-1}$ [66]). The LCR circuit used was the one represented in Fig. 6.1 with component values as follows:  $L=680 \pm 10\% \mu\text{H}$ ,  $R=1 \pm 1\% \text{ M}\Omega$ . The capacitance values used in this experiment were assigned the following values:  $C_1=11 \mu\text{F}$  (Figs. 6.2, 6.3, 6.6 and 6.7) and  $C_2=0.5 \mu\text{F}$  (Figs. 6.4 and 6.5), in order to investigate if the imaging capability of the system showed any dependence on the capacitance and, therefore, skin depth (Eq. 2.13).

Values of skin depth through copper and manganese, corresponding to each of the selected capacitance, were as follows:

- 1)  $C=11 \mu\text{F} \rightarrow \delta(\text{Cu}) = 2.6 \text{ mm}$  (Figs. 6.2 and 6.3);  $\delta(\text{Mn}) = 27.7 \text{ mm}$  (Figs. 6.6 and 6.7);
- 2)  $C=0.5 \mu\text{F} \rightarrow \delta(\text{Mn}) = 12.7 \text{ mm}$  (Figs. 6.4 and 6.5).

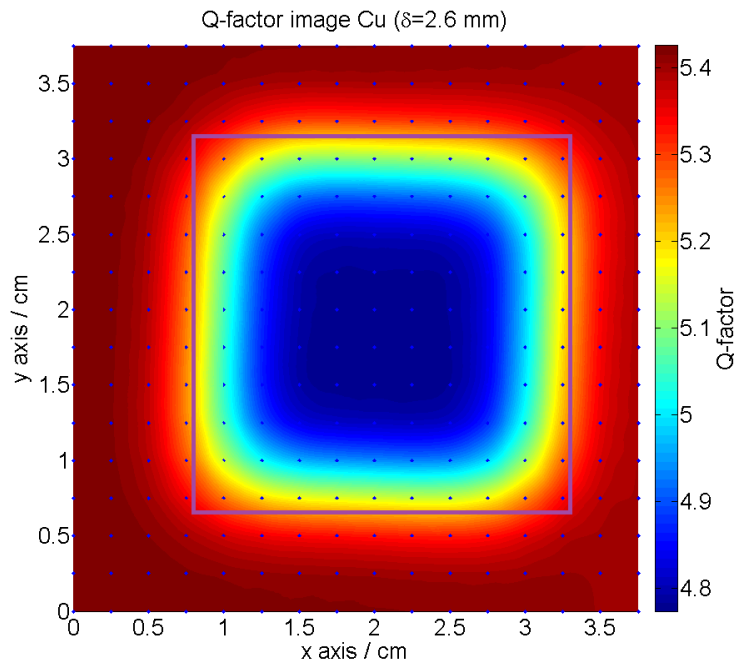


Fig. 6.2. Image of a copper sample ( $25 \times 25 \times 1 \text{ mm}^3$ ) obtained by means of position-resolved-measurements of the Q-factor. The system's capacitance was set to the value  $C=11 \mu\text{F}$ ; the corresponding skin depth in copper was equal to  $\delta=2.6 \text{ mm}$ . The data points in Figs. 6.2-6.7 represent the positions along the scanning area where the measurements were taken.

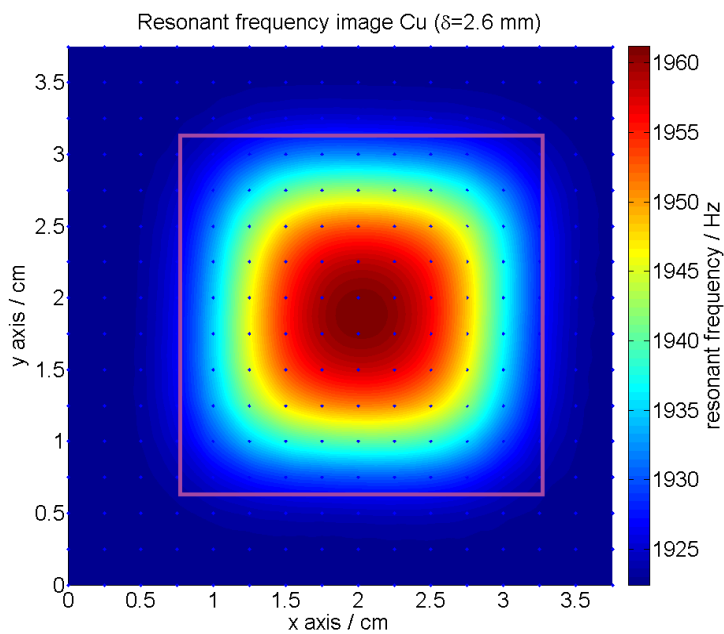


Fig. 6.3. Image of a copper sample ( $25 \times 25 \times 1 \text{ mm}^3$ ) obtained by means of position-resolved-measurements of the resonant frequency. The system's capacitance was set to the value  $C=11 \mu\text{F}$ ; the corresponding skin depth in copper was equal to  $\delta=2.6 \text{ mm}$ .

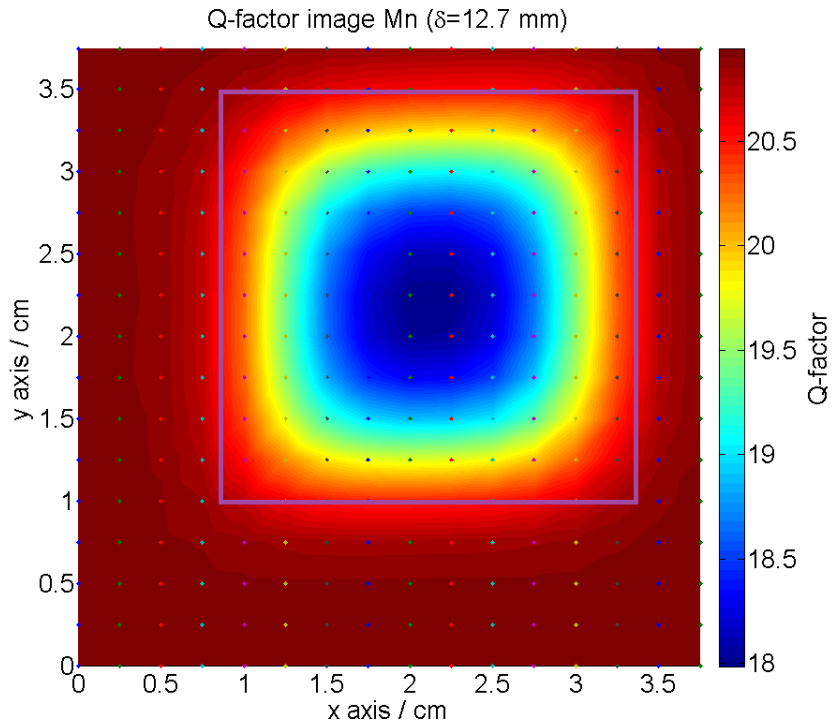


Fig. 6.4. Image of a manganese sample ( $25 \times 25 \times 1$  mm<sup>3</sup>), obtained by means of position-resolved-measurements of the Q-factor, with the system's capacitance set to the following value:  $C_1=0.5$   $\mu$ F; the corresponding skin depth was equal to  $\delta_1=12.7$  mm.

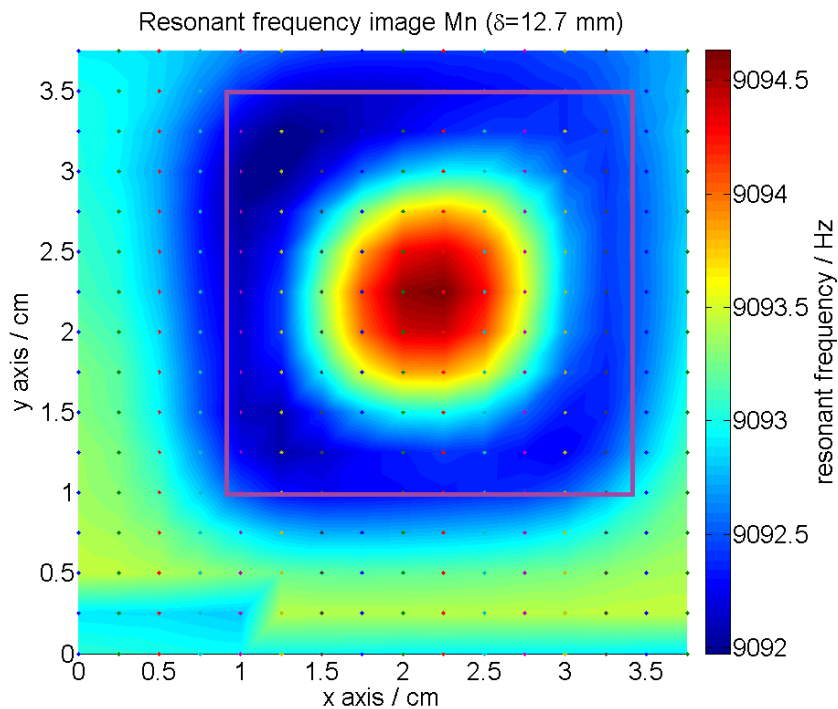


Fig. 6.5. Image of a manganese sample ( $25 \times 25 \times 1$  mm<sup>3</sup>), obtained by means of position-resolved-measurements of the resonant frequency, with the system's capacitance set to the following value:  $C_1=0.5$   $\mu$ F; the corresponding skin depth was equal to  $\delta_1=12.7$  mm.

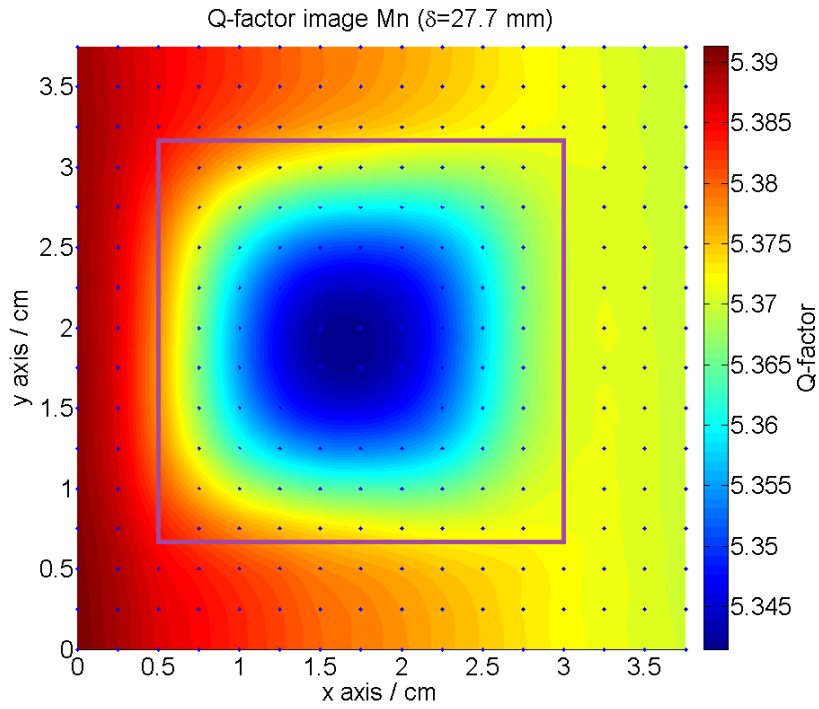


Fig. 6.6. Image of a manganese sample ( $25 \times 25 \times 1 \text{ mm}^3$ ), obtained by means of position-resolved-measurements of the Q-factor, with the system's capacitance set to the following value:  $C_2 = 11 \text{ } \mu\text{F}$ ; the corresponding skin depth was equal to  $\delta_2 = 27.7 \text{ mm}$ .

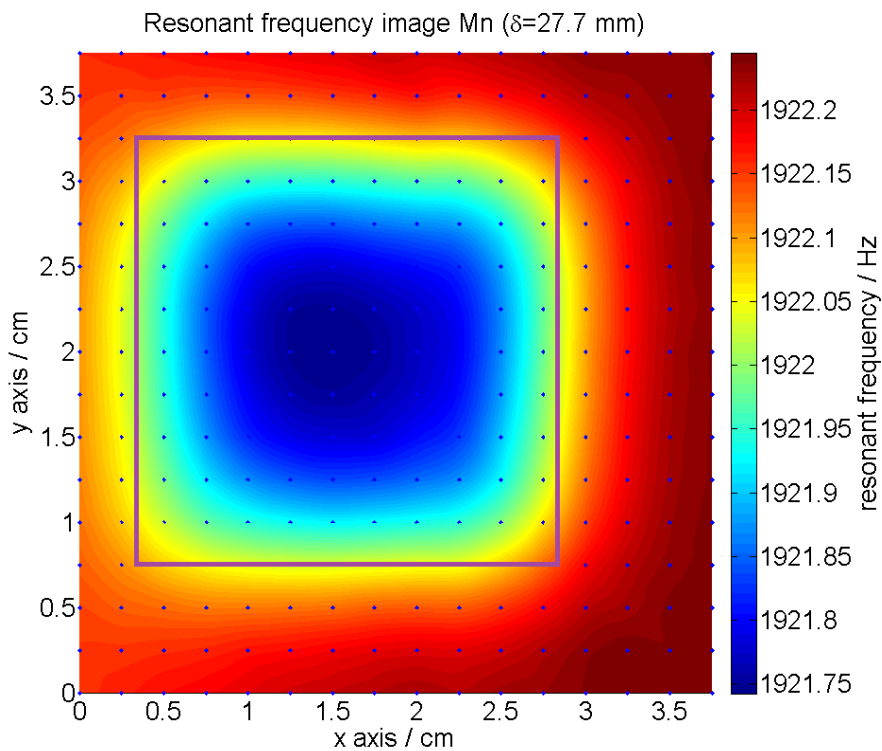


Fig. 6.7. Images of a manganese sample ( $25 \times 25 \times 1 \text{ mm}^3$ ), obtained by means of position-resolved-measurements of the resonant frequency, with the system's capacitance set to the following value:  $C_2 = 11 \text{ } \mu\text{F}$ ; the corresponding skin depth was equal to  $\delta_2 = 27.7 \text{ mm}$ .

Qualitatively, the images obtained showed the system's ability to reproduce samples' shapes by means of both resonant-frequency and Q-factor measurements (Figs. 6.2-6.7). This was the case when the capacitance of the system was assigned the specified values, and the skin depth was modified accordingly. The skin depth values were calculated by using Eqs. 2.13-2.16.

The resonant frequency of the system comprising the LCR circuit and the metallic sample was measured by placing the sample under the coil (vertically aligned to it, with lift-off equal to 1 cm), and was dependent on the capacitance set through the decade box (Eq. 2.16). The choice of lift-off is justified in Section 5.1. It was empirically determined as a compromise between the need to develop a contactless detection technique and the observed decrease, with lift-off, of the measured resonance frequency and Q-factor shifts, due to the presence of a highly conductive metal (aluminium).

Given the images reported above and the ones obtained by selecting other values of capacitance, with "unshielded" copper and manganese (Fig. 5.3 and Figs. 5.6-5.9, respectively), a conclusion could be drawn about the system's imaging capability. This was found to not be influenced by the chosen capacitance values, in the case of "unshielded metals", in the sense that the images showed the presence of the metals and allowed their identification, at all values of capacitance (and skin depth) used in the experiments. No dependence of the measured parameters (i.e., resonant frequency and Q-factor shifts) on eddy current penetration depth was observed with unshielded samples, since the shift of the measured quantities caused by the presence of the metal enabled to distinguish it from the 'background' corresponding to the situation when no metal was present. This is in contrast with what was occurred with samples shielded by conductive layers, as shown in the next section which highlights the dependence of the obtained images on the system's capacitance.

The images reported here were included to show that a 'signature' showing the presence of an unshielded conductive sample and reproducing its shape was resulting from the 2D imaging technique developed in this work. A more quantitative analysis of the images of unshielded samples was done by adopting a Canny edge detection method, as reported in Sections 5.4 and 5.6.

It is observed that images of higher-conductivity metals showed in Figs. 6.2-6.3 revealed more accurate reproduction of the samples' shapes and sizes, compared to the images of manganese reported in Figs. 6.4-6.7. This demonstrated the higher suitability of the proposed method for imaging of high-conductivity metals, due to the copper sample's edges being more well-defined (closer to 90 degrees) and its dimensions being more similar to the ones of the actual sample (between 22 mm and 25 mm  $\pm$  2 mm), compared to the more distorted manganese images (edge of the images varying between 20 and 28  $\pm$  2 mm). This behaviour was attributed to the larger change in the measured quantities (i.e., resonant frequency and Q-factor) that was produced by highly conductive metals, due to the larger magnitude of eddy currents induced inside them [46].

The images reported in this section and in Section 5.3 proved the suitability of the proposed method for imaging of high- and low-conductivity metals. On the other hand, the manganese images obtained with resonant frequency measurements at different values of skin depths ( $\delta=12.7$  mm and  $\delta=27.7$  mm) looked different (see Figs. 6.5 and 6.7). In particular, the sample's size was smaller in the image obtained with the lower skin depth ( $\delta=12.7$  mm, Fig. 6.5). This showed a dependence of the resonant frequency shift, due to the presence of this metal, on the penetration depth. Such dependence was justified by the smaller amount of eddy currents produced inside this metallic target, which made it more difficult to reveal its shape and size, despite the larger values of skin depth compared to the target's thickness (1 mm) [75].

## 6.2 Investigations on 2D imaging of shielded conductive targets

Once the system capability of imaging unshielded metallic samples was assessed, the penetrating power of the imaging system was investigated. The goal was to see whether imaging of conductive targets in the "shielded configuration" (as shown in Fig. 6.8) was possible, by varying the value of skin depth to allow penetration through the shield [75]. In this experimental investigation, a sheet of highly-conductive material, i.e. an aluminium shield having an area of  $A=(110.0\pm 0.5)\times(80.0\pm 0.5)\times(1.5\pm 0.5)$  mm<sup>3</sup>, was introduced between the target and the sensor (Fig. 6.8). The LCR circuit used was the one represented in Fig. 6.8 with

component values as follows:  $L=680\pm 10\%$   $\mu\text{H}$ ,  $R=1\pm 1\%$   $\text{M}\Omega$  and  $C=11$   $\mu\text{F}$ . This capacitance value was chosen in order for the skin depth through Al to be larger than the shield's thickness ( $\delta=3.3$  mm). Experimental results obtained in this part were compared to corresponding ones obtained without the shield, with the same values of circuit's components, as reported in Section 6.1. An imaging procedure like the one adopted for 2D imaging of unshielded conductive targets (described in Section 4.2) was applied to 2D imaging of conductive samples hidden behind 1.5-mm-thick Al shields. The experimental procedure is summarised in the following section. The main difference between this method and the one adopted before is that no normalisation was performed with the measured data, since normalising the values produced artifacts in the 2D surface plots obtained with shielded samples, whereas no issues were found when no normalisation was performed.

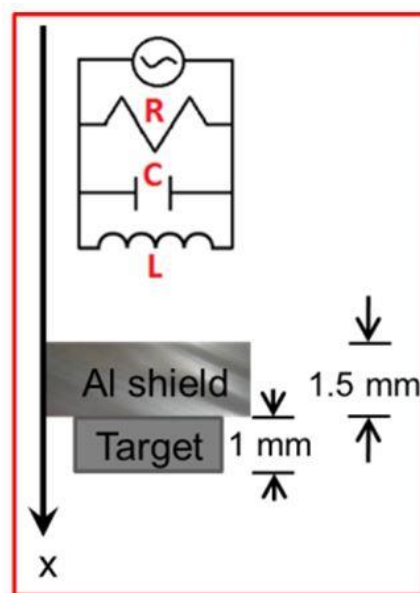


Fig. 6.8. Sketch representing the LCR parallel circuit used to image a conductive target, with rectangular cross section ( $25\times 25\times 1$   $\text{mm}^3$ ), hidden behind a conductive shield in the shape of a  $110.0\times 80.0\times 1.5$   $\text{mm}^3$  piece of Al. The x axis is included to show that the concept of lift-off changed from the scenario represented in Fig. 6.1, due to the presence of the Al shield.

### 6.2.1 Experimental method

Position-resolved-measurements of the resonant frequency were performed in the absence of the sample to be imaged, by moving the XY stage along an “n x n” scanning area (“background readings”). These acted as “control readings” and were acquired to verify that the “background data” obtained in the absence of the sample was uniform. The scanning area was shown in Fig. 3.8, which has been reproduced on the next page (Fig. 6.9). It was set to be larger than the area occupied by the samples to be imaged, to allow the samples’ dimensions to fit the plot area. Ten independent values of resonant frequency were acquired for each of the nodes of the grid represented in Fig. 6.9. Resonant frequency values were then acquired when the conductive sample was present, as described in the following. The sample was placed onto the xy stage, by using non-conductive materials of different thicknesses to lift it up and avoid contact between the sample and the sensor coil. The first ten independent readings were taken when the sample was in the position labelled as 1 in Fig. 6.9. After these readings were acquired, the sample was moved onto the next position (position 2 in Fig. 6.9) and the next ten independent readings were taken, using the impedance analyser. This procedure was repeated for all positions along the first row of the scan, and then for the next rows, until the entire scanning area was completed. A LabVIEW control program was written and the first part of it was run to initiate the instruments to be used and acquire measurements. Q-factor readings were also acquired in a similar fashion, by taking measurements first in the absence of the sample and then when the sample was present. Two matrices were thus obtained for each conductive sample, which contained values of the resonant frequency and the Q-factor, respectively. A third matrix was obtained containing the positional values covering the scanned area. After the first part of the LabVIEW structure was run, a second one executed a *Matlab* script which called the measurement matrices and concatenated them to create a 2D surface plot, by means of interpolation using a cubic piecewise fit. Specifically, the values in the resonant frequency matrix were plotted against the corresponding x and y coordinates and interpolated with a piecewise cubic function generated by *Matlab*. This was done to obtain 2D surface plots representing the imaged samples, as the ones shown in Section 6.1. Similarly, the values in the Q-factor matrix were plotted against the corresponding x and y coordinates and interpolated with a piecewise cubic

function generated by *Matlab*. This resulted in two images being produced for each conductive sample, resulting from the resonant frequency and Q-factor acquisitions respectively.

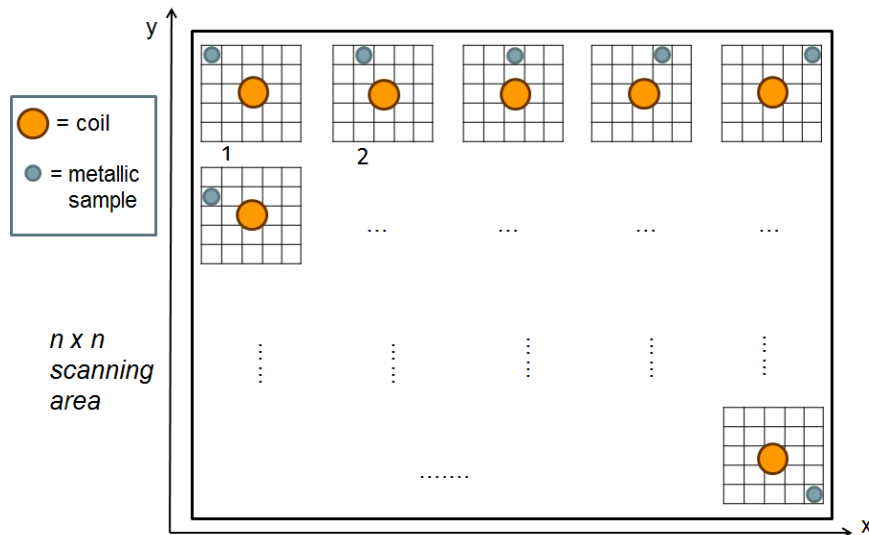


Fig. 6.9. Sketch representing the scanning area (“ $n \times n$ ” total positions, or nodes), where the coil (yellow circle) is maintained at a fixed position, and the metallic sample (light blue) is moved onto different positions, starting from “1”, going to “2”, tracing a horizontal path forming the first row of the scan, and then proceeding onto the next rows below.

Four sets of position-resolved-measurements of the resonant frequency and the Q-factor were performed, by adjusting the system capacitance to four different values, thus varying the skin depth  $\delta$  between 0.4 mm and 2.9 mm, as detailed in Tab. 6.1. Values of  $\delta$  were calculated by using Eqs. 2.13-2.16, with  $f_r$  values as in Tab. 6.1 and tabulated  $\sigma$  and  $\mu_r$  from [66]. The selected capacitance values caused the system to resonate at the values reported in Tab. 6.1, which were measured after placing a 25x25x1 mm<sup>3</sup> copper target, covered with the aluminium shield, under the coil, with lift-off equal to 0.5 cm.

Tab. 6.1. Capacitance values ( $C$ ), resonant frequency values ( $f_r$ )- measured at the centre of the shielded copper target- and corresponding skin depths in aluminium and copper, for each of the images shown in Figs. 6.10-6.17 (see next section).

Figure number	$C$	$f_r / \text{kHz}$	$\delta(\text{Al}) / \text{mm}$	$\delta(\text{Cu}) / \text{mm}$
6.10, 6.14	20 nF	144.2	0.4	0.3
6.11, 6.15	10 nF	66.7	0.6	0.4
6.12, 6.16	1 $\mu\text{F}$	6.6	1.8	2.1
6.13, 6.17	7 $\mu\text{F}$	2.5	2.9	2.3

## 6.2.2 Results and discussion

The images obtained with the copper target mentioned above for each capacitance value listed in Tab. 6.1 are shown in Figs. 6.10-6.17. Figs. 6.10- 6.13 show 2D surface plots obtained by means of Q-factor position-resolved-measurements, whereas Figs. 6.14-6.17 were obtained with resonant frequency measurements. It is worth noticing that Figs. 6.10 and 6.14 do not reveal the presence of the target, due to the skin depth being too low for the eddy currents to penetrate through the aluminium shield, thus preventing them to reach the target. In this case, the skin depth was much smaller than the thickness of the shield, being equal to  $\delta_1=0.4 \text{ mm} \ll 1.5 \text{ mm}$ . The target could be revealed, using both resonant frequency and Q-factor position-resolved-measurements, for a slightly larger skin depth, equal to  $\delta_2=0.6 \text{ mm}$  (Figs. 6.11 and 6.15), and smaller than the thickness of the shield. However, a greater skin depth, equal to  $\delta_3=1.8 \text{ mm}$ , was required to achieve more accurate reproduction of the target shape, when resonant frequency measurements were performed (Figs. 6.15 and 6.16), due to the lower sensitivity of the imaging technique based on resonant frequency measurements, compared to the one based on Q-factor measurements (p. 98).

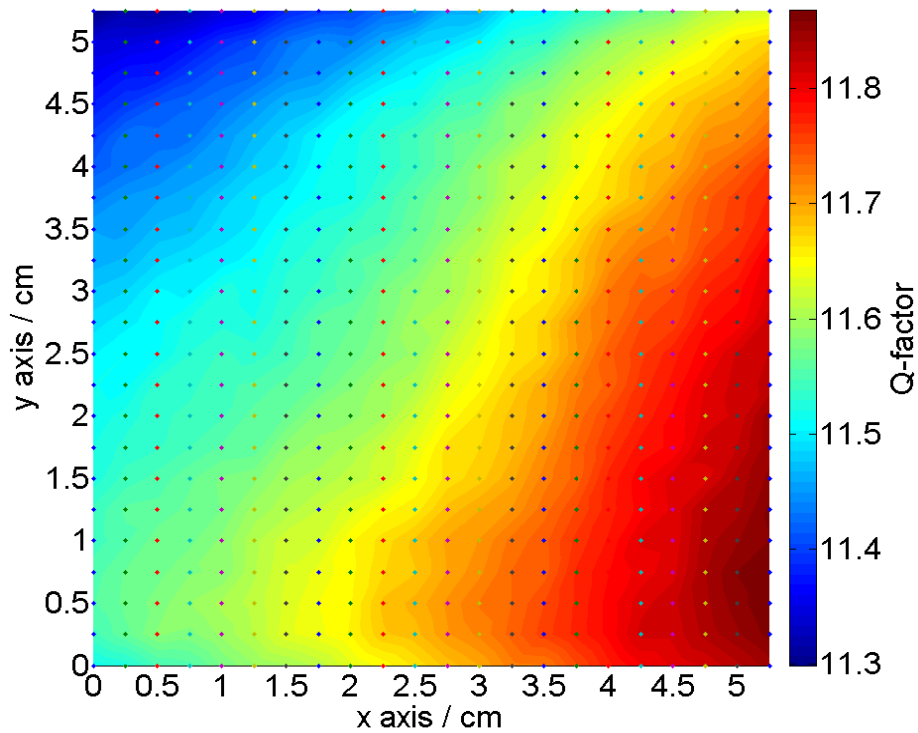


Fig. 6.10. Image of a copper target ( $25 \times 25 \times 1 \text{ mm}^3$ ) obtained by means of position-resolved-measurements of the Q-factor, at the following value of skin depth:  $\delta_1 = 0.4 \text{ mm}$ . During these measurements, the target was shielded by a 1.5-mm-thick aluminium sheet.

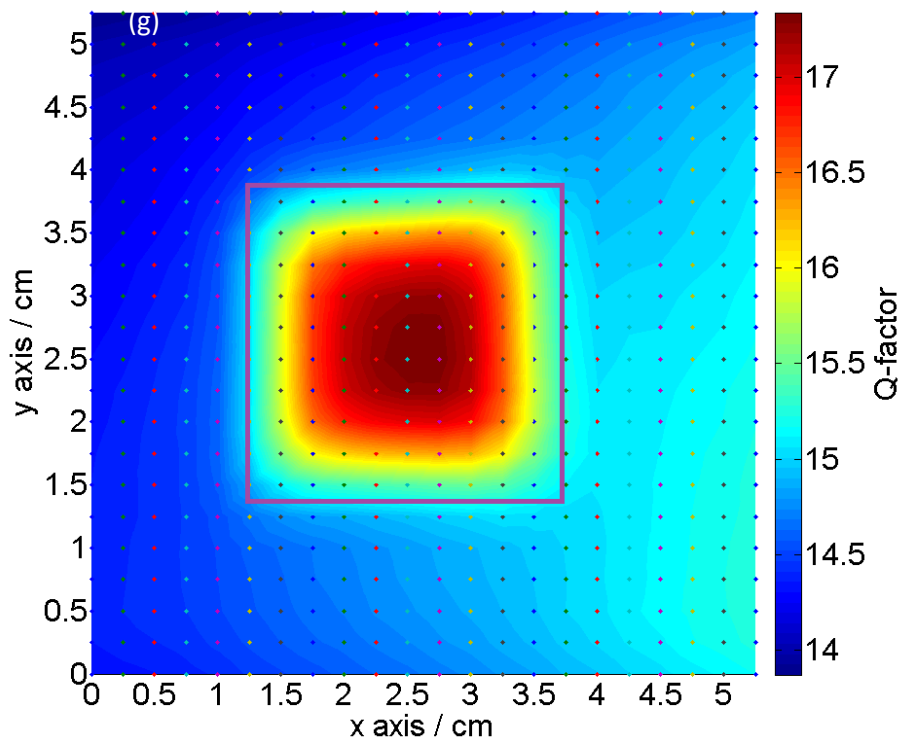


Fig. 6.11. Image of a copper target ( $25 \times 25 \times 1 \text{ mm}^3$ ) obtained by means of position-resolved-measurements of the Q-factor, at the following value of skin depth:  $\delta_2 = 0.6 \text{ mm}$ . During these measurements, the target was shielded by a 1.5-mm-thick aluminium sheet.

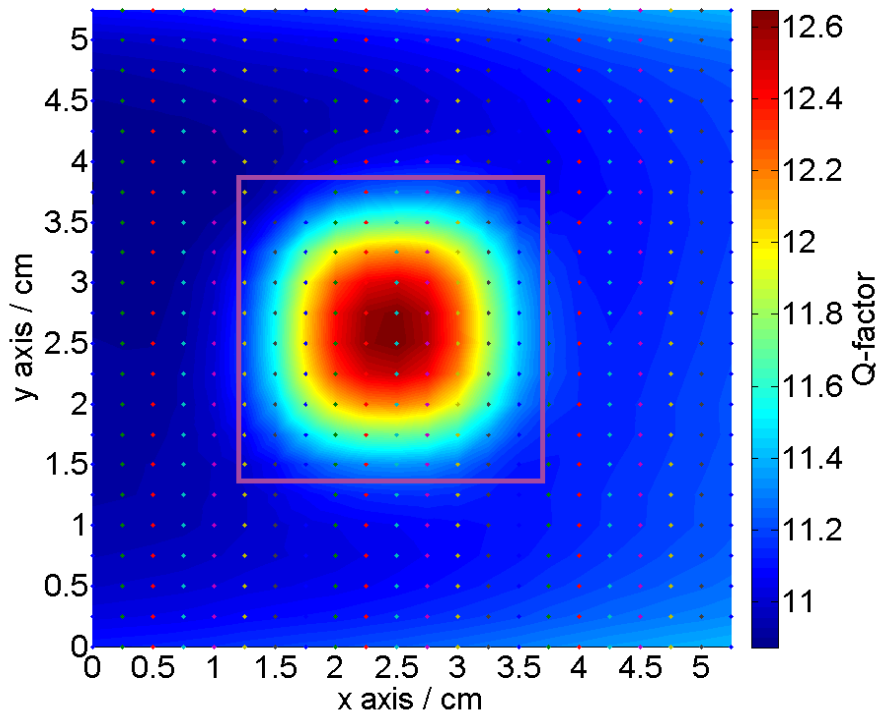


Fig. 6.12. Image of a copper target ( $25 \times 25 \times 1 \text{ mm}^3$ ) obtained by means of position-resolved-measurements of the Q-factor, at the following value of skin depth:  $\delta_3 = 1.8 \text{ mm}$ . During these measurements, the target was shielded by a 1.5-mm-thick aluminium sheet.

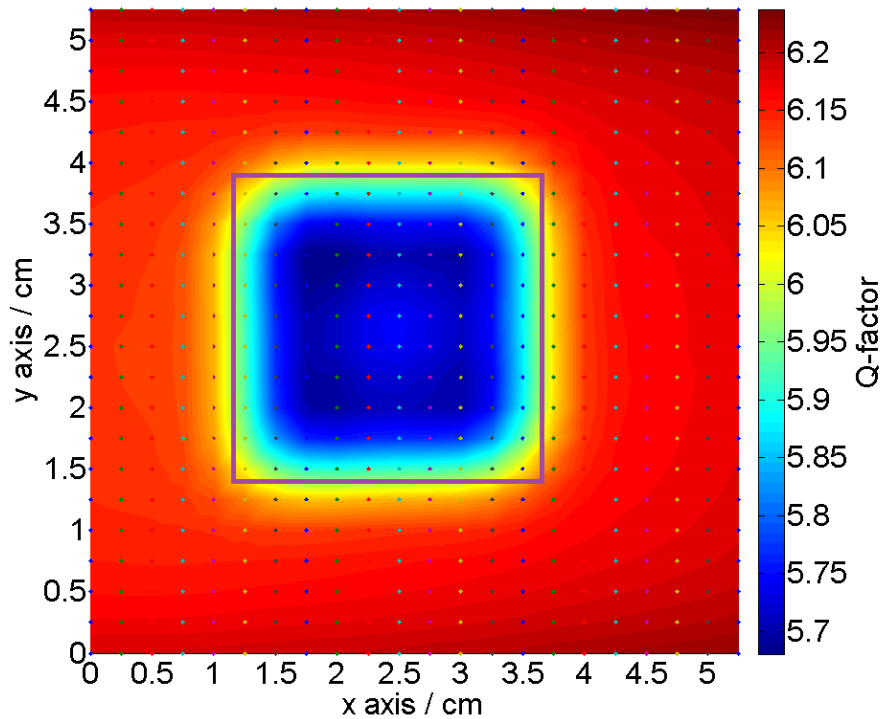


Fig. 6.13. Image of a copper target ( $25 \times 25 \times 1 \text{ mm}^3$ ) obtained by means of position-resolved-measurements of the Q-factor, at the following value of skin depth:  $\delta_4 = 2.9 \text{ mm}$ . During these measurements, the target was shielded by a 1.5-mm-thick aluminium sheet.

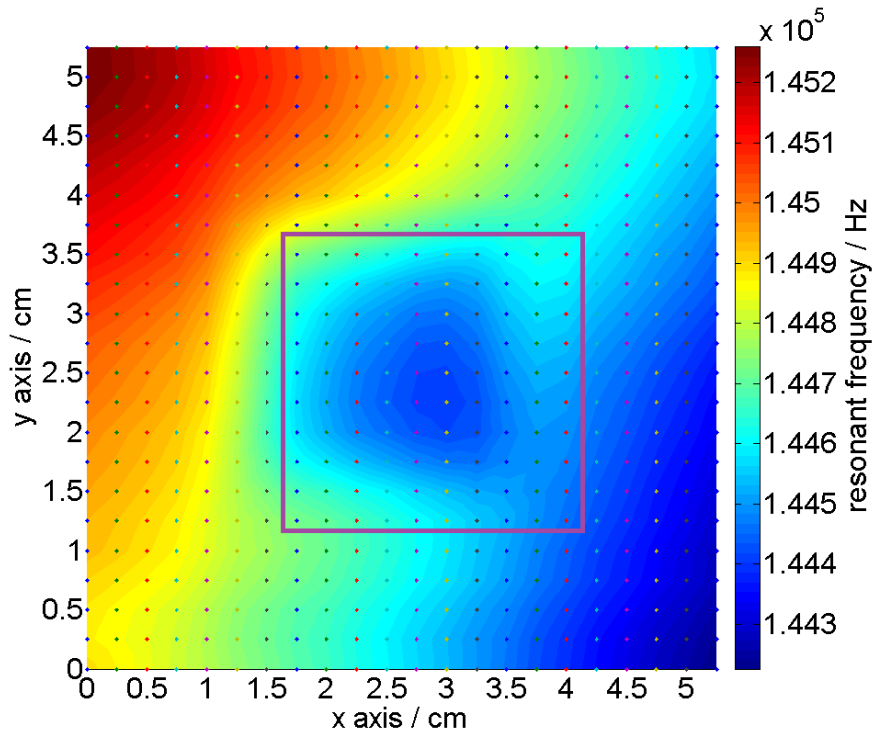


Fig. 6.14. Image of a copper target ( $25 \times 25 \times 1 \text{ mm}^3$ ) obtained by means of position-resolved-measurements of the resonant-frequency, at the following value of skin depth:  $\delta_1 = 0.4 \text{ mm}$ . During these measurements, the target was shielded by a 1.5-mm-thick aluminium sheet.

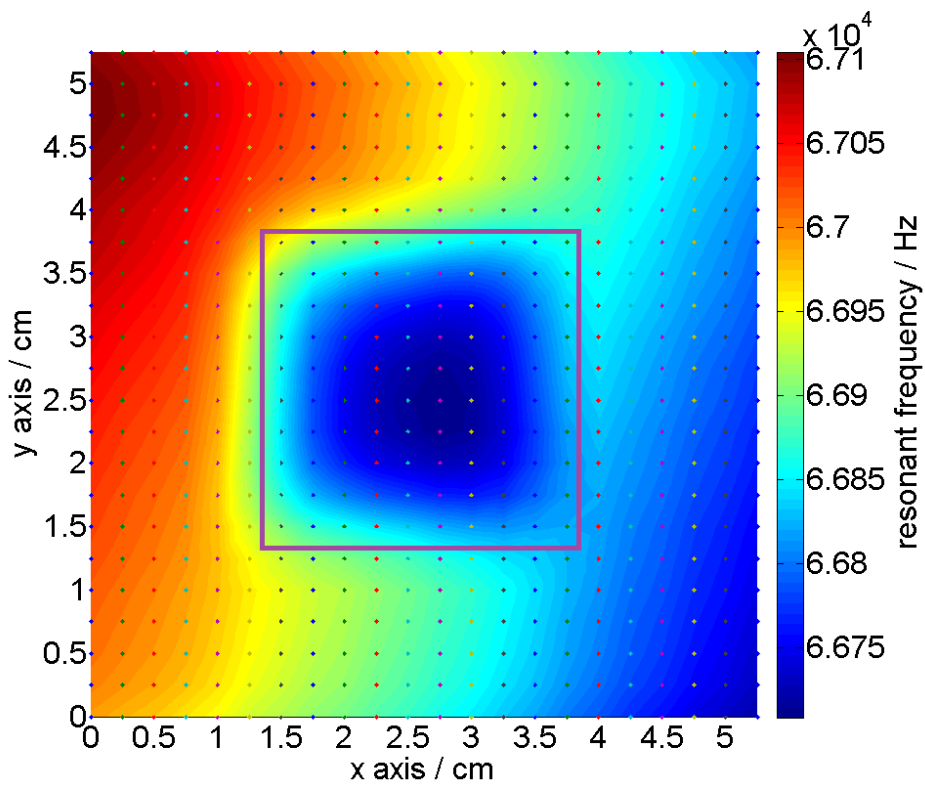


Fig. 6.15. Image of a copper target ( $25 \times 25 \times 1 \text{ mm}^3$ ) obtained by means of position-resolved-measurements of the resonant-frequency, at the following value of skin depth:  $\delta_2 = 0.6 \text{ mm}$ . During these measurements, the target was shielded by a 1.5-mm-thick aluminium sheet.

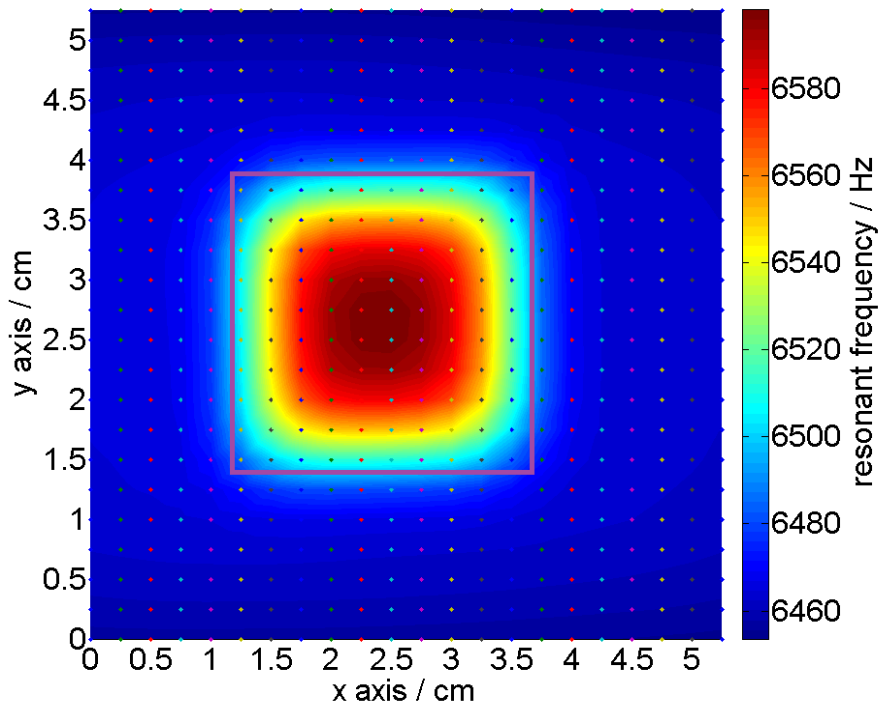


Fig. 6.16. Image of a copper target ( $25 \times 25 \times 1 \text{ mm}^3$ ) obtained by means of position-resolved-measurements of the resonant-frequency, at the following value of skin depth:  $\delta_3 = 1.8 \text{ mm}$ . During these measurements, the target was shielded by a 1.5-mm-thick aluminium sheet.

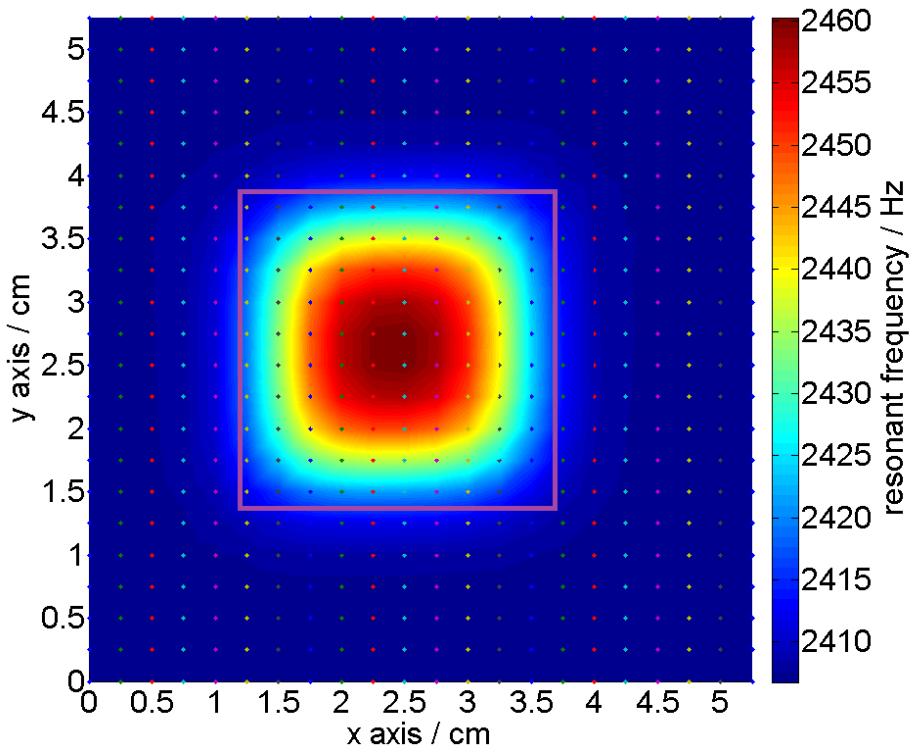


Fig. 6.17. Image of a copper target ( $25 \times 25 \times 1 \text{ mm}^3$ ) obtained by means of position-resolved-measurements of the resonant-frequency, at the following value of skin depth:  $\delta_4 = 2.9 \text{ mm}$ . During these measurements, the target was shielded by a 1.5-mm-thick aluminium sheet.

Results shown in Figs. 6.10-6.17 demonstrated imaging of high-conductivity metals hidden behind a 1.5-mm-thick aluminium shield. These breakthrough results proved the capability for our system to penetrate through conductive shields. Penetration would occur when shields made of materials having lower conductivity than Al were to be used [75]. This is because aluminium is a highly conductive material and therefore the skin depth through it is smaller than the skin depth through non-magnetic materials having lower  $\sigma$ , thus making imaging of metals shielded behind Al “less easy”, thus validating the method used here.

Investigations around the possibility of revealing the presence of low-conductivity shielded targets were also conducted. Figs. 6.18-6.19 show 2D plots representing a manganese target, obtained by adjusting the capacitance of the system to the value  $C=(11\pm 1\%)\ \mu F$ , corresponding to a skin depth through aluminium equal to  $\delta=3.3\ \text{mm}$ . This skin depth value was calculated by inserting the value of resonant frequency  $f_r=(1.90\pm 0.05)\ \text{kHz}$ , measured at the centre of the target, into Eq. 2.13. It is observed that the skin depth required to image this low-conductivity sample was higher than the one required for imaging the copper target, due to the lower magnitude of eddy currents produced by this low-conductivity metal.

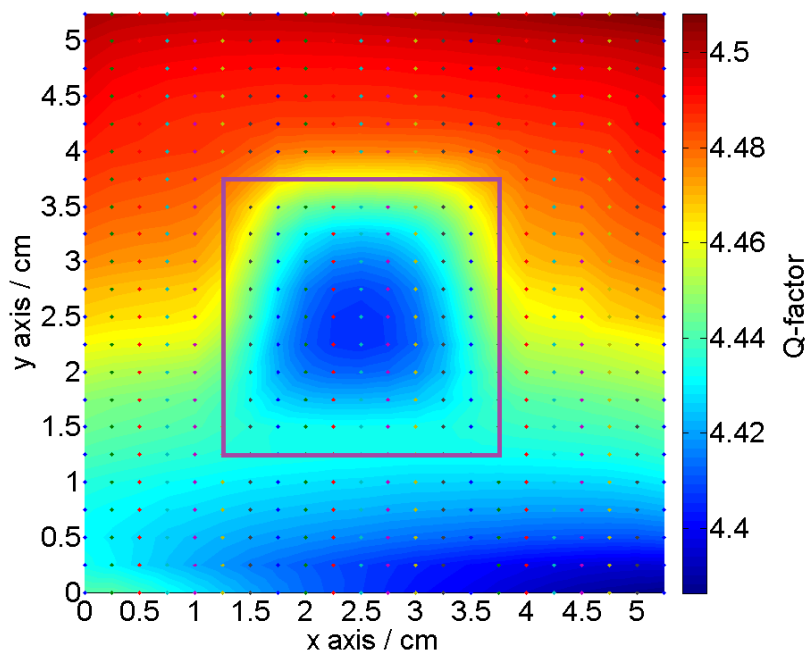


Fig. 6.18. Image reproducing a manganese target ( $25\times 25\times 1\ \text{mm}^3$ ), shielded by a 1.5-mm-thick aluminium sheet, obtained by means of position-resolved-measurements of the Q-factor, with a skin depth through aluminium equal to 3.3 mm.

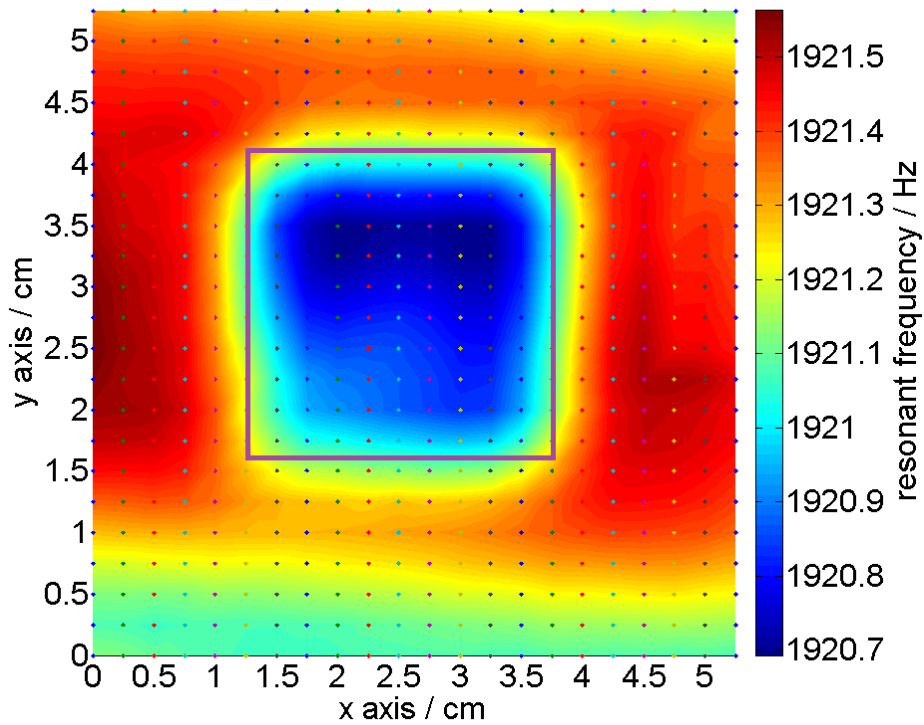


Fig. 6.19. Image reproducing a manganese target ( $25 \times 25 \times 1 \text{ mm}^3$ ), shielded by a 1.5-mm-thick aluminium sheet, obtained by means of position-resolved-measurements of the resonant-frequency, with a skin depth through aluminium equal to 3.3 mm.

To complete the investigations about 2D imaging of metals concealed behind conductive shields, a quantitative analysis of the faithfulness of the images reproducing the samples was conducted. This was achieved in a similar fashion to what was previously done using unshielded targets, as described in Section 5.6 (see Figs. 5.23-5.24). In this case, a set of aluminium disks of different diameter, shielded by a 1.5-mm-thick aluminium shield, were imaged both via Q-factor and resonant frequency measurements, and the contours of the disks were derived using the same Canny edge technique (“estimated diameter” in Fig. 6.20). This was compared with the actual disk diameters (“measured diameter” in Fig. 6.20).

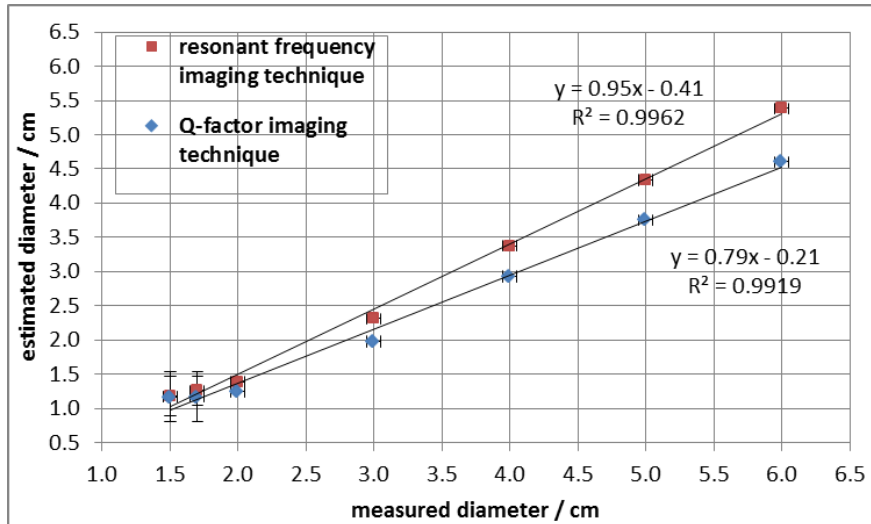


Fig. 6.20. Plot equivalent to the one shown in Fig. 5.23, obtained for aluminium disks of different diameter, shielded by a 1.5-mm-thick aluminium shield. *Estimated diameter* stands for the diameter derived by applying a Canny edge detection algorithm to the images of the disks; *measured diameter* indicates the actual sample diameter.

The diameter estimated from the images displayed a linear relationship with the samples' measured diameters, for both Q-factor and resonant frequency images, with a coefficient of determination equal to unity within a few percent. This demonstrated the reliability of the imaging system for screened conductive target objects. A comparison between the plots reported in Figs. 5.23 and 6.20 revealed a difference in the capability of reproducing the targets' dimensions of the imaging techniques based on Q-factor and resonant frequency measurements. In the case of unshielded targets, the Q-factor technique allowed more accurate reproduction of the targets' dimensions than the resonant frequency technique, with an agreement within 2% between the estimated diameters and the measured ones (for disk diameters larger than 4 cm). These results were very satisfactory and showed the potential of the proposed imaging technique to reproduce samples' dimensions. An opposite scenario occurred with 'shielded' targets, as images obtained with resonant frequency measurements reproduced the targets' dimensions more accurately than the Q-factor ones. Nevertheless, in both cases the diameter of the imaged 6-cm diameter disk was underestimated (by 10% and 23%, with  $f_r$  and Q measurements, respectively), as can be seen in Fig. 6.20. This behaviour was attributed to the presence of the aluminium shield covering the targets and 'masking' them. The consistency of the results above, which were obtained

for all samples in the entire diameter range considered in this experiment, is attested by the coefficient of determination  $R^2$  close to 1 in both fits of the data points obtained with  $f_r$  and Q measurements, as reported in Fig. 6.20. This  $R^2$  value represents a very good agreement between measured and estimated diameters. Relations similar to those reported in Section 5.6 could be derived from the fitting equations reported in Fig. 6.20, which would allow to determine the samples' diameters by using the images obtained with the procedure developed in this work, after applying the Canny edge detection algorithm to them. The usefulness of the proposed method for the estimation of imaged samples' dimensions was thus established in the case of "shielded" samples, as well as in the scenario based of unshielded samples (Sections 5.4 and 5.6).

### 6.2.3 Mathematical model for the problem

The discussion of results reported in Section 6.2.2 can be complemented by adding a theory section relative to shielded conductive samples, which aims at stating the problem and describing the forward solution, by adopting the simplified scenario introduced by Moulder *et al.* [76]. The geometry of the problem is simplified in Fig. 6.8, with the coil differing from the one used in the experiments described in this section because it has an air core rather than a ferrite core. The coil cross section is rectangular and its geometrical characteristics (in analogy with Section 2.4) are as follows:

$r_1$  = inner radius,

$r_2$  = outer radius,

$h_1$  = lift-off (vertical distance between coil lower base and first layer, as specified in the next paragraph),

$h_2$  = vertical distance between top of coil and first layer,

$L = h_2 - h_1$  = coil length.

The coil is placed over two layered half spaces of conductivity  $\sigma_1$  and  $\sigma_2$  (first layer being the one located closer to the coil, second layer being the one farther from the coil), and its axis is perpendicular to them. Assuming these materials to be nonferrous, their magnetic permeability is equal to the permeability of free space,  $\mu_0$ . The thickness of the layer closer to the coil, having conductivity  $\sigma_1$ , is denoted by  $d$ .

The conductivity and thickness of the first layer can be determined by solving the inverse problem, in which the conductivity of the second layer,  $\sigma_2$ , is known. The problem is solved by experimentally determining the frequency-dependent impedance of the coil, specified analytically in Section 2.4. The forward problem consists in determining the impedance, upon knowledge of the frequency, the layer thicknesses and the conductivity and permeability of the materials. In the experiments reported in Section 6.2.2, the resonant frequency and Q-factor are measured, after setting the frequency to different values, thus varying the skin depth. The other quantities are fixed and known, since the nature of the materials making up the sample and the shield is known from tabulated data, and the thicknesses were experimentally measured. For a given frequency  $\omega$ , the coil impedance in the presence of two layers of conductivities  $\sigma_1$  and  $\sigma_2$  can be written as [76]:

$$Z = Kj\omega \int_0^\infty \frac{I^2(\alpha, r_1, r_2)}{\alpha^5} \left( 2L + \frac{1}{\alpha} [2e^{-\alpha L} - 2 + A(\alpha)\varphi(\alpha)] \right) d\alpha, \quad (6.1)$$

where the prefactor  $K$  is given by:

$$K = \frac{\pi\mu_0 n^2}{L^2(r_2 - r_1)^2} \quad (6.2)$$

The function  $I = I(\alpha, r_1, r_2)$  includes the coil dimensions:

$$I(\alpha, r_1, r_2) = \int_{\alpha r_1}^{\alpha r_2} x J_1(x) dx \quad (6.3)$$

The function  $A = A(\alpha)$  incorporates lift-off and the length of the coil:

$$A(\alpha) = e^{-2\alpha h_1} + e^{-2\alpha h_2} - 2e^{-\alpha(h_1 + h_2)} \quad (6.4)$$

Most relevant for this section, the effects of frequency and skin effect are embedded within  $\alpha_1$  and  $\alpha_2$  which are inside function  $\varphi = \varphi(\alpha)$ , as detailed below:

$$\varphi(\alpha) = \frac{(\alpha + \alpha_1)(\alpha_1 - \alpha_2) + (\alpha - \alpha_1)(\alpha_1 + \alpha_2)e^{2d\alpha_1}}{(\alpha - \alpha_1)(\alpha_1 - \alpha_2) + (\alpha + \alpha_1)(\alpha_1 + \alpha_2)e^{2d\alpha_1}} \quad (6.5)$$

$$\alpha_{1,2} = \sqrt{\alpha^2 + j\omega\mu_0\sigma_{1,2}} \quad (6.6)$$

The quantities that were measured in the experiment reported in Section 6.2 are the resonant frequency and Q-factor, which are dependent on the impedance having analytical function as in Eq. 6.1. The dependence on the frequency is not linear, due to the presence of function  $\varphi = \varphi(\alpha)$ . The resonant frequency and Q-factor images shown in Figs. 6.2-6.7 and Figs. 6.10-6.19 show that the dimension of the imaged samples does not change monotonically by decreasing the frequency of operation, i.e. increasing the skin depth. This behaviour is reflected by results shown in Fig. 3.21, where the change in resonant frequency and Q-factor was measured for increasing values of capacitance. Since the experiments reported in this Chapter relies on varying the frequency by changing the capacitance of the LCR circuit, the behaviour observed in the images of metals cannot be explained by using eddy current theory only. Whereas the increase in the coil frequency implies larger amount of eddy currents induced and is therefore equivalent to increasing the sample's conductivity, the capacitance variation must be taken into account too. The dependence of the resonant frequency and Q-factor on the capacitance is detailed in Eqs. 2.6 and 2.12. These equations would suggest an increase of Q with increasing capacitance and a decrease of resonant frequency with increasing capacitance. The observed dimensions of the imaged samples do not follow a defined trend when the capacitance is increased, when the two scenarios of unshielded and shielded metals are taken into account. This is accounted for by the resistance variation which occurs as a consequence of eddy current induction (Section 2.4). This sentence will be justified for by the theoretical considerations exposed in the following paragraph. Nevertheless, a note should be made about the choice of skin depths in the experimental work detailed in the present Chapter. The resistance variation is not picked up by the coil in the same way because of the different penetration depths, which in some cases exceed by a large amount the sum of the thickness of the sample plus the thickness of the shielding material.

To study the frequency dependence of the real and imaginary part of the impedance with the assumptions detailed at the beginning of this Section, the difference in impedance  $\Delta Z$  can be taken into account. This approach allows for simplifications in the calculations, due to the cancellation of the term related to the electrical resistance of the circuit wires. The impedance difference is defined as:

$$\Delta Z = Z - Z_2 \quad (6.7)$$

where  $Z$  denotes the impedance of the coil over two layers having conductivities  $\sigma_1$  and  $\sigma_2$ , as in Eq. 6.1, and  $Z_2$  represents the impedance of the coil over the second layer only. The assumption here is that the thickness of the second layer (the deeper one) is much larger than the skin depth [76]. This assumption is not met everywhere, in the experimental approach adopted in this chapter, which explains the divergence between the model and the results obtained and shown in the previous sections. When the above assumption is true, the impedance difference  $\Delta Z$  can be expressed as:

$$\Delta Z = Kj\omega \int_0^\infty \frac{I^2(\alpha, r_1, r_2)}{\alpha^6} A(\alpha) \left( \frac{\alpha - \alpha_2}{\alpha + \alpha_2} - \varphi(\alpha) \right) d\alpha \quad (6.8)$$

Analysis of the impedance function  $\Delta Z = \Delta Z(\omega)$  shows the following behaviour for the resistive and reactive components of the complex impedance change. The reactive component  $\Delta X$  (imaginary part of  $\Delta Z$ ) increases monotonically as a function of frequency, whereas the resistive component  $\Delta R$  (real part of  $\Delta Z$ ) starts from zero, has a minimum, crosses zero and then rises monotonically with the opposite sign as the frequency increases. This specific behaviour occurring when changing the operational frequency can explain the observed variation of the dimensions of the imaged samples obtained with resonant frequency and Q-factor measurements. The physical interpretation of the zero occurring in the resistive component of the complex impedance can be given as follows. The power dissipation in the first layer is the same as in the second layer at the frequency  $\omega_0$  at which  $\Delta R = \Delta R(\omega_0)$  is minimum. The frequencies of the minimum and the zero in  $\Delta R$  are strongly dependent upon the layer's thickness and their electromagnetic properties.

An argument can be made to explain the presence of a zero in the resistive component of the impedance change, based on showing that the low- and high- frequency asymptotics of  $\Delta R$  have opposite signs, which implies that a zero must occur, under the assumption of a continuous function  $\Delta Z = \Delta Z(\omega)$  [76]. The following formula for the power dissipated by the system stands [76]:

$$R = \int_2 d^3 \mathbf{r} \operatorname{Re}[\mathbf{J}] \cdot \operatorname{Re}[\mathbf{E}] \quad (6.9)$$

where  $\mathbf{J}$  represents the current,  $\mathbf{E}$  denotes the electric field, and the integration takes place over the half space occupied by the second layer (having conductivity  $\sigma_2$ ). The current is related to the electric field through Eq. 6.10 [76]:

$$\mathbf{J} = \sigma \mathbf{E} \quad (6.10)$$

The sign of  $\Delta R$  can be demonstrated to be dependent on the conductivity difference only, as shown by Eq. 6.11, in which the electric field produced by the coil in free space is indicated by  $\mathbf{E}_0$  (the integral must be positive as it is over the square of  $Re[\mathbf{E}_0]$ ). The low frequency limit of  $\Delta R$  is exemplified by Eq. 6.11, which was obtained by using the fact that the electric field in layered solids is equal to  $\mathbf{E}_0$  at lowest order in the frequency expansion [76]. This means that at sufficiently low frequencies a metallic solid is transparent to the applied magnetic field and that, in the absence of induced charges, the resulting electric field is the same as the field that would occur in free space due to Faraday's law. These considerations lead to:

$$\Delta R = (\sigma_1 - \sigma_2) \int d^3\mathbf{r} Re[\mathbf{E}_0] \cdot Re[\mathbf{E}_0] \quad (6.11)$$

The high frequency limit is then considered to determine the sign of  $\Delta R$ . For simplicity, let us consider a coil with a single turn that is placed at the surface of the half space, i.e., with lift-off equal to zero. At a sufficiently high frequency  $f_{high}$ , the drive current will be equal and opposite to the induced counter-current (perfect screening). By denoting the drive current  $I_0$  and the induced current density  $\mathbf{J}$ , the way in which the latter quantity scales with the screening depth in the material  $\delta$  can be given by [76]:

$$\mathbf{J} \approx \frac{I_0}{\delta} \quad (6.12)$$

When a sufficiently high frequency is obtained, the current in the layered metal is entirely concentrated in the layer half space. In this case, Eqs. 6.9 and 6.10 can be used to obtain a rough estimate for the power dissipated by the layered metal:

$$R_L \approx \frac{I_0^2}{\delta_L^2} \delta_L \frac{1}{\sigma_L} \quad (6.13)$$

The dissipation in the second layer can be shown to be similar to Eq. 6.13. Subtraction of these two expressions, as well as the dependence of the skin depth on the conductivity ( $\delta \sim \sqrt{\sigma}$ ) lead to the following expression for the reactive component of the impedance change:

$$\Delta R \approx I_0^2 \left( \frac{1}{\sqrt{\sigma_1}} - \frac{1}{\sqrt{\sigma_2}} \right) F(f) \quad (6.14)$$

Comparison between Eq. 6.11 for the low frequency limit and Eq. 6.14 for the high frequency limit is now done to complete this theoretical demonstration. Since the function  $F(f)$  is a positive-valued function of frequency and does not depend on conductivity, for any choice of  $\sigma_1$  and  $\sigma_2$  the low- and high- frequency limits have opposite signs. Therefore,  $\Delta R$  must be equal to zero at some intermediate frequency  $\omega_0$ .

#### 6.2.4 Conclusions

In conclusion, the images reported in Figs. 6.10-6.20 show the suitability of the proposed EII system for imaging both high and low conductivity metals shielded by a conductive shield and therefore not visible from the outside. This represented a breakthrough result that validated the PhD work reported in this thesis.

There is an important advantage related to using a single coil acting both as a magnetic field inductor and as a sensor. Such coil faces the hidden side of the object to be imaged, in the technique here developed. This specific detection configuration is of particular interest because the object may not be accessible from other sides. This opens up the possibility of turning the proposed EII detection system into a portable device for identifying materials of suspicious nature.

## 7 An improved EII system based on active filters

The research work described up to this point was established on resonating systems based on LC and LCR circuits. This choice was made upon considerations reported in Horowitz, which highlight that combining inductors with capacitors can produce very sharp frequency characteristics compared to RC filters, even when RC sections are cascaded [77]. An alternative way of achieving sharp resonance responses is using active filters [77, p. 52].

The results obtained with LCR parallel circuits (Chapters 5 and 6) highlighted some limitations in the EII technique based on the use of this type of resonant system. The most important one, which is addressed in this chapter, is related to the Q-factor low absolute values obtained with the LCR systems introduced in Chapter 4 (Q between 7 and 23, as shown in Figs. 5.20 and 5.21). The requirement for an imaging system to allow distinguishing between conductive materials having similar values of electrical conductivities translated into looking for a method to enhance the system's Q-factor. The difference between the Q-factor measured with a Cu and an Al sample having the same geometry was equal to  $\Delta Q = 0.33 \pm 0.06$ , when the LCR-based system described in Section 4.3 was used (with lift-off  $L = 1$  cm). The difference between the Q-factor values obtained with Cu and Al samples by means of the LCR system was not large enough to allow visually discriminating between the two samples by looking at their images. Therefore, focus was directed towards implementing a system and an imaging technique based on the attainment of larger values of Q-factor. This feature would prove beneficial to satisfy the requirement for an EII detection system to distinguish between different values of resonant frequencies, which could not be resolved with the previously adopted LCR system. Specifically, achieving larger Q-factor values should contribute to improve the system's performance for imaging of 2D conductive samples, for two reasons. Firstly, larger Q-factor absolute values would lead to larger Q-factor differences, produced by two different samples, which would increase the system's resolution power, i.e., its ability to resolve two resonance peaks produced by samples having different values of electrical conductivity. This would improve the capability of the system to distinguish between samples of different electrical nature. Secondly, a detection system characterised by intrinsically larger Q-factor values would lead to achieving larger Q-factor shifts between air and poorly

conductive materials, compared to the shifts obtained with the previously developed EII system (refer to Section 5.3). This would improve the suitability of the detection system for imaging of low-conductivity samples, as well as higher-conductive ones. Therefore, investigations were conducted, aimed at finding and implementing a novel resonating imaging system having higher Q-factor values than the previously used one. These investigations involved the following:

- 1) Studying the behaviour of different types of active bandpass filters (see Section 7.1);
- 2) Finding the most suitable active filter for our purposes, i.e., a filter that could be turned into an EII system for detection and imaging of conductive materials - as explained at point 3) below - characterised by Q-factor values larger than those obtained with the previously implemented EII system;
- 3) Modifying the filter by including an inductor of appropriate value, connected to the circuit components such that the resonance characteristics of the original filter remained unvaried. The inductor had to be included to the system in order to allow the implementation of an imaging method similar to the one previously adopted (Chapter 4), to image conductive samples by measuring the changes in the Q-factor of the system, by means of a coil, playing the role of the sensor. This strategy should allow using the modified active filter as an EII system for detection and imaging purposes.

Active bandpass filters were considered in this work as an alternative to LCR parallel circuits used in the previous part of these investigations, because they resonate at a defined frequency depending on the circuit design, thus allowing the use of the EII technique that was developed for LCR parallel circuits (Chapter 4), in order to detect and image conductive materials. Active bandpass filters of appropriate design can be advantageous because of their larger Q-factor values, compared to LCR parallel circuits. The procedure described above was followed in order to improve the previously developed EII system based on LCR circuits, without having to change the EII method based on position-resolved-measurements of Q-factor shifts due to the presence of conductive samples. Chapters 5-6 proved that this method was successful for EII imaging of both “unshielded” and “shielded” metals, consequently this

method was adopted for the measurement acquisition implemented with the new EII system, based on active bandpass filters (Section 7.4).

A brief introduction about active bandpass filters is given in Section 7.1. Experimental investigations carried out to determine a suitable type of active filter that could be used for the scope of this research are reported in Sections 7.2-7.3. The following sections involve the development of a circuit based on an active filter and report on the initial experiments that were carried out to test this circuit as a potential EII system. This includes description of the experimental method and results obtained by means of measurements of the Q-factor shifts obtained with the novel EII system, in the presence of metallic samples (Section 7.6). Sections 7.8-7.10 detail investigations that were conducted with the goal of improving the proposed system and establishing a measurement method for detection and imaging of conductive samples, including samples that were shielded by metallic shields. This includes a comparison between the new EII system with the previously developed LCR-based system (Section 7.9). The chapter ends with “Results and discussion” (Section 7.11).

## 7.1 Active bandpass filters

Active bandpass filters are typically built by cascading a high-pass and a low-pass filter (Figs. 7.1-7.2), with the insertion of an operational amplifier (op-amp) in between the two [77]. The amplifier works as an active element and therefore gives this type of filters the name of active filters. By using op-amps as part of the filter design, it is possible to synthesize any RLC filter characteristic without using inductors, which depart from the ideal by being lossy (as they have significant series resistance), as well as by causing problems such as nonlinearity, distributed winding capacitance, and susceptibility to magnetic pickup of interference [77].

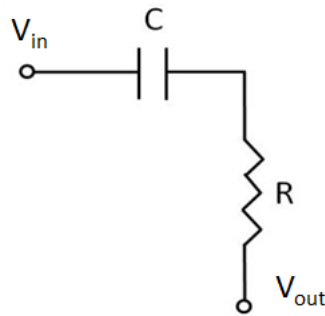


Fig. 7.1. Circuit schematic of a RC highpass filter.

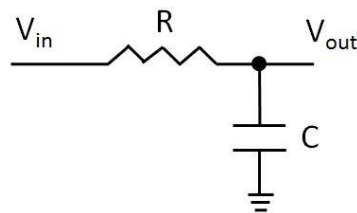


Fig. 7.2. Circuit schematic of a RC low-pass filter.

Several filter designs are available to optimise each of the filter's characteristics, for example the sharpness of the transition to the stopband and, therefore, the Q-factor. One type of active filter is represented by the infinite gain multiple feedback (IGMF) active filter, which is described in the next section.

## 7.2 IGMF active filters

The active bandpass filter that was initially chosen as a potential candidate to build the new version of the EII system developed in this work was the IGMF active filter represented in Fig. 7.3 [76, p. 413]. This type of active filter has one op-amp configured as an integrator, implying that the output voltage is proportional to the time integral of the input voltage. The op-amp chosen for this work was a OP27 (Fig. 7.4), because of its low-noise (80 nV p-p in the frequency range 0.1 Hz to 10 Hz [77]).

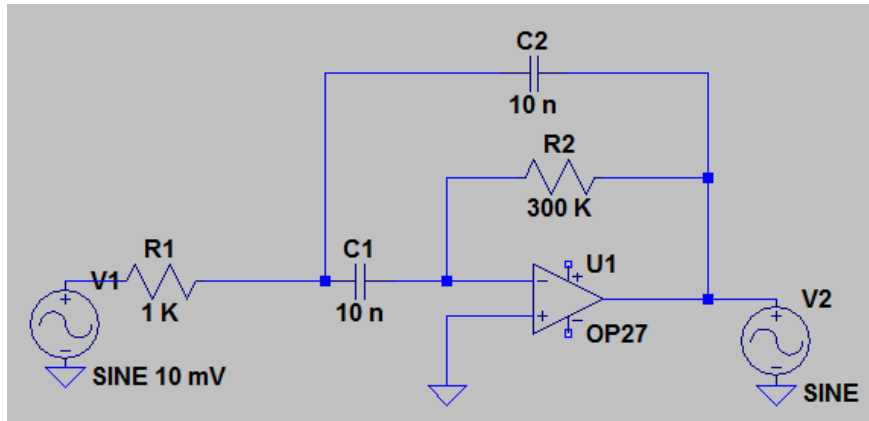


Fig. 7.3. Schematic of IGMF circuit (in a 2-pole lowpass configuration) used to investigate the possibility of using this configuration to build a new version of the EII system used in this research. This sketch was created with LTSpiceXVII.

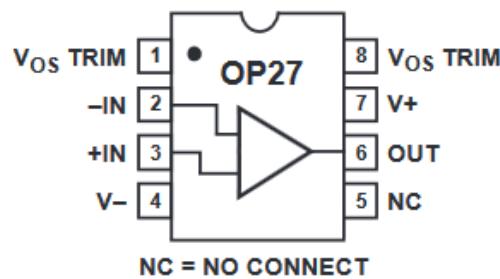


Fig. 7.4. Sketch of the pinouts constituting the op-amp OP27GPZ [78].

Initial investigations were conducted to familiarise with the IGMF active filter and verify whether it could become a useful tool for EII investigations, representing an improvement from previously used LCR circuits. These included determining the components' values in order to have the active filter resonate at values of resonant frequency that could be useful for penetrating through metallic shields and imaging samples, in a similar fashion to what was described in Chapter 6. The rationale behind the choice for the components' values (shown in the electronic schematic in Fig. 7.3) is described in the following. The circuit's components were chosen such that two requirements were satisfied. The first requirement was for the circuit's Q-factor to be larger than the largest Q-factor attained with the previously used LCR-based EII system ( $Q \approx 20$ ). The second requirement was for the resonant frequency to be sufficiently low to allow penetration through shielding materials (Chapter 6).

Once the component values were determined, the circuit was built and then tested to check its performance.

The following relations stand for IGMF filters [77]:

$$f_r = \frac{1}{2\pi\sqrt{R_1 R_2 C_1 C_2}} \quad (7.1)$$

$$Q = \frac{1}{2} \sqrt{\frac{R_2}{R_1}} \quad (7.2)$$

After choosing  $C_1=C_2$ , as suggested by Horowitz [77], the component values indicated in Fig. 7.3 were determined by using Eqs. 7.1 and 7.2 and imposing the following conditions: 1)  $Q=10$  and 2)  $f_r = 1$  kHz. This choice of values was established with the purpose of reproducing resonance characteristics similar to the ones of the LCR-based systems used in Chapters 4 to 6.

The maximum gain (i.e. gain at resonance) of an IGMF filter is given by [77]:

$$G = \frac{R_2}{2R_1} = 2Q^2 \quad (7.3)$$

The expected values of resonant frequency ( $f_r$ ), Q-factor ( $Q$ ) and maximum gain ( $G$ ), calculated using Eqs. 7.1-7.3 with values of components  $R_1$ ,  $R_2$ ,  $C_1$  and  $C_2$  as in Fig. 7.3, were the following:

$$f_r = 918.9 \text{ Hz} \quad (7.4)$$

$$Q = 8.7 \quad (7.5)$$

$$G = 150 \quad (7.6)$$

The circuit's performance was tested to verify that its characteristics were in line with those expressed by Eqs. 7.4-7.6. This involved measuring the filter's resonance curve by using the following instruments:

- ISO-TECH IDS-6052-U digital oscilloscope (Fig. 7.5);

- Hameg Instruments 25 MHz HMF 2525 signal generator (Fig. 7.5);
- $\pm 12$  V 100 mA power supply (made in-house) to supply voltage to the op-amp.

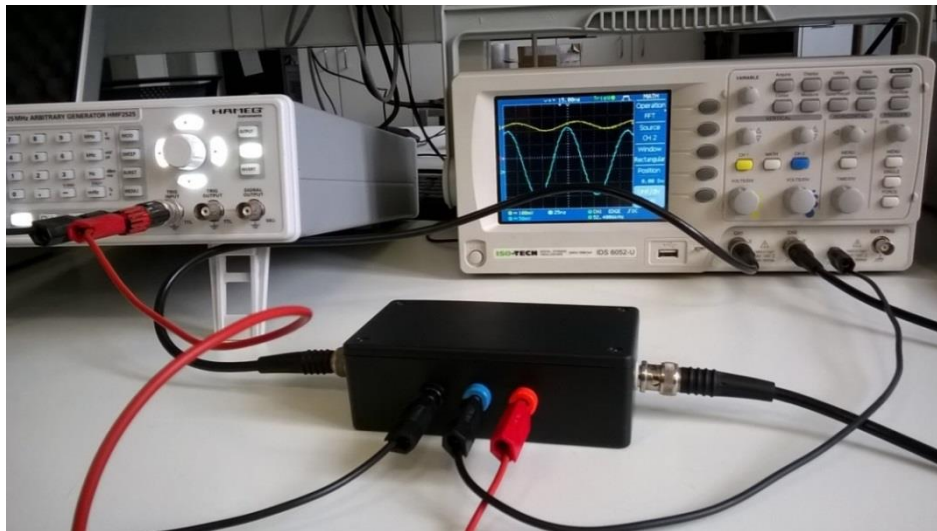


Fig. 7.5. Experimental set-up assembly. The IGMF filter (Fig. 7.3) is contained inside the black plastic enclosure at the centre of the picture. The signal generator Hameg Instruments 25 MHz HMF 2525 is shown on the left. The oscilloscope ISO-TECH IDS-6052-U is shown on the right side.

The experimental procedure described below was followed to study the filter's frequency response.

- 1) Sinusoidal input signals of different frequencies - covering a range centred around the predicted resonant frequency, given by Eq. 7.4 - were generated with the signal generator (Fig. 7.5). The amplitude of these signals was maintained equal to 10 mV. This value was chosen in order for the output voltage to not exceed the maximum supply voltage, equal to 12 V. The output of the circuit (of gain equal to 150), was calculated as follows:  $V_{out} = 10 \text{ mV} \times 150 = 1500 \text{ mV} = 1.5 \text{ V} < 12 \text{ V}$ .
- 2) Amplitudes of input and output signals ( $V_{in}$  and  $V_{out}$ , labelled V1 and V2 in Fig. 7.3) were measured with the oscilloscope (Fig. 7.5), for each selected frequency.
- 3) The gain was calculated by dividing the output voltage by the input voltage, using:  $G = V_{out}/V_{in}$ .

- 4) The resonance curve was drawn by plotting the gain calculated as specified above vs the frequency (Fig. 7.6).
- 5) The Q-factor was estimated from the curve by applying Eq. 7.7:

$$Q = \frac{\omega_0}{FWHM}, \quad (7.7)$$

where  $\omega_0$  was the resonant frequency ( $\text{rad s}^{-1}$ ) (estimated as the frequency at which the gain measured as in point 3) was maximum);  $FWHM$  was the frequency difference  $\Delta\omega = \omega_2 - \omega_1$ , where the two frequencies are such that the following relation holds:

$$G(\omega_2) = G(\omega_1) = G_{max}/\sqrt{2} \quad (7.8)$$

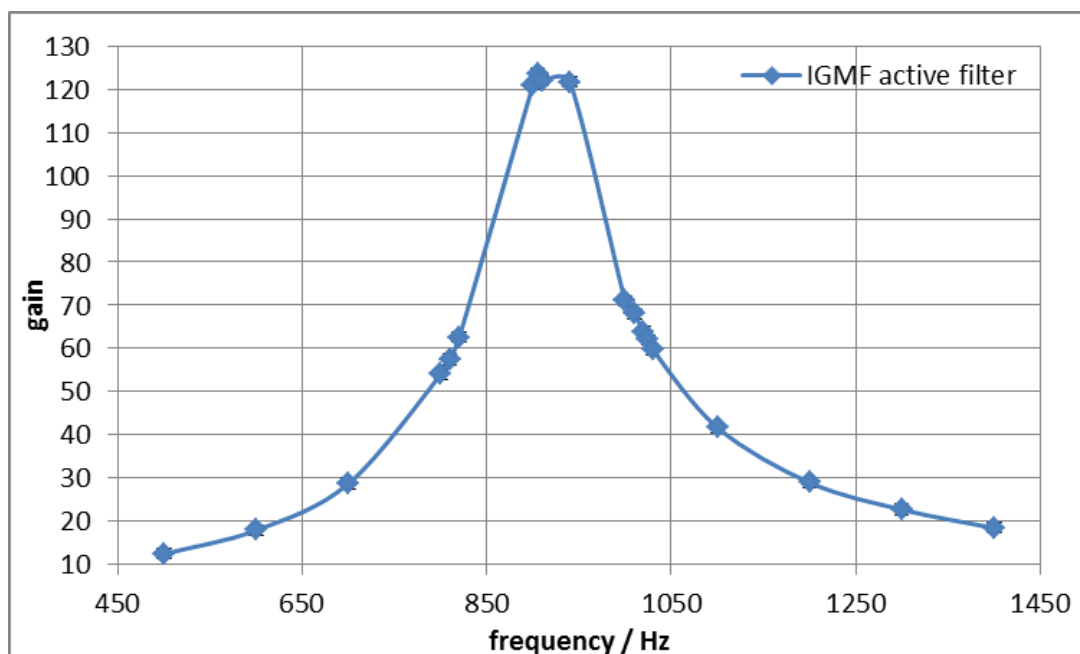


Fig. 7.6. Curve obtained by measuring the IGMF active filter gain and plotting it against the frequency of the signal generator.

The following values for Q-factor, resonant frequency and maximum gain of the filter were obtained, by adopting the measurement procedure described above:  $Q=7.5\pm0.6$ ,  $f_r=920\pm2$  Hz,  $G=123.9\pm0.8$ .

Due to the interdependence between the maximum gain and the Q-factor, expressed by Eq. 7.3, the Q-factor increase that could be achieved with this circuit was intrinsically

limited by the necessity to keep the gain sufficiently low to prevent signal saturation. As a consequence, the maximum input p.d. that could be applied was also limited. For this reason, a different type of filter, and in particular a state-variable active filter (Section 7.3) was considered as a potential candidate to build an improved version of the EII system based on LCR parallel circuits. This choice was justified by three characteristics of state-variable filters, which were established to be beneficial for the scope of this research. Firstly, despite its large number of components, the design of this type of filters allows obtaining high Q-factor values that can be maintained constant [77], as required to allow differentiation between similar values of resonance frequency, produced by metals having similar electromagnetic properties. Secondly, the filter design would easily allow tuning the resonant frequency  $f_r$ , by adjusting one of the resistor values by means of a rotary switch potentiometer [77]. Therefore, the filter's resonant frequency could be tuned to several values, while maintaining Q constant and high enough to allow penetration through materials. This implied the possibility of achieving larger values of skin depth, allowing penetration through materials thicker than the 1.5-mm-thick shield used in previous investigations (Chapter 6). A third advantage of using a state-variable filter was that its gain did not depend on Q, unlike what occurred with IGMF filters (Eq. 7.3). This allowed building a high-Q filter with lower gain than the corresponding gain that would be obtained with an IGMF having the same Q value (due to Eq. 7.3), thus giving more freedom in the selection of input voltages without the risk of incurring in signal saturation.

### 7.3 State-variable active filters

A 2-pole “state-variable filter”, with schematic shown in Fig. 7.7, was selected as a better candidate than the IGMF filter described in Section 7.2, for the reasons explained at the end of the previous section. In this filter, the two resistors labelled “Rf” in Fig. 7.7 set the centre frequency, and RQ and Rg together determine the Q and band-centre gain [77]. The filter’s resonant frequency was made adjustable by using a 2-section variable resistor with a double rotatory switch for the “Rf” pair (Fig. 7.7).

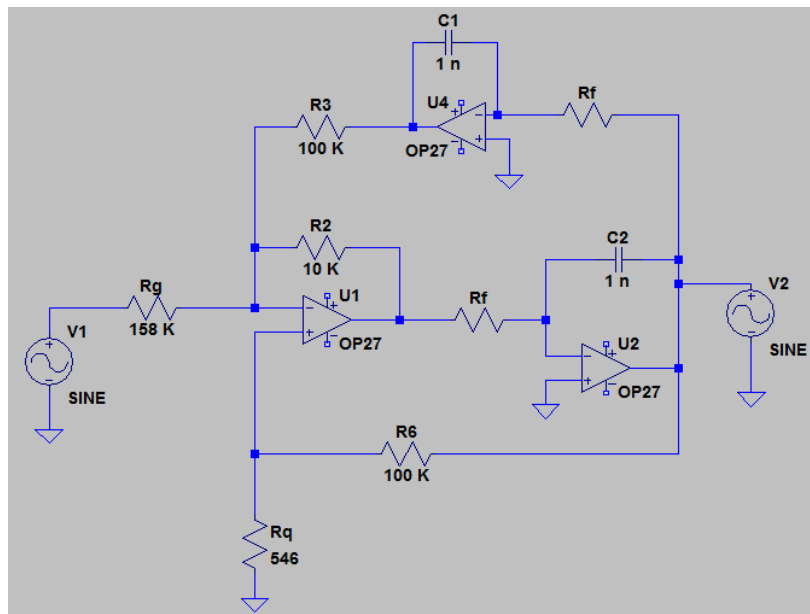


Fig. 7.7. Schematic of the 2-pole filter “state-variable filter” built for this investigation [77].

Firstly, Eqs. 7.9-7.10 below [77, p. 411] were used to determine resistor values that would make the Q-factor equal to  $Q=50$  and the maximum gain equal to  $G=10$  (to prevent signal saturation). These two values were inserted into Eq. 7.9 to determine the values of resistors  $R_Q$  and  $R_G$  (labelled “Rq” and “Rg” in Fig. 7.7), to be used to build the circuit:

$$R_Q = \frac{10^5}{3.48Q+G-1} = 546 \Omega \quad (7.9)$$

$$R_G = \frac{3.16 \cdot 10^4 Q}{G} = 158 K\Omega \quad (7.10)$$

Secondly, the circuit was made to resonate at 7 different values between 50 Hz to 50 kHz, as reported in the first column of Tab. 7.1. This was done by using two rotary switches ( $R_F$  in Fig. 7.7), each having 7 positions, allowing selection of resistance values ranging from 1 k $\Omega$  to 1 M $\Omega$ . These values were determined such that the filter's resonant frequencies would cause obtaining values of skin depth in Al between 0.38 mm and 12 mm (determined by using Eqs. 2.13-2.16 and listed in the second column of Tab. 7.1). This range of penetration depths was chosen in order to be able to adopt the method based on active filters for imaging of metals covered by shields having different values of thicknesses, potentially larger than the 1.5-mm value of the shield used in previous investigations (Section 6.2). This characteristic would make the new EII system more interesting for practical use than the previously adopted solution.

Tab. 7.1. Values of resonant frequency at which the electronic system was made to resonate (first column), and corresponding values of skin depth (second column), obtained by using Eqs. 2.25-2.28, and assuming that the EII system's operational frequency was equal to the active filter's resonant frequency  $f_r$  (first column).

Frequency $f_r$ (Hz)	Skin depth in Al (mm)
50329 $\pm$ 4	0.38 $\pm$ 0.02
10066 $\pm$ 4	0.85 $\pm$ 0.03
5033 $\pm$ 3	1.20 $\pm$ 0.03
1007 $\pm$ 2	2.68 $\pm$ 0.04
503 $\pm$ 2	3.79 $\pm$ 0.04
101 $\pm$ 1	8.48 $\pm$ 0.05
50 $\pm$ 1	11.99 $\pm$ 0.06

The circuit's resonant frequency is dependent on the component values  $R_2$ ,  $R_3$ ,  $R_F$  and  $C_F = C_1 = C_2$  (Fig. 7.7), as expressed by Eq. 7.11 [46]:

$$f_r = \frac{1}{2\pi} \left( \frac{R_2}{R_3} \right)^{1/2} \frac{1}{R_F C_F} \quad (7.11)$$

Eq. 7.11 shows that, once the other quantities were fixed, the resonant frequency of the circuit was only dependent on the values of the resistor  $R_F$ . Therefore, for convenience purposes,  $R_2$ ,  $R_3$  and  $C_F$  were maintained fixed and assigned values recommended in Horowitz and showed in Fig. 7.7. With this choice of components, Eq. 7.11 could be written as:

$$f_r = \frac{1}{2\pi} \frac{10^{17/2}}{R_F} \quad (7.12)$$

The component values, measured with a Keysight U1731C handheld LCR meter, are listed in Tab. 7.2.

Tab. 7.2. Values of components used to build the circuit represented in Fig. 7.6, measured with Keysight U1731C handheld LCR meter. Tolerance ranges for resistance and capacitance values were equal to 1%.

Resistor name	Measured resistance ( $\Omega$ )
RG	157800
RQ	568
R2	9990
R3	91500
R6	99200
Capacitor name	Measured capacitance (pF)
C1	1275.7
C2	1194.3

By inverting Eq. 7.12 to express  $R_F$  in terms of  $f_r$ , the resistor values for the rotary switch were determined by means of Eq. 7.13:

$$R_F = \frac{5.03 \cdot 10^7}{f_r} \Omega \quad (7.13)$$

Values of resistors corresponding to the 7 positions of the rotary switches are reported in Tab. 7.3. Values on the last two columns ("Theoretical  $f_r$ ") were obtained by inserting 'theoretical' values of  $R_F$  (second column) into Eq. 7.12. The frequency values at which the circuit was expected to resonate, for each of the measured resistor values, are listed in Tab. 7.4.

Tab. 7.3. Column 1: positions on rotary switch, numbered 1 to 7; column 2: ‘theoretical’ values of resistors  $R_F$ , each corresponding to a position on the rotary switch; column 3: theoretical values of  $f_r$  (predicted by using Eq. 7.13); column 4: values of  $f_r$  expressed in kHz.

Switch position	$R_F(\Omega)$	Theoretical $f_r$ (Hz)	Theoretical $f_r$ (kHz)
1	1000	50329.21	50.33
2	5000	10065.84	10.07
3	10000	5032.92	5.03
4	50000	1006.58	1.01
5	100000	503.29	0.50
6	500000	100.66	0.10
7	1000000	50.33	0.05

Tab. 7.4. Expected values of resonant frequency  $f_r$ , derived by inserting the measured values for  $R_F$  into Eq. 7.13. Resistance values were measured with a tolerance range of 1%.

$R_F$ measured ( $\Omega$ )	Expected $f_r$ (Hz)
1010	49830.90
5610	8971.34
10000	5032.92
56100	897.13
98800	509.41
559000	90.03
1006000	50.03

The gain and Q-factor of the circuit were derived by manipulating Eqs. 7.9 and 7.10 in order to write  $G$  and  $Q$  in terms of  $R_G$  and  $R_Q$ , resulting in the equations below:

$$G = 3.16 \cdot 10^4 \frac{R_Q + 10^5}{R_Q} \frac{1}{3.48 \cdot R_G + 3.16 \cdot 10^4} \quad (7.14)$$

$$Q = \frac{G R_G}{3.16 \cdot 10^4} \quad (7.15)$$

Once the filter was built, it was tested to verify that its characteristics were in agreement with the theoretically predicted ones. Specifically, Q was measured by following the procedure detailed below.

- 1) The filter was supplied with a  $\pm 15$  V voltage obtained by using a RS 591-124 power supply ( $\pm 15$  V, 200 mA);
- 2) An input voltage of 100 mV was produced by the signal generator “Hameg Instruments 25 MHz HMF 2525”;
- 3) The gain curve of  $V_{out}/V_{in}$  vs frequency was measured, by means of the digital oscilloscope ISO-TECH IDS-6052-U (Fig. 7.5);
- 4) The resonant frequency  $f_r$  (labelled “measured  $f_r$ ” in Tab. 7.5), defined as the frequency for which the gain was maximum ( $maxG$ ), was estimated from the gain vs frequency plot;
- 5) The frequencies  $f_1, f_2$  at which the gain was equal to:  $G' = maxG/\sqrt{2}$  were determined;
- 6) The maximum gain was determined with Eq. 7.8, inserting the frequency values determined as in 5), by using the following identity:  $\omega_i = 2\pi f_i$ ;
- 7) The Q-factor was estimated from the curve by applying Eq. 7.7:

$$Q = \frac{\omega_0}{FWHM}, \quad (7.7)$$

where  $\omega_0$  was the resonant frequency ( $\text{rad s}^{-1}$ ) (estimated as the frequency at which the gain measured as in point 3) was maximum);  $FWHM$  was the frequency difference  $\Delta\omega = \omega_2 - \omega_1$ , where the two frequencies are such that the following relation holds:

$$G(\omega_2) = G(\omega_1) = G_{max}/\sqrt{2} \quad (7.8).$$

The response curve obtained by plotting the filter’s gain against the frequency, for the lowest value of resonance frequency selectable with the rotary switch ( $f_r = 50$  Hz, as in the second column of Tab. 7.4), is reported in Fig. 7.8. Similar curves were obtained for the other values of resonance frequency.

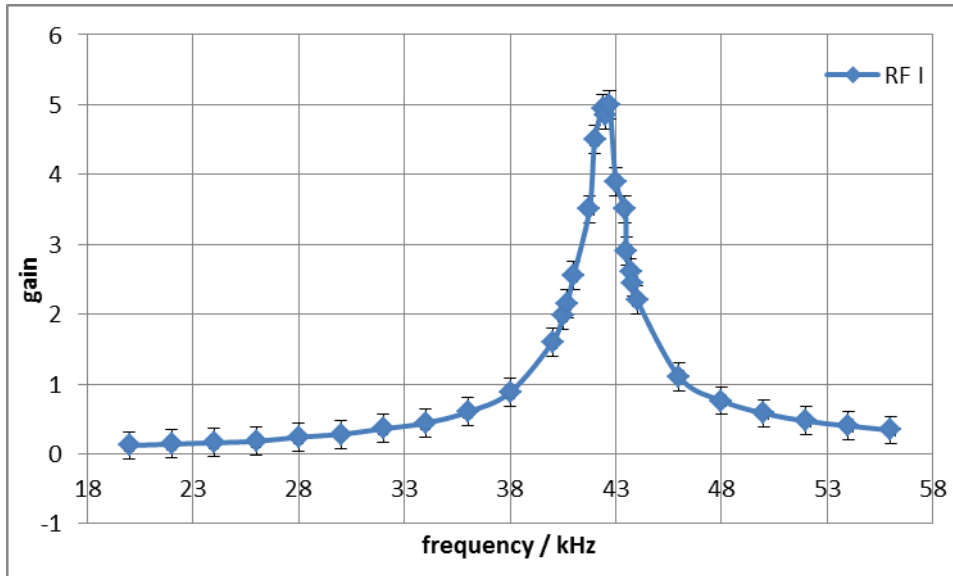


Fig. 7.8. Resonance curve of the filter shown in Fig. 7.7, obtained with a resistor value  $R_F = 1 \text{ M}\Omega$ , corresponding to the last position on the rotary switch (Tab. 7.4).

Unexpectedly, values for  $f_r$  that were determined as in 4) from curves of gain vs frequency were different from the expected values reported in Tab. 7.4. These values are reported in the third and second column of Tab. 7.5, respectively.

Tab. 7.5. Expected and measured values of resonant frequency, plus ratio between them.

Switch position	Expected $f_r$ (Hz)	Measured $f_r$ (Hz)	Ratio
1	49830.9	42400±4	1.2
2	8971.3	7500±3	1.2
3	5032.9	4200±3	1.2
4	897.1	730±2	1.2
5	509.4	410±1	1.2
6	90.0	72±1	1.3
7	50.0	40±1	1.3

‘Expected’ values of gain and Q were found by inserting the measured values of  $R_G$  and  $R_Q$  (listed in Tab. 7.2) into Eqs. 7.14-7.15 above. A mismatch was found between these values (labelled “Exp. G” and “Exp. Q” in Tab. 7.6) and the ‘measured’ ones obtained as detailed in bullet points 6) and 7) on page 162 (“Meas. G” and “Meas. Q” in Tab. 7.6). Ratios

between expected and measured resonant frequency ( $f_r$ ), maximum gain ( $maxG$ ) and Q-factor ( $Q$ ) are reported in Tabs. 7.5 and 7.6.

Tab. 7.6. Expected and measured values of G and Q, plus ratio between each pair of them.

Switch position	Exp. G	Exp. Q	Meas. G	Meas. Q	Ratio G	Ratio Q
1	9.6	48.1	5.0	25.4	1.9	1.9
2	9.6	48.1	5.0	42.0	1.9	1.1
3	9.6	48.1	3.9	20.1	2.5	2.4
4	9.6	48.1	4.0	20.5	2.4	2.3
5	9.6	48.1	4.0	21.3	2.4	2.3
6	9.6	48.1	4.1	20.8	2.3	2.3
7	9.6	48.1	4.0	19.0	2.4	2.5

The mismatch between expected and measured values reported in Tabs. 7.5-7.6 was attributed to the output signal's instability around resonance, which constituted a significant issue for measurements of the Q-factor that were done by determining the gain vs frequency response, based on the procedure described on page 161. Because of the adopted procedure, the Q-factor and gain values were strongly dependent on the quality of the signal in the resonance frequency region, which was poor due to the signal instability. The latter was attributed to the choice to assign resistor  $R_Q = 546 \Omega$  a lower value than those of other resistors in the circuit ( $\approx k\Omega$ ). This choice was made with the purpose of achieving  $Q=50$  and  $G=10$ , but did not take into account the risk of variations in the current circulating through the filter's different components. The circuit instability was corrected for by modifying the circuit shown in Fig. 7.7 such that all resistors had similar values. Specifically, the following components were used:

$$R_6 = 150 \text{ K}\Omega \quad (7.16)$$

$$R_Q = 1 \text{ K}\Omega \quad (7.17)$$

These specific values were chosen to satisfy the condition  $Q=50$ . The Q-factor of the state-variable active filter depended on the two resistors above, as given by Eq. 7.18.

$$Q = \frac{R_6 + R_Q}{3R_Q} \quad (7.18)$$

The resonant frequency of the state-variable active filter was linked to the circuit's Q-factor and electronic components through Eq. 7.19:

$$f_r = \frac{1}{2\pi} Q \frac{3R_Q}{CR_F(R_6+R_Q)} \quad (7.19)$$

The components' actual values, measured using the Keysight U1731C handheld LCR meter, are reported in Tab. 7.7. The values of resistors  $R_F$ , selected through the rotary switches, are listed in the first column of Tab. 7.8; resonant frequency values, derived by using Eq. 7.19, are reported in the second column of Tab. 7.8, and the corresponding skin depth values through Al (predicted by Eqs. 2.25-2.28) are listed in the third column of the table.

Tab. 7.7. Measured values of the circuit's components. Their tolerance value was equal to 1%.

$R_G$ (k $\Omega$ )	$R_2$ (k $\Omega$ )	$R_3$ (k $\Omega$ )	$R_6$ (k $\Omega$ )	$R_Q$ ( $\Omega$ )
9.9	10.0	9.9	150.8	998

Tab. 7.8. Measured values of resistors making up the rotary switch; corresponding resonant frequency values that were expected; corresponding skin depth in Al at those frequencies. Resistor tolerance was equal to 1%.

$R_F$ (k $\Omega$ )	$f_r$ (kHz)	Skin depth in Al (mm)
6.8	23.28±0.04	0.56±0.02
8.2	19.30±0.05	0.61±0.03
9.9	16.12±0.06	0.67±0.03

The filter's response in a range of frequencies centred around the resonant frequency was determined by using the ENA series E5061B Network Analyser (Keysight), to improve the measurements' precision [79]-[80]. The Network Analyser (NA) can measure the response in frequency of a DUT by measuring the S-parameters "S21", defined as the ratio of the output signal of port 2 on the DUT with the input signal of port 1 on the DUT. This can be achieved by applying a stimulus in a defined frequency range to the DUT. The power supply "elc" ALF 1502D was used in the following investigations to supply  $\pm 12$  V to the op-amp included in the filter. A picture of the experimental apparatus, including the Network Analyser, is shown in Fig. 7.9. The response curves obtained with the state-variable active filter resonating at values indicated in Tab. 7.8 are shown in Figs. 7.10-7.12. These figures show plots of the S-parameter

S21 vs frequency, obtained after applying a stimulus characterised by a starting frequency equal to 10 kHz and a final frequency 30 kHz. The three plots were obtained by selecting resistor values as in the first column of Tab. 7.8, causing the filter to resonate at the values listed in the second column of the table.

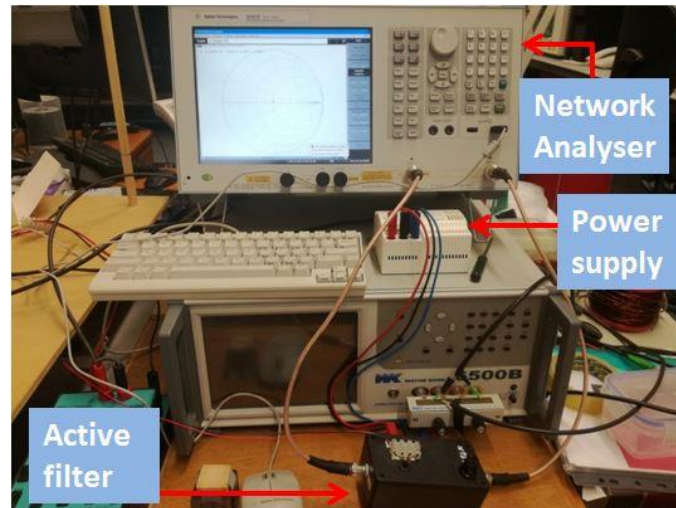


Fig. 7.9. Picture of the experimental setup, including the active filter, the Network Analyser E5061B (Keysight) and the power supply “elc” ALF 1502D.

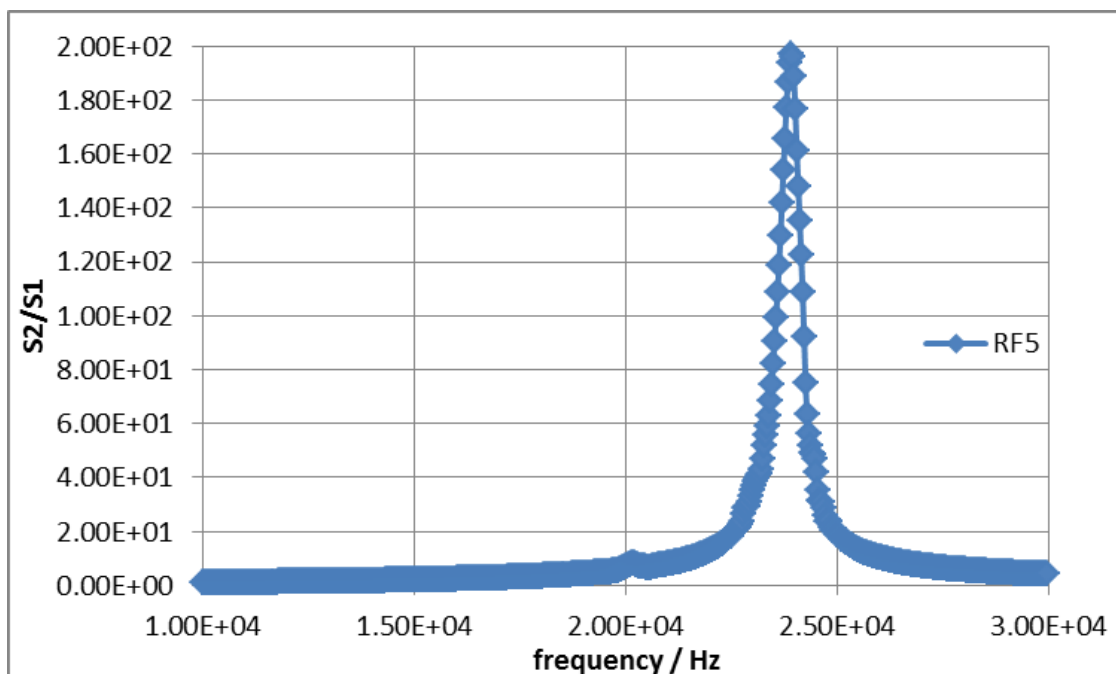


Fig. 7.10. Resonance curve obtained from data acquired using the Network Analyser, when the circuit's resonant frequency was equal to 23.6 kHz.

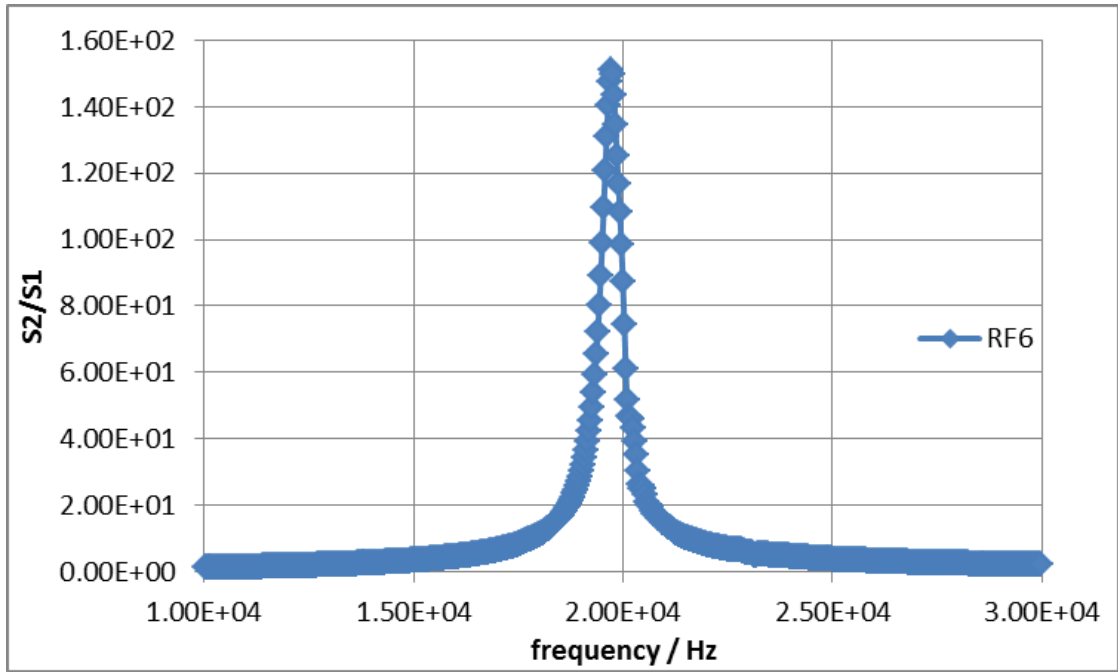


Fig. 7.11. Resonance curve obtained from data acquired using the Network Analyser, when the circuit's resonant frequency was equal to 19.9 kHz.

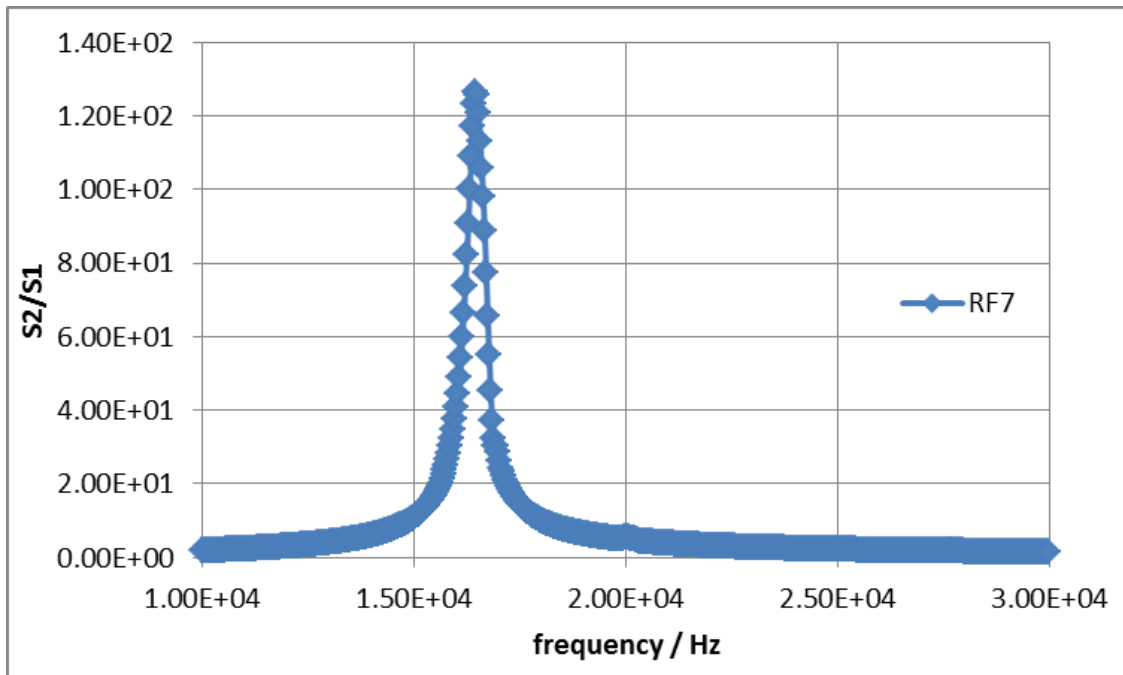


Fig. 7.12. Resonance curve obtained from data acquired using the Network Analyser, when the circuit's resonant frequency was equal to 16.1 kHz.

The values of Q-factor and maximum gain were measured with the Network Analyser for each of the state-variable filters with resonant frequency values as in Tab. 7.8. These values were obtained by calculating the average and standard deviation of ten consecutive measurements obtained with the NA (Tab. 7.9).

Tab. 7.9. First column: resonant frequency of the three state variable filters that were built; second column: Q-factor, measured with the Network Analyser as average values of 10 consecutive measurements; third column: uncertainties of Q, as standard deviation; fourth column: measured values of maximum gain (average of 10 consecutive measurements); fifth column: standard deviation of gain.

$f_r$ (kHz)	Q	err(Q)	G	err(G)
23.6	318.6	0.3	196.7	0.3
19.9	258.8	0.2	150.8	0.2
16.1	192.3	0.2	125.2	0.2

Results reported in Figs. 7.10-7.12 and Q-factor values shown in Tab. 7.9 demonstrated that the state-variable active filter was a better solution compared to the IGMF filter previously tested, due to its response in terms of Q-factor, which was larger than the Q-factor measured with the LCR-parallel circuit by a factor between 8 and 46. This represented a substantial improvement from the scenario resulting from the use of the LCR parallel circuits that were object of the first part of this research work. The next step of the investigations was directed towards modifying the active filter by adding an inductor to it, in order to use the circuit for EII of conductive materials, as detailed in the next section.

## 7.4 Modified state-variable filter with inductor for EII of conductive samples

An inductor was added to the state-variable active filter having schematic as in Fig. 7.7 and component values as in Tabs. 7.7 and 7.8. Three circuits were built, the first one as in the schematic shown in Fig. 7.13, and the others having similar schematics with the only exception of resistors R4=R5, which had values as in the third and fourth rows of Tab. 7.8.

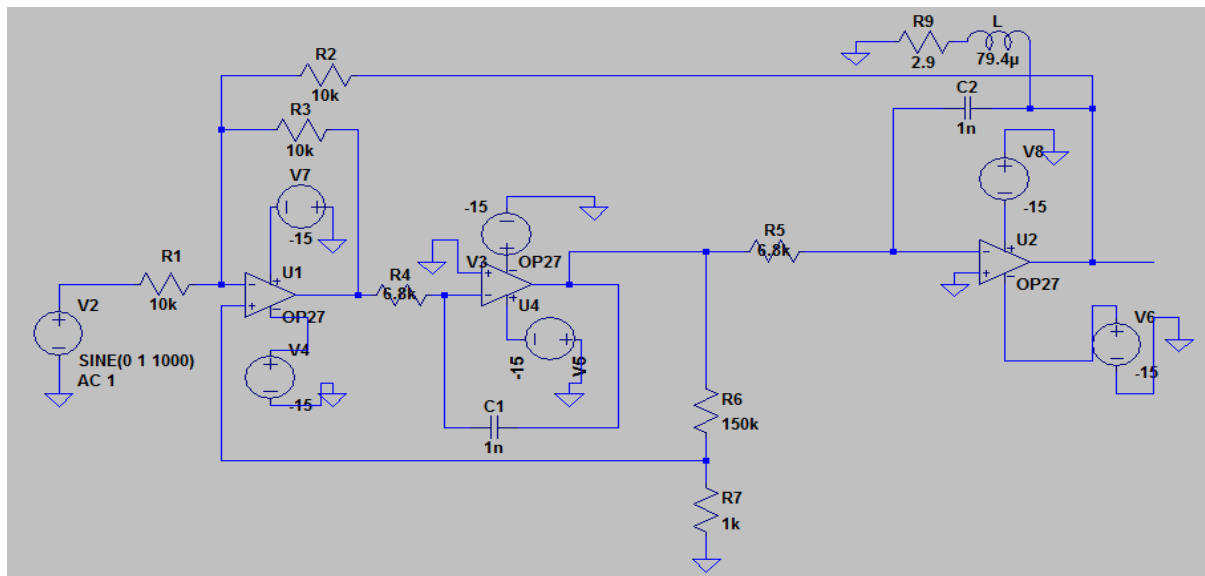


Fig. 7.13. Electronic schematic produced with LTSpiceXVII, representing the electronic circuit on which the improved version of the EII system, object of this work, was based.

The measured curve of S21 vs frequency, obtained with the Network Analyser (NA) by connecting the instrument to the circuit shown in Fig. 7.13, was compared with the circuit's response (gain vs frequency), resulting from a simulation performed with LTSpiceXVII, to ensure that the results obtained with the NA were as expected. The curves obtained in this way are reported in Figs. 7.14-7.15. Similar curves were obtained by using circuits similar to the one shown in Fig. 7.13, with R4=R5 taking on the values listed in the third and fourth rows of Tab. 7.8. The circuits' responses in frequency obtained with the NA are shown in Figs. 7.16 and 7.18. Results of simulations obtained with LTSpiceXVII are reported in Figs. 7.17 and 7.19. Figs. 7.14, 7.16 and 7.18 represent screenshots of the NA, each of which indicate the resonant frequency (first value on the top left of each figure) and the Q-factor, also indicated in the key to each plot of S21 vs frequency.

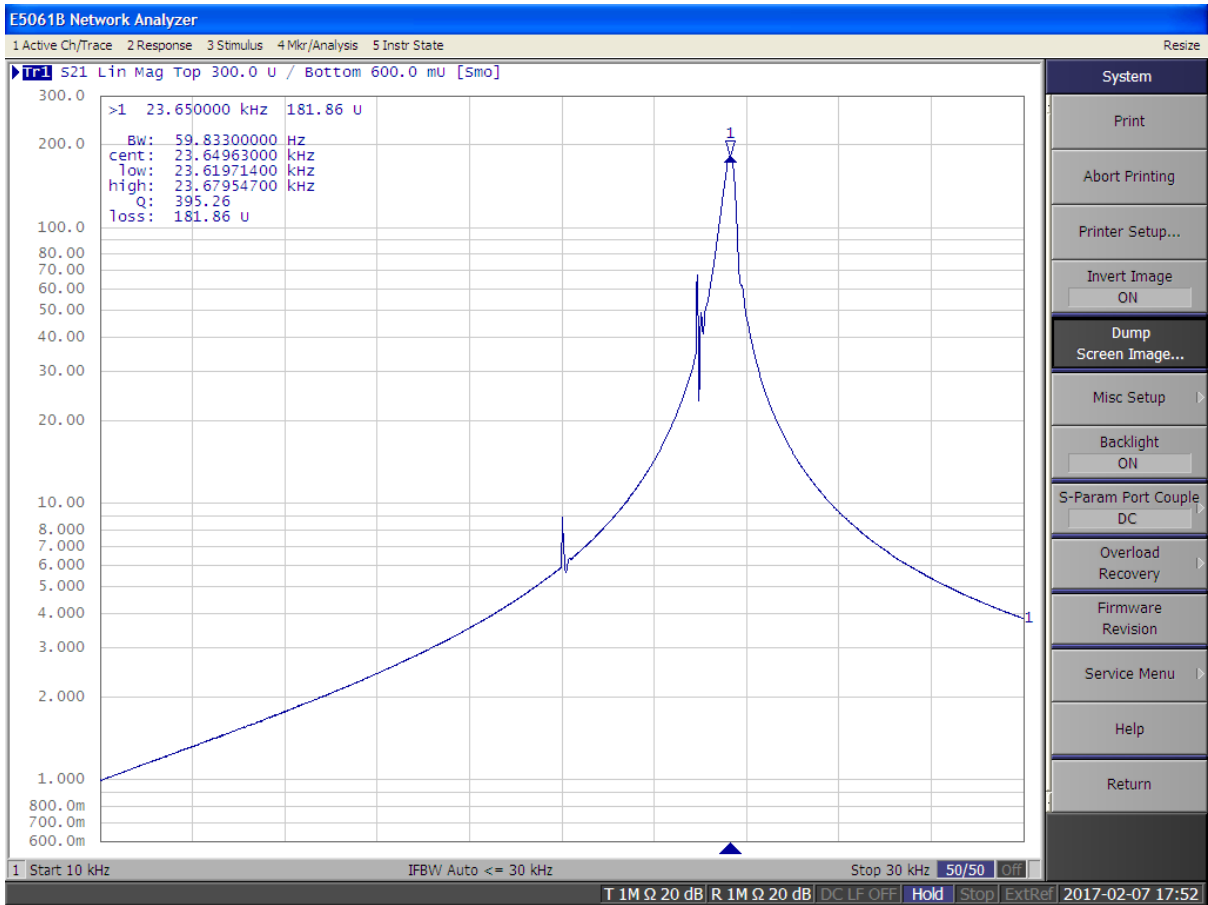


Fig. 7.14. Screenshot from the Network Analyser, obtained after inducing a stimulus (start frequency 10 kHz – stop frequency 30 kHz) in the circuit, having set the circuit’s resistance to  $R_F = 6.8 \text{ K}\Omega$ .

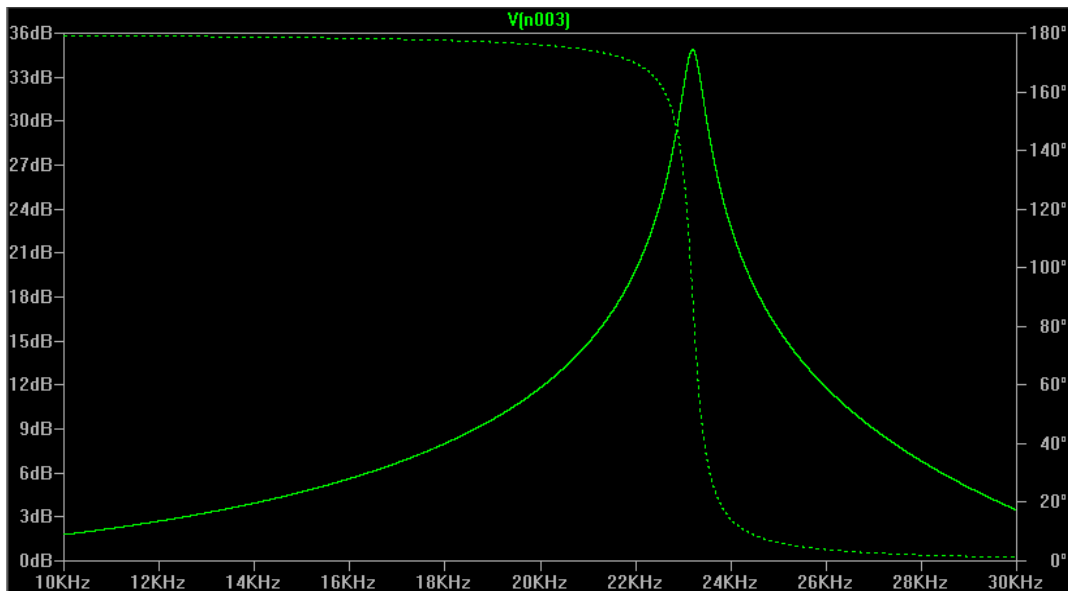


Fig. 7.15. Simulation (from LTSpiceXVII) of the electronic circuit’s response, when its components had values as in Fig. 7.13, and its resistance  $R_F$  was equal to  $R_F = 6.8 \text{ K}\Omega$ .

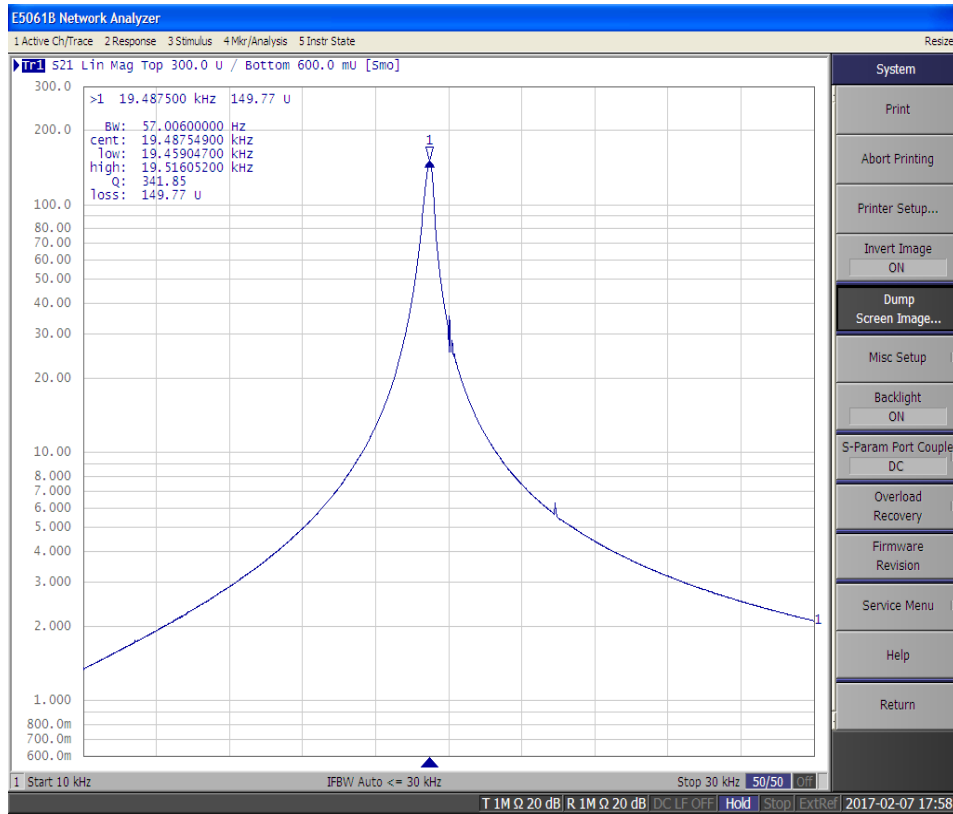


Fig. 7.16. Screenshot from the Network Analyser, obtained after inducing a stimulus (start frequency 10 kHz – stop frequency 30 kHz) in the circuit, having set the circuit’s resistance to  $R_F = 8.2 \text{ K}\Omega$ .

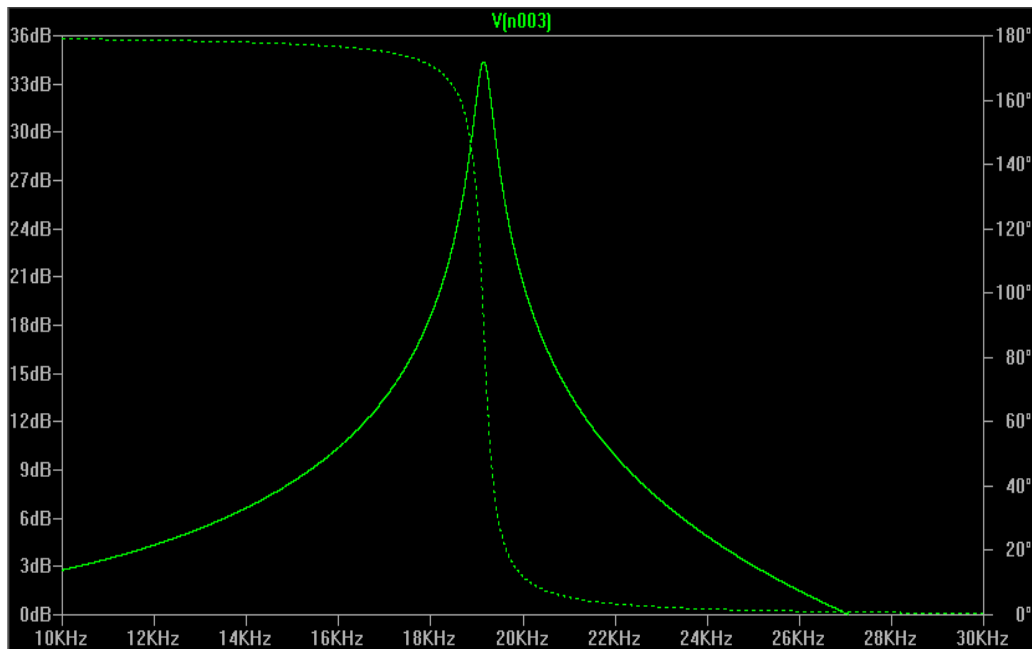


Fig. 7.17. Simulation (from LTSpiceXVII) of the electronic circuit’s response, when its components had values as in Fig. 7.13, and its resistance  $R_F$  was equal to  $R_F = 8.2 \text{ K}\Omega$ .

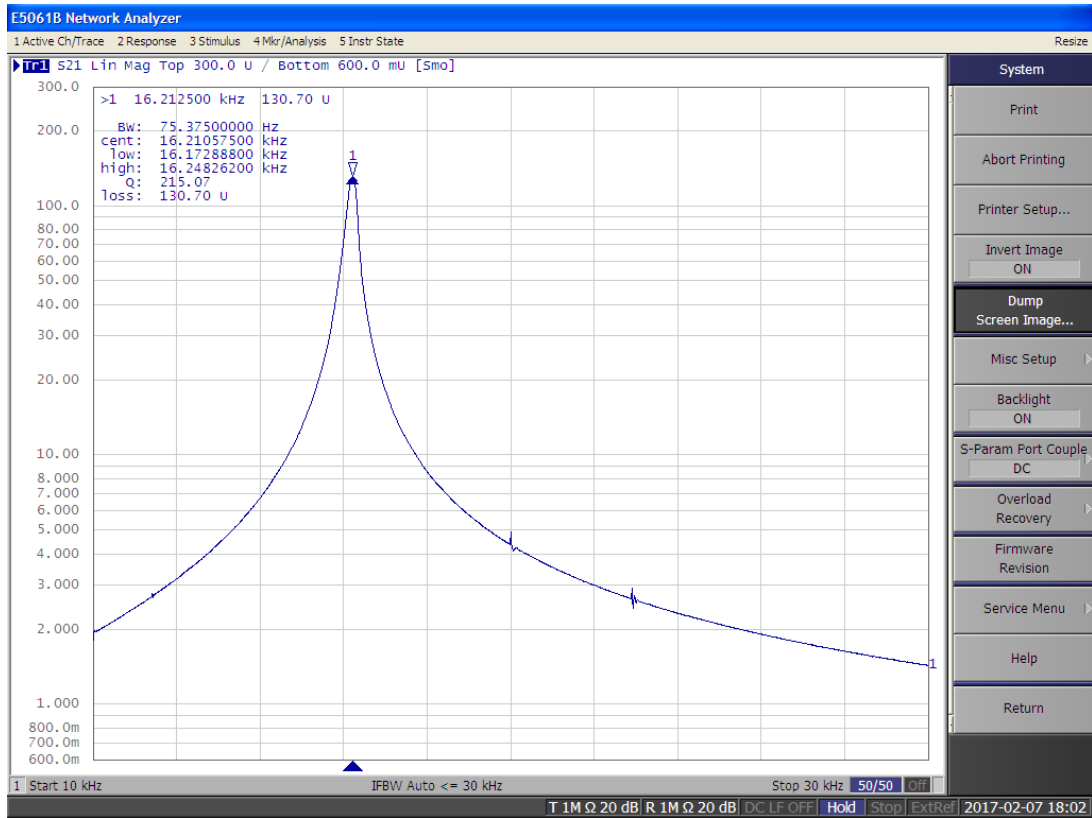


Fig. 7.18. Screenshot from the Network Analyser, obtained after inducing a stimulus (start frequency 10 kHz – stop frequency 30 kHz) in the circuit, having set the circuit’s resistance to  $R_F = 9.9 \text{ k}\Omega$ .

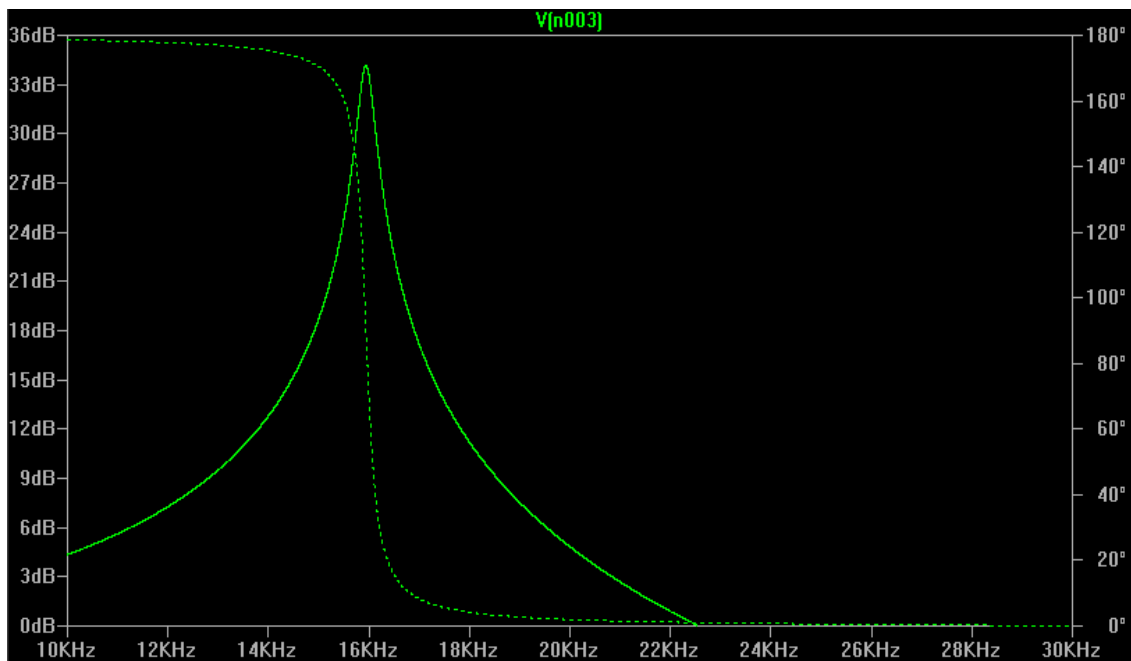


Fig. 7.19. Simulation (from LTSpiceXVII) of the electronic circuit’s response, when its components had values as in Fig. 7.13, and its resistance  $R_F$  was equal to  $R_F = 9.9 \text{ k}\Omega$ .

The curve reported in Fig. 7.14 showed that the measure system's response vs frequency at the value of resonant frequency  $f_{r1}=23.65$  kHz had a spurious peak of non-negligible amplitude that interfered with the Q-factor calculation performed by the NA, because it fell within the bandwidth of the resonance curve. This will be object of a further analysis, conducted in the following section. The resonant frequency values obtained from the simulations reported in Figs. 7.15, 7.17 and 7.19 were, respectively, equal to:  $f_r=23.2$  kHz,  $f_r=19.2$  kHz,  $f_r=15.9$  kHz. These results showed an agreement between measured and simulated data within 2%.

## 7.5 Discussion

The values of resonant frequency obtained with the Network Analyser and from the simulation were in agreement within 2%. The results shown in Figs. 7.14-7.19 demonstrated that the developed system, based on the circuit shown in Fig. 7.13, could be used for detection purposes, given the results of measurements obtained with the NA, which were in agreement with the predicted response resulting from the simulation software (LTSpiceXVII). The values of Q-factor obtained with this active-filter-based circuit were substantially larger by a factor between 17 and 56, compared with the values obtained with the previously used LCR-based system. This result represented a significant improvement for the EII investigations carried out in this research activity. The novel EII system should take detection and imaging of conductive samples to the next level, by enabling material characterisation of samples made of conductive materials ranging from low  $\sigma$  to high  $\sigma$ , as well as detection of samples hidden behind conductive shields.

## 7.6 Measurements of Q-factor shifts to detect the presence of metals

The previous section reported on measurements of Q-factor values of the EII system shown in Fig. 7.13. These measurements have to be put into the context of exploring the system's capabilities with regards to the accomplishment of 2D imaging of metallic samples. Firstly, the choice of measuring Q, rather than the system's resonant frequency, lies on the result reported in Chapter 5, according to which the most sensitive method for imaging was found to be the one based on position-resolved-measurements of the Q-factor (rather than the resonant frequency). Satisfactory results reported in Section 7.6 led to assess the feasibility of the proposed system to achieve results similar to those reported in Chapters 5 and 6. The first question to be answered on this subject was to verify that the novel system enabled measurements of the Q-factor shifts due to the presence of metallic objects having different values of electrical conductivity. Initially, a test was done to quantify the response of the developed EII system when the inductor (labelled "L" in Fig. 7.13 and shown in Fig. 7.20) was in air, i.e., no metal was placed in the vicinity of the coil, and when it was positioned over an Al sample (6-cm-diameter, 2-mm-thick disk). The coil was used both in an air-cored configuration and a ferrite-cored one, for comparison purposes. This was done by inserting a ferrite core into the coil's former and comparing the results with the ones obtained without the core. Upon selection of the value of resistance  $R_F = 6.8 \text{ k}\Omega$  (Tab. 7.8), the system in air was made to resonate at a frequency  $f_r = 23.75 \pm 0.81 \text{ kHz}$  (measured with the NA). The Q-factor was measured using the coil in the two configurations, as follows: 1) when the system was in air; 2) when the Al sample specified above was introduced into the system. The resulting average values (obtained by taking 10 consecutive measurements with the NA) are shown in Tab. 7.10, which includes differences "Delta" between the values obtained for Q in the two configurations, and relative errors, obtained by taking the standard deviation of Q values, and propagating the errors to determine the error on "Delta" ( $\text{Err}(\text{Delta})$ ).



Fig. 7.20. Picture of the coil used in this study ( $L=79.4\pm 10\% \mu\text{H}$ , height  $1.8\pm 0.1 \text{ cm}$ , inner diameter  $2.0\pm 0.1 \text{ cm}$ , outer diameter  $2.3\pm 0.1 \text{ cm}$ ). The coil was connected to the other circuits' components as in Fig. 7.13.

Tab. 7.10. Values of Q measured with Network Analyser when the EII system was in air, when an Al sample was placed under the coil, for both the air-cored and the ferrite-cored coil. The percentage difference between the Q factors in air and Al was calculated (last column).

Coil type	Q in air	Err(Q <sub>air</sub> )	Q with Al	Err(Q <sub>Al</sub> )	Delta	Err(Delta)
Air cored	189	9%	195	10%	3.2 %	16%
Ferrite cored	243	8%	242	10%	-0.4 %	14%

In the investigations conducted in this section and the following ones, the measurement acquisition performed with the NA was optimised by setting the parameters detailed below, both when measurements were taken in air and when the metallic samples were introduced, for consistency.

- Number of points during a sweep of  $S_2/S_1$  vs frequency: 1601
- Average factor (number of repeated independent measurements of which the average was computed by the NA): 16
- Scale of y axis ( $S_2/S_1$  minimum and maximum): 300m - 600
- Frequency range of the applied stimulus: start frequency 10kHz, stop frequency 30 kHz
- Power level of output: -45 dB
- 0.05% smoothing applied to the curve of  $S_2/S_1$  vs frequency.

Resonance curves were obtained by using the NA in the following two scenarios: 1) when the system was "in air" (i.e., in the absence of the metal); 2) when the Al disk was put in contact with the coil, as shown in Figs 7.21-7.22.

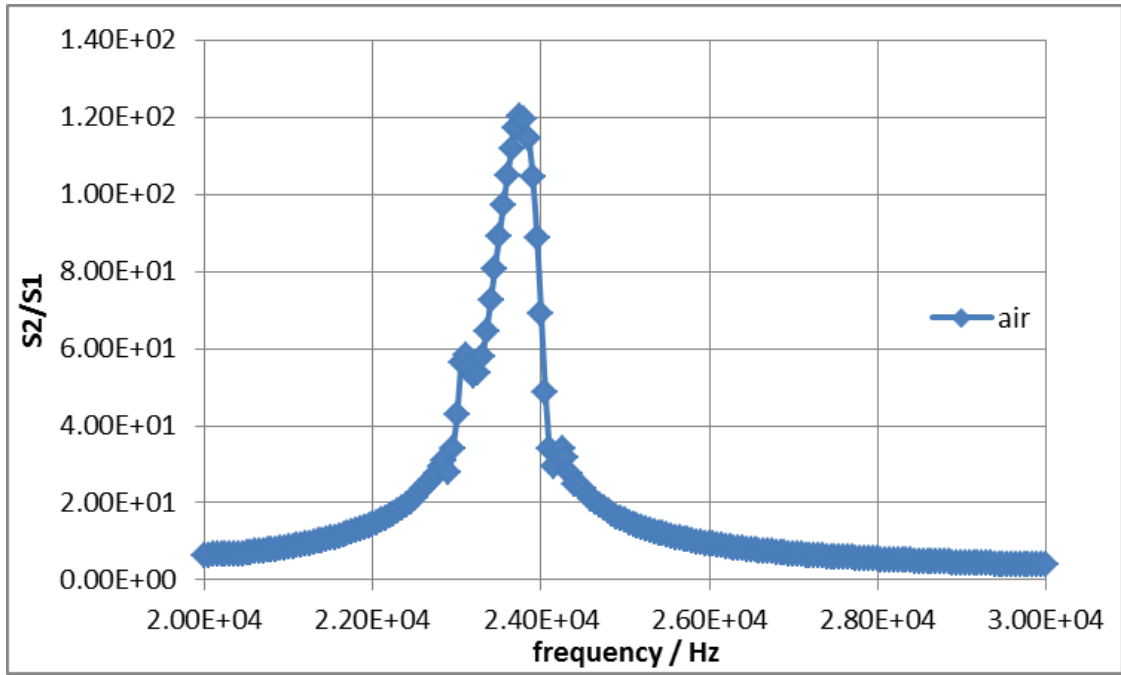


Fig. 7.21. Resonance curve obtained with the Network Analyser when the coil of the EII system was in air, i.e., no metallic sample was present.

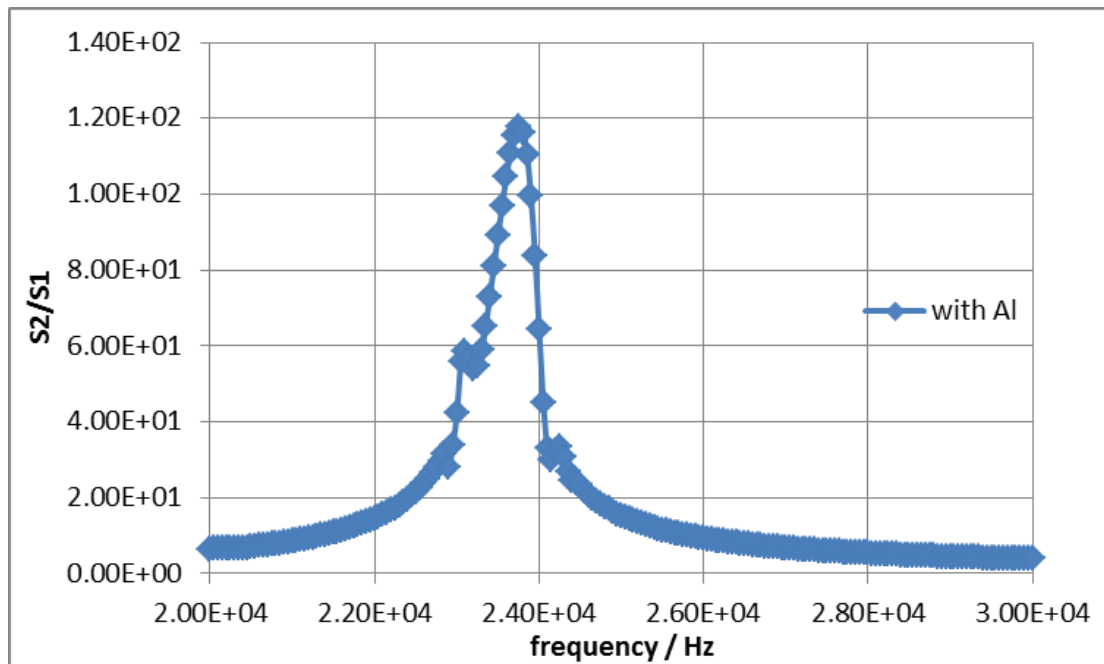


Fig. 7.22. Resonance curve obtained with the Network Analyser, when the coil part of the EII system with schematic as in Fig. 7.13 was in contact with the Al disk sample.

The shift in Q showed by results reported in Tab. 7.10 demonstrated that imaging with the new EII system could be achieved. The circuit's responses obtained with the system in air and with Al, reported in Figs. 7.21 and 7.22, showed a similar trend in the two scenarios, characterised by an unwanted peak at a fixed frequency of 23 kHz, in agreement with what was found in the "S21 vs frequency" plots showed in Figs. 7.14, 7.16 and 7.18.

One clarification must be made about values labelled "Delta" in Tab. 7.10. These values represented the *contrast* of the image reproducing the metallic sample. They were not indications of the capability of the imaging system to distinguish between two different conductors having similar values of electrical conductivity. Such capability was the performance parameter that was the object of the following investigations. These involved calculating the difference between the values of Q-factor obtained when the system was in air and when a Cu sample (with geometry 25x25x1 mm<sup>3</sup> and electrical conductivity values as in Tab. 5.1) was inductively coupled to the system's coil.

The main goal of this part of the investigations was to assess the measurement feasibility of the system for metal samples' detection and, particularly, testing the reproducibility of results in terms of measured Q-factor shifts. For this purpose, a procedure was adopted, based on taking 20 independent measurements of the Q-factor with the NA, at the three values of resonant frequency selectable by tuning  $R_F$  from the circuit shown in Fig. 7.13: 1) 23.6 kHz; 2) 19.9 kHz; 3) 16.1 kHz. The Q-factor average and standard deviation values were calculated in the following scenarios: 1) system in the absence of any metallic sample ("in air") and 2) system coupled to a 25x25x1 mm<sup>3</sup> Cu sample.

Results of this experimental work are reported in Tab. 7.11, which shows measured average Q-factor values obtained in air (second column) and when the Cu sample was coupled to the inductor (fourth column), together with their uncertainties (standard deviation) and Q-factor shifts ("DeltaQ"). The last row of Tab. 7.11 reports values obtained with the previously used LCR-based EII system described in Section 4.3, with  $L=680\pm 10\% \mu\text{H}$ ,  $R=1\pm 1\% \text{M}\Omega$ ,  $C=1 \mu\text{F}$ .

Tab. 7.11. Comparison between the Q-factor values obtained when the new EII system with air-cored coil and ferrite-cored coil was in air (second column) and when a Cu sample was introduced (third column). These Q-factor differences (DeltaQ) were compared to the ones obtained with the previously used LCR-based system (“Old system”, described in Chapter 5).

$f_r=24$ kHz	Q in air	Err(Q <sub>air</sub> )	Q with Cu	Err(Q <sub>Cu</sub> )	DeltaQ	Err(DeltaQ)
Air-cored	138	9%	126	9%	12	13%
Ferrite-cored	146	8%	149	8%	-3	11%
“Old” system	18	1%	14	1%	4	1%

Results shown in Tab. 7.11 highlighted that the Q-factor values of the new EII system were larger by a factor of 8-11, compared to values measured with the previously developed LCR-based system (Tab. 7.11). This showed that the new system represented an improvement from the “old” version. Large measurement uncertainties, though, prevented differences in Q-factor values to allow discrimination between air and Cu. The cause of these large measurement uncertainties will be object of the next sections.

For a more complete investigation, more samples with different conductivity values were included, to assess the EII system’s response when it was coupled to each of them, and its feasibility for detection of low, medium and high conductivity samples, both of ferromagnetic and non-magnetic nature. The following pieces of metal were chosen as representative among the metals listed in Tab. 5.1: copper, manganese, iron (with geometry 25x25x1 mm<sup>3</sup> and electrical conductivity values as in Tab. 5.1).

Tab. 7.12 reports differences DeltaQ between Q-factors measured after placing a 25x25x1 mm<sup>3</sup> metal sample (made of Cu, Mn and Fe) in touch with the coil included in the EII system represented in Fig. 7.13, and Q-factors measured with the system in the absence of the metal, i.e., “in air” (DeltaQ=Q(air)-Q(metal)). The error of these values were calculated by taking the standard deviation of 10 consecutive measurements of Q, and propagating the errors to derive the error of DeltaQ (e.g. “err(air-Cu)” in Tab. 7.12).

Figs. 7.23-7.25 represent values of average Q and their standard deviation obtained as described in the previous paragraph (Tab. 7.12). Values on the y axis of the graphs stand for the three metallic samples described above (material “1”: air, material “2”: Cu, material

“3”: Mn, material “4”: Fe). Each graph reports measurements obtained after making the EII system resonate at the three values of resonant frequency  $f_{ri}$  selectable by tuning the rotary switch: 23.6 kHz, 19.9 kHz, 16.1 kHz. A plot of  $\Delta Q = Q(\text{air}) - Q(\text{metal})$  vs  $f_{ri}$  is shown in Fig. 7.26, in which results of 20 consecutive Q-factor shift measurements (as in Tab. 7.12) are compared to the shifts measured with the “old” LCR-based system, in the following scenarios: system in air and coupled to copper (blue, diamond data-set); system in air and couple to manganese (red, square data-set); system in air and coupled to iron (green, triangle data-set).

Tab. 7.12. Values of average and standard deviation of DeltaQ (first column), at the following resonant frequency values:  $f_{r1}=24$  kHz (second column),  $f_{r2}=20$  kHz (third column) and  $f_{r3}=16$  kHz (fourth column).  $\Delta Q/Q(\text{air})$  are ratios of DeltaQ divided by the Q-factor values measured in air.

DeltaQ	$f_{r1}=23.6$ kHz	$f_{r2}=19.9$ kHz	$f_{r3}=16.1$ kHz
air-Cu	14.2	4.1	4.6
err(air-Cu)	7.7	5.0	4.1
<b>DeltaQ/Q(air) %</b>	4.8	1.6	2.1
air-Mn	-0.3	-2.0	0.9
err(air-Mn)	7.9	4.7	4.1
<b>DeltaQ/Q(air) %</b>	0.1	-0.8	0.4
air-Fe	3.2	-8.4	1.1
err(air-Fe)	7.2	5.2	4.6
<b>DeltaQ/Q(air) %</b>	1.1	-3.4	0.5

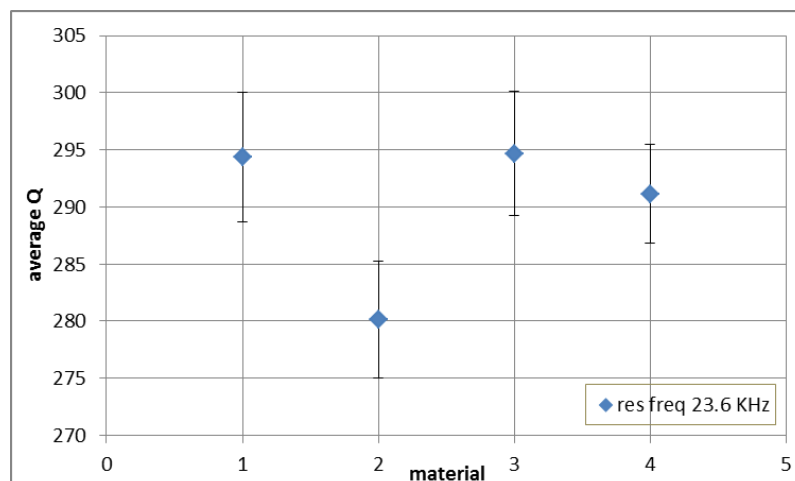


Fig. 7.23. Comparison between the average Q measured with the Network Analyser, when the system was resonating at 23.6 kHz and it was coupled to the following materials: material “1”: air, material “2”: Cu, material “3”: Mn, material “4”: Fe. Error bars were added, by calculating the standard deviation of the measured quantities.

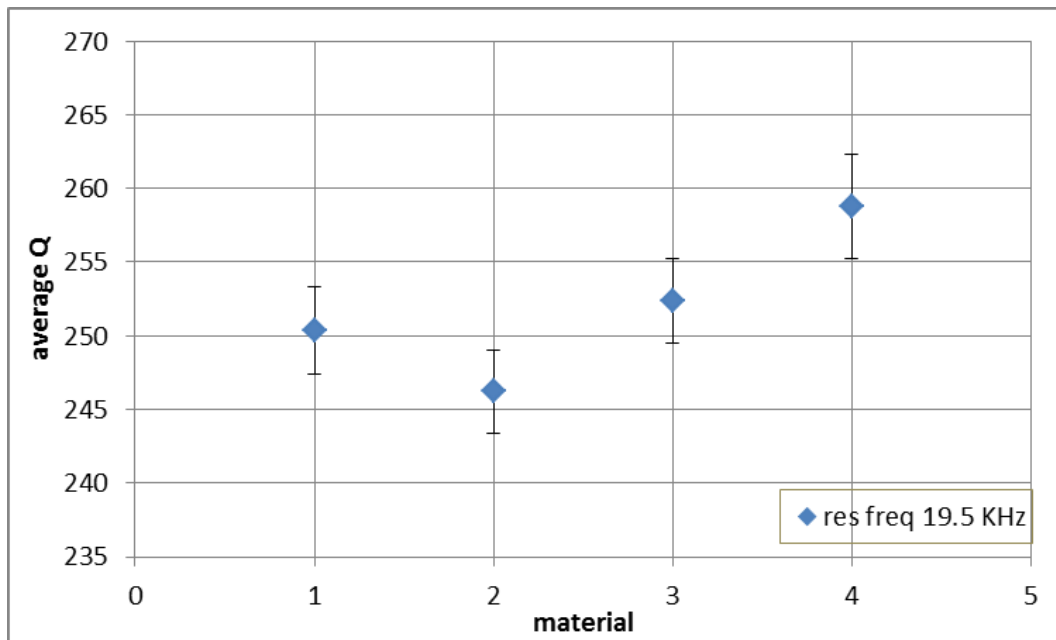


Fig. 7.24. Comparison between the average Q measured with the Network Analyser, when the system was resonating at 19.5 kHz and it was coupled to the following materials: material “1”: air, material “2”: Cu, material “3”: Mn, material “4”: Fe. Error bars were added, by calculating the standard deviation of the measured quantities.

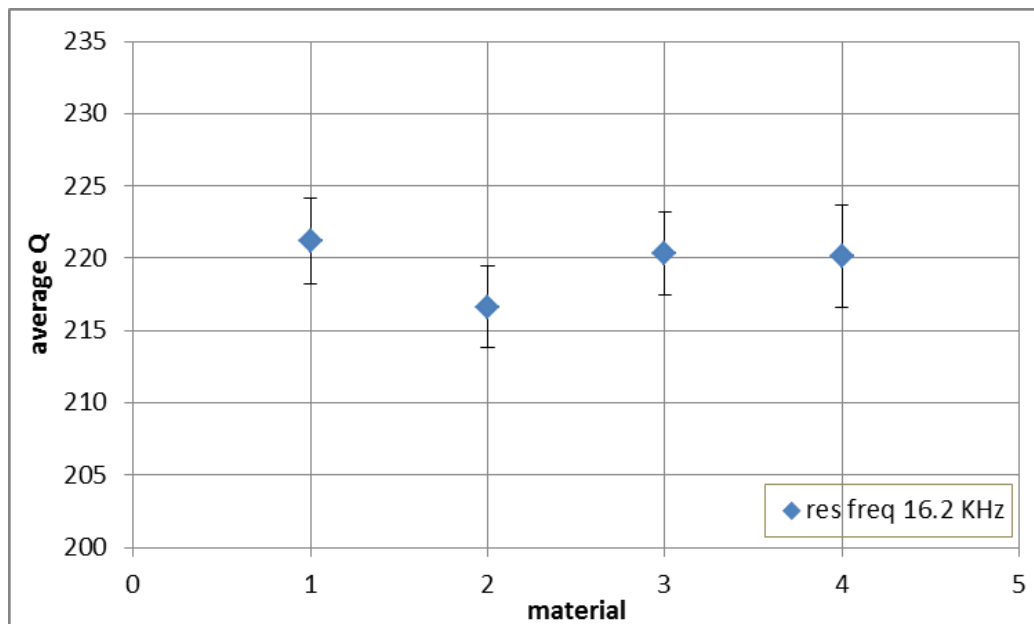


Fig. 7.25. Comparison between the average Q measured with the Network Analyser, when the system was resonating at 16.2 kHz and it was coupled to the following materials: material “1”: air, material “2”: Cu, material “3”: Mn, material “4”: Fe. Error bars were added, by calculating the standard deviation of the measured quantities.

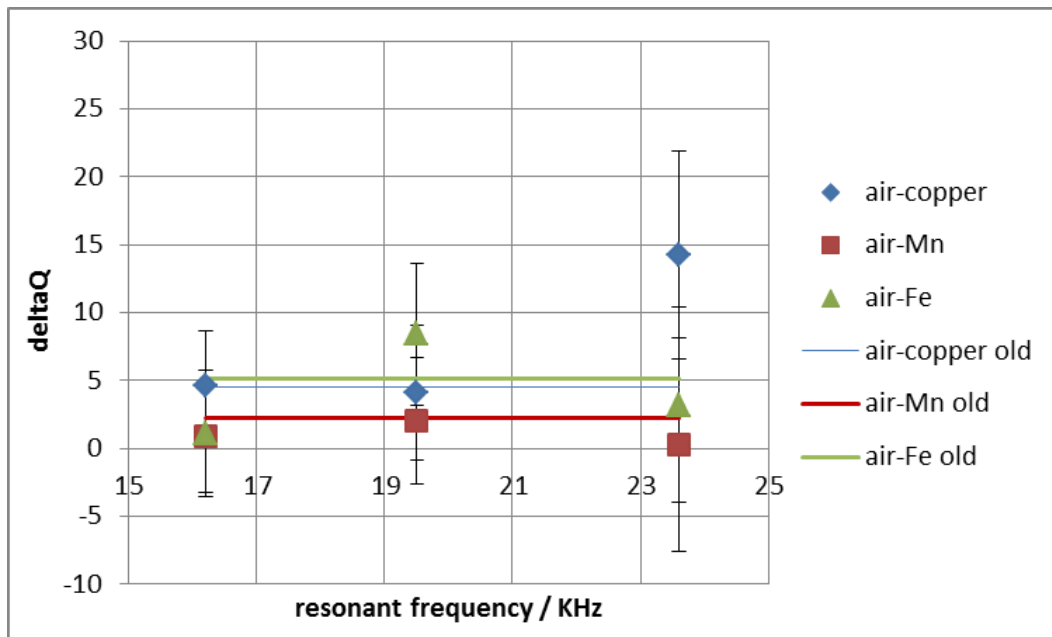


Fig. 7.26. Plot of  $\Delta Q = Q(\text{air}) - Q(\text{metal})$  vs resonant frequency values  $f_{ri}$  (as in Tab. 7.12), obtained from results of 20 consecutive Q-factor shift measurements (Tab. 7.12), compared to the shifts measured with the “old” LCR-based system, in the following scenarios: system in air and coupled to copper (blue, diamond data-set); system in air and couple to manganese (red, square data-set); system in air and coupled to iron (green, triangle data-set).

## 7.7 Discussion

The larger Q-factor values of the new EII system, compared to those measured with the previously developed LCR-based system, showed that the new system represented an improvement from the “old” version (Tab. 7.11). However, poor reproducibility of results was observed when taking consecutive measurements of the same parameter (e.g. Q-factor) in equivalent conditions. Specifically, Q values differed from one measurement to the next one by an amount up to 10% (Tab. 7.10, Figs. 7.23-7.25). This issue became even more serious when the error in the Q-factor shifts ( $\Delta Q$ ) was taken into account (Tab. 7.12, Fig. 7.26). This is because the relative standard errors of the measurements (third and fourth columns of Tab. 7.10) were too large to allow the change in Q-factor values due to the presence of the metal to be significant (Tab. 7.10, sixth column). The large Q-factor uncertainties (“err(air-Cu)”, “err(air-Mn)” and “err(air-Fe)” in Tab. 7.12), compared to the difference in the Q-factor values obtained when the system was in air and when a piece of metal was coupled to it

("DeltaQ/Q(air)" in Tab. 7.12), implied that the EII system could not discriminate between the presence of a high-conductivity sample, at this stage, due to the large measurement uncertainties.

Figs. 7.23-7.26 showed that the measurement uncertainties were dependent on the frequency at which the system resonated and not on the material coupled to the system. In particular, absolute values of Q-factor were found to be larger when the EII system was resonating at 23.6 kHz than at the other two values (Figs. 7.23-7.26). The larger error bars of Q-factor values shown in Fig. 7.23 showed the poorer reproducibility of results obtained at 23.6 kHz, compared to those obtained at lower values of frequency. This behaviour was attributed to the presence of spurious peaks at 23 kHz, already detected with the system and reported in Figs. 7.14, 7.16, 7.18, 7.21 and 7.22 in Section 7.4. These figures showed that the curve of the system's response vs frequency at this value of resonant frequency had a 'spurious' peak of non-negligible amplitude that interfered with the Q-factor calculation performed by the NA, because it fell within the bandwidth of the resonance curve (Figs. 7.14, 7.21 and 7.22). The presence of the spurious peak at 23 kHz 'disturbed' the measurements around this frequency while having no impact on the ones at the other two frequency of operation, because of the fixed frequency position of the spurious peak. This explained the higher standard deviation values of the sets of measurements obtained at 23.6 kHz, compared to the ones obtained for smaller resonant frequencies (19.9 and 16.1 kHz), where the spurious peaks did not fall within the region of the curves where the Q-factor values were calculated. The graph reported in Fig. 7.23, obtained with  $f_{r1}=23.6$  kHz, confirmed this explanation, since it showed that the system's Q-factor values produced by the presence of Mn and Fe samples did not significantly differ from the corresponding values measured with the same system when this was in air, due to the large error bars.

These results are important because they underline that the current system and measurement method did not allow distinguishing between the presence of low and medium conductivity metals such as Mn and Fe, due to the large uncertainties of measurements. High-conductivity copper was the only metal that produced a significant shift from the scenario in which the system was in air. The larger Q-factor shift produced by this metal, compared to

the other two, is in agreement with results found with the old LCR-based EII system (Chapter 5).

As regards measurement results obtained with values of resonant frequency equal to  $f_{r2} = 19.5$  kHz and  $f_{r3} = 16.2$  kHz, two observations can be made by looking at Figs. 7.24 and 7.25. Firstly, the absolute values of Q-factor are lower than those measured at resonant frequency  $f_{r1} = 23.6$  kHz, thus implying that this value represented the most suitable operational frequency of the EII system. At the frequency  $f_{r2} = 19.5$  kHz, the only metal that produced a significant shift in the system's Q-factor was iron. The values of Q obtained with non-magnetic metals did not differ significantly from the value measured in air. The lowest selectable resonant frequency  $f_{r3} = 16.2$  kHz did not allow to distinguish any of the metal samples from the "air" scenario.

Investigations were carried out to determine the source of the spurious peaks found at 23 kHz in all resonance plots (Figs. 7.14, 7.16, 7.18), as will be detailed in Section 7.8. This was beneficial because the largest Q-factor absolute values were obtained with the system resonating at  $f_r = 23.6$  kHz, thus making this value of resonant frequency ideal for the investigations carried out in this work.

## 7.8 Initial investigations to determine the sources of spurious peaks

Investigations around the origin of the unwanted peaks that were causing large uncertainties in the Q-factor measurements are object of this section. Improvements in the measurement precision could be attained by either acting on the measurement system, or improving the measurement method, or both. This needed to be done before focusing the attention towards investigating the effect that different conductive materials produced on the novel EII system. The measurement system and method were based on the use of the Network Analyser, the electronic circuit and the power supply feeding it. With this in mind, two hypotheses were initially made and tested, in order to identify the origin of the unwanted

peaks, which was causing the poor measurement reproducibility. The first hypothesis was that the NA averaging function had introduced the unwanted peaks at 23 kHz into the “S21 vs frequency” plots. The second hypothesis was that the power supply might have been the cause of the unwanted peaks.

To test the first hypothesis, the fit done by the NA on the data of the circuit’s frequency response was compared to the response obtained without using the averaging function of the NA. This was accomplished by taking one frequency sweep after inducing a stimulus in the circuit, and switching off the data averaging function. After this, 9 more sweeps were taken, the 10 resulting curves were overlapped to see whether they were different. The result was that no differences were found, implying that the NA averaging function was unlikely to cause problems. To further investigate the impact of the NA averaging function on measurements, Q was measured “in air” (setting the following parameters with the NA: 1601 points, log y axis 300m – 600, stimulus 10 kHz – 30 kHz, power -45 dBm, 0.05% smoothing) in two different ways. Firstly, the NA averaging function was set to “OFF”, single measurements of Q were taken with the instrument and then averaged manually. Secondly, the NA averaging function was switched to “ON”, the same number of total measurements as before was taken and the NA performed the average and standard deviation of measurements. Results are shown in Tab. 7.13, in which the first two columns report Q values obtained with the averaging function switched off, by taking 30 and 100 consecutive measurements (third and fourth rows, respectively); the last two columns report Q values obtained by setting the averaging factor of the NA to 10 and taking, respectively, three and ten consecutive measurements of Q (third and fourth rows).

Tab. 7.13. Results of the study of the influence of the automatic averaging of the NA. In the table, “meas” stands for “measurements”; av(Q) stands for average of Q, calculated by taking 30 and 100 consecutive measurements without using the NA averaging function (3<sup>rd</sup> and 4<sup>th</sup> rows of the first column) and performed using the NA averaging function of the same number of measurements (third column); corresponding standard deviations are reported in the second and fourth columns ( $\sigma Q$ ).

av(Q)	$\sigma Q$	av(Q)	$\sigma Q$
AVERAGING OFF	AVERAGING OFF	AVERAGING ON (10)	AVERAGING ON (10)
363 (30 meas)	37 (30 meas)	339 (3x10 meas)	12 (3x10 meas)
313 (100 meas)	29 (100 meas)	297 (10x10 meas)	4 (10x10 meas)

The difference between values of  $av(Q)$  reported in the second and fourth of Tab. 7.13 were attributed to the varying amplitude of the spurious peaks systematically found at 23 kHz, which caused the Q-factor values to vary from one measurement to the next one. Discussion of these results is reported in the next two pages.

The potential effect of leaving the power supply on while taking measurements was investigated to test the second hypothesis that was made to find the source of the spurious peaks at 23 kHz. For this purpose, a series of measurement acquisitions was done by switching off the power supply after each measurement sweep, with details as below and results as in Tab. 7.14:

- a) 30 single measurements were taken with the NA, by switching off the power supply between each of the measurement acquisitions (2<sup>nd</sup> and 3<sup>rd</sup> columns of Tab. 7.14);
- b) The NA averaging factor was set to 10, and 3 consecutive measurements were taken, by switching off the power supply as before, and waiting 30 mins after the power supply was switched on again, before starting the measurement acquisition (4<sup>th</sup> and 5<sup>th</sup> columns of Tab. 7.14).

Tab. 7.14. Results showing the influence of the power supply being left on, or switched on and off in between consecutive measurements.

	<b>av(Q)</b>	<b><math>\sigma Q</math></b>	<b>av(Q)</b>	<b><math>\sigma Q</math></b>
	AVERAGING OFF	AVERAGING OFF	AVERAGING ON (10)	AVERAGING ON (10)
Power supply switched off each time	332 (30 meas)	40 (30 meas)	291 (3x10 meas)	4 (3x10 meas)
Power supply left on	363 (30 meas)	37 (30 meas)	339 (3x10 meas)	12 (3x10 meas)

The lowest measurement uncertainty found when the NA automatic averaging function was switched on (Tabs. 7.13-7.14) implied that using it increased the measurement precision and it was established that this should be done when taking Q-factor measurements.

The issue linked to the presence of spurious peaks was not solved by switching off the power supply after each measurement sweep, which led to eliminating this hypothesis, as well as the one based on the use of the NA automatic averaging function. Lowest measurement uncertainties observed from values in the third and fifth columns of Tab. 7.14 were in agreement with results reported in Tab. 7.13 and confirmed the decision of adopting the NA automatic averaging function to improve the measurements' precision.

Finally, the awaiting time between the moment at which the power supply was turned on and the start of the measurement acquisition was varied, to see whether this impacted the measurements and to determine an 'ideal' awaiting time. The aim of this investigation was determining the optimal conditions for the measurement acquisition process. The following measurement scenarios were used for this purpose:

- 1) After the power supply had just been turned on, 10 frequency sweeps were performed with the NA averaging function being set to ON (with averaging factor=10).
- 2) 30 minutes after the power supply was switched on, 10 sweeps were performed in the same conditions as in 1).

The results in terms of average Q and standard deviation were as follows:

- 1)  $av(Q)=303, \sigma Q=6$ .
- 2)  $av(Q)=297, \sigma Q=4$ .

The smaller uncertainty found with a 30-minutes-waiting-time led to establishing that this awaiting time was to be used when taking Q-factor measurements, in order to contain their random uncertainties.

In conclusion, neither the power supply nor the NA automatic averaging function were found to have an impact on Q-factor measurements that could explain the origin of the unwanted peak observed at 23 kHz in plots of S21 vs frequency. Further investigations were conducted to solve the issue linked to the presence of this peak that prevented the system to be optimal for detection and imaging of conductive samples. The next section reports on an analysis which was conducted to compare the EII system based on active filters to the "old"

LCR-based circuit and Section 7.9 describes a method developed to remove the unwanted peak and perform measurements of Q-factor with the proposed system.

## 7.9 Towards the optimisation of a novel EII system for detection of conductive objects

The purpose of this part of the research was to test the new system based on active filters and check whether this could produce better results than the LCR-based system developed in the first half of this research work (Chapters 4-6). The final goal was to test the new system in terms of its capability of producing 2D imaging of metallic samples for security applications (Section 7.9). A crucial dilemma needed to be resolved in the first place, which was whether the new EII system represented an optimised version of the previous one, or whether the higher Q-factor values (Section 7.5-7.7) were the result of a more precise measurement acquisition achieved by using the NA instead of the previously used impedance analyser (IA). With this in mind, an issue arose by considering that the investigations carried out so far involved changes of two parameters, one being linked to the two different measurement systems (LCR-parallel circuit and active-filter-based circuit as in Fig. 7.13), the other one being given by the different instruments that were used to perform the measurements (IA vs NA). As long as two parameters were changed at the same time, no answer to the dilemma above could be found. For this reason, a consistent method needed to be determined to assess whether the new system, based on active filters, represented an improvement w.r.t. the “old” LCR-based system. This was based on changing a single parameter at a time, to understand where the cause for the larger values of Q-factor lied, and establish an improved method for detection and imaging of conductive samples. For this purpose, the following actions were taken.

- 1) The active filter-based system was connected to the impedance analyser (IA) and a series of 10 consecutive Q-factor measurements were performed with this instrument. This was done by placing a piece of Cu (25x25x1 mm<sup>3</sup>) under the coil

shown in Fig. 7.20, which was part of the EII system based on the circuit represented in Fig. 7.13. This experiment is reported in Section 7.9.1.

- 2) The same series of measurements as in 1) was performed by using the LCR circuit constituting the “old” system, by means of the impedance analyser. This experiment is reported in Section 7.9.2.
- 3) Results obtained from 1) and 2) were compared and differences in the Q-factor measurements evaluated.

At this point, the following plan was established. If the active filter-based system produced better results, then the conclusion would be that the new system represented an improvement of the older one, and was worth investigating further. To this extent, the following should be done:

- 1) The active-filter based system needed to be connected to the NA and measurements acquired in this configuration, first in air and then by placing a piece of Cu (25x25x1 mm<sup>3</sup>) under the coil;
- 2) The Q-factor shifts produced when the system was in air and when a metallic sample was placed under it should be compared with the ones obtained with the LCR-based system.

If the active filter-based system was not found to be better than the older one, based on the comparison of results obtained from 1) and 2), then it would mean that future investigations should be directed towards finding a more precise instrument than the IA to perform measurements, for instance the NA.

### 7.9.1 Active-filter-based circuit connected to the impedance analyser

Q-factor measurements were performed with the active-filter-based circuit shown in Fig. 7.13, by connecting it to the impedance analyser, and conducting a frequency sweep of the impedance  $Z$  vs frequency, in a range of frequency centred around the system's resonant frequency, with start and end frequency values as follows:  $f(\text{start})=5$  kHz,  $f(\text{stop})=15$  kHz. Resonant frequency values obtained from the "Z vs frequency curve", as well as inductance, capacitance and resistance values of the system, measured with the IA, are reported in Tab. 7.15.

Tab. 7.15. Results of 10 consecutive measurements of Q-factor, resonant frequency, inductance, capacitance and resistance, measured when the active filter-based system was in air and when a piece of Cu was placed under the coil.

	Air					Cu				
	Q	$f_r$ (kHz)	L ( $\mu\text{H}$ )	C ( $\mu\text{F}$ )	R ( $\Omega$ )	Q	$f_r$ (kHz)	L ( $\mu\text{H}$ )	C ( $\mu\text{F}$ )	R ( $\Omega$ )
1	52.8	32.6	2.6	9.0	28.5	40.8	32.4	2.0	12.4	16.2
2	21.6	31.0	9.8	2.7	41.1	17.2	30.8	9.5	2.8	31.8
3	5.9	32.5	18.4	1.3	22.0	10.9	30.9	15.1	1.8	32.1
4	18.6	31.0	10.5	2.5	38.0	16.6	31.6	6.7	3.8	22.2
5	18.7	31.3	11.1	2.3	40.8	13.4	30.9	13.0	2.0	33.8
6	13.1	31.4	15.4	1.7	39.6	7.3	31.0	22.3	1.2	31.8
7	13.5	32.3	11.3	2.2	30.9	17.0	30.9	9.2	2.9	30.3
8	35.3	32.5	3.2	7.5	23.1	7.9	30.9	21.5	1.2	33.0
9	23.9	32.5	5.6	4.3	27.2	16.1	30.9	10.2	2.6	32.1
10	36.0	31.1	6.2	4.2	43.5	43.2	32.4	2.2	11.1	19.2

The following values were found after taking the average and standard deviation of values reported in Tab. 7.15. In air:  $\text{av}(Q)=20.7$ ,  $\sigma Q=10.0$ ; with Cu:  $\text{av}(Q)=13.3$ ,  $\sigma Q=4.1$ . The Q-factor shift between air and Cu was found to equal  $\Delta Q=7$ , with an uncertainty equal to  $\sigma(\Delta Q)=11$ . Such a large uncertainty was due to the background noise which prevented the Q-factor measurement to be more precise and implied that this measurement system did not produce a significant Q-factor shift that could be used to identify the presence of conductive samples. The Z vs frequency sweeps obtained in this part did not include any spurious peaks as the one observed in plots of  $S_{21}$  vs frequency obtained with the NA.

## 7.9.2 LCR system used in conjunction with the impedance analyser

Q-factor measurements were performed with the “old” LCR system, based on a ferrite-cored coil ( $L=680\pm 10\% \mu\text{H}$ ), a capacitor  $C=0.5\pm 1\% \mu\text{F}$ , and a resistor  $R=10\pm 1\% \text{K}\Omega$ , by connecting it to the impedance analyser, as described in Chapter 4.

Resonant frequency values, measured in air and with Cu with the IA, were respectively equal to: 9.1 kHz and 10.2 kHz. Results were reported in Tab. 7.16.

Tab. 7.16. Results of 10 consecutive measurements of Q-factor, inductance, capacitance and resistance, measured with the IA when the LCR system was in air and when a piece of Cu was placed under the coil.

	Air				Cu			
	Q	L ( $\mu\text{H}$ )	C (nF)	R ( $\Omega$ )	Q	L ( $\mu\text{H}$ )	C (nF)	R ( $\Omega$ )
1	21.3	612.3	501.1	743.1	11.3	490.4	497.0	354.6
2	21.4	613.5	500.3	748.8	11.3	490.9	496.5	354.4
3	21.4	613.4	500.3	751.0	11.3	491.0	496.2	354.5
4	21.2	613.0	500.4	741.4	11.3	491.0	496.2	354.8
5	21.2	613.1	500.5	741.0	11.3	491.1	496.1	354.9
6	21.2	613.2	500.2	743.3	11.3	491.1	496.0	355.0
7	21.2	613.5	500.0	743.3	11.3	491.1	496.1	355.0
8	21.2	613.4	500.3	741.7	11.3	491.2	496.0	355.0
9	21.2	613.2	500.3	743.2	11.3	491.1	496.2	354.9
10	21.2	613.3	500.4	742.1	11.3	491.0	496.3	355.1

The following values were found after taking the average and standard deviation of values reported in Tab. 7.16. In air:  $\text{av}(Q)=21.3$ ,  $\sigma Q=0.1$ ; with Cu:  $\text{av}(Q)=11.3$ ,  $\sigma Q=0.01$ . The Q-factor shift between air and Cu was found to equal  $\Delta Q=10$ , with an error equal to  $\sigma(\Delta Q)=0.1$ . Comparison of these uncertainties with the much larger values obtained with the NA and reported in Tabs. 7.12-7.14 implied the best measurement precision obtained with the IA. This was caused by the absence of spurious peaks found with the NA at fixed frequency (around 23 kHz), from plots obtained with the IA. However, the Q-factor absolute values were much smaller than the ones obtained with the active filter-based system (Sections 7.5-7.7), as already noted from results shown in Chapter 5.

The results obtained from this experiment were compared to those obtained with the active-filter-based system and the IA (Section 7.9.1), and with those obtained using the active-filter-based system and the NA, as reported in Tab. 7.17.

Tab. 7.17. Q-factor average values in air and with Cu (2<sup>nd</sup> and 4<sup>th</sup> columns), differences between these two values, DeltaQ=Q(air)-Q(metal) (6<sup>th</sup> column), standard deviations (3<sup>rd</sup>, 5<sup>th</sup> and 7<sup>th</sup> columns); measurements were obtained with the IA=impedance analyser (first two rows) and the NA (last three rows).

	<b>Q(air)</b>	<b><math>\sigma</math>Q(air)</b>	<b>Q(Cu)</b>	<b><math>\sigma</math>Q(Cu)</b>	<b>DeltaQ</b>	<b><math>\sigma</math>(DeltaQ)</b>
LCR – IA	21.3	0.1	11.3	0.01	10	0.1
FILTER – IA	21	10	13	4	7	11
FILTER – NA 23.6 kHz	294	6	280	5	14	8
FILTER – NA 16.1 kHz	221	3	217	3	5	4
FILTER – NA 19.9 kHz	250	4	246	3	4	5

Three observations should be pointed out after examining results reported in Tab. 7.17. Firstly, absolute values of Q reported in Tab. 7.17 highlight the larger values obtained with the active-filter-based system w.r.t. those obtained with the IA. The Q-factor values measured when the active-filter-based system was in air and when a Cu sample was coupled to it were larger by a factor of 14 and 25, respectively, compared to corresponding values obtained with the LCR-based system. Secondly, the largest difference between Q in air and Q with Cu (DeltaQ) was attained when the active-filter-based system resonating at 23.6 kHz was used. Thirdly, the measurement uncertainties for the active-filter-based system were larger than those obtained with the LCR-based system. This was attributed to the presence of the spurious peak affecting measurements taken with the filter resonating at 23.6 kHz and removal of the spurious peak is addressed in the next Section.

## 7.10 Removal of spurious peaks and 2D imaging of conductive samples

The spurious peaks found at fixed frequency (around 23 kHz) were not present with the IA, meaning that they were unlikely to be due to the filter-based system, since if that was the case, these peaks would rise in the presence of both the IA and the NA. Based on this conclusion, a hypothesis was made, based on which the cables connecting the filter-based circuit to the NA may be the source of the unwanted peaks. According to this hypothesis, the cables' parasitic capacitance was causing the peaks at 23 kHz. If this had been the case, then changing the cable length would have shifted the frequency of the peaks. This experiment was done by connecting two coaxial BNC cables to the ones originally used (each with an N-type connector on one ending), by means of two double male connectors. The frequency of the peaks did not vary, which meant that the hypothesis was false.

Following this, the influence of computer's monitors and signals from the surrounding instrumentation was checked, thinking those may have been possible sources of the unwanted peaks. The results were negative, though.

Finally, the hypothesis that the spurious signal might come from the surrounding experimental equipment was made. To test this hypothesis, the experimental set-up, including the box containing the active-filter-based circuit, the cables connecting it to the NA and the power supply, and the power supply itself, were wrapped up with Al foil. The spurious peaks could not be eliminated this way either. Therefore, the following hypotheses were rejected: 1) the source of the unwanted peak was coming from the environment, and 2) the signal producing it could be screened by using Al foil.

A method was then developed to remove the spurious peaks from the data. Two options were considered, which were based on the observation that the peak amplitude was not constant when different frequency sweeps were performed, and changed from one measurement to the next one in an uncontrolled way (it also changed when the Al foil was used). The important observation that was taken into account was that the unwanted peak was always falling within the same range of frequencies, between 22.9 kHz to 23.1 kHz. This

constituted the criteria on which the choice of a method to remove the unwanted peak was based. The first option which was considered was to modify the hardware in order for the circuit to filter the frequencies around which the unwanted peak was found. The second option, which was adopted, as described in the following, was to use a peak removal algorithm to modify the data measured with the NA and remove the spurious peak from the curve of S21 vs frequency. The measurement acquisition was performed by setting the resonant frequency of the active-filter-based circuit to the value  $f_r= 23.6$  kHz, because this value produced larger Q-factor absolute values, as noted in Section 7.7. This was achieved by initially performing a frequency sweep of the S-parameter S21 with the NA, as described on page 165. A *Matlab* script was written to do the following:

- 1) read the data from the NA;
- 2) plot the S-parameter S21 against the frequency values;
- 3) fit the curve of S21 vs frequency with the function expressed by Eq. 7.20:

$$y(x) = \frac{1}{\sqrt{a^2 + \left(\frac{b}{2\pi x} - 2\pi cx\right)^2}} \quad (7.20)$$

In Eq. 7.20, the parameters  $a$ ,  $b$  and  $c$  satisfied the following equations:  $a=1/R$ ,  $b=1/L$ ,  $c=C$  ( $R$ =effective resistance,  $L$ =effective inductance,  $C$ =effective capacitance).

- 4) derive  $R$ ,  $C$ ,  $L$  from the fit parameters, and use them to calculate  $Q$  as in Eq. 4.2;
- 5) follow point 1) and remove 13 data points contributing to the spurious peak. These were data points lying within a range of frequency characterised by the lower frequency  $f_1=22.9$  kHz and the upper frequency  $f_2=23.1$  kHz;
- 6) follow points 2) to 3) and fit the new data curve with the function expressed by Eq. 7.20;
- 7) find values of  $R'$   $C'$   $L'$  and  $Q'$  from the fit of the new curve (after data point removal).

The procedure above was repeated for ten curves of S21 vs frequency, acquired in sequence with the NA, and calculating the average and standard deviation of the quantities  $L$ ,  $R$ ,  $C$  and  $Q$ , and  $R'$   $C'$   $L'$  and  $Q'$ . The measurement errors of these quantities were calculated

by propagating the errors of the fit parameters  $a$ ,  $b$  and  $c$  (estimated by *Matlab* with 95% confidence bounds).

A comparison was made between values of  $Q'$  and  $L'$  obtained when the system was in air and when three  $25 \times 25 \times 1 \text{ mm}^3$  samples made of Cu, Mn and Fe, respectively, were placed under the coil.

## 7.11 Results and discussion

The original resonance curve was characterised by the following value of Q-factor, measured with the NA:  $Q=79.1 \pm 1.9$ . The Q-factor of the modified curve, after the data removal algorithm was applied, had the following value:  $Q'=82.9 \pm 1.3$ . These results imply that reduction of the measurement percentage error was successfully achieved by adopting the algorithm.

Tab. 7.18 shows  $Q'$  and  $L'$  values obtained in air and with Cu (2<sup>nd</sup> and 3<sup>rd</sup> columns). Differences between values of  $Q$  and  $L$  in air and when the metal was introduced into the system are reported in the fourth and sixth columns of Tab. 7.18. Uncertainties of these values are listed in the fifth and seventh columns of the table.

Tab. 7.18. Average values of Q-factor  $Q'$  and inductance  $L'$ , obtained after the Matlab fitting routine was run, after applying the peak removal algorithm to the curve of  $S_{21}$  vs frequency, measured with the NA. Uncertainties were calculated as standard deviation of the measurements. The 4<sup>th</sup> and 6<sup>th</sup> column list relative variations between values obtained in air and after a Cu sample was coupled to the system, calculated using Eqs. 7.21-7.22. These results were obtained when the resonant frequency of the active-filter-based system was set to the value  $f_r = 23.6 \text{ kHz}$ .

	$Q'$	$L'$	DeltaQ	ErrDeltaQ	DeltaL	ErrDeltaL
Air	51.0	1.6E-5	69.5%	0.7%	30.8%	0.3%
Cu	86.5	1.1E-5				

The algorithm for the spurious peak removal successfully increased the system capability of detecting conductive samples, since the Q-factor and L-shifts were significantly larger than the measurement uncertainties obtained with this method (ErrDeltaQ and ErrDeltaL in the 5<sup>th</sup> and 7<sup>th</sup> columns of Tab. 7.18).

The differences between the Q-factor values obtained with the system in air and when Cu, Mn and Fe were placed under the coil were as follows:  $\Delta Q(\text{air-Cu})=35$ ,  $\Delta Q(\text{air-Mn})=0.24$  and  $\Delta Q(\text{air-Fe})=1.5$ . The ratios between each of these values and the Q-factor value measured in air were equal to:  $\Delta Q/Q(\text{air})_1=69\%$ ,  $\Delta Q/Q(\text{air})_2=0.4\%$  and  $\Delta Q/Q(\text{air})_3=2.8\%$ . The efficiency of the developed algorithm for spurious peak's removal was attested by comparing the values with the ones obtained before applying the algorithm, when the measurement errors negatively impacted the results, as shown by results reported in Sections 7.4-7.7 (see Tab. 7.12).

It is useful to compare the values of  $\Delta Q$  above with the ones obtained with the LCR system (second row of Tab. 7.17). When copper was introduced into the system, the Q-factor shifted by a quantity equal to  $\Delta Q=10$ , and the ratio between this value and the Q-factor value measured in air was equal to  $\Delta Q/Q(\text{air})=48\%$ . This means that, with regards to imaging of copper, the sensitivity of the new EII system based on active filters is higher by a factor of 3.5 than the sensitivity of the previously used LCR-based system. However, based on the results of the investigations carried out in this work, this conclusion seems to be limited to copper and cannot be extended to lower conductivity samples such as manganese and lead. The active-filter-based system did not represent a significant improvement when these metals were to be detected. However, it could make possible to distinguish between copper and aluminium samples, based on the measurements of the Q-factor shifts produced by them.

The results shown here proved that: 1) the active-filter based EII system was more sensitive than the LCR-based one ( $\Delta Q$  larger by a factor of 3.5); 2) images having higher contrast could be produced with the new system, as demonstrated by the Q-factor larger absolute values of the active-filter based system (e.g. 86.5 vs 11.3, for a  $25 \times 25 \times 1 \text{ mm}^3$  sample made of Cu, as in Tabs. 7.17 and 7.18). This implied the possibility to obtain clearer images that would help identifying hazardous materials, also in the case of objects having complicated shapes.

The results demonstrated that the proposed EII method based on the use of an active-filter-based system and the application of a data removal algorithm represented a better solution than the method based on LCR circuits, previously developed. The further step that

was taken to demonstrate this achievement was to adopt the imaging technique described in Section 4.3 to image a Cu sample by means of the active-filter-based system proposed in Section 7.4, with the measurement method described in Section 7.10. For this purpose, a 3-cm-diameter Cu disk was placed under the coil and the scanning technique based on position-resolved-measurements of the Q-factor described in Section 4.3 was adopted. Additionally, the *Labview* program previously created (Section 4.3) was modified to allow the remote control of the NA and the XY stage that was used to move the sample. This allowed an automated imaging process similar to the one used with the LCR-based EII system to take place. The *Matlab* data removal algorithm was embedded in the *Labview* program.

The proposed method was successful as an image reproducing the 3-cm-diameter Cu disk was obtained, as shown in Fig. 7.27.

This result proved the capability of the proposed EII method to image high conductivity samples. To complete these investigations, the feasibility of the system to identify metals hidden behind a conductive shield was assessed, by placing a 1.5-mm-thick Al shield in between the 3-cm-diameter Cu disk previously used and the coil part of the active-filter-based circuit. The result of this final part of the investigation is reported in Fig. 7.28.

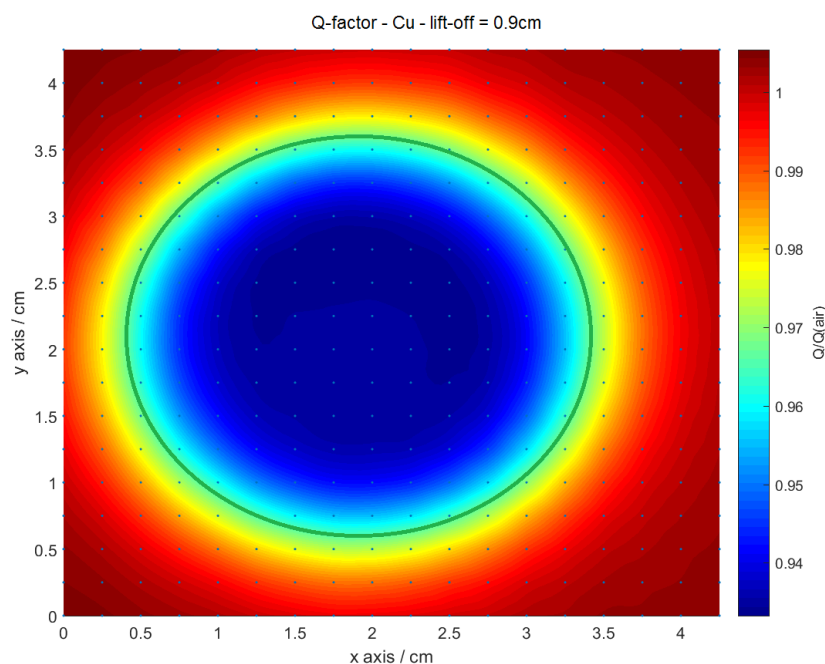


Fig. 7.27. Image representing a 3-cm-diameter Cu disk, obtained with the EII active filter-based system developed in this study.

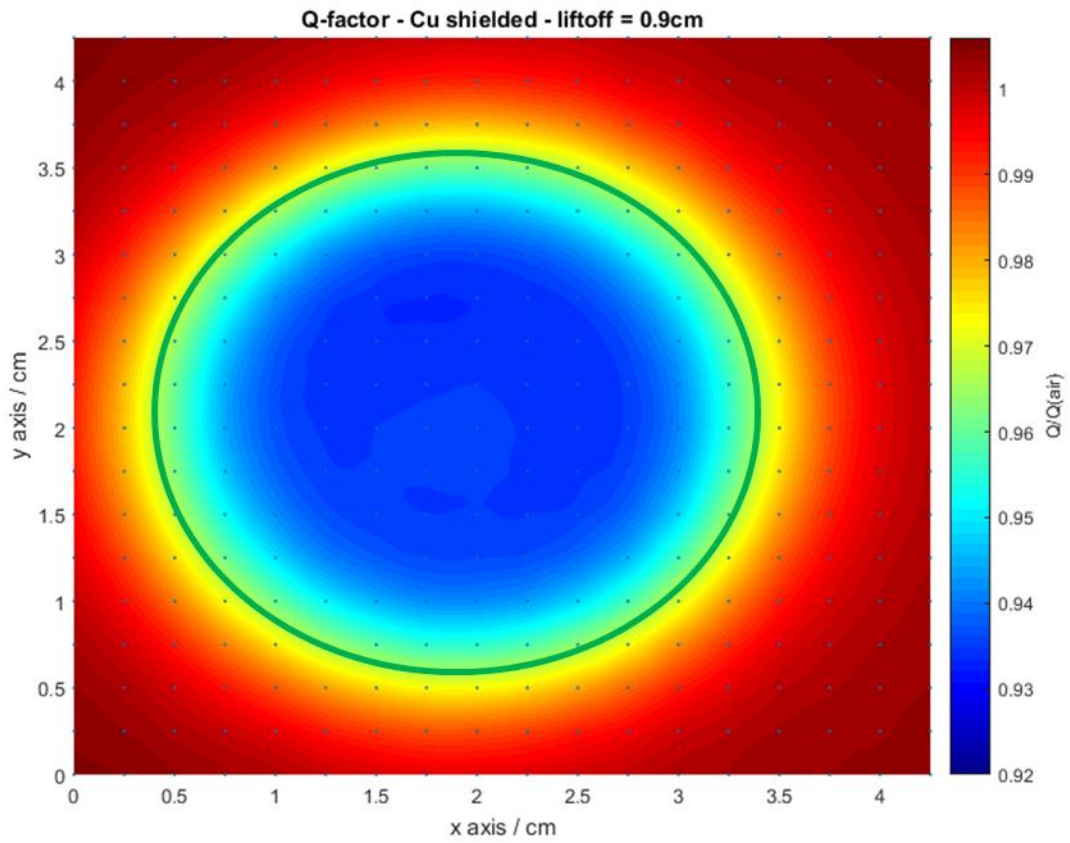


Fig. 7.28. Image representing a 3-cm-diameter Cu disk, shielded with a 1 mm-thick Al shield. The image was obtained with the EII active filter-based system developed in this study, resonating at a frequency  $f_r=23.6$  kHz.

## 8 Conclusions

This work describes the development of a method which opened a route to imaging and characterisation of conductive samples. The proposed method successfully imaged high-conductivity samples (made of copper, Cu, and aluminium, Al), which were covered with Al foil. Further investigations addressed the problem of adopting the developed method for imaging metals that were hidden behind thicker shields than the Al foil used at this stage. Setting up an automated measurement system allowed achieving higher precision in the positioning of the samples, and made the measurement process faster and remotely controlled. This led to establishing a new experimental method that was successful at producing 2D images of 14 metallic objects, both magnetic and non-magnetic, with few different planar geometries, and values of conductivity ranging from  $0.54 \times 10^6$  to  $59.77 \times 10^6$  S/m. These images were conductivity maps obtained by means of two imaging techniques based on position-resolved measurements of the system's Q-factor and resonant frequency, respectively. Both techniques enabled to produce conductivity maps of the samples included in this study.

Experimental results highlighted the higher sensitivity of the Q-factor technique compared to the resonant frequency one. The sensitivity for Q-factor measurements was quantified as the relative difference between the Q-factor value measured with the system in the presence of a metallic sample and the Q-factor value of the system in the absence of the sample. In a similar fashion, the sensitivity for resonant frequency measurements was assessed by measuring the resonant frequency of the system in the presence of the sample and calculating the difference between the resonant frequency measured 'in air'. The higher sensitivity of the Q-factor technique is shown by looking at the measured Q-factor and resonant frequency values, which were found to vary within the following ranges, for the 14 conductive samples considered in these investigations:  $\Delta Q = [-11, -2]\%$ ,  $\Delta f = [-0.3, 0.7]\%$ . These brackets represent intervals of Q-factor and resonant frequency shifts, measured in the presence of the 14 samples used in these investigations. The values on the left correspond to the lower values of  $\Delta Q$  and  $\Delta f_r$  within the given intervals, those on the right correspond to the higher values.

Images were obtained for a set of aluminium disks of different diameters, and a Canny-edge detection algorithm was applied to them, to find the contour of the imaged disk. The diameter estimated from the images displayed a linear relationship with the samples' tabulated diameters, for both Q-factor and resonant frequency images, with a coefficient of determination equal to unity within a few percent. Results obtained by applying the Canny-edge detection method to images obtained by means of the two proposed techniques, based on position-resolved measurements of the Q-factor and resonant frequency shifts, revealed differences between the two techniques. In particular, results obtained with respect to 2D imaging of 'unshielded' conductive samples highlighted that the Q-factor technique allowed more accurate reproduction of the samples' dimensions than the resonant frequency technique, with an agreement within 2% between the estimated diameters and the measured ones (for disk diameters larger than 4 cm). Results obtained with both imaging techniques were very satisfactory as they showed that the contours of the imaged samples could be determined with an agreement between 1% and 8% for Q-factor and resonant frequency measurements of disks with diameters between 1.5 and 7.6 cm, respectively. This validated the reliability of the proposed imaging system for reproducing the samples' dimensions in the case of 'unshielded' conductive samples.

Further investigations aimed at optimising the values of components that were used to build the LCR-based system with a capacitor bank, used to adjust its resonant frequency to achieve penetration through shielding materials. This led to identifying the best choice of resistance and capacitance, for achieving the highest Q-factor shift that could be obtained, when a conductive sample was placed in the vicinity of the coil. By using the LCR-based EII system with a capacitance  $C$  causing the skin depth through Al to be equal to  $\delta=3$  mm, 2D imaging of concealed metallic samples hidden behind 1.5-mm-thick Al shields was successful. In particular, the proposed method enabled to reveal the presence of concealed metallic objects (having conductivities ranging from 0.54 to 59.77  $\text{MSm}^{-1}$ ), as well as accurately estimate their shape, thus demonstrating that the proposed EII system represented an effective detection tool that could be used for security applications.

The same quantitative analysis previously used to determine the imaged samples' diameters was conducted for images of 'shielded' samples, aimed at identifying the dimensions of imaged 'shielded' samples. This analysis showed that the images obtained with resonant frequency measurements reproduced the samples' dimensions more accurately

than the Q-factor images. In both cases, the diameter of the imaged 6-cm-diameter disk was underestimated (by 10% and 23%, with  $f_r$  and Q measurements, respectively), due to the presence of the aluminium shield covering the targets and 'masking' them. An agreement within 1% was obtained after using fitting equations to determine the diameters of the imaged samples. This represented an important result, as it proved that utilising the method based on a LCR-based EII system with a variable capacitor could successfully enable imaging of conductive samples shielded and therefore not visible from the outside.

The second part of this work involved the implementation of a novel version of the EII system, which was based on an active bandpass filter, allowing high Q-factor values to be achieved. The progress following the implementation of this novel EII system constituted the breakthrough of this research work. In particular, the novel system's design allowed Q-factor values larger by a factor up to 46, to be achieved, and Q-factor shifts, due to the presence of a sample made of Cu, larger by a factor of 3.5, compared to the shifts measured with the previously adopted LCR-based system. These improvements were achieved by adopting a measurement procedure based on an algorithm for the removal of a spurious peak that was contaminating the data acquired with the active-filter-based system, by utilising a Network Analyser.

The larger sensitivity of the new system described in Chapter 7 could allow material characterisation of metals having similar electromagnetic properties, to a larger extent compared to the previously adopted solution, based on LCR circuits. Furthermore, the relative variation of Q obtained by dividing the Q-factor shift produced by a copper sample by the Q-factor value measured with the system in the absence of the sample, returned the value of  $\Delta Q (\%) = 69.5\%$ . This variation used to be equal to 48% with the 'old' EII system. This meant that an improvement in the image contrast was also obtained, thus implying the possibility to obtain clearer images that would help identifying hazardous materials. With this regard, the possibility of using the proposed EII solution for imaging of conductive samples hidden by conductive shields was also investigated. For this purpose, a method based on position-resolved-measurements of the Q-factor was tested by inductively coupling a Cu sample hidden behind an aluminium shield, to the inductor inserted into the active filter constituting the EII system. As a result, an image revealing the presence of the hidden sample was obtained, thus proving that the proposed method could also allow the identification and imaging of shielded conductive objects.

Results of the EII techniques described in this work showed the suitability of both the LCR-based and the active-filter-based EII systems for imaging of both high and low conductivity metals, even when these were shielded by a metallic shield. A sensitivity higher by a factor of 3.5 was obtained with the method based on the use of active filters to image copper, thus making this method more suitable for imaging of highly conductive samples, compared to the previously developed method, based on LCR circuits.

A final remark is about an important advantage that is related to using an EII technique like the one proposed here, which is based on a single coil acting as a sensor and detecting the shifts in the system's resonant frequency and Q-factor, to image conductive samples. This specific technique relies on the coil being facing the hidden side of the sample object during the measurement process. Adopting this particular detection configuration makes the developed EII system extremely useful for practical applications, as the hidden sample is often not accessible from all sides. Having demonstrated the working principle of such system adds value to this work and project it to practical applications, such as detection of unexploded items, often not accessible from all sides. This opens up the possibility of turning the proposed EII system into a portable device for identification of materials of suspicious nature (e.g., unexploded items).

Limitations of the developed imaging system are mainly connected to electromagnetic interference, which would constitute an issue if the system was to be deployed for measurements outside the lab environment (for example, at airport security checks). Suitable shielding should be developed for this purpose, which would enhance the sensitivity and diminish the noise contribution due to the presence of metallic materials in the surrounding of either the coil or the active-filter system. Low-frequency measurements are limited by the larger noise in the quantities of interest (e.g. inductance) and therefore noise reduction methods would be needed to enhance penetration through shields to identify hidden samples. Using more advanced equipment such as impedance analysers with wider functionalities, such as averaging and measurement bandwidth, is a possible solution.

## 9 Future work

The results highlighted in the conclusions to this work raise some questions that could be answered by carrying out further investigations. In particular, the potentiality of the proposed EII system based on active filters for the identification of hidden samples has not been fully exploited yet. To start with, imaging shielded conductive materials, also by penetrating through shields thicker than the one used in this work should be investigated. The EII systems developed in this work and based on a parallel LCR circuit and an active-filter-based circuit allowed imaging a copper sample hidden behind a 1.5-mm-thick Al shield. Whereas this result is significant, given that Al is the most difficult non-ferromagnetic metal to penetrate through, due to its largest value of conductivity, it would be necessary to test the possibility of the system to image through thicker shields. Materials such as lead are currently employed to hide hazardous objects and bombs, since lead is X-ray absorbent. Therefore, investigating the possibility to image by penetrating through thick shields made of this type of metal would be interesting for detection and imaging aimed at security applications. This is possible in principle, as long as electromagnetic radiation of appropriate skin depth is employed. It could be achieved by using the EII system here proposed, by introducing resistors of higher values into the rotary switch, thus enabling the active-filter-based system to resonate at lower values of frequency, leading to larger values of skin depth. For this purpose, the behaviour of the system at low values of resonance frequency, i.e., of the order of magnitude of the Hz, should be investigated. Provided that the system electronics works and the noise/interference sources are under control, the system should allow imaging through shields of much larger thicknesses than the one with which the system was tested.

Another open question would be about imaging metals of lower conductivities than copper, especially in shielded configurations. The possibility of tuning the system's resonant frequency, thus adjusting the skin depth, was beneficial in allowing penetration through materials having both different values of thickness and different electromagnetic properties, which is fundamental for practical applications. One of the other parameters, on which the performance of EII systems depends, is given by the amount of eddy currents induced inside the system, which in turns depends on the coil's inductance. On this subject, these studies have one limitation: there will always need to be a compromise between having good spatial

resolution and the ability to discriminate between different materials, including the target material and the material screening it. This is because using larger coils having larger inductance might impact the image resolution, due to the measurement method here proposed being based on a coil that is used both to induce eddy currents inside the sample and to detect the resonance shifts due to the presence of the sample. Two alternatives to the use of a coil with a larger diameter should be explored. The first one relies on the use of a coil having a larger number of turns thus producing a higher magnetic field. The second one involves investigating the impact of increasing the current circulating in the coil, in order to increase the eddy current amount. These investigations should be carried out with the purpose of finding a trade-off between the need to induce a larger amount of eddy currents in the sample to be imaged, and the need for the image spatial resolution to allow reproduction of the objects' shape, especially in the more interesting case of non-simple geometries.

From a theoretical point of view, modelling of the EII system based on the active-filter-based circuit and the conductive sample may be useful to understand the effects due to the presence of a metal which is inductively coupled to a resonant circuit, in terms of both eddy currents and magnetic field enhancement.

Finally, further investigations should be carried out to assess the possibility to turn the active-filter-based system into a 3D system that could allow 3D images of conductive objects to be obtained. One possibility would be to use a similar resonant circuit and move this coil w.r.t. the sample to be imaged, while maintaining the sample in a fixed position. A first section of the 3D image could be obtained by adopting a scanning procedure similar to the one proposed and tested in this work. The sample would then need to be rotated by different angles in order to produce more sections to create a 3D image, by using a suitable reconstruction algorithm.

## 10 List of Author's Publications and Presentations

1. Guilizzoni, R., Watson, J. C., Bartlett, P., Renzoni, F., "Penetrating power of resonant electromagnetic induction imaging". Published in: AIP Advances 6, 095017 (2016); <http://dx.doi.org/10.1063/1.4963299>.
2. Guilizzoni, R., Watson, J. C., Bartlett, P., Renzoni, F., "Electromagnetic Induction Imaging of concealed metallic objects by means of resonating circuits". Published in: Proc. SPIE 9823, Detection and Sensing of Mines, Explosive Objects, and Obscured Targets XXI, 98230P (2016); <http://dx.doi.org/10.1117/12.2223594>.
3. Guilizzoni, R., Watson, J. C., Bartlett, P., Renzoni, F., "Electromagnetic Induction Imaging of concealed metallic objects". Poster presented at the national competition *Set for Britain 2016* (500 entrants), Attlee Suite, Portcullis House, House of Commons, London, UK, March 7, 2016.
4. Guilizzoni, R., Watson, J. C., Bartlett, P., Renzoni, F., "Electromagnetic Induction Imaging of concealed conductive samples". Poster presented at the *UCL Doctoral School Research Poster Competition 2015/16* (category: Built Environment, Engineering Sciences, Mathematical & Physical Sciences – 89 attendees), UCL, South Cloisters, London, UK, March 1, 2016.
5. Guilizzoni, R., Watson, J. C., Bartlett, P., Renzoni, F., "2D imaging of metallic samples by using an inductive system operated at resonance". Presented at the *Defence and Security Doctoral Symposium*, Defence Academy of the United Kingdom, Shrivenham, Swindon, Wiltshire SN6 8LA, UK, November 25-26, 2015.
6. Guilizzoni, R., Watson, J. C., Bartlett, P., Renzoni, F., "Imaging by electromagnetic induction with resonant circuits". Published in: Proc. SPIE 9481, Image Sensing Technologies: Materials, Devices, Systems, and Applications II, 94810Q (2015); <http://dx.doi.org/10.1117/12.2183180>.
7. Guilizzoni, R., Bartlett, P., Watson, J. C., Renzoni, F., "2D imaging of metallic samples by means of resonant frequency measurements". Poster presented at the *Nuclear Detection Showcase*, Atomic Weapons Establishment, Aldermaston, Reading, RG7 4PR, UK, January 29, 2015.

## 11 References

- [1] S. Al-Zeibak and N. Saunders, "A feasibility study of in vivo electromagnetic imaging," *Phys. Med. Biol.*, vol. 38, no. 1, pp. 151–160, 1993.
- [2] A. J. Peyton, Z. Z. Yu, G. Lyon, S. Al-Zeibak, J. Ferreira, J. Velez, F. Linhares, A. R. Borges, H. L. Xiong, N. H. Saunders and M. S. Beck, "An overview of electromagnetic inductance tomography: description of three different systems," *Meas. Sci. Technol.*, vol. 7, no. 3, pp. 261–271, 1996.
- [3] A. Korjenevsky and V. Cherepenin, "Progress in realization of magnetic induction tomography," *Ann. N. Y. Acad. Sci.*, vol. 873, pp. 346–352, 1999.
- [4] H. Griffiths, W. R. Stewart and W. Gough, "Magnetic induction tomography: a measuring system for biological tissues," *Ann. N. Y. Acad. Sci.*, pp. 335–345, 1999.
- [5] H. Griffiths, "Magnetic Induction Tomography," *Magn. induction Tomogr.*, vol. 12, no. 8, pp. 1126–1131, 2001.
- [6] M. Zolgharni, H. Griffiths and P. D. Ledger, "Frequency-difference MIT imaging of cerebral haemorrhage with a hemispherical coil array: numerical modelling," *Physiol. Meas.*, vol. 31, no. 8, pp. S111–25, 2010.
- [7] H. Scharfetter, R. Casañas and J. Rosell, "Biological tissue characterization by magnetic induction spectroscopy (MIS): requirements and limitations.," *IEEE Trans. Biomed. Eng.*, vol. 50, no. 7, pp. 870–880, 2003.
- [8] X. Ma, A. J. Peyton, M. Soleimani and W. R. B. Lionheart, "Imaging internal structure with electromagnetic induction tomography," in *Conference Record - IEEE Instrumentation and Measurement Technology Conference*, p. 300, 2006.
- [9] M. Zolgharni, "Magnetic Induction Tomography for Imaging Cerebral Stroke," Swansea University, 2010.
- [10] J. McFerran, "An electromagnetic method for cancer detection," The Ohio State University, 2009. [http://rave.ohiolink.edu/etdc/view?acc\\_num=osu1253558341](http://rave.ohiolink.edu/etdc/view?acc_num=osu1253558341).
- [11] A. Korjenevsky, V. Cherepenin and S. Sapetsky, "Magnetic induction tomography: experimental realization," *Physiol. Meas.*, vol. 21, no. 1, pp. 89–94, 2000.
- [12] S. R. Higson, P. Drake, D. W. Stamp, A. Peyton, R. Binns, A. Lyons and W. Lionheart, "Development of a sensor for visualization of steel flow in the continuous casting nozzle," *Rev. Metall. d'Informations Tech.*, vol. 100, pp. 629–632, 2003.
- [13] H. Griffiths, W. Gough, S. Watson, and R. J. Williams, "Residual capacitive coupling and the measurement of permittivity in magnetic induction tomography," *Physiol. Meas.*, vol. 28, no. 7, pp. S301–S311, 2007.

- [14] M. Soleimani, "Simultaneous reconstruction of permeability and conductivity in magnetic induction tomography," *J. Electromagn. Waves Appl.*, vol. 23, pp. 785–798, 2009.
- [15] H.-Y. Wei and M. Soleimani, "A Magnetic Induction Tomography System for Prospective Industrial Processing Applications," *Chinese J. Chem. Eng.*, vol. 20, no. 2, pp. 406–410, 2012.
- [16] H.-Y. Wei, L. Ma and M. Soleimani, "Volumetric magnetic induction tomography," *Meas. Sci. Technol.*, vol. 23, pp. 1–9, May 2012.
- [17] M. H. Pham, Y. Hua and N. B. Gray, "Eddy Current Tomography for Metal Solidification Imaging," Derbyshire, UK, April 17<sup>th</sup>, pp. 451–458, 1999.
- [18] M. Soleimani, W. R. B. Lionheart, A. J. Peyton and X. Ma, "Image Reconstruction in 3D Magnetic Induction Tomography Using a FEM Forward Model," in *3rd World Congress on Industrial Process Tomography*, Banff, Canada, pp. 252–255, 2003.
- [19] L. Ma, "Magnetic Induction Tomography for Non-destructive Evaluation and Process Tomography," Thesis (Doctor of Philosophy (PhD)). University of Bath, 2014.
- [20] L. Ma, H.-Y. Wei and M. Soleimani, "Planar magnetic induction tomography for 3D near subsurface imaging," *Prog. Electromagn. Res.*, vol. 138, pp. 65–82, 2013.
- [21] L. Ma, A. Hunt, and M. Soleimani, "Experimental evaluation of conductive flow imaging using magnetic induction tomography," *Int. J. Multiph. Flow*, vol. 72, pp. 198–209, 2015.
- [22] M. Noel and B. Xu, "Archaeological investigation by electrical resistivity tomography: a preliminary study," *Geophys. J. Int.*, vol. 107, no. 1, pp. 95–102, 1991.
- [23] W. Daily and A. Ramirez, "Environmental process Tomography in the United States," *The Chemical Engineering Journal*, vol. 56. pp. 159–165, 1995.
- [24] P. J. Shull, "Nondestructive evaluation: theory, techniques, and applications," New York, Marcel Dekker Inc., 2002.
- [25] L. F. S. G. Rosado, "Non-Destructive Testing Based on Eddy Currents," Master's Degree Dissertation in Electronics Engineering, Technical University of Lisbon, 2009.
- [26] P. Lorrain and D. Corson, "Electromagnetic fields and waves," San Francisco: W. H. Freeman and Company, 1970.
- [27] A. C. Kak and M. Slaney, "Tomographic Imaging with Diffracting Sources," in *Principles of Computerized Tomographic Imaging*, Society of Industrial and Applied Mathematics, pp. 203–273, 2001.
- [28] R. A. Brooks and G. Di Chiro, "Principles of computer assisted tomography (CAT) in radiographic and radioisotopic imaging.," *Phys. Med. Biol.*, vol. 21, no. 5, pp. 689–732, 1976.

- [29] W. R. B. Lionheart, "EIT reconstruction algorithms: pitfalls, challenges and recent developments.," *Physiol. Meas.*, vol. 25, no. 1, pp. 125–126, 2004.
- [30] G. J. Saulnier, R. S. Blue, J. C. Newell, D. Isaacson and P. M. Edic, "Electrical impedance tomography," *Signal Process. Mag. IEEE*, vol. 18, no. 6, p. 31, 2001.
- [31] Q. Marashdeh, L.-S. Fan, B. Du and W. Warsito, "Electrical Capacitance Tomography – A Perspective," *Ind. Eng. Chem. Res.*, vol. 47, no. 10, pp. 3708–3719, 2008.
- [32] H. Y. H. Yan, L. J. L. L. J. Liu and D. Z. Q. D. Z. Qiang, "An Iterative Electrical Capacitance Tomography Image Reconstruction Algorithm," *2009 Second Int. Symp. Comput. Intell. Des.*, vol. 1, no. 2, pp. 9–12, 2009.
- [33] M. Zhang, L. Ma and M. Soleimani, "Magnetic induction tomography guided electrical capacitance tomography imaging with grounded conductors," *Measurement*, vol. 53, pp. 171–181, 2014.
- [34] W. Daily, A. Ramirez, A. Binley and D. LeBrecque, "Electrical resistance tomography," *Lead. Edge*, vol. 23, no. 5, pp. 438–442, 2004.
- [35] F. Dickin and M. Wang, "Electrical resistance tomography for process applications," *Meas. Sci. Technol.*, vol. 7, no. 3, pp. 247–251, 1999.
- [36] E. Somersalo, "Introduction to Inverse Problems In imaging," Copenhagen, 2014.
- [37] D. Placko and I. Dufour, "Eddy current sensors for nondestructive inspection of graphite composite materials," in *Proceedings of the IEEE Conference of the Industry Applications Society (IAS'92)*, Houston, TX, USA, October 1992; pp. 1676-1682, 1992.
- [38] J. García-Martín, J. G. Gil and E. V. Sanchez, "Non-destructive techniques based on eddy current testing," *Sensors* 11, 2525-2565, 2011.
- [39] Y. Chung, J. Galayda and A. P. Source, "Effect of Eddy Current in the Laminations on the Magnet Field," *LS Note No. 200*, 1992.
- [40] R. C. McMaster, "Nondestructive testing handbook," New York: The Ronald Press Company, 1959.
- [41] G. R. Quinn, "Handbook of nondestructive evaluation," C. J. Hellier, Ed. New York: McGraw-Hill, 2003.
- [42] P. B. Nagy, "Ultrasonic and Electromagnetic NDE for Structure and Material Characterization: Engineering and Biomedical Applications," Boca Raton: CRC Press Talyor & Francis Group, 2012.
- [43] B. Darrer, P. Bartlett, J. Watson and F. Renzoni, "Magnetic induction tomography : resolution and penetrating power through metal shields," in *7th World Congress on Industrial Process Tomography, WC IPT7*, 2-5 September 2013, Krakow, Poland, pp. 51–60, 2013.
- [44] B. J. Darrer, J. C. Watson, P. Bartlett and F. Renzoni, "Magnetic Imaging: a New Tool for UK National Nuclear Security," *Sci. Rep.*, vol. 5, no. 7944, pp. 1–6, 2015.

- [45] B. J. Darrer, J. C. Watson, P. Bartlett and F. Renzoni, "Toward an Automated Setup for Magnetic Induction Tomography," *IEEE Trans. Magn.*, vol. 51, no. 1, 2015.
- [46] B. J. Darrer, J. C. Watson, P. A. Bartlett and F. Renzoni, "Electromagnetic imaging through thick metallic enclosures," *AIP Adv.*, vol. 5, no. 087143, pp. 1–8, 2015.
- [47] L. Marmugi, S. Hussain, C. Deans and F. Renzoni, "Magnetic induction imaging with optical atomic magnetometers: towards applications to screening and surveillance," *Proc. SPIE*, vol. 9652, no. October, pp. 1–11, 2015.
- [48] L. Marmugi and F. Renzoni, "Optical Magnetic Induction Tomography of the Heart," *Sci. Rep.*, vol. 6, no. 23962, 2016.
- [49] C. Deans, L. Marmugi, S. Hussain and F. Renzoni, "Electromagnetic induction imaging with a radio-frequency atomic magnetometer," *Appl. Phys. Lett.*, vol. 108, no. 10, 2016.
- [50] P. Gaydecki, S. Quek, G. Miller, B. T. Fernandes and M. A. M. Zaid, "Design and evaluation of an inductive Q-detection sensor incorporating digital signal processing for imaging of steel reinforcing bars in concrete," *Meas. Sci. Technol.*, vol. 13, no. 8, pp. 1327–1335, 2002.
- [51] L. Du, X. Zhu, Y. Han, L. Zhao and J. Zhe, "Improving sensitivity of an inductive pulse sensor for detection of metallic wear debris in lubricants using parallel LC resonance method," *Meas. Sci. Technol.*, vol. 24, no. 7, p. 075106 (10pp.), 2013.
- [52] C. M. Boutry, H. Chandralalim, P. Streit, M. Schinhammer, A. C. Hänzi and C. Hierold, "Characterization of miniaturized RLC resonators made of biodegradable materials for wireless implant applications," *Sensors and Actuators A: Physical*, 189, pp. 344-355, 2013.
- [53] P.A. Bartlett, T. Meydan, S.C. Lea, A.J. Moses, P.I. Williams, G. Landini and A.D. Walmsley, "A comparison of and the compensation for magnetostrictive core inductances in magnetic transducer systems," *Journal of Magnetism and Magnetic Materials*, vol. 320, pp. 1061– 1064, 2008.
- [54] R. Guilizzoni, J. C. Watson, P. Bartlett and F. Renzoni, "Imaging by electromagnetic induction with resonant circuits," *Proc. SPIE*, vol. 9481, *Image Sensing Technologies: Materials, Devices, Systems, and Applications II*, 94810Q, 2015.
- [55] R. Guilizzoni, J. C. Watson, P. Bartlett and F. Renzoni, "Penetrating power of resonant electromagnetic induction imaging," *AIP Adv.* 6, 095017, 2016.
- [56] R. Guilizzoni, J. C. Watson, P. Bartlett and F. Renzoni, "Electromagnetic Induction Imaging of concealed metallic objects by means of resonating circuits," *Proc. SPIE*, vol. 9823, *Detection and Sensing of Mines, Explosive Objects, and Obscured Targets XXI*, 98230P, 2016.
- [57] H. D. Young and R. A. Freedman, "University Physics," 10th ed. San Francisco: Addison Wesley Longman, Inc., 2000.

- [58] J. O'Malley, A. Jones, J. Threadgold, P. Adsley, S. Quillin, S. Robertson, M. Owen, G. Weston, L. Cox, A. Thandi, S. Cullen and I. D. Smith, "Current Status of AWE Programmes into stand-off Detection of Special Nuclear Material (SNM)," Proc. SPIE, vol. 7304, Chemical, Biological, Radiological, Nuclear, and Explosives (CBRNE) Sensing X, 73041J, 8 May 2009.
- [59] J. O'Malley, A. Jones, J. Threadgold, K. Omar, P. Adsley, S. Quillin, S. Robertson, M. Owen, G. Weston, L. Cox, A. Thandi, S. Cullen and I. D. Smith, "Advanced active interrogation sources for remote detection of special nuclear material," Published in: Technologies for Homeland Security, 279–286, 2009. HST '09, IEEE Conference on, Waltham, MA, USA, 11-12 May 2009.
- [60] W. J. Duffin, "Electricity and Magnetism," Fourth edition, McGraw Hill, London, 1998.
- [61] S. Chikazumi, "Physics of Magnetism," United States of America: John Wiley & Sons, Inc., 1964.
- [62] C. Hellier, "Handbook of non-destructive evaluation," Mc Graw-Hill, USA, 2003.
- [63] Q. H. Nguyen, L. D. Philipp, D. J. Lynch, A. F. Pardini, "Steam tube defect characterization using eddy current Z-Parameters," Res. Nondestruct. Eval., 10, pp. 227-252, 1998.
- [64] J. D. Jackson, "Classical electrodynamics," Wiley, 1975.
- [65] Free, George, "High-accuracy conductivity measurements in nonferrous metals," Eddy-current characterization of materials and structures, ASTM STP 722, George Birnbaum and George Free, Eds., American Society for testing and materials, 1981, pp. 121-128, 1981.
- [66] "CRC handbook of chemistry and physics: A ready-reference book of chemical and physical data," CRC Press, p. E-85 – E-125, 1981.
- [67] "Wayne Kerr ENA Series Precision Impedance Analyzer 6500B," Manual, 2013.
- [68] J. F. Canny, "A computational approach to edge detection," IEEE Transactions on pattern analysis and machine intelligence 8(6), pp. 679-698, 1986.
- [69] J. R. Parker, "Algorithms for image processing and computer vision," United States of America: John Wiley & Sons, Inc., 1997.
- [70] R. C. Gonzalez and R. E. Woods, "Digital image processing," 3rd ed. Upper Saddle River: Pearson Prentice Hall, 2008.
- [71] R. Deriche, "Using Canny's criteria to derive a recursively implemented optimal edge detector," Int. J. Comput. Vis., vol. 1, no. 2, p. 179, 1987.
- [72] J. Canny, "Finding edges and lines in images," Technical Report, Massachusetts Institute of Technology, Cambridge, MA, USA 1983.

- [73] B. J. Darrer, J. C. Watson, P. Bartlett and F. Renzoni, "Magnetic Imaging through Metallic Enclosures," Conference: 7<sup>th</sup> International Symposium on Process Tomography, at Dresden, Germany, September 2015.
- [74] B. J. Darrer, "Electromagnetic induction imaging through metallic shields," PhD thesis, Physics & Astronomy Dept., University College London, August 2016.
- [75] H. A. Wheeler, "Formulas for the Skin Effect," Proc. IRE, vol. 30, no. 9, p. 415, 1942.
- [76] J. C. Moulder, E. Uzal and J. H. Rose, "Thickness and conductivity of metallic layers from eddy current measurements," Rev. Sci. Instrum. 63 (6), 3455, 1992.
- [77] P. Horowitz and W. Hill, "The art of electronics," 3rd ed. New York, NY 10013-2473, USA: Cambridge University Press, 2015.
- [78] <http://www.analog.com/media/en/technical-documentation/data-sheets/OP27.pdf>
- [79] "Keysight E5061B Network Analyzer, 100 kHz to 1.5/3 GHz, 5 Hz to 500 M/1.5 G/3 GHz," Data sheet, Keysight Technologies.
- [80] "Agilent E5061B Network Analyzer," Manual, 2010.